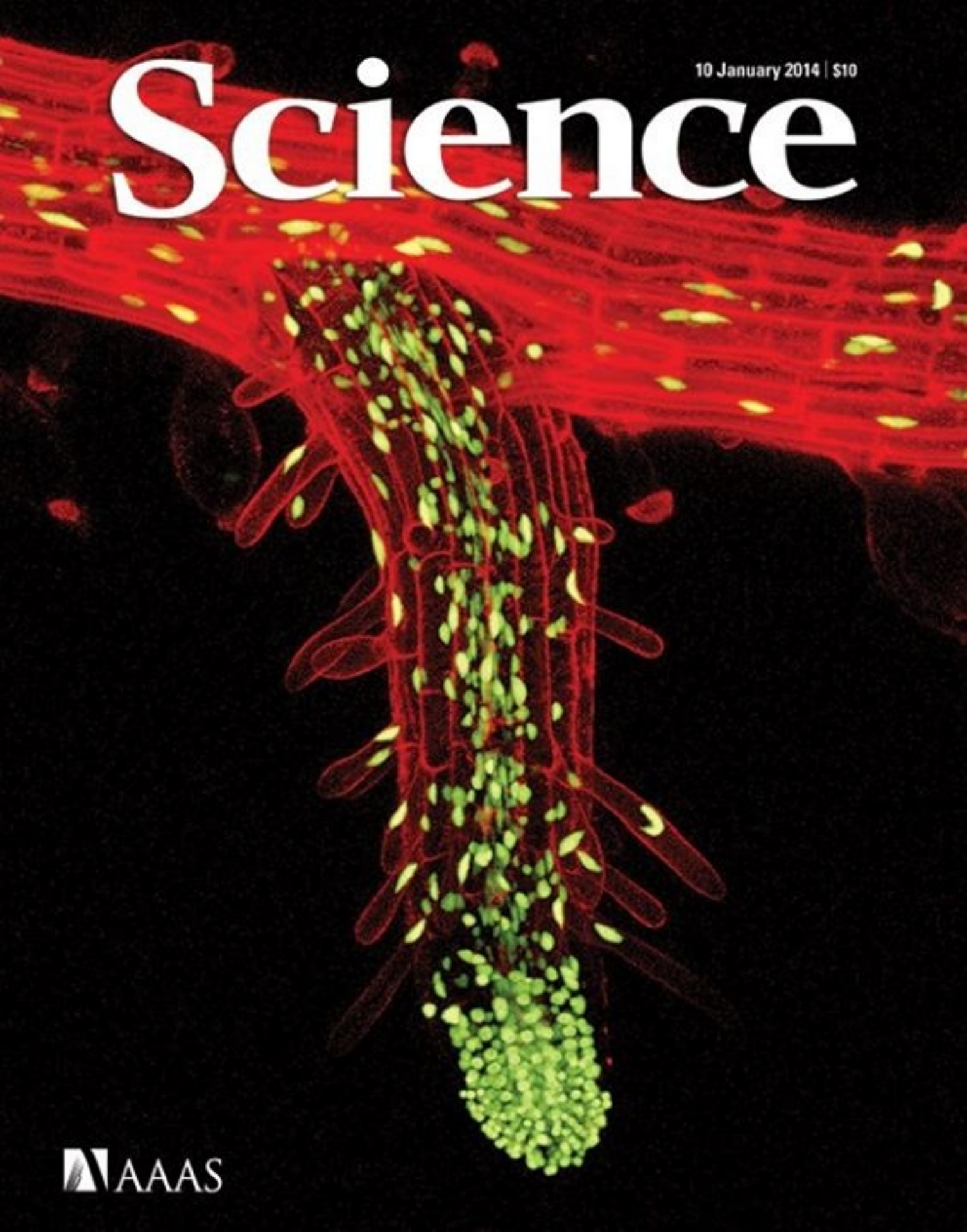
10 January 2014 | $10

Science



AAAS

EDITORIAL

117 EMBO at 50
Paul Nurse

NEWS OF THE WEEK

122 A roundup of the week's top stories

NEWS & ANALYSIS

125 Studies Suggest Two-Way Street for College Majors

126 Rare Celestial Trio to Put Einstein's Theory to the Test

127 Europe Focuses Fusion Research on Building a Working Power Reactor

128 U.S. Regulators Unveil New Ocean Noise Rules for Marine Mammals

129 Once Failing Biology Society Thrives as It Nurtures New Disciplines

NEWS FOCUS

130 Mariners of the Lost Sea
Time Capsule in the Desert

133 A Pancreas in a Box

LETTERS

136 Antibiotics: Call for Real Change
K. E. Nachman et al.

Antibiotics: Discontinue Low-Dose Use
R. J. Tarpley

Science for Sale: Fair Evaluation Standards
C. Luo

Science for Sale: Authorship Confirmed
R. Chen

Science for Sale: Improve Ethics Education
C. Mitcham and R. Snieder

137 CORRECTIONS AND CLARIFICATIONS

BOOKS *ET AL.*

138 China's Urban Billion
T. Miller, reviewed by X. Meng

139 MaddAddam
M. Atwood, reviewed by M. A. Goldman

POLICY FORUM

140 Coping with Uncertainty in Space Science Planning
C. Kennel and A. Dressler

PERSPECTIVES

142 A Pardon for the Dingo
R. G. Roberts
>> Review p. 151

143 Bacterial Vesicles in the Ocean
D. Scanlan
>> Report p. 183

144 Enabling Optical Analog Computing with Metamaterials
A. Sihvola
>> Report p. 160

146 Young Neurons Sever Ties to the Parental Niche
S. Tozer and X. Morin
>> Report p. 200

147 Can Cancer Trigger Autoimmunity?
M. W. L. Teng and M. J. Smyth
>> Research Article p. 152

148 Glimpsing Eruptions on Europa
J. R. Spencer
>> Report p. 171

150 Retrospective: Nelson R. Mandela (1918–2013)
S. S. A. Karim

REVIEW

151 Status and Ecological Effects of the World's Largest Carnivores
W. J. Ripple et al.
Review Summary; for full text: http://dx.doi.org/10.1126/science.1241484
>> Perspective p. 142

CONTENTS continued >>



page 130

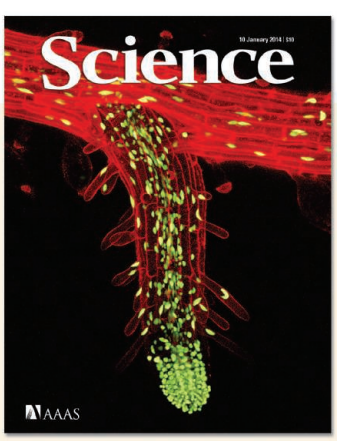


page 138

ON THE WEB THIS WEEK

>> *Science* Podcast
This week's show features the abundance and diversity of bacterial vesicles in the world's oceans and a roundup of stories from our daily news site.

>> Find More Online
Check out *Science* Express, our podcast, videos, daily news, our research journals, and *Science* Careers at **www.sciencemag.org**.



COVER

Confocal light microscopy image of a lateral root emerging from the main root (width: ~130 to 150 micrometers) of a young *Arabidopsis thaliana* plant (green, nuclei; red, cell walls). Lateral roots initiate deep within the primary ("mother") root. Their emergence from the mother root is a highly regulated process requiring adjacent cells to shrink and make way for the developing lateral root. See page 178.

Image: Dr. John Runions/Science Source

DEPARTMENTS

116 This Week in *Science*
119 Editors' Choice
120 *Science* Staff
209 New Products
210 *Science* Careers

Published by AAAS

RESEARCH ARTICLE

152 Association of the Autoimmune Disease Scleroderma with an Immunologic Response to Cancer
C. G. Joseph et al.
The immune system's response to a mutant protein produced by an incipient cancer may help to explain an autoimmune disease.
>> *Perspective p. 147*

REPORTS

157 Giant Spin Oscillations in an Ultracold Fermi Sea
J. S. Krauser et al.
Long-lived oscillations of the internal state of a trapped fermionic potassium-40 gas occur within a single spatial mode.

160 Performing Mathematical Operations with Metamaterials
A. Silva et al.
An approach is described whereby metamaterials can be designed to perform a suite of mathematical functions.
>> *Perspective p. 144*

163 Heteroepitaxial Growth of Two-Dimensional Hexagonal Boron Nitride Templated by Graphene Edges
L. Liu et al.
The orientation of a growing boron nitride film is determined by its graphene template and not the underlying substrate.

167 Self-Accelerating CO Sorption in a Soft Nanoporous Crystal
H. Sato et al.
A soft nanoporous crystalline solid exhibits self-accelerating, selective carbon monoxide adsorption.

171 Transient Water Vapor at Europa's South Pole
L. Roth et al.
Hubble Space Telescope images of Jupiter's moon Europa reveal emission consistent with transient water vapor plumes.
>> *Perspective p. 148*

174 Strong Sensitivity of Pine Island Ice-Shelf Melting to Climatic Variability
P. Dutrieux et al.
Colder surface ocean waters decreased the rate of melting under the Pine Island Glacier ice shelf in 2012.

178 A Spatial Accommodation by Neighboring Cells Is Required for Organ Initiation in *Arabidopsis*
J. E. M. Vermeer et al.
Localized disruption of surrounding plant cell walls paves the way for lateral root development.

183 Bacterial Vesicles in Marine Ecosystems
S. J. Biller et al.
The abundant marine cyanobacterium *Prochlorococcus* sheds membrane vesicles that may contribute to carbon budgets.
>> *Perspective p. 143*; Science *Podcast*

186 Progenitor Outgrowth from the Niche in *Drosophila* Trachea Is Guided by FGF from Decaying Branches
F. Chen and M. A. Krasnow
Progenitor cells in flies form new trachea by following an embryonic inducer reactivated in decaying branches.

189 Mutational Analysis Reveals the Origin and Therapy-Driven Evolution of Recurrent Glioma
B. E. Johnson et al.
Primary brain tumors and their recurrences can exhibit vastly different mutational profiles.

193 Single-Cell RNA-Seq Reveals Dynamic, Random Monoallelic Gene Expression in Mammalian Cells
Q. Deng et al.
Independent allelic transcription generates fluctuations in the single-cell transcriptome.

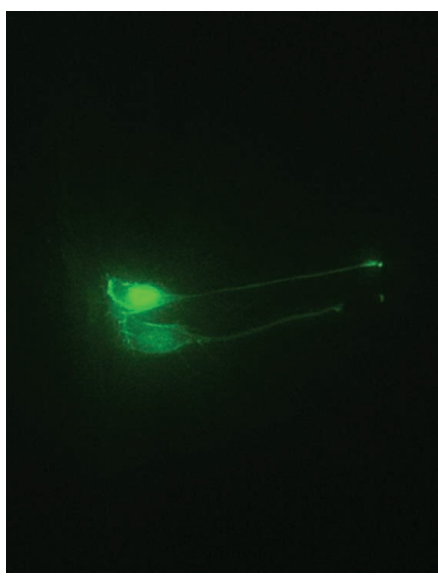
197 Modular Organization of Axial Microcircuits in Zebrafish
M. W. Bagnall and D. L. McLean
Larval zebrafish show more refined musculature control than expected.

200 Apical Abscission Alters Cell Polarity and Dismantles the Primary Cilium During Neurogenesis
R. M. Das and K. G. Storey
During vertebrate neuronal development, the apical membrane is shed, allowing further differentiation.
>> *Perspective p. 146*

204 Internalization of *Salmonella* by Macrophages Induces Formation of Nonreplicating Persisters
S. Helaine et al.
Upon internalization, intracellular *Salmonella* choose between replication or a form of quiescence known as persistence.



pages 148 & 171



pages 146 & 200

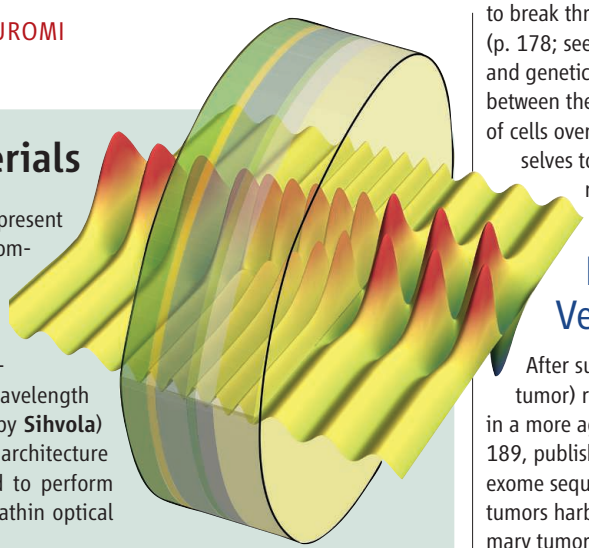
CREDIT: (BOTTOM) RAMAN M. DAS/STOREY LAB, COLLEGE OF LIFE SCIENCES, UNIVERSITY OF DUNDEE, UK

SCIENCE (ISSN 0036-8075) is published weekly on Friday, except the last week in December, by the American Association for the Advancement of Science, 1200 New York Avenue, NW, Washington, DC 20005. Periodicals Mail postage (publication No. 484460) paid at Washington, DC, and additional mailing offices. Copyright © 2014 by the American Association for the Advancement of Science. The title SCIENCE is a registered trademark of the AAAS. Domestic individual membership and subscription (51 issues): $149 ($74 allocated to subscription). Domestic institutional subscription (51 issues): $990; Foreign postage extra: Mexico, Caribbean (surface mail) $55; other countries (air assist delivery) $85. First class, airmail, student, and emeritus rates on request. Canadian rates with GST available upon request, GST #1254 88122. Publications Mail Agreement Number 1069624. **Printed in the U.S.A.**

Change of address: Allow 4 weeks, giving old and new addresses and 8-digit account number. **Postmaster:** Send change of address to AAAS, P.O. Box 96178, Washington, DC 20090–6178. **Single-copy sales:** $10.00 current issue, $15.00 back issue prepaid includes surface postage; bulk rates on request. **Authorization to photocopy** material for internal or personal use under circumstances not falling within the fair use provisions of the Copyright Act is granted by AAAS to libraries and other users registered with the Copyright Clearance Center (CCC) Transactional Reporting Service, provided that $30.00 per article is paid directly to CCC, 222 Rosewood Drive, Danvers, MA 01923. The identification code for *Science* is 0036-8075. *Science* is indexed in the *Reader's Guide to Periodical Literature* and in several specialized indexes.

EDITED BY PHIL SZUROMI

Computational Metamaterials



Optical signal processing of light waves can represent certain mathematical functions and perform computational tasks on signals or images in an analog fashion. However, the complex systems of lenses and filters required are bulky. Metamaterials can perform similar optical processing operations but with materials that need only be a wavelength thick. **Silva *et al.*** (p. 160; see the Perspective by **Sihvola**) present a simulation study that shows how an architecture based on such metamaterials can be designed to perform a suite of mathematical functions to create ultrathin optical signal and data processors.

Collective Coherent Spin Dynamics

Ultracold gases have shown considerable promise for the quantum simulation of more complicated systems, such as correlated electrons in solids. Usually, researchers use two hyperfine states of the atoms to correspond to the spin up and down states of the electrons; however, these gases typically have a much richer internal state structure. **Krauser *et al.*** (p. 157) observed the coherent behavior of a gas of potassium-40 atoms that had 10 accessible internal spin states and that evolved through collisions. The spin state of the system oscillated as a whole, a surprising finding given that the atoms are fermions.

Soft, Selective CO Sorption

Many industrial processes produce CO, which could be used as a chemical feedstock, but separation of CO from other gases, especially N_2, is too difficult to be economically viable. **Sato *et al.*** (p. 167, published online 12 December 2013) now report that a porous coordination polymer containing Cu^{2+} ions can selectivity bind CO through serial structural changes reminiscent of allosteric effects in proteins. The separation of CO-N_2 mixtures can be achieved with a low input energy for CO desorption.

Europa's Plumes

Jupiter's moon Europa has a subsurface ocean and a relatively young icy surface. **Roth *et al.*** (p. 171, published online 12 December 2013; see the Perspective by **Spencer**) analyzed spectral images taken by the Hubble Space Telescope that show ultraviolet emissions from the moon's atmosphere, and report a statistically significant emission signal extending above the satellite's southern hemisphere. This emission is consistent with two 200-km-high plumes of water vapor. Tidal stresses likely play a role in opening and closing fractures at the surface.

Cancer Immunosurveillance Gone Bad?

A subset of patients who develop scleroderma, a debilitating autoimmune disease, have an elevated risk of developing cancer. These patients harbor autoantibodies to RPC1, an RNA polymerase subunit encoded by the *POLR3A* gene. **Joseph *et al.*** (p. 152, published online December 5; see the Perspective by **Teng and Smyth**) explored whether the RPC1 autoantibodies target a "foreign" antigen derived from a mutated *POLR3A* gene. Sequence analysis revealed that *POLR3A* mutations were present in tumors from six of eight patients with RPC1 autoantibodies but in no tumors from eight control patients who lacked RPC1 autoantibodies. Cell culture data suggested that the *POLR3A* mutations triggered cellular and humoral immune responses in the patients. These results provide support for the "immunosurveillance" hypothesis, which posits the continual eradication of nascent tumor cells via immune responses.

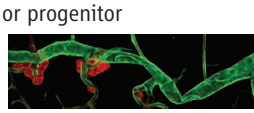
Make Way for the Emerging Rootlet

Plant cells are immobilized by their rigid cells walls, and the root endodermal cell layer maintains a impervious perimeter seal made of an indigestible irregular polymer. Despite these mechanical obstacles, lateral root primordia, which initiate in the deep layers of the root, manage to break through to the surface. **Vermeer *et al.*** (p. 178; see the cover) used live-tissue imaging and genetics to show that signals are exchanged between the root primordium and the handful of cells overlying it, which then cave in on themselves to open up a channel for the growing root primordium.

Back with a Vengeance

After surgery, gliomas (a type of brain tumor) recur in nearly all patients and often in a more aggressive form. **Johnson *et al.*** (p. 189, published online 12 December 2013) used exome sequencing to explore whether recurrent tumors harbor different mutations than the primary tumors and whether the mutational profile in the recurrences is influenced by postsurgical treatment of patients with temozolomide (TMZ), a chemotherapeutic drug known to damage DNA. In more than 40% of cases, at least half of the mutations in the initial glioma were undetected at recurrence. The recurrent tumors in many of the TMZ-treated patients bore the signature of TMZ-induced mutagenesis and appeared to follow an evolutionary path to high-grade glioma distinct from that in untreated patients.

Out with the Old, In with the New



In adult animals, resident stem or progenitor cells residing in niches replenish old tissues with new cells, but how they form new tissue is not well understood. **Chen and Krasnow** (p. 186) examined how progenitor cells in the fruit fly form new tracheae as the old tracheae are destroyed during metamorphosis. Proliferating progenitors move out of their niche by crawling along the surface of decaying tracheal branches. The decaying branches express the chemoattractant FGF (fibroblast growth factor) and create a track that directs progenitors.

Spinal Circuit Complexity in Fish

Rapid coordination of opposing muscle groups helps zebrafish zip through water. **Bagnall and McLean** (p. 197) now describe the neuronal circuits that stabilize swimming fish in their three-dimensional environment. By studying the self-righting behavior of larval zebrafish immobilized in agar, the authors identified parallel excitatory and inhibitory circuits driving dorsal and ventral hemisegments that could be activated independently.

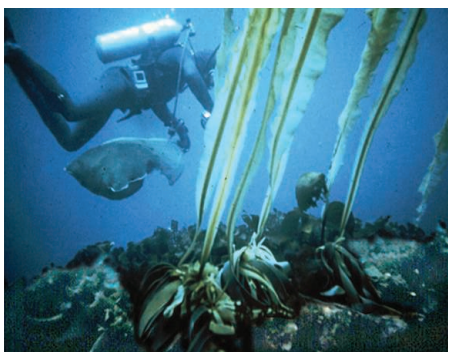
CREDITS (TOP TO BOTTOM): ALEXANDRE SILVA/UNIVERSITY OF PENNSYLVANIA; CHEN AND KRASNOW

Published by AAAS

Additional summaries

Preserving Predators

Large-bodied animals play essential roles in ecosystem structuring and stability through both indirect and direct trophic effects. In recent times, humans have disrupted this trophic structure through both habitat destruction and active extirpation of large predators, resulting in large declines in numbers and vast contractions in their geographic ranges. **Ripple *et al.*** (p. 151; see the Perspective by **Roberts**) review the status, threats, and ecological importance of the 31 largest mammalian carnivores globally. These species are responsible for a suite of direct and indirect stabilizing effects in ecosystems. Current levels of decline are likely to result in ecologically ineffective population densities and can lead to ecosystem instability. The preservation of large carnivores can be challenging because of their need for large ranges and their potential for human conflict. However, the authors demonstrate that the preservation of large carnivores is ecologically important and that the need for conservation action is immediate, given the severity of the threats they face.



CREDIT: RIPPLE *ET AL.*

Heteroepitaxy Writ Thin

A common method for creating a thin single-crystal layer of a semiconductor for use in an electronic device is heteroepitaxy—growing the layer on the face of a single crystal of a different material that acts as a template for assembly. **Liu *et al.*** (p. 163) now describe a similar process in which the edge of a graphene layer that was grown on a copper surface directs the assembly of a monolayer of hexagonal boron nitride. The boron nitride grew from inside edge of holes created in the graphene layer. The interface and the relative orientation of the two layers were determined by a variety of scanning microscopy and surface diffraction techniques.

Cold Glacier Growth

Pine Island Glacier in Antarctica has thinned significantly during the last two decades and has provided a measurable contribution to sea-level rise as a result. Both glacier dynamics and climate are thought to be responsible for thinning, but exactly how they influence the glacier are incompletely known. **Dutrieux *et al.*** (p. 174, published online 2 January) provide another layer of detail to our understanding of the process through observations of ocean temperatures in the surrounding waters. The thermocline adjacent in the sea adjacent to the glacier calving front (where ice is discharged) lowered by 250 meters in the austral summer of 2012. This change exposed the bottom of the ice shelf to colder surface waters rather than to the warmer, deeper layer, thereby reducing heat transfer from the ocean to the overlying ice and decreasing basal melting of the ice by more than 50% compared to 2010. Those 2012 ocean conditions were partly caused by a strong La Niña event, thus illustrating how important atmospheric variability is for regulating how the Antarctic Ice Sheet responds to climate change.

Carbon Budding in the Ocean

Bacterial vesicles are gaining increasing attention for their roles in pathogenesis, but the abundance of these structures and their ecological roles in nonpathogenic contexts have received little notice. **Biller *et al.*** (p. 183; see the Perspective by **Scanlan**) provide evidence that membrane vesicles ~100 nm in diameter are released by marine cyanobacteria and are a major feature of marine ecosystems. Studies of cultures of *Prochlorococcus*—the most abundant photoautotroph in the oligotrophic oceans—show that vesicles are continually released by this cyanobacterium and are abundant in the marine environment. These vesicles have properties that change the way we think about genetic and biogeochemical exchange among plankton and the dissolved organic carbon pool in marine ecosystems.

Expressing One Allele at a Time

Although genetic traits are often dominant or recessive, the impact of the same heterozygous genotype can vary quite a bit between individuals. **Deng *et al.*** (p. 193), analyzed global gene expression in hundreds of individual mouse cells and found that a substantial fraction of the genes only expressed one of the alleles, chosen randomly, at any given point in time. Such stochasticity in transcription increases the heterogeneity among cells and likely contributes to the phenotypic variance among individuals of identical genotype.

Developing Neurons Make the Cut

Neurons in the developing central nervous system of vertebrates derive from cells adjacent to the ventricles that then proliferate and differentiate to populate the brain. As one of these cells begins to differentiate, the cell nucleus migrates toward its new residence, away from the ventricle surface, and the cell stretches out. At some point, like any maturing adolescent, the cell has to leave home. **Das and Storey** (p. 200; see the Perspective by **Tozer and Morin**) show that instead of letting go and drawing the trailing process up into the migrating cell, the cell cuts off and discards its first roots. The abscission process leaves behind the primary cilium and any signaling systems localized to the cilium.

Persistent Survival

The role of persister cells—dormant cells that survive multidrug treatment—in the context of bacterial pathogenesis has not been explored in depth. Using a single-cell fluorescent dilution technique, **Helaine *et al.*** (p. 204) examined *Salmonella* Typhimurium persister-cell formation in vitro and in infections in mice. Within 30 min after phagocytosis by macrophages, *Salmonella* cells follow one of two fates, either to replication and generation of virulence effectors or to remaining viable but become nonreplicating persisters. *Salmonella* living within a macrophage vacuole are exposed to potentially stressful conditions that induce the expression of 14 Type II toxin-antidote loci in a ppGpp/lon protease-dependent manner, and this system appears to play a role in both virulence factor induction and persister-cell formation. The nonreplicating bacteria represent at least four distinct subpopulations, as defined by their ability to resume growth and their metabolic activity, but different phenotypes are observed in different pathogens and *Escherichia coli* persisters are distinct from *Salmonella* persisters.

Published by AAAS



Paul Nurse is Secretary General of EMBO. E-mail: paul.nurse@royalsociety.org

EMBO at 50

50 YEARS AGO, IN 1964, THE EUROPEAN MOLECULAR BIOLOGY ORGANIZATION (EMBO) WAS FOUNDED by leading scientists who wished to create a network of cooperation in molecular biology. Since then, EMBO has had a major influence on the life sciences in Europe through important but often quite modest objectives and a clear mission to help scientists do their best research. We should celebrate half a century of EMBO's achievements and ensure that it gets the visibility and support it deserves. In this respect, EMBO scientists are an important resource to promote the value of the organization and speak up for why we need to strengthen discovery research in the life sciences for the benefit of society.

Since the early days under the guidance of Raymond Appleyard, EMBO has introduced activities to support the career advancement of young scientists and underrepresented groups in science and has launched a series of high-quality peer-reviewed journals. It also has built strong courses and workshops and an EMBO fellowship program that is an internationally recognized label of excellence for a scientist. EMBO has awarded approximately 6000 long-term postdoctoral fellowships since 1964. Established in 2000, the EMBO Young Investigator Programme was one of the first initiatives in Europe to recognize the needs of young scientists who lead research groups and has helped more than 300 such investigators establish their first independent laboratories. Many of them have become distinguished senior scientists. And installation grants administered by EMBO are supporting young scientists who return to European countries where there are less developed infrastructures.



Speaking more personally, EMBO has been important to me in several ways. It has provided my own training opportunities and has supported postdoctoral fellows in my laboratory. In particular, a DNA cloning course held at the European Molecular Biology Laboratory in 1980 played a crucial role in my early career. It was organized by Noreen and Kenneth Murray, who were instrumental in developing a vaccine against hepatitis B, the first genetically engineered vaccine approved for human use. The course trained participants in gene cloning: how to construct plasmid and phage vectors, generate recombinant DNA molecules, and produce proteins in bacteria. Much of this work can be done with off-the-shelf kits today, but not then. The work was intense and exhausting but enormously instructive. As a student, I received lots of hands-on experience and exposure to some of the great lecturers in molecular genetics. I was starting my first independent laboratory at the University of Sussex in the United Kingdom and was making a transition from classical to molecular genetics with fission yeast to study the molecular basis of cell cycle control. This change was made much easier by this course, and I am sure many scientists worldwide have had similar EMBO experiences.

Today, the core of EMBO is its more than 1500 members and associate members—some of the most renowned scientists worldwide. This community is in an enviable position to build on the successes of EMBO's activities for researchers. The input of the membership allows EMBO to guarantee the highest quality in its selection procedures for members and awards. This expertise will continue to guide the future direction of the organization, from objectives to support research to promoting sound science policies. I encourage scientists to communicate more widely to the public, funding agencies, politicians, policy-makers, and other opinion leaders about the accomplishments and goals of EMBO. By effectively describing what EMBO has achieved in the life sciences, we can argue for increased support to strengthen and expand its activities and ties with the international scientific community in the years ahead.

– Paul Nurse

10.1126/science.1247701

CREDITS (TOP TO BOTTOM): THE ROYAL SOCIETY, UK; SCANRAIL/ISTOCKPHOTO.COM

Downloaded from www.sciencemag.org on January 9, 2014

Published by AAAS



GEOPHYSICS

Tremor Sweet Spots

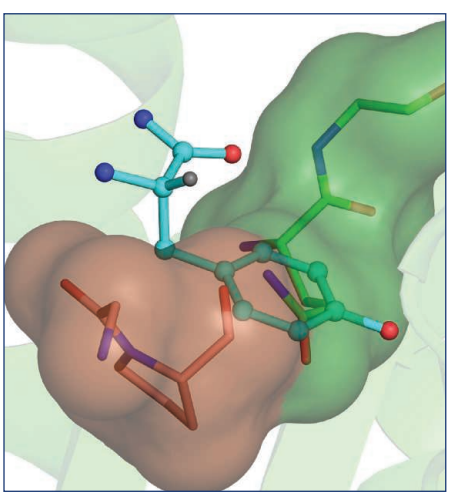
Seismic tremor is thought to be indicative of the slow release of small amounts of stress along plate boundaries, but it can also be triggered by large-amplitude seismic waves generated during large earthquakes. Gomberg and Prejean determined the distribution of tremor in Alaska after 11 of the largest earthquakes (M < 7.2) around the globe between 2006 and 2012. As in previous observations, triggered tremor in the Aleutian Islands is related to the transition of friction along the subducting plate boundary from a locked state to a creeping state. However, tremor was also triggered in central mainland Alaska—a region far away from the subduction zone and devoid of any major crustal faults or appreciable seismic activity. Because there was no single characteristic of the triggering wave source or tectonic environment associated with the two regions, transient frictional processes at the plate interface may be responsible for tremor triggering. However, according to GPS data, neither zone shows any clear evidence of other concurrent related seismic processes such as slow slip events. — NW

J. Geophys. Res. **118**, 10.1002/2013JB010273 (2013).

BIOCHEMISTRY

Chirality Check

Most biological macromolecules are homochiral, and enzymes help to maintain this state of affairs; for example, checkpoints ensure that only L-amino acids are incorporated into proteins during translation. Among these enzymes is D-aminoacyl-tRNA deacylase (DTD), which removes D-amino acids mischarged onto tRNAs. Three types of DTDs have been identified, with the most common form being present in many bacteria and all eukaryotes. DTD faces the mechanistic challenge of acting on diverse D-aminoacyl-tRNAs (D-aa-tRNAs) while not harming L-aminoacyl-tRNAs (L-aa-tRNAs) that are present at much higher concentrations. Although crystal structures have been determined for DTD in the apo form and bound to free D-amino acids, the structural basis of enantioselectivity remained unclear. Ahmad *et al.* report the crystal structure of dimeric DTD from *Plasmodium falciparum* in complex with a substrate analog that mimics D-tyrosine attached to the 3′-OH of the terminal adenosine of tRNA. A critical role in shaping the active site for enantioselectivity is played by a Gly-*cis*Pro motif that is inserted from one DTD monomer into the active site of the other monomer. Mainly main-chain atoms from DTD interact with the substrate, facilitating interaction with a range of D-aa-tRNAs. On the basis of mutational studies of active site residues, the authors suggest an RNA-assisted catalytic mechanism in which the RNA 2′-OH activates a water molecule. — VV



eLife **2**, e01519 (2013).

CELL BIOLOGY

Sugar Sabotage

In patients with diabetes, too much of a good thing—glucose—in the bloodstream causes the debilitating loss of biological functions and can eventually lead to death. Scientists continue to home in on the precise mechanisms by which this occurs, in hope of mitigating the damage. Warren *et al.* have found a mechanism by which excess glucose can alter the functions of vascular endothelial cells, one of the main sites of complications in diabetes. In mouse endothelial cells, too much glucose leads to the overproduction of reactive oxygen species (ROS) in the mitochondria. This excess of ROS causes the phosphorylation of the receptor for vascular endothelial growth factor (VEGF) within the Golgi, rendering the receptor vulnerable to proteolysis. This reduces the levels of VEGF receptor at the cell surface, where it would be able to detect circulating VEGF. Thus, cells chronically exposed to excess glucose become less responsive to VEGF, which is necessary for the proper growth, function, and survival of endothelial cells. — LBR

Sci. Signal. **7**, ra1 (2014).

CHEMISTRY

As Thin As Clay Gets?

Thin films of aluminosilicates can mimic the reactivity of zeolites but avoid the kinetic limitations of diffusion through pore networks. Włodarczyk *et al.* build on their recent work on creating monolayers of aluminosilicates on the surfaces of single crystals of Ru to create thin films of Fe-containing silicates similar to the layers in smectite clays. Analysis of Si-O-Si stretching bands from infrared reflection-absorption spectroscopy revealed that the addition of Fe led to the formation of two-component films containing pure silica and an iron silicate. X-ray photoelectron spectroscopy (XPS) of an oxide with a 1:1 ratio of Fe to Si revealed a high coordination of O to Fe, and low-energy electron diffraction revealed greatly increased ordering even for small amounts of Fe incorporation. Density functional theory confirmed that uniform mixing of Fe is unfavorable thermodynamically as compared to phase separation, and favored a structure in which Fe atoms substitute for Si in the layer adjacent to the substrate and the formation of bridge Fe-O-Ru bonds. Although the Fe oxidation state could not be assigned from the XPS data, assuming that the Fe is in the 3+ oxidation state, the bilayer formed would represent a dehydroxylated form of nontronite, an Fe-rich smectite. — PDS

J. Am. Soc. Chem. **135**, 19222 (2013).

CREDITS (TOP TO BOTTOM): © WIEDE, U. & M./ARCO IMAGES GMBH/ALAMY; S. AHMAD *ET AL.*, *ELIFE* **2** (3 DECEMBER 2013)

www.sciencemag.org

Science

1200 New York Avenue, NW
Washington, DC 20005
Editorial: 202-326-6550, FAX 202-289-7562
News: 202-326-6591, FAX 202-371-9227
Bateman House, 82-88 Hills Road
Cambridge, UK CB2 1LQ
+44 (0) 1223 326500, FAX +44 (0) 1223 326501

Subscription Services For change of address, missing issues, new orders and renewals, and payment questions: 866-434-AAAS (2227) or 202-326-6417, FAX 202-842-1065. Mailing addresses: AAAS, P.O. Box 96178, Washington, DC 20090-6178 or AAAS Member Services, 1200 New York Avenue, NW, Washington, DC 20005

Institutional Site Licenses please call 202-326-6755 for any questions or information

Reprints: Author Inquiries 800-635-7181
Commercial Inquiries 803-359-4578

Permissions 202-326-6765, permissions@aaas.org

Member Benefits AAAS Travels: Betchart Expeditions 800-252-4910; Apple Store www.store.apple.com/us/go/eppstore/aaas; NASA Federal, 1-888-NASA-FCU (1-888-627-2328) or www.nasafcu.com; Cold Spring Harbor Laboratory Press Publications www.cshlpress.com/affiliates/aaas.htm; Hertz 800-654-2200 CDP#343457; Seabury & Smith Life Insurance 800-424-9883; Subaru VIP Program 202-326-6417; Nationwide Insurance http://nationwide.com/aaas; Other Benefits: AAAS Member Services 202-326-6417 or http://membercentral.aaas.org/discounts.

science_editors@aaas.org	(for general editorial queries)
science_letters@aaas.org	(for queries about letters)
science_reviews@aaas.org	(for returning manuscript reviews)
science_bookrevs@aaas.org	(for book review queries)

Published by the American Association for the Advancement of Science (AAAS), *Science* serves its readers as a forum for the presentation and discussion of important issues related to the advancement of science, including the presentation of minority or conflicting points of view, rather than by publishing only material on which a consensus has been reached. Accordingly, all articles published in *Science*—including editorials, news and comment, and book reviews—are signed and reflect the individual views of the authors and not official points of view adopted by AAAS or the institutions with which the authors are affiliated.

AAAS was founded in 1848 and incorporated in 1874. Its mission is to advance science, engineering, and innovation throughout the world for the benefit of all people. The goals of the association are to: enhance communication among scientists, engineers, and the public; promote and defend the integrity of science and its use; strengthen support for the science and technology enterprise; provide a voice for science on societal issues; promote the responsible use of science in public policy; strengthen and diversify the science and technology workforce; foster education in science and technology for everyone; increase public engagement with science and technology; and advance international cooperation in science.

Information for Authors
See pages 716 and 717 of the 8 February 2013 issue or access www.sciencemag.org/about/authors

EDITOR-IN-CHIEF **Marcia McNutt**
EXECUTIVE EDITOR **Monica M. Bradford** NEWS EDITOR **Tim Appenzeller**
MANAGING EDITOR, RESEARCH JOURNALS **Katrina L. Kelner**
DEPUTY EDITORS **Barbara R. Jasny, Andrew M. Sugden, Valda J. Vinson**

Editorial senior editors/commentary Lisa D. Chong, Brad Wible; **senior editors** Gilbert J. Chin, Pamela J. Hines, Paula A. Kiberstis (Boston), Marc S. Lavine (Toronto), Beverly A. Purnell, L. Bryan Ray, Guy Riddihough, H. Jesse Smith, Phillip D. Szuromi (Tennessee), Jake S. Yeston, Laura M. Zahn (San Diego); **associate editors** Melissa R. McCartney (Education Projects), Kristen L. Mueller, Jelena Stajic, Sacha Vignieri (Oregon), Nicholas S. Wigginton (Michigan); **book review editor** Sherman J. Suter; **associate letters editor** Jennifer Sills; **editorial manager** Cara Tate; **senior copy editors** Jeffrey E. Cook, Chris Filiatreau, Cynthia Howe, Harry Jach, Lauren Kmec, Barbara P. Ordway, Trista Wagoner; **senior editorial coordinators** Carolyn Kyle, Beverly Shields; **editorial coordinators** Ramatoulaye Diop, Joi S. Granger, Lisa Johnson, Anita Wynn; **publications assistants**, Aneera Dobbins, Jeffrey Hearn, Dona Mathieu, Le-Toya Mayne Flood, Shannon McMahon, Scott Miller, Jerry Richardson, Brian White; **editorial assistant** Patricia M. Moore; **executive assistant** Alison Crawford; **administrative support** Maryrose Madrid; **intern** Fanny Bernardon

Editorial director, web and new media Stewart Wills; **senior web editor** Sarah Crespi; **web development manager** Martyn Green; **interns** Kristine Hamilton, Linda Poon

News managing editor John Travis; **international news editor** Richard Stone; **deputy news editors** Robert Coontz, Elizabeth Culotta, David Grimm (Online), David Malakoff, Leslie Roberts; **senior correspondents** Eliot Marshall, Jeffrey Mervis, Elizabeth Pennisi **news writers** Yudhijit Bhattacharjee, Adrian Cho, Jennifer Couzin-Frankel, Carolyn Gramling, Jocelyn Kaiser, Richard A. Kerr, Robert F. Service (Pacific NW), Erik Stokstad, Emily Underwood; **web developer** Daniel Berger; **social media strategist** Meghna Sachdev; **intern** Kelly Servick; **contributing correspondents** John Bohannon, Jon Cohen (San Diego, CA), Ann Gibbons, Sam Kean, Eli Kintisch, Andrew Lawler, Mitch Leslie, Charles C. Mann, Virginia Morell, Heather Pringle; **copy editors** Kara Estelle, Nora Kelly; **administrative support** Scherraine Mack; **bureaus** San Diego, CA: 760-942-3252, FAX 760-942-4979; Pacific Northwest: 503-963-1940

Production director Wendy K. Shank; **assistant manager** Rebecca Doshi; **senior specialists** Steve Forrester, Anthony Rosen; **specialist** Jacob Hedrick **Preflight director** David M. Tompkins; **manager** Marcus Spiegler; **specialists** Jason Hillman, Tara Kelly

Art director Yael Fitzpatrick; **associate art director** Laura Creveling; **senior illustrators** Chris Bickel, Katharine Sutliff; **illustrator** Valerie Altounian; **senior art associates** Holly Bishop, Preston Huey; **art associates** Kay Engman, Garvin Grullón, Chrystal Smith; **photo editor** Leslie Blizard

***Science* International**

Europe (science@science-int.co.uk) **editorial: international managing editor** Andrew M. Sugden; **senior editor/commentary** Julia Fahrenkamp-Uppenbrink; **senior editors** Caroline Ash, Stella M. Hurtley, Ian S. Osborne, Peter Stern, Maria Cruz; **contributing editor** Helen Pickersgill; **editorial support** Rachel Roberts, Alice Whaley; **administrative support** Janet Clements, Joan Cuthbert, John Wood; **news: deputy news editor, u.k.** Daniel Clery; **contributing editor, europe** Martin Enserink; **contributing correspondents** Michael Balter (Paris), Kai Kupferschmidt (Berlin), Tania Rabesandratana (Brussels), Gretchen Vogel (Berlin)

Asia Japan Office: Asca Corporation, Tomoko Furusawa, Rustic Bldg. 7F, 77 Tenjin-cho, Shinjuku-ku, Tokyo 162-0808, Japan; +81 3 6802 4616, FAX +81 3 6802 4615, inquiry@sciencemag.jp; **contributing editor, asia** Mara Hvistendahl [China: mhvisten@aaas.org]; **contributing correspondents** Dennis Normile [Japan: dnormile@gol.com]; Christina Larson [China: christina.larson@gmail.com]; Pallava Bagla [South Asia: pallava.bagla@gmail.com]

Latin America contributing correspondent Lizzie Wade [Mexico City: lizziewade@outlook.com]

EXECUTIVE PUBLISHER **Alan I. Leshner**
PUBLISHER **Beth Rosner** CHIEF DIGITAL MEDIA OFFICER **Rob Covey**

Fulfillment Systems and Operations (membership@aaas.org); **customer service supervisor** Pat Butler; **specialists** LaToya Casteel, Michelle Ofordire, Javia Jennings, Chanta Stewart; **manager, data entry** Mickie Napoleoni; **data entry specialists** JJ Regan, Jaimee Wise, Fiona Giblin

Business Operations and Administration director Deborah Rivera-Wienhold; **business systems and financial analysis director** Randy Yi; **manager of fulfillment systems** Neal Hawkins; **systems analyst** Nicole Mehmedovich; **manager, business analysis** Eric Knott; **manager, business operations** Jessica Tierney; **business analysts** Cory Lipman, Cooper Tilton, Celeste Troxler; **financial analyst** Jeremy Clay; **rights and permissions: assistant director** Emilie David; **associate** Elizabeth Sandler; **marketing director** Ian King; **marketing managers** Alison Chandler, Julianne Wielga, Justin Sawyers; **marketing associates** Mary Ellen Crowley, Elizabeth Sattler, Rebecca Riffkin; **senior marketing executive** Jennifer Reeves; **director, site licensing** Tom Ryan; **director, corporate relations** Eileen Bernadette Moran; **senior publisher relations specialist** Kiki Forsythe; **publisher relations manager** Catherine Holland; **publisher relations, eastern region** Keith Layson; **publisher relations, western region** Ryan Rexroth; **customer relations manager** Iquo Edim; **customer relations analysts** Simon Chong, Lana Guz; **associate director, marketing** Christina Schlecht; **marketing associates** Paulina Curto, Mitchell Edmund; **electronic media: director** Lizabeth Harman; **assistant manager** Lisa Stanford; **production specialists** Antoinette Hodal, Nichele Johnston, Lori Murphy, Kimberly Oster; **web and new media: senior project manager** Trista Smith, **project leader** Luke Johnson **computer specialists** Walter Jones, Kai Zhang, **web developer** Chris Coleman; **program director, aaas member central** Peggy Mihelich

director, global collaboration, custom publications, advertising Bill Moran

editor, custom publishing Sean Sanders: 202-326-6430

assistant editor, custom publishing Tianna Hicklin 202-326-6463

sponsored content specialist Candice Nulsen 202-256-1528

associate director, collaboration, custom publications/china/taiwan/korea/singapore Ruolei Wu +86-1367-101-5294

Product (science_advertising@aaas.org); **midwest** Rick Bongiovanni: 330-405-7080, FAX 330-405-7081; **east coast/e. canada** Laurie Faraday: 508-747-9395, FAX 617-507-8189; **west coast/w. canada** Lynne Stickrod: 415-931-9782, FAX 415-520-6940; **uk europe/asia** Roger Goncalves: TEL/FAX +41 43 243 1358; **japan**, Makiko Hara: +81 (0) 3 6802 4616, FAX +81 (0) 3 6802 4615; ads@sciencemag.jp; **china/taiwan** Ruolei Wu: +86 1367 1015 294 rwu@aaas.org

worldwide associate director of *Science* Careers Tracy Holmes: +44 (0) 1223 326525, FAX +44 (0) 1223 326532

Classified (advertise@sciencecareers.org); **u.s./canada/south america** Tina Burks: 202-326-6577; **u.s. corporate** Candice Nulsen 202-256-1528; **sales administrator** Marci Gallun; **europe/row sales** Axel Gesatzki, Sarah Lelarge; **sales assistant** Kelly Grace; **japan** Yuri Kobayashi +81 (0)90-9110-1719; careerads@sciencemag.jp; **china/taiwan** Ruolei Wu: +86 1367 1015 294 rwu@aaas.org; **advertising support manager** Karen Foote: 202-326-6740; **advertising production operations manager** Deborah Tompkins; **senior production specialist/graphic designer** Amy Hardcastle; **production specialist** Yuse Lajiminmuhip; **senior traffic associate** Christine Hall; **sales coordinator** Shirley Young; **marketing manager** Allison Pritchard; **marketing associate** Aimee Aponte

AAAS Board of Directors retiring president, chair William H. Press; **president** Phillip A. Sharp; **president-elect** Gerald R. Fink; **treasurer** David Evans Shaw; **chief executive officer** Alan I. Leshner; **board** Bonnie L. Bassler, May R. Berenbaum, Claire M. Fraser, Elizabeth Loftus, Stephen L. Mayo, Raymond Orbach, Sue V. Rosser, Inder M. Verma

AAAS
ADVANCING SCIENCE, SERVING SOCIETY

SENIOR EDITORIAL BOARD

A. Paul Alivisatos, *Lawrence Berkeley Nat'l. Laboratory*
Ernst Fehr, *Univ. of Zurich*
Michael S. Turner, *University of Chicago*

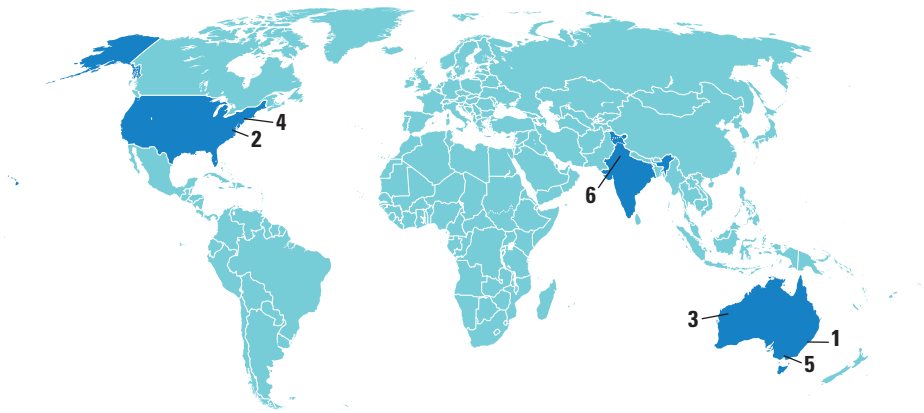
BOARD OF REVIEWING EDITORS

Adriano Aguzzi, *Univ. Hospital Zürich*
Takuzo Aida, *Univ. of Tokyo*
Leslie Aiello, *Wenner-Gren Foundation*
Sonia Altizer, *Univ. of Georgia*
Virginia Armbrust, *Univ. of Washington*
Sebastian Amigorena, *Institut Curie*
Kathryn Anderson, *Memorial Sloan-Kettering Cancer Center*
Siv G. E. Andersson, *Uppsala Univ.*
Peter Andolfatto, *Princeton Univ.*
Meinrat O. Andreae, *Max Planck Inst., Mainz*
Paola Arlotta, *Harvard Univ.*
Johan Auwerx, *EPFL*
David Awschalom, *Univ. of California Santa Barbara*
Ben Barres, *Stanford Medical School*
Jordi Bascompte, *Estación Biológica de Doñana, CSIC*
Facundo Batista, *London Research Inst.*
Ray H. Baughman, *Univ. of Texas, Dallas*
David Baum, *Univ. of Wisconsin*
Mark Bear, *Massachusetts Inst. of Technology*
Yasmine Belkaid, *NIAID, NIH*
Philip Benfey, *Duke Univ.*
Stephen J. Benkovic, *Penn State Univ.*
Christophe Bernard, *Aix-Marseille Univ.*
Gregory C. Beroza, *Stanford Univ.*
Gabriele Bergers, *Univ. of California, San Francisco*
Peer Bork, *EMBL*
Bernard Bourdon, *Ecole Normale Superieure de Lyon*
Chris Bowler, *Ecole Normale Supérieure*
Ian Boyd, *Univ. of St. Andrews*
Christian Büchel, *Universitätskrankenhaus Hamburg-Eppendorf*
Joseph A. Burns, *Cornell Univ.*
William P. Butz, *Population Reference Bureau*
Gyorgy Buzsaki, *New York Univ., School of Medicine*
Mats Carlsson, *Univ. of Oslo*
David Clapham, *Children's Hospital, Boston*
David Clary, *Univ. of Oxford*
Jonathan D. Cohen, *Princeton Univ.*
Robert Cook-Deegan, *Duke Univ.*
James Collins, *Boston Univ.*
Alan Cowman, *Walter & Eliza Hall Inst.*
Robert H. Crabtree, *Yale Univ.*
Wolfgang Cramer, *Mediterranean Inst. of Biodiversity and Ecology*
Janet Currie, *Princeton Univ.*
Jeff L. Dangl, *Univ. of North Carolina*
Tom Daniel, *Univ. of Washington*
Frans de Waal, *Emory Univ.*
Stanislas Dehaene, *Collège de France*
Robert Desimone, *MIT*
Claude Desplan, *New York Univ.*
Ap Dijksterhuis, *Radboud Univ. of Nijmegen*
Dennis Discher, *Univ. of Pennsylvania*
Gerald W. Dorn II, *Washington Univ. School of Medicine*
Jennifer A. Doudna, *Univ. of California, Berkeley*
Bruce Dunn, *Univ. of California, Los Angeles*
Christopher Dye, *WHO*
Todd Ehlers, *University of Tuebingen*
David Ehrhardt, *Carnegie Inst. of Washington*
Tim Elston, *Univ. of North Carolina at Chapel Hill*
Gerhard Ertl, *Fritz-Haber-Institut, Berlin*
Barry Everitt, *Univ. of Cambridge*
Paul G. Falkowski, *Rutgers Univ.*
Ernst Fehr, *Univ. of Zurich*
Tom Fenchel, *Univ. of Copenhagen*
Michael Feuer, *The George Washington Univ.*
Alain Fischer, *INSERM*
Susan Fiske, *Princeton Univ.*
Anne C. Ferguson-Smith, *Univ. of Cambridge*
Peter Fratzl, *Max Planck Inst.*
Elaine Fuchs, *Rockefeller Univ.*
Wulfram Gerstner, *EPFL Lausanne*
Daniel Geschwind, *UCLA*
Andrew Gewirth, *Univ. of Illinois*
Karl-Heinz Glassmeier, *TU Braunschweig*
Julia R. Greer, *Caltech*
Elizabeth Grove, *Univ. of Chicago*
Kip Guy, *St. Jude's Children's Research Hospital*
Taekjip Ha, *Univ. of Illinois at Urbana-Champaign*
Christian Haass, *Ludwig Maximilians Univ.*
Steven Hahn, *Fred Hutchinson Cancer Research Center*
Gregory J. Hannon, *Cold Spring Harbor Lab.*
Martin Heimann, *Max Planck Inst., Jena*
Yka Helariutta, *Univ. of Finland*
Isaac Held, *NOAA*
James A. Hendler, *Rensselaer Polytechnic Inst.*
Janet G. Hering, *Swiss Fed. Inst. of Aquatic Science & Technology*
Ray Hilborn, *Univ. of Washington*
Michael E. Himmel, *National Renewable Energy Lab.*
Kai-Uwe Hinrichs, *Univ. of Bremen*
Kei Hirose, *Tokyo Inst. of Technology*
David Hodell, *Univ. of Cambridge*
David Holden, *Imperial College*
Lora Hooper, *UT Southwestern Medical Ctr at Dallas*
Jeffrey A. Hubbell, *EPFL Lausanne*
Thomas Hudson, *Ontario Inst. for Cancer Research*
Raymond Huey, *Univ. of Washington*
Steven Jacobsen, *Univ. of California, Los Angeles*
Kai Johnsson, *EPFL Lausanne*
Peter Jonas, *Inst. of Science & Technolgy (IST) Austria*
Matt Kaeberlein, *Univ. of Washington*
William Kaelin Jr., *Dana-Farber Cancer Inst.*
Daniel Kahne, *Harvard Univ.*
Daniel Kammen, *Univ. of California, Berkeley*
Joel Kingsolver, *Univ. of North Carolina at Chapel Hill*
Robert Kingston, *Harvard Medical School*
Roberto Kolter, *Harvard Medical School*
Alberto R. Kornblihtt, *Univ. of Buenos Aires*
Leonid Kruglyak, *Princeton Univ.*
Thomas Langer, *Univ. of Cologne*
Mitchell A. Lazar, *Univ. of Pennsylvania*
David Lazer, *Harvard Univ.*
Virginia Lee, *Univ. of Pennsylvania*
Stanley Lemon, *Univ. of North Carolina at Chapel Hill*
Ottoline Leyser, *Cambridge Univ.*
Marcia C. Linn, *Univ. of California, Berkeley*
Jianguo Liu, *Michigan State Univ.*
Luis Liz-Marzan, *CIC biomaGUNE*
Jonathan Losos, *Harvard Univ.*
Ke Lu, *Chinese Acad. of Sciences*
Christian Lüscher, *Univ. of Geneva*
Laura Machesky, *CRUK Beatson Inst. for Cancer Research*
Anne Magurran, *Univ. of St Andrews*
Oscar Marin, *CSIC & Univ. Miguel Hernández*
Charles Marshall, *Univ. of California, Berkeley*
Chris Marshall, *Inst. of Cancer Research*
Martin M. Matzuk, *Baylor College of Medicine*
C. Robertson McClung, *Dartmouth College*
Graham Medley, *Univ. of Warwick*
Yasushi Miyashita, *Univ. of Tokyo*
Richard Morris, *Univ. of Edinburgh*
Edvard Moser, *Norwegian Univ. of Science and Technology*
Sean Munro, *MRC Lab. of Molecular Biology*
Thomas Murray, *The Hastings Center*
Naoto Nagaosa, *Univ. of Tokyo*
James Nelson, *Stanford Univ. School of Med.*
Daniel Neumark, *Univ. of California, Berkeley*
Stuart Newman, *New York Medical College*
Timothy W. Nilsen, *Case Western Reserve Univ.*
Pär Nordlund, *Karolinska Inst.*
Helga Nowotny, *European Research Advisory Board*
Luke O'Neill, *Trinity College, Dublin*
Ben Oliken, *MIT*
N. Phuan Ong, *Princeton Univ.*
Joe Orenstein, *Univ. of California, Berkeley & Lawrence Berkeley National Lab*
Harry Orr, *Univ. of Minnesota*
Andrew Oswald, *Univ. of Warwick*
Steve Palumbi, *Stanford Univ.*
Jane Parker, *Max-Planck Inst. of Plant Breeding Research*
Donald R. Paul, *Univ. of Texas at Austin*
P. David Pearson, *Univ. of California, Berkeley*
John H. J. Petrini, *Memorial Sloan-Kettering Cancer Center*
Simon Phillpot, *Univ. of Florida*
Joshua Plotkin, *Univ. of Pennsylvania*
Philippe Poulin, *CNRS*
Colin Renfrew, *Univ. of Cambridge*
Trevor Robbins, *Univ. of Cambridge*
Jim Roberts, *Fred Hutchinson Cancer Research Ctr.*
Barbara A. Romanowicz, *Univ. of California, Berkeley*
Jens Rostrup-Nielsen, *Haldor Topsoe*
Mike Ryan, *Univ. of Texas, Austin*
Shimon Sakaguchi, *Kyoto Univ.*
Miquel Salmeron, *Lawrence Berkeley National Lab*
Jürgen Sandkühler, *Medical Univ. of Vienna*
Alexander Schier, *Harvard Univ.*
Randy Seeley, *Univ. of Cincinnati*
Vladimir Shalaev, *Purdue Univ.*
Joseph Silk, *Institut d'Astrophysique de Paris*
Denis Simon, *Arizona State Univ.*
Alison Smith, *John Innes Centre*
Peter Sorger, *Harvard Medical School*
John Speakman, *Univ. of Aberdeen*
Allan C. Spradling, *Carnegie Institution of Washington*
Jonathan Sprent, *Garvan Inst. of Medical Research*
Eric Steig, *Univ. of Washington*
Molly Stevens, *Imperial College London*
Paula Stephan, *Georgia State Univ. and National Bureau of Economic Research*
Elsbeth Stern, *ETH Zürich*
V. S. Subrahmanian, *Univ. of Maryland*
Ira Tabas, *Columbia Univ.*
Yoshiko Takahashi, *Kyoto University*
Sarah Teichmann, *Cambridge Univ.*
John Thomas, *North Carolina State Univ.*
Christopher Tyler-Smith, *The Wellcome Trust Sanger Inst.*
Herbert Virgin, *Washington Univ.*
Bert Vogelstein, *Johns Hopkins Univ.*
Cynthia Volkert, *Univ. of Göttingen*
Bruce D. Walker, *Harvard Medical School*
Douglas Wallace, *Dalhousie Univ.*
Ian Walmsley, *Univ. of Oxford*
David A. Wardle, *Swedish Univ. of Agric Sciences*
David Waxman, *Fudan Univ.*
Jonathan Weissman, *Univ. of California, San Francisco*
Kathy Willis, *Oxford Univ.*
Ian A. Wilson, *The Scripps Res. Inst.*
Timothy D. Wilson, *Univ. of Virginia*
Rosemary Wyse, *Johns Hopkins Univ.*
Jan Zaanen, *Leiden Univ.*
Kenneth Zaret, *Univ. of Penn. School of Medicine*
Jonathan Zehr, *Univ. of California, Santa Cruz*
Len Zon, *Children's Hospital Boston*
Maria Zuber, *MIT*

BOOK REVIEW BOARD

John Aldrich, *Duke Univ.*
David Bloom, *Harvard Univ.*
Angela Creager, *Princeton Univ.*
Richard Shweder, *Univ. of Chicago*
Ed Wasserman, *DuPont*
Lewis Wolpert, *Univ. College London*

AROUND THE WORLD



Sydney, Australia **1**

Stranded Antarctic Team Rescued

After an experience he describes as "sobering," climate scientist Chris Turney of the University of New South Wales, along with 51 other scientists, doctoral students, tourists, and reporters, was airlifted to safety last week following 10 days stuck in Antarctic ice. Their ship, the *Akademik Shokalskiy*, was on the final leg of a privately funded expedition retracing Australian geologist Douglas Mawson's 1911 to 1914 adventure when it hit thick ice from a 2010 collision between an iceberg and the Mertz Glacier Tongue. The team is now aboard the Australian icebreaker *Aurora Australis*, due to reach Hobart, Tasmania, between 18 and 20 January.



Safe passage. Members of the marooned Australasian Antarctic Expedition board a Chinese helicopter.

Despite the delay, "every science target set was virtually nailed," says Alvin Stone, the expedition's Sydney-based spokesperson. Detailed analysis will begin on shore, but a paper based on new observations about the impact of ocean temperatures on seabird populations is already under way.

The *Akademik Shokalskiy* eventually freed itself, as did the Chinese icebreaker *Xue Long* that assisted in the rescue but itself became trapped.

Washington, D.C. **2**

USDA Moving Forward With GM Crops for Weed Control

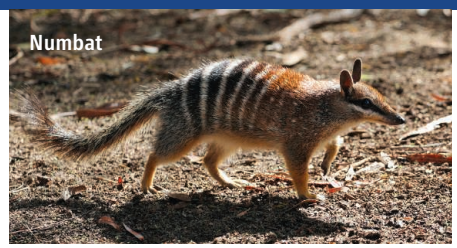
The U.S. Department of Agriculture (USDA) wants to approve three new and controversial varieties of genetically modified (GM) crops in order to help farmers deal with a growing weed problem. In a draft environmental impact statement released last week, USDA said its preference is to fully deregulate corn and soybean varieties that can tolerate 2,4-D and other herbicides. Dow AgroSciences created the varieties because weeds have evolved to survive glyphosate, a cheap and relatively benign herbicide that farmers have used on GM crops for nearly 20 years. But critics fear the new crops because they could increase the use of 2,4-D by as much as 300% and lead to further resistance in weeds.

USDA has authority to regulate GM crops only if they pose a risk to other plants, which these do not. The agency will be accepting public comments until 17 February. Meanwhile, the Environmental Protection Agency is conducting a risk assessment of the proposed use of 2,4-D on crops.

Western Australia **3**

New Sanctuary to Fence In Native Species

Woylies and bilbies and numbats. Oh my. The Australian Wildlife Conservancy (AWS) is building a 43-kilometer-long fence to help protect these three endangered mammals and six others threatened by foxes and feral cats. The fenced sanctuary inside the 7800-hectare Mount Gibson Wildlife Sanctuary in Western Australia is part of a landmark effort to reintroduce regionally extirpated species. A $1.2 million grant for the project was announced 27 December by the mining company Top Iron Pty Ltd., as compensation for environmental damage near Perth.


Numbat

The planned residents include the woylie (*Bettongia penicillata*), also called the brush-tailed bettong; the bilby (*Macrotis lagotis*); and the termite-eating numbat (*Myrmecobius fasciatus*). They'll be joined by the nocturnal western barred bandicoot (*Perameles bougainville*), which jumps straight up when startled. And if AWS reaches its target of nurturing 1200 greater stick-nest rats (*Leporillus conditor*), the country's population will increase 40%.

New York City **4**

U.S. Cancer Centers Receive Magnate's Final Endowments

Six medical centers got $540 million—$90 million each—this week to study cancer in perpetuity or until it is no longer a problem, as specified in the will of Daniel K. Ludwig, who died in 1992. Through his estate, the shipping magnate has contributed $2.5 billion to cancer research. The new money goes to centers launched in 2006 with Ludwig support at Harvard Medical School in Boston, Johns Hopkins University in Baltimore, the Massachusetts Institute of Technology in Cambridge, the Memorial Sloan-Kettering Cancer Center in New York City, Stanford University in Palo Alto, and the University of Chicago.

The sheer size of the Ludwig endowments makes a difference, says cancer immunologist Jedd Wolchok of Memorial Sloan-Kettering, who figures that the endowment will increase his annual budget by several million dollars. His group plans to

Science LIVE

Join us on Thursday, 16 January, at 3 p.m. EST for a live chat with experts about **new data on how college students drop in and out of science and engineering**. **http://scim.ag/science-live**

CREDITS (TOP TO BOTTOM): MARTIN POT/WIKIMEDIA COMMONS; XINHUA/ZHANG JIANSONG/NEWSCOM

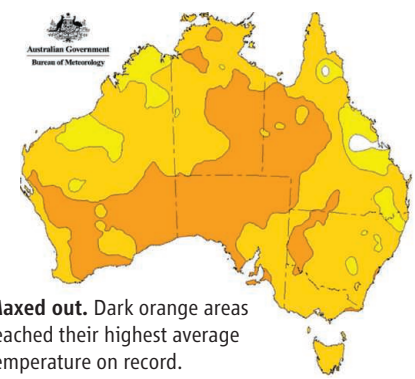
Published by AAAS

use the money to investigate cancer–immune system interactions through an upcoming clinical trial testing a new therapeutic antibody that could be used to modulate T cells. **http://scim.ag/_ludwig**

Melbourne, Australia **5**

2013 Temperature Sets All-Time High

After a string of record-breaking days and an especially destructive bushfire season, a new report makes it official: 2013 was Australia's warmest year on record. An annual climate statement released last week by the country's Bureau of Meteorology reports that the year's average temperature outstripped every previous year since data collection began in 1910 and exceeded the national long-term average by 1.20°C. Climate scientists say global warming has played an undeniable role in the record-breaking conditions. The warming effect of greenhouse gas emissions "vastly increased the odds" of setting a new high, wrote climate scientist David Karoly of the University of Melbourne in a statement. "[I]t is NOT possible to reach such a temperature record due to natural climate variations alone," he said, adding that the record is especially remarkable because it occurred without the warming effect of an El Niño.



Maxed out. Dark orange areas reached their highest average temperature on record.

Jhajjar, India **6**

Indian Cancer Institute Under Way

Concerned about rising cancer rates in the country, Indian Prime Minister Manmohan Singh laid the foundation stone for a new National Cancer Institute last week, to be set up 60 kilometers from New Delhi. Styled after its U.S. counterpart, the $500 million institute is expected to be operational in 4 years. Singh said it will be the "single biggest health institute of the country" with more than 700 hospital beds and 500 doctors and researchers.

According to the Indian Ministry of Health and Family Welfare, the nation's cancer treatment facilities have lagged behind World Health Organization standards. The institute will focus on cancers especially prevalent in India: tobacco-related cancers of the mouth and lungs, and cervical, gallbladder, and liver cancers.



Bridges That Breathe

Fire ants sometimes arrange themselves into living structures—floating rafts or bridges that help them traverse gaps in their paths. Those bridges are self-repairing, Sulisay Phonekeo, a graduate student at the Georgia Institute of Technology in Atlanta, reported this week at the annual meeting of the Society for Integrative and Comparative Biology in Austin. Using time-lapse videography, he observed that even without a leader, fire ants gather to mend any holes in their bridges. And when a bridge starts to vibrate too fast, as can happen when wind or water currents shake the leaves or stems at its base, the ants close ranks, curling their legs more tightly around their neighbors to shorten and stiffen the bridge. "The construction rules followed by the ants represent a formidable source of inspiration for people working on self-assembling robots and self-repairing materials," says Simon Garnier, a complex systems scientist at Rutgers University in Newark, New Jersey. http://scim.ag/_ant

NEWSMAKERS

Battery Innovators, Science Educators Nab Engineering Prizes

The National Academy of Engineering (NAE) announced the winners of its two top engineering prizes this week, recognizing the creators of the lithium-ion battery and the developers of an innovative education curriculum. The Charles Stark Draper Prize for Engineering, awarded for accomplishments that have significantly benefited society, went to **John B. Goodenough**, **Yoshio Nishi**, **Rachid Yazami**, and **Akira Yoshino**, who will share a $500,000 award. NAE noted that each scientist played a critical role in developing the now prevalent lithium-ion battery technology.



The Bernard M. Gordon Prize for Innovation in Engineering and Technology Education went to the Dartmouth Engineering Entrepreneurship Program at the university's Thayer School of Engineering. NAE recognized **John Collier**, **Robert Graves**, **Joseph Helble**, and **Charles Hutchinson** for fostering entrepreneurship and leadership in the department's undergraduate and graduate engineering programs. The awardees share half of the $500,000 prize; the rest will go to their institution.



THEY SAID IT

"A big win for ignorance. General Mills falls to pressure on Cheerios."

—Tweet from biologist J. Craig Venter after news that the company has dropped genetically modified corn and beets from its original Cheerios recipe.

CREDITS (TOP TO BOTTOM): YANUAR AKBAR/CATERS NEWS; © COMMONWEALTH OF AUSTRALIA 2014, AUSTRALIAN BUREAU OF METEOROLOGY, WWW.BOM.GOV.AU/CLIMATE/CURRENT/ANNUAL/AUS/2013; NATIONAL ACADEMY OF ENGINEERING (2)

Published by AAAS

FINDINGS

Muscle Molecule Spurs Fat Cells to Slim Down

How your body turns the pain of exercise into the gain of health benefits has become a bit clearer, thanks to a new discovery: When you work out, your muscles release a molecule that modifies fat cells.

The protein PGC-1α helps orchestrate the body's response to exercise. But because it doesn't travel outside muscle cells, researchers have been hunting for its molecular emissaries. Now, Robert Gerszten of Harvard Medical School in Boston and colleagues have found that PGC-1α–making muscle cells secrete a messenger called β-aminoisobutyric acid (BAIBA).

BAIBA induces energy-storing white fat cells to become more like brown fat cells, which burn calories, the researchers report this week in *Cell Metabolism*. Mice that lapped up water laced with BAIBA lost weight and showed other metabolic benefits. The researchers also found low BAIBA levels in subjects from the famous Framingham Heart Study who had risk factors for heart disease and diabetes. Gerszten and colleagues intend to further study BAIBA in animals, and we may soon know whether it can deliver gain without the pain. **http://scim.ag/BAIBA**

Bacteria Tell Tubeworms Where to Settle

For their first few days of life, the larvae of the ocean-dwelling tubeworm *Hydroides elegans* drift over the sea floor in search of a home. The signal that causes them to settle down and take on their adult tubular form has long been mysterious. New research shows how bacteria on the ocean floor—or on the hulls of ships—play a role.

Biologists knew that the presence of certain bacteria growing on a surface helps trigger a larva's decision to settle and metamorphose, but no one could explain how bacteria prompt this. Online this week in *Science*, researchers report that the bacterial cells release elaborate structures resembling bits of viruses called phages, which link to form a 3D net. Touching the net prompts the larvae to attach to a surface (whether a rock or a ship's hull) and become adults. The discovery might lead to new ways to discourage tubeworms and other organisms from taking up residence on ship hulls. Such biofouling costs the shipping industry billions of dollars each year. **http://scim.ag/_tube**

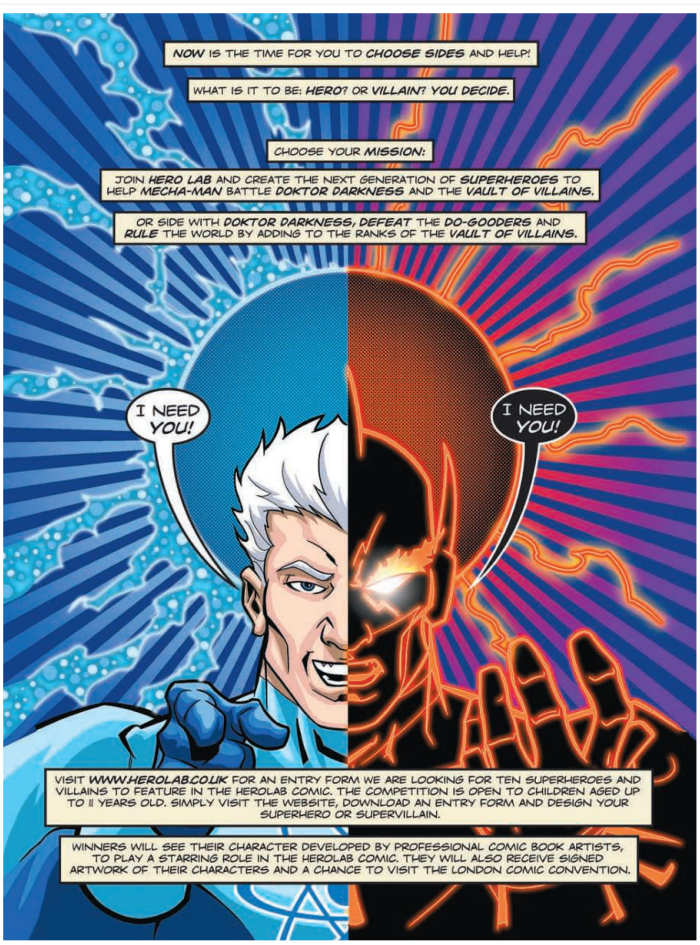


Looking for home. A free-floating larva of the tubeworm species *Hydroides elegans*.

BY THE NUMBERS

6 tons Confiscated elephant ivory pulverized in the first destruction by the Chinese government—an attempt to reduce poaching in other countries amid high Chinese demand.

42% Decrease in cigarette smoking prevalence in women worldwide between 1980 and 2012, according to a new report (versus a 25% decrease for men).



CREDITS (TOP TO BOTTOM): IMAGE COURTESY OF BRIAN NEDVED; ANDY LANNING AND ANT WILLIAMS, COMIC STRIPPER STUDIOS

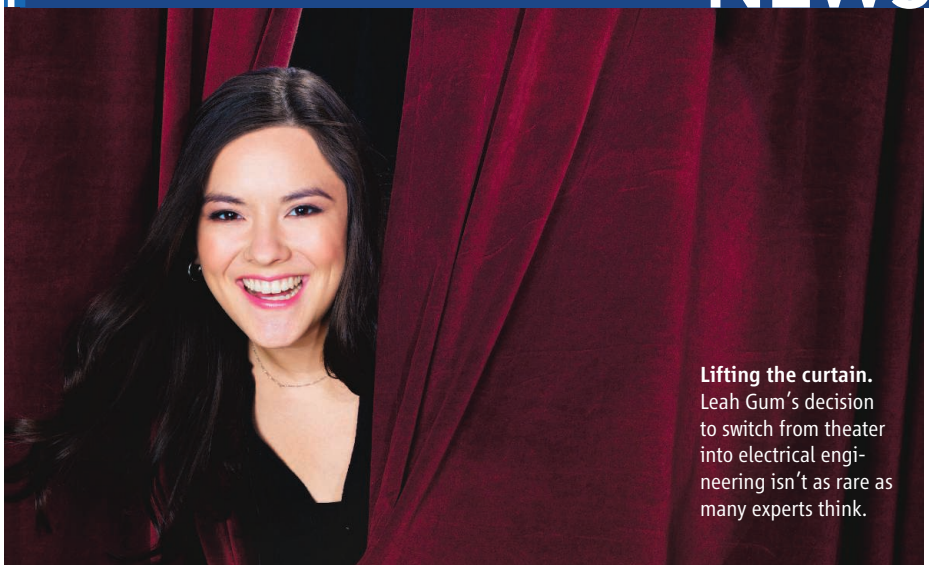
Random Sample

Science-Powered Super-Sidekicks

Ask card-carrying geeks about the science in comic books and you'll get an angry rant. "When Superman catches people falling from skyscrapers just before they hit the street, why don't they go splat right in his Kryptonian arms? And don't even get me started on the Hulk's flagrant violation of the first law of thermodynamics … ." But then they'll gush about their most beloved comic books. See the tension? Now, scientists and comic book artists in the United Kingdom are teaming up to create an antidote: Hero Lab.

The idea is to create superheroes and villains whose powers are grounded in real science and distribute them as a comic book to schoolchildren. Scientists at the University of Central Lancashire in the United Kingdom and two professional comic book artists have created a pair of characters, Mecha-man and Doktor Darkness, who are now recruiting teams of good and evil sidekicks, respectively. Children worldwide have until 28 February to propose heroes and villains with science-based powers. One of the entries received so far, Magma Man, can harness the energy of underground magma to shoot heat blasts. (Sure, the scheme has a few scientific gaps, but you have to learn some geology to appreciate his power.) Keep tabs on the action at www.herolab.co.uk.

Published by AAAS



Lifting the curtain. Leah Gum's decision to switch from theater into electrical engineering isn't as rare as many experts think.

CREDIT: ISSAC STERLING/WWW.ISAACSTERLING.COM

SCIENCE EDUCATION

Studies Suggest Two-Way Street for Science Majors

To win acceptance to Cornell University, Will Najar had to convince the philosophy department that he would be a perfect fit for the program. But after taking mostly humanities classes in his freshman year, the 19-year-old Najar changed his mind. "I wanted to build things or help people," he says, "and I realized that I wasn't going to be able to make that kind of an impact on the world as a philosophy guy."

So Najar switched his major to biology. The change meant "working harder for lower grades," Najar says. But he persevered, and along the way he taught himself some computer and Web skills. After graduating last May, he snared a well-paying job as a technical account manager at Microsoft, where he uses his scientific training to help customers solve their computing problems.

Najar's academic path has long been thought to be an anomaly. Conventional wisdom holds that few college students ever transfer into a STEM (science, technology, engineering, and mathematics) field because they lack the necessary academic preparation. The field is already plagued by high attrition rates: At least one-half of students who declare their intention to major in a STEM field either switch majors or never earn a degree, some driven out by poor instruction and a chilly climate for women and minorities. Both the low inflow and high outflow have long been thought to be unique characteristics of STEM disciplines.

The unfortunate result, experts say, is a dearth of technically savvy workers that U.S. companies need to compete in a global economy. That alleged crisis has prompted the federal government, industry, and private foundations to spend billions of dollars trying to understand and reverse the pattern.

But new data poke major holes in that conventional wisdom. The findings could have important implications for an issue that for 2 decades has spawned bitter ideological battles between those who say that the leaky STEM pipeline is a national crisis and those who say that the supply of STEM workers is more than adequate.

One study, a first-ever look at attrition rates outside the STEM fields, has found that STEM majors are no more likely to switch out than are students in the humanities, business, and education. In November, Xianglei Chen of RTI International in North Carolina reported on her analysis of a nationally representative sample of 19,000 students who began college in 2003.

The study, which tracked the students for 6 years, found an attrition rate of 48% for STEM majors (20% dropped out and 28% switched to a non-STEM major). That compares with 56% for initial humanities majors and 50% for business majors. "We've never really looked at attrition in non-STEM fields, so we never really knew the comparative size of the problem for STEM," says Matthew Soldner of the Education Department's National Center for Education Statistics, which commissioned the RTI study.

A second study, also released in November, looked at how student preferences change during their first year of college. The data, from the Beginning College Survey of Student Engagement (BCSSE) and the National Survey of Student Engagement, involve 78,000 students at 119 institutions in 2012. Researchers at Indiana University found that 24% of the students who entered college with plans to earn a STEM degree had shifted into a non-STEM field by the end of their freshman year. But they also discovered that 27% not originally planning to major in STEM had switched into a STEM field by spring.

Those two findings come as no surprise to Hal Salzman, a professor of public policy at Rutgers University in New Brunswick, New Jersey. Salzman's previous work has questioned those claiming a shortage of STEM-trained workers. And in a new paper not yet in print, Salzman argues that the leaky STEM pipeline metaphor should be replaced by a two-way street, with students continually moving into and out of STEM disciplines.

"If you talk to 17-year-olds about their plans, or ask adults how they got into their profession, you'll find that their interests change and they change majors," Salzman says. "I think what has happened is that we defined [attrition] as the problem, and that led researchers down a certain path." Salzman thinks educators should focus on understanding the factors that affect whether students stick with any given major, including STEM.

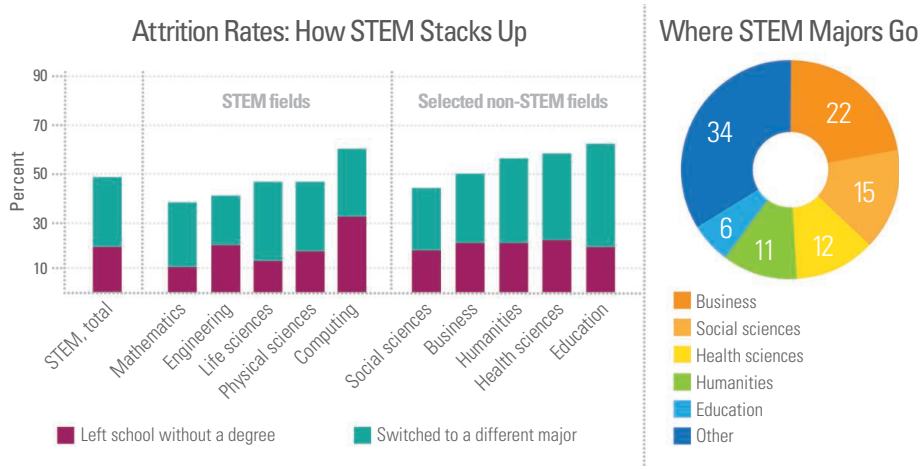
Talking back

The push to improve U.S. science education across the board dates from the post-Sputnik era. But it was a 1997 book by Elaine Seymour and Nancy Hewitt, *Talking About Leaving: Why Undergraduates Leave the Sciences*, that made undergraduate STEM education a hot research topic. In lengthy interviews with 335 students at seven U.S. institutions, the authors found, as one reviewer put it, that "students are very disappointed with college [STEM] courses and professors."

The book was a call to arms for improving how STEM courses are taught and attracting and retaining more women and minorities, all with the goal of stemming the high attrition rates. (Seymour and Hewitt pegged the rate at 55% for their diverse sample of colleges and research universities.)

For 2 decades, that philosophy has ruled: A 2012 report by a White House science

Published by AAAS



Changing majors. Attrition rates are no higher for students in STEM fields than in the humanities, education, and business, and business is the most popular destination for STEM majors moving into a new field.

advisory panel, for example, concluded that the single most effective way to preserve U.S. competitiveness would be to lower the STEM attrition rate in college. The National Science Foundation and the Alfred P. Sloan Foundation are even funding a follow-up to the original study, tabbed *Talking About Leaving Revisited*, aimed at understanding why efforts to retain students in STEM majors haven't made a dent in attrition rates.

But the new studies suggest that efforts to reverse the outflow have ignored a critical factor: It takes time for students to find their way before ultimately choosing a major that's right for them. "We need to develop programs to help students gain a better understanding of the broad array of educational and career options before them," Soldner says.

Those involved in the follow-up to the 1997 study think the RTI data make an important contribution to the debate but don't reduce the importance of efforts to attract and retain students in STEM fields, including a strong focus on women and minorities. "Just because the attrition rate is no higher doesn't mean there isn't a problem," says Joseph Ferrare of the University of Wisconsin, Madison, co–principal investigator on the follow-up study. "And ensuring diversity is also important."

Few would argue with the need to make the STEM workforce more diverse. But the studies provide no clear guidance on where to focus attention. Chen finds, for example, that women are more likely than men to switch majors, while men are more likely to drop out—but only among those seeking bachelor's degrees. (The RTI study included those enrolled in associate degree programs as well.) Looking at racial and ethnic differences, she finds that fewer Asians than blacks switched out of STEM majors but that there was "no measurable difference" in the rates among Asians, whites, and Hispanics.

The influx documented by BCSSE raises a new question: How can institutions trying to grow their STEM programs tap into a potentially much larger pool of talent on college campuses? Leah Gum, who entered the University of Southern California in Los Angeles in 2009 as a theater major, says she is living proof of how to bridge that gap.

"An actor is all I ever wanted to be," Gum says. But after devoting the first semester to courses on her craft, she decided that a career in theater "wouldn't be satisfying in the long run." She also longed for a greater intellectual challenge—what she calls the "academic side" of college. She switched tracks and is now in the last year of a combined, 5-year bachelor's–master's degree program in electrical engineering. After graduation she will join Apple to work as a sensor engineer in their human interfaces devices group at the company's headquarters in Cupertino, California.

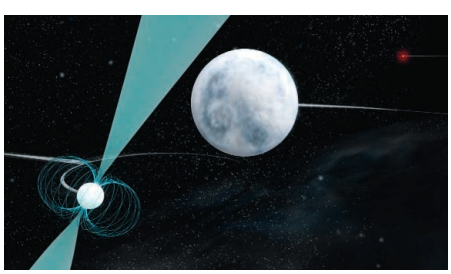
"Most people think there's no overlap between being an artist and being a scientist," she notes. "But I disagree. Actors are always trying to understand what motivates their character. And thinking about how people behave translates directly into engineering, where the human-machine interaction is so important." **–JEFFREY MERVIS**

ASTROPHYSICS

Rare Celestial Trio to Put Einstein's Theory to the Test

In a cosmic coup, astronomers have found a celestial beacon known as a pulsar in orbit with two other stars. The first-of-its-kind trio could soon be used to put Einstein's theory of gravity to an unprecedented test. "It's a wonderful laboratory that nature has given us," says Paulo Freire, a radio astronomer at the Max Planck Institute for Radio Astronomy in Bonn, Germany, who was not involved in the work. "It's almost made to order."

A pulsar consists of a neutron star, the leftover core of a massive star that has exploded in a supernova. The core's intense gravity squeezes atomic nuclei into a single sphere of neutrons. The spinning neutron star also emits a beam of radio waves that sweeps the sky as steadily as the ticking of an atomic clock. Tiny variations in the flashing



Ménage à trois. A pulsar (*left*) and one star (*center*) are orbited by a more distant star (*right*).

can reveal whether the pulsar is in orbit with another object: As the pulsar cycles toward and away from Earth, the pulse frequency oscillates. Roughly 80% of the more than 300 fast-spinning "millisecond" pulsars have a partner.

But a single partner couldn't explain the peculiar warbles in the frequency of pulsar PSR J0337+1715, which Scott Ransom, an astronomer at the National Radio Astronomy Observatory in Charlottesville, Virginia, and colleagues discovered in 2007 with the Robert C. Byrd Green Bank Telescope in West Virginia. Training other radio telescopes on the object, Ransom and colleagues monitored it almost constantly for a year and a half. Eventually, Anne Archibald, a graduate student at McGill University in Montreal, Canada, figured out exactly what's going on.

The pulsar, which has 1.4 times the sun's mass and spins 366 times a second, is in a tight orbit lasting 1.6 days with a white dwarf star only 20% as massive as the sun. A second white dwarf that weighs 41% as

CREDITS: (GRAPHS SOURCE) U.S. DEPARTMENT OF EDUCATION; BPS AND PETS, 2009; (PHOTO) BILL SAXTON/NRAO/AUI/NSF

Published by AAAS

much as the sun orbits the inner pair every 327 days, Ransom and colleagues reported this week in *Nature*. "We think that there are not more than 100 of these [trios] in our galaxy," Ransom says. "They really are one-in-a-billion objects."

The distinctive new system opens the way for testing a concept behind Einstein's theory of gravity, or general relativity. Called the equivalence principle, it relates two different conceptions of mass: inertial mass, which quantifies how an object resists accelerating when it's pushed or pulled, and gravitational mass, which determines how much a gravitational field pulls on it.

The simplest version of the principle says inertial mass and gravitational mass are equal. It explains why ordinary objects like baseballs and bricks fall to Earth at the same rate regardless of their mass. The strong equivalence principle takes things an important step further. According to Einstein's famous equation, $E = mc^2$, energy equals mass. So energy in an object's own gravitational field can contribute to its mass. The strong equivalence principle states that even if one includes mass generated through such "self-gravitation," gravitational and inertial mass are still equal.

The strong equivalence principle holds in Einstein's general theory of relativity but not in most alternative theories, says Thibault Damour, a theoretical physicist at the Institute for Advanced Scientific Studies in Bures-sur-Yvette, France. So poking a pin in the principle would prove that general relativity is not the final word on gravity.

Researchers have tried to test the strong equivalence principle by scrutinizing how the moon and Earth orbit in the gravitational field of the sun and how pulsar–white dwarf pairs cavort in the gravitational field of the galaxy. But Earth's self-gravitation is tiny, and the galaxy's gravity is weak. So such tests have yielded a precision of only parts per thousand, Damour says.

The new pulsar system opens the way to a much more stringent test by combining the powerful self-gravitation of the pulsar with the strong gravitational field of the outer white dwarf. By tracking whether either the inner white dwarf or the pulsar falls faster toward the outer white dwarf, Ransom and colleagues should be able to test strong equivalence about 100 times as precisely as before, Damour says. If strong equivalence falters, Freire says, the result would mark "a complete revolution" in physics.

Ransom says his team should be able to test the principle within a year.

–ADRIAN CHO

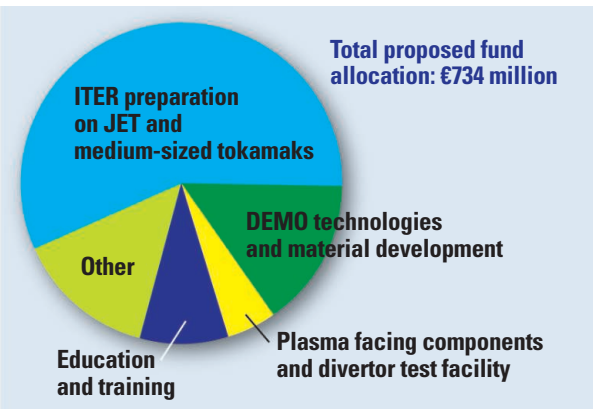
CREDIT: (SOURCE) FRANCESCO ROMANELLI/EFDA/JET

NUCLEAR FUSION

Europe Focuses Fusion Research on Building a Working Power Reactor

As the new year dawned, nuclear fusion researchers in the European Union woke to an entirely new funding system aimed at sharpening their focus on generating energy. Gone are the annual block grants to national fusion laboratories; now, teams must compete to participate in "work packages" supporting the international ITER reactor in France and preparing for a prototype power reactor before the middle of the century. "It's a substantial change in the way we work," says Francesco Romanelli, acting head of EUROfusion, a consortium of all of Europe's fusion labs that will manage the new program.

The change is the handiwork of the European Union's nuclear research arm, Euratom. It funds both ITER construction, shouldering 45% of the cost—a €6.6 billion share by the time the reactor is completed in 2020—and related fusion research in labs across the continent. That is the part of the budget that the new system redirects.



On a mission. Europe's fusion research effort now has the goal of generating electricity before 2050.

In the old system, in place since the 1950s, Euratom simply gave each of the national labs a lump of money every year equal to as much as 20% of the lab's budget and gently coordinated research. Euratom also funded the only common facility, the Joint European Torus (JET) reactor in Culham, U.K., through the European Fusion Development Agreement (EFDA).

In 2011, Euratom appointed a panel to recommend how to organize fusion research in the European Union's next 7-year financial period, starting in 2014. Headed by Albrecht Wagner, former head of the DESY particle physics lab in Germany, the panel recommended a more mission-oriented approach focusing on fusion energy. "If ITER is not a success, there is no need for future research," says Alain Bécoulet, head of France's Research Institute for Magnetic Fusion.

In 2012, Euratom tasked EFDA with drawing up a road map for refocusing Europe's fusion efforts. Published at the beginning of 2013, the road map called for the European Union to concentrate on finishing and operating ITER while also preparing for its successor, a power-producing prototype, dubbed DEMO. In response, Euratom announced that the annual grants would cease at the end of the year and that the fusion community must devise a 5-year program of research based on the aims of the road map.

Since then, the heads of the fusion labs have been working furiously to comply, and they finalized the work program last month. The program, which Euratom will spend the next 3 months evaluating, includes a campaign of experiments on JET to simulate ITER operation plus experiments at smaller reactors across Europe. There's money for technology R&D for ITER and DEMO, for training future fusion scientists, and for a neutron source to test materials in the sort of neutron bombardment they will experience in a working reactor. The program also hedges its bets by supporting work on stellarators, an alternative fusion technology that could play a role if ITER fizzles.

Bécoulet worries that the program focuses too much on the future—ITER operation and DEMO—and not on the immediate needs of ITER construction. "We're very upset with the proposal," he says, adding that the program "needs to focus more on what is urgent now." Romanelli responds that the program already addresses urgent needs, with 85% of the funding directly or indirectly supporting ITER. "ITER is the first priority," he says.

–DANIEL CLERY

Downloaded from www.sciencemag.org on January 10, 2014

Published by AAAS



Seismic shift? New guidelines aim to clarify risks that marine mammals face from ocean noise, such as the seismic air blasts being studied by this research vessel in the Gulf of Mexico.

CREDIT: JONATHAN GORDON/U.S. DEPT. OF INTERIOR/AP PHOTO

MARINE POLICY

U.S. Regulators Unveil New Ocean Noise Rules for Marine Mammals

When an energy company explores for oil or gas underneath the sea floor, it's not a hush-hush affair. A survey ship tows "air guns" that shoot high-pressure bubbles into the sea, creating blasts of sound that penetrate the sea floor to reveal the geology. Although companies insist that the noise rarely injures whales, dolphins, and other marine life, environmentalists disagree. And the U.S. government, which grants permits for seismic surveys and other sources of marine racket, lacks a solid scientific foundation for deciding.

Now, after a decadelong wait, that foundation is about to get a bit sturdier. On 27 December, the U.S. National Marine Fisheries Service (NMFS) released updated technical guidance—dubbed a "Highly Influential Scientific Assessment"—that calls for analyses more sophisticated than are now required of how noise from air guns, pile drivers, and underwater explosions might injure a marine mammal. The proposal recognizes "that there's more to sound than just how loud it is," says marine acoustics specialist Brandon Southall of SEA, a consulting firm in Aptos, California. Regulators will also have to take into account, for example, that species have ears that are tuned to various frequencies.

Concerns about impacts of ocean noise on marine mammals, which depend on hearing for communication, feeding, and navigation, have rippled through courtrooms and legislative bodies around the world. Over the past decade, environmentalists and military agencies have jousted over the impact of naval sonars, which researchers say have caused certain types of whales to panic, strand, and die (*Science*, 26 January 2001, p. 576). Shipping firms have been under pressure to reduce the racket generated by their vessels (*Science*, 18 June 2010, p. 1502). And federal agencies, settling lawsuits by environmentalists, have required companies to reduce air gun use in some whale-rich waters.

But few studies could help regulators predict just how a proposed activity, such as a seismic survey, might affect nearby animals. As a result, in the 1990s, U.S. regulators adopted some rough guides. Existing NMFS rules, for instance, assume that a whale will experience temporary hearing loss if exposed to a nearby sound exceeding 160 decibels (dB), which might be created by a mine exploding 100 meters away. At 180 dB, NMFS assumes that cetaceans experience permanent hearing loss, while seals and other pinnipeds would go deaf at 190 dB.

The new guidelines, however, say that a small but growing body of research shows that regulators need to take into account many more factors. For example, relatively constant sounds like sonar would be handled differently than bursts of "impulsive" sound, such as the boom of a pile driver, which can create a higher peak pressure. That pressure burst "can cause more damage to the inner ear," says Amy Scholik-Schlomer, a NMFS acoustics specialist. The guidelines also divide marine mammals into five groups, based on their hearing characteristics. Beluga whales, for example, might be disturbed by the initial high-pitched bang from a seismic air gun, researchers say, but not the subsequent thud. Finally, the rules don't just set a single redline sound threshold; they also call for assessing an animal's cumulative exposure.

Some environmentalists believe that such guidance, once implemented, will show that noise threatens more marine mammals than once believed—and will lead to stronger protection, at least for some species. Studies suggest that relatively common harbor porpoises, for instance, are much more sensitive to noise than previously believed.

Others are skeptical. The main result, predicts Bruce Tackett of Resource Access International, an energy industry consulting firm in Dallas, Texas, will be thicker and more detailed assessment studies, but not necessarily stricter permits. "NMFS is going to need a bigger loading dock," he says. "There will be FedEx tractor-trailors lining up."

A continuing challenge, all sides agree, is the scarcity of data: The new exposure thresholds for harbor porpoises, for instance, are derived from a handful of studies of two individuals in captivity. And there are still are no solid direct studies of large whales. Still, many see the NMFS proposal as a step forward. "In the past, the guidelines were scattered and changeable," says Roger Gentry, a former top government scientist who now advises the energy industry on marine noise.

NMFS is accepting public comment on the injury guidance until 27 January and hopes to finalize it in the spring. Meanwhile, it is working on a separate review of how noise can affect the feeding and other behaviors of marine mammals. **–ERIK STOKSTAD**

Downloaded from www.sciencemag.org on January 10, 2014

Published by AAAS

SCIENTIFIC MEETINGS

Once Failing Biology Society Thrives As It Nurtures New Disciplines

To understand the success of the Society for Integrative and Comparative Biology (SICB), start with the name. It is purposefully vague, hinting that the organization has a niche for everyone, and that synthetic and interdisciplinary fields are especially welcome. The approach has paid off. While many scientific societies are struggling with declining memberships and red ink, SICB is booming. Since 2009, its numbers have swelled by almost 50% to almost 3500, and its $900,000 budget is balanced.

The society, which held its annual meeting this week in Austin, is "an incubator for emerging fields," says James Adelman, a disease ecologist at the Virginia Polytechnic Institute and State University in Blacksburg. In the past, the society has embraced up-and-coming fields like evo-devo, a melding of evolutionary biology and development, and comparative biomechanics, which studies animal movement and locomotion. Earlier this week in Austin, another subdiscipline joined SICB, as those who study immune systems in natural settings set up shop as the new Division of Ecoimmunology and Disease Ecology.



Ecology meets immunology. Cynthia Downs draws blood from a mule deer as part of her ecoimmunology research.

CREDIT: DANIELLE WALSH

Cynthia Downs of the University of Nevada, Reno, is delighted with the recognition for her research focus. When she first attended SICB 7 years ago as a graduate student studying physiological trade-offs in mice bred to have ever higher metabolic rates, immunology was not on her mind. Yet after hearing talks about how costly immune responses were for animals, she began studying the issue in her mice. Now, she studies immune responses in wild mule deer and elk. She and Adelman just co-organized what was the third SICB ecoimmunology symposium. Past symposia have yielded "some of the foundational papers" in the field, she says.

SICB officials and members credit the society's constant self-renewal largely to its open-door policy. All it takes to set up a new division is a petition by 25 existing members and approval from the SICB executive committee. The division writes up its own bylaws and elects its own officers, and defines its focus. "I think the reason we are doing so well is we've got this flexibility," says evo-devo researcher Billie Swalla of the University of Washington, Seattle, who is SICB's president. SICB's divisions "can respond to opportunities and fade when matured," adds Robert Full, an integrative biologist at the University of California, Berkeley.

Full belongs to the comparative biomechanics division, which he helped start in 2007. "I was frustrated," he recalls. "There was an increasing number of young investigators in the exploding field that needed to be connected to a community." The division started with 132 members, and its ranks have swelled to more than 1000 as it has attracted new researchers, including engineers, to SICB. Full says he and his colleagues have no intention of abandoning the society. "We value the diversity and synthetic approaches of SICB."

But SICB sometimes sees its progeny leave home. Comparative endocrinologists, who composed one of SICB's bigger divisions from the 1970s to early '90s, have begun to leave the fold, in 2011 establishing a society of their own. "It's a way to make [the field] visible and to say something to young people" about its vitality, says Stacia Sower, a comparative endocrinologist at the University of New Hampshire, Durham. "We were buried in the SICB."

Evo-devo, too, is setting out on its own. More than 20 years ago, Swalla and others within SICB organized early symposia and helped find a home for the nascent discipline within SICB. Last month, however, U.S. evo-devo researchers decided they have outgrown that home; by 2015, they expect to have their own society up and running, ready to host its first meeting.

This ebb and flow has been the modus operandi of SICB almost from its earliest days. It started out as the American Morphological Society in 1890 but by 1913 had morphed into the American Society of Zoologists (ASZ) to reflect additional research fields, such as ecology and genetics. But not everyone was satisfied. In 1915, a faction established the Ecological Society of America, which now dwarfs SICB with 10,000 members. Some geneticists split off as well 15 years later, forming a new society.

By 1959, new discipline-focused divisions had emerged: developmental biology, comparative endocrinology, comparative physiology, and animal behavior, among them. But in the 1990s, ASZ was teetering, so weak financially that it appealed to its members for bailout donations. Soul-searching resulted in a greater emphasis on cross-cutting topics. "People thought that having a program that was truly integrative was more important than having the disciplines," says comparative physiologist Louis Burnett of the College of Charleston in South Carolina, who has been the SICB secretary for the past 8 years. Another name change reflected the shift: By 1996, ASZ became SICB.

Yet the divisions have continued to proliferate, thanks to new disciplines spawned in part from cross-cutting approaches encouraged at SICB. And even when these disciplines split off as independent societies, SICB retains many of their members by offering the chance to connect with other disciplines at meetings and symposia.

"Some people say, 'How dare they go off and start their own society,' " Swalla says. "I tend not to be a panicky person. My thing is if you have good symposia, people will come." **–ELIZABETH PENNISI**

Downloaded from www.sciencemag.org on January 10, 2014

Published by AAAS



Downloaded from www.sciencemag.org on January 10, 2014

Mariners of the Lost Sea

Charting the rise and fall of the ancient Paratethys Sea may help explain how Central Asia's lush forests gave way to steppe and desert

CHILDARA, TAJIKISTAN—Under a broiling midday sun, Guillaume Dupont-Nivet pushes a drill into a sloping outcrop near this village in southwestern Tajikistan. Dozens of soldiers in olive drab uniforms rush by, a reminder of the turmoil across the nearby Afghan border. Unfazed, Dupont-Nivet, a geologist at the National Center for Scientific Research (CNRS) in Rennes, France, painstakingly removes the drill and cradles his prize: a cylinder of fine, greenish sedimentary rock. "This is a perfect core," he says, wiping mud from his face.

The core is a remnant of the bottom of the Paratethys Sea, a vast body of water that vanished long before humans walked the earth. At its peak 50 million years ago, the shallow sea covered much of Eurasia, from present-day northwestern China to the Mediterranean. In a project launched in 2008, Dupont-Nivet and his colleagues have been crisscrossing Central Asia's isolated basins, extracting hundreds of cores on a quest to "unveil the mystery of why Central Asia has become such an arid, desolate land," he says. "It's a story of a paradise lost."

In the days of the Paratethys, Central Asia was covered in warm, damp forest inhabited by horses with long front limbs that knuckle-walked like gorillas and gargantuan rhinos that dwarfed modern elephants. Within a few million years—a geological eye blink—Central Asia's climate turned cooler and drier. Lush forests gave way to grasslands, and rodents and rabbits supplanted the megafauna. The lurch toward a more arid climate was "among the most dramatic events since the extinction of the dinosaurs," says Jin Meng, a paleontologist at the American Museum of Natural History in New York City.

Scientists have long blamed the drying of Central Asia on rain shadows—parched areas in the lee of mountainous terrain—that formed as the Tibetan Plateau rose during the collision of Eurasia and the Indian subcontinent starting about 50 million years ago. Dupont-Nivet and others argue that the retreat of the Paratethys Sea was equally important, if not more so, in driving the shift. They suspect that the loss of a moisture source during the sea's disappearance turned much of the region into the desert it is today.

The Paratethys Sea's importance extends beyond Central Asia. The sea connected the Indian and Atlantic oceans; its demise therefore "should have [caused] a pretty big change in global climate," says David Battisti, a climate scientist at the University of Washington, Seattle. Reconstructing the Paratethys's rise and fall, he predicts, "will change many aspects of our fundamental understanding of the Earth's climate system."

Until recently, the region's political instability kept geologists from tracing the ancient sea and its history in detail. But

CREDIT: JANE QIU

Published by AAAS

Leaving its mark. This pale green limestone outcrop in southwestern Tajikistan marks the last stand of the Paratethys, which vanished some 37 million years ago.

fieldwork in once-inaccessible corners of Tajikistan and neighboring countries has enabled the CNRS team to begin piecing together when the Paratethys inundated Central Asia, how extensive it was, and when it vanished. Such data, Dupont-Nivet says, are "critical for linking the sea fluctuations to climate and environmental changes in Central Asia."

The effort to paint a more nuanced picture of the Paratethys, says Carmala Garzione, a geologist at the University of Rochester in New York who is not affiliated with the project, is "long overdue."

Disappearing acts

The Paratethys formed about 150 million years ago, when global sea levels rose and water from the Tethys Ocean separating two supercontinents—Laurasia and Gondwana—spilled into present-day Eurasia. Rock layers spanning tens of millions of years contain a "fantastic encyclopedia" of the sea's geological history, says project member Jean-Noël Proust, a sedimentologist at CNRS in Rennes. Sediments deposited in seas and on exposed land differ in appearance and have distinct chemical compositions and fossil assemblages, making it easy to distinguish them. By measuring the direction of ancient magnetic fields frozen in rocks, the team can date the shift from marine sediments to continental rock and thus infer when the sea retreated. The embedded fossils, meanwhile, open a window on the links between the sea's retreat and regional climate.

For the CNRS team, gaining access to inhospitable terrain is only half the battle. To precisely date the Paratethys Sea's advances and retreats, Proust says, the researchers must locate intact outcrops that haven't been twisted by mountain building.

About a week into their field campaign in Tajikistan, the researchers stumble upon just such a rock sequence. Below the rim of a canyon, they identify a massive section of marlstone, a type of soft lime-rich mudstone formed in shallow water. "Welcome to the Paratethys," says Jovid Aminov, a graduate student at the Institute of Geology in Dushanbe, Tajikistan's capital. Several meters away lies another clue that the area was once submerged: scads of fossilized oyster shells, some topping 14 centimeters in length, embedded in the marlstone.

Deeper in the canyon, Dupont-Nivet crouches on a slab of green rock, examining its fine grain studded with fossilized fish scales. "This was likely a deep marine environment with quiet waters," he says. Alternating layers of green limestone (seabed) and red continental sandstone (dry land) divulge when the Paratethys advanced and retreated, until the beginning of continuous continental rock demarcating the end of the final sea incursion.

To connect other dots on the map, the researchers have surveyed in western China and southern Kyrgyzstan. "The sequences of the rock layers are exactly the same, and they host very similar fossils," says team member Roderic Bosboom, a graduate student at Utrecht University in the Netherlands. This suggests that "the rocks shared the same history" and were once connected by the Paratethys before the rise of big mountains, he says.

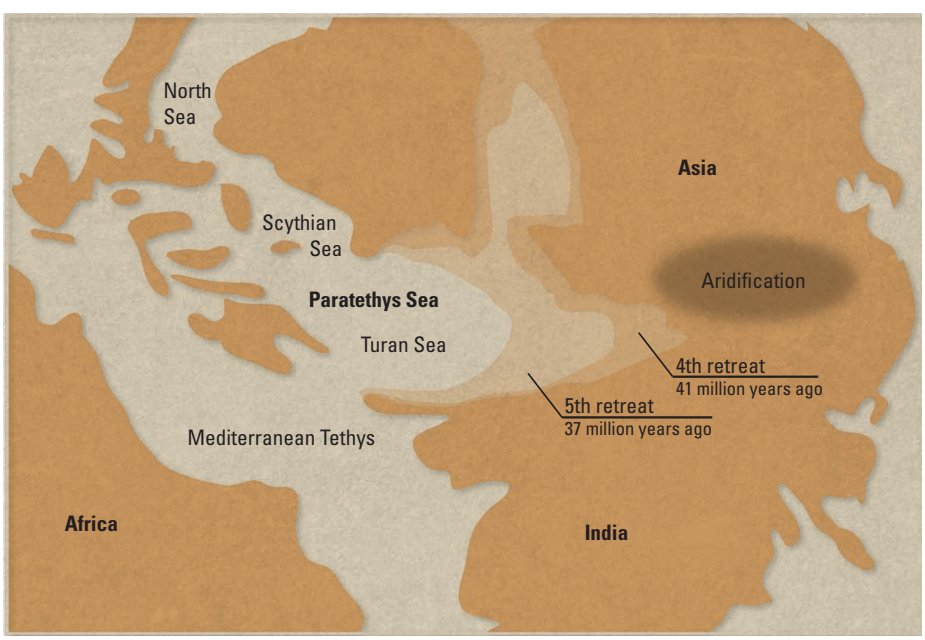
Dating the limestone-sandstone transition at various locations, the team has found that the Paratethys Sea retreated westward, from China to Kyrgyzstan and finally to Tajikistan. The retreat wasn't uniform: The sea shrank and expanded five times, with each expansion more anemic than the previous one, as revealed by thinner and thinner marlstone layers and more dominant fossils of shallow-water fauna.



High and dry. Laurie Bougeois examines an oyster shell, which may yield clues to the ancient marine environment.

"The sea got shallower and receded more rapidly," Bosboom says. The researchers peg the last two retreats from Central Asia to 41 million and 37 million years ago (see map, below).

Other team members are probing whether the sea's demise triggered the drying in Central Asia. The giant oysters may have a story to tell. For instance, in summertime, when the mollusks have an ample food supply, they accumulate calcite, forming light-colored layers in their shells. In winter, as they conserve energy, their shells tend to store darker organic matter. Thus, the thicknesses of the alternating light and dark bands in the shells reflect seasonal temperature



Beginning of the Big Dry. Researchers have dated the Paratethys's final two retreats. Now they hope to decipher why the sea vanished and how its loss shaped Central Asia's climate.

CREDITS (TOP TO BOTTOM): JANE QIU; ADAPTED FROM RODERIC BOSBOOM

Published by AAAS

Time Capsule in the Desert

BEIJING—Wind-sculpted mounds and bizarre rock formations dot the Qaidam Basin, a mineral-rich swath of the northern Tibetan Plateau spanning 125,000 square kilometers of western China. "Setting foot in the Qaidam is like landing on Mars," says Fang Xiaomin, a geologist here at the Institute of Tibetan Plateau Research of the Chinese Academy of Sciences. But deep beneath this forbidding landscape are lost worlds: traces of gigantic freshwater lakes and lush forests that gave way to steppe and desert over tens of millions of years.



Martian-like chronicles. Desolate Qaidam Basin contains fossil and climate records tracing the transformation of Central Asia over tens of millions of years.

Fossils tell part of that story. Over the past 23 million years, "massive faunal turnovers" in the region accompanied the shift to a more arid climate, says Wang Xiaoming, a paleontologist at the Natural History Museum of Los Angeles County in California. One strange denizen was a shovel-tusked elephant that inhabited the swampy edges of lakes 16 million years ago, indicating that substantial freshwater bodies persisted long after the final retreat of the Paratethys Sea about 37 million years ago (see main story). The death knell for these lakes came in the last few million years, as reflected in a fish species whose bones were so stout that they left little room for flesh. Its bones thickened, apparently, as mineral concentrations soared in the shrinking lakes. "Their body just couldn't get rid of so much minerals and, therefore, stored them in the bones," Wang says.

To develop a more complete picture of the region's climate convulsions, Fang and his colleagues over the past 5 years have been drilling into Qaidam's 15-kilometer-thick sediments. So far, they have retrieved cores from as deep as 4.3 kilometers below the surface: "the first continuous terrestrial records going back to the base of the Miocene," 23 million years ago, Fang says.

These "pristine records" should help tease out the factors that triggered and sustained the drying in Central Asia, says Guillaume Dupont-Nivet, a geologist at the National Center for Scientific Research in Rennes, France, who is not involved in the project. So far, one intriguing finding from the sediment cores is a pronounced stretch of aridity about 7 million years ago that was out of step with global climate as written in marine records. Around that time, the northern Tibetan Plateau was rising to full height, says Fang, who suspects that "mountain building might have played a dominant role" in the drying by blocking moisture from the south.

Fang hopes to muster support to drill down another 5 kilometers, into 50-million-year-old sediments. That would allow the team to penetrate a formative time for Eurasia, when the Tibetan Plateau was first rising, levels of atmospheric carbon dioxide were falling, and the Paratethys Sea was beginning to retreat. There, they might find clues to how those forces conspired to turn a verdant Asia into today's austere landscape. **–J. Q.**

variations. Meanwhile, a shell's magnesium and oxygen isotopes reveal precisely the temperature and salinity of surrounding seawater. By analyzing hundreds of oyster shells collected across Central Asia, the scientists intend to piece together how environmental conditions changed at different stages of the sea's retreat.

One clear signal in the fossil record is pollen recovered from 40-million- to 30-million-year-old rock layers showing that plants that thrive in dry climates came to dominate Central Asia. That shift has been commonly attributed to the rise of the Tibetan Plateau, which impedes moisture transport from the south. That the drying took place at the same time as the Paratethys Sea's death throes is surely no coincidence, says Matthew Huber, a climate scientist at Purdue University in West Lafayette, Indiana, who is not affiliated with the project. East of the Paratethys, he says, "a drying signal may have nothing to do with the uplift, but rather may be related to how far away the sea was."

Paleoclimate data may also hold clues to another mystery: why the Paratethys retreated. The sea, Dupont-Nivet says, receded at a time when global atmospheric CO_2 levels fluctuated before falling precipitously, transforming the hothouse world tens of millions of years ago into one more closely resembling the present day. This "triggered glaciation in Antarctica and caused a massive drop in the global sea level," Dupont-Nivet says, and "might have led to the ultimate demise of the Paratethys."

The driver for the sharp decline in CO_2 levels is "one of the greatest riddles in the Earth's climate history," says William Ruddiman, a climate scientist emeritus at the University of Virginia in Charlottesville. In 1998, he and colleagues proposed that mountain building accelerated the process of chemical weathering, which sucks CO_2 out of the air as the gas reacts with freshly exposed rock. Ancient marine deposits also point to a boom in chemical weathering and a decline in CO_2 concentrations, says Jérôme Gaillardet, a geochemist at Université Paris Diderot. But there is still plenty of uncertainty. "The global carbon cycle is extremely complicated," he says. "It's a matter of the balance between processes that absorb CO_2 and those that release it."

Over a dinner of lamb stew and flatbread in a hilltop camp, Dupont-Nivet explains how his team hopes to reveal the entire history of the Paratethys. Little is known, he says, about the sea's first three advances and retreats. And there is plenty of work to be done in paleoclimate modeling, which he expects will show how the sea's retreat and the Tibetan Plateau's rise conspired with other climate factors to transform Eurasia. In the quest to truly understand the legacy of the long-lost Paratethys Sea, Dupont-Nivet says, we're "only at the beginning."

–JANE QIU

Jane Qiu is a writer in Beijing. Her trip to Tajikistan was supported by a journalism fellowship from the European Geosciences Union.

CREDIT: WANG XIAOMING

Published by AAAS



Rest easy. An artificial pancreas will protect diabetics from low blood sugar while sleeping.

CREDIT: ROMAN HOVORKA/UNIVERSITY OF CAMBRIDGE METABOLIC RESEARCH LABORATORIES

MEDICINE

A Pancreas in a Box

Sophisticated sensors, insulin pumps, and algorithms may help give type 1 diabetics a more normal life while researchers work on a cure

One morning last April, a woman named Jane checked out after an overnight stay in Addenbrooke's Hospital in Cambridge, U.K. She had spent 24 hours connected by tubes to several medical devices—mostly bored, she says, but also "mildly apprehensive." Now, she was taking them home to do something she hadn't done for 3 decades, something that she and the rest of the world's 30 million type 1 diabetics are never able to do: forget about her diabetes.

The devices—an insulin pump, a blood glucose sensor, and a computer about the size of a paperback book—make up a prototype of what researchers call an artificial pancreas. Together, they replicate the function of the pancreas that is lacking in diabetics: producing insulin in response to rises in blood glucose level. Groups in Europe, the United States, and elsewhere are now testing such systems in small groups of patients, hoping to show that the technology can work efficiently and safely. If so, it could transform the lives of diabetics, improving their health and allowing them something closer to an ordinary life. After controlling her diabetes with blood tests and injections for most of her life, having an artificial pancreas "would be magical," Jane says.

With its tubes and needles and gadgets, an artificial pancreas is not an elegant solution to the problem of diabetes. But researchers say it could provide a valuable stopgap until effective biological treatments—or even cures—come along. The principle is simple: Connect a commercially available glucose sensor to a commercially available insulin pump via a computer programmed to interpret the sensor readings and decide how much of the drug is needed. But implementing it has turned out to be far from straightforward. Controlling the level of sugar in the blood from outside the body is fiendishly difficult because sensors are slow and error-prone, while injected insulin can take hours to have an effect and overdoses can be fatal. For a person with diabetes, used to calculating insulin doses multiple times every day and dealing with the consequences, handing over that responsibility to a computer is daunting. Patients may be clamoring for such a solution, but researchers will have to convince them that it is safe.

Glucose, ingested in the form of sugar and other carbohydrates, is the body's energy source. But without the hormone insulin to help glucose out of the bloodstream and into cells, muscle and brain can't consume it, and liver and fat tissue can't store it for later use. Type 1 diabetics, whose condition develops early in life, lack insulin because their own immune system has attacked insulin-producing cells in their pancreas known as β cells. (Another form of diabetes, type 2, usually affects older people and results from insensitivity to insulin rather than a lack of it.)

Before the discovery of insulin in the early 1920s, type 1 diabetics would simply wither away, fall into a coma, and die within months or years. In the developed world at least, today's diabetics (including the writer of this article) can live a relatively normal life—although one dominated by a never-ending round of blood sugar tests, usually achieved with a finger prick to draw blood and an electronic meter, insulin injections, and meals carefully weighed to estimate how much carbohydrate is being eaten.

The consequences of getting it wrong can be severe. Give slightly too much insulin and glucose in the blood drops to low levels. Starved of fuel, the brain first shows symptoms similar to drunkenness, followed by unconsciousness and even death. Allow sugar levels to get too high and the syrupy blood can damage delicate blood vessels, leading to long-term complications that include heart disease, blindness, kidney failure, and limb amputation. Completely uncontrolled blood sugar leads to a coma and a trip to the hospital by ambulance, which is how many type 1 diabetics find out that they have the disease. So living with diabetes is a continual balancing act: trying to keep blood sugar levels close to those of a normal person using sporadic and erratic information (finger-prick tests) and inadequate tools (injected insulin).



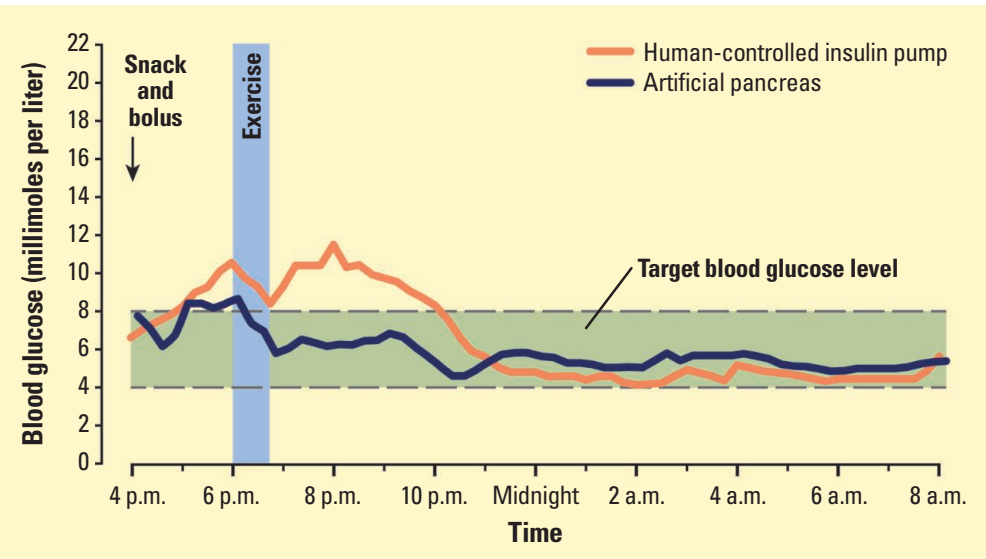
"We're trying to do this invisibly and automatically. But we need faster insulin and we need faster [sensors]."

—FRANK DOYLE, UC SANTA BARBARA

Researchers worldwide are working on biological

Published by AAAS

cures for type 1. But progress is slow, and it could be many years or even decades before they are ready for widespread use. So, over the past decade, many researchers and physicians have begun working on a technological solution—the artificial pancreas—to fill the gap. Their job has been made easier by huge advances in diabetes management—new types of insulin, insulin pumps, blood glucose sensors—introduced by drug companies and medical device manufacturers.



On target. A diabetic's main goal is to keep his or her blood glucose level within the same levels as a normal person. An artificial pancreas does this better than manual control, with fewer potentially dangerous excursions.

The first insulin pumps that patients could take home and manage themselves emerged in the 1980s. Today's models, the size of a pager, pump insulin via a thin tube into the body through a cannula: a needle or tube inserted a few millimeters into subcutaneous tissue, usually in the stomach area. Pumps trickle in tiny doses of insulin—known as a basal dose—day and night, just as a pancreas does. Meals call for a much larger and immediate dose of insulin, known as a bolus, which patients program into the pump depending on how large the meal is. Pumps provide better control of blood sugar levels than insulin injections do, but their high cost has limited their popularity.

Pumps don't eliminate the need for finger-prick glucose testing, but continuous glucose monitors (CGMs) do. Introduced in the late 1990s, these devices use a sensor that projects through the skin into the interstitial fluid between cells and measures its electrical characteristics to determine blood glucose levels. A transmitter attached to the body sends the results to a handheld receiver. CGMs give better real-time data on blood glucose levels than finger-prick tests do—but again, because of their high cost very few diabetics now use them.

"The advent of a portable, reliable CGM was the missing link" that encouraged funders to take the idea of an artificial pancreas seriously, says Aaron Kowalski, vice president for treatment therapies at JDRF, a worldwide diabetes research foundation. JDRF set up an artificial pancreas project in 2006 to fund research in centers and companies in the United States and Europe.

But it was the medical device industry that took the first step. In 2009, device manufacturer Medtronic released the most basic type of artificial pancreas system: an insulin pump able to receive signals from a CGM transmitter. The hybrid device isn't smart enough to control blood sugar to within a narrow range, but it can avert emergencies. The company adapted it to set off an alarm when blood sugar gets low; if no action is taken, the system simply stops the basal insulin dose for 2 hours.

Such a system is ideally suited to dealing with low-glucose events—otherwise known as hypoglycemia or "hypos"—during the night. Nighttime hypos are particularly worrisome because people are unaware they are happening and respond too slowly or not at all, which can result in coma or hypoglycemic seizures. Medtronic's system was approved for use in Europe relatively quickly; the U.S. Food and Drug Administration (FDA), which is more cautious about medical devices, followed suit in September 2013.

Medtronic's system can stop hypos from getting worse, but it doesn't prevent them in the first place. For that, you need an intelligent algorithm that can analyze what a user's blood sugar is doing and predict what it will do in the future. Groups around the world have been working on such algorithms for a number of years.

Algorithms fall into three main types. The simplest is a common feedback loop used in the industrial control industry called a proportional-integral-derivative (PID) controller. This looks at a user's past and current blood glucose level and, based on the rate of change, calculates the best insulin dose to restore a target glucose level. "It's very simple, very intuitive," Kowalski says, but many now think PID controllers are too simplistic for the complex array of factors involved in controlling blood sugar, including food ingested, the slowness of insulin absorption, amount of insulin already in circulation, and exercise.

Many groups are working on a second algorithm type, which forecasts future blood sugar levels on the basis of the diabetic's own physiology. Such model predictive control (MPC) algorithms "incorporate a model of insulin and carbohydrate absorption, tuned to the particular patient," says Lalantha Leelarathna of the Institute of Metabolic Science at the University of Cambridge in the United Kingdom. The third type of algorithm attempts to replicate how a physician would advise a patient to control his or her blood sugar and applies the recommendation using fuzzy logic, which makes decisions based not on binary yes-no answers but on truth variables that range between 0 and 1. "We took our experience and incorporated it into an algorithm," says Moshe Phillip of the Schneider Children's Medical Center of Israel in Petah Tikva.

Researchers are now testing these more advanced systems by inviting subjects for short stays in the hospital. In 2013, several teams let subjects take the systems home for a few days, as Jane did, or test them in hotels or at a children's "diabetes camp." Not all the results of these trials have been published yet, but Kowalski says that "the results have been amazing, showing a dramatic decrease in hypos and hypers [high blood glucose] and a positive effect on the social aspects of diabetes," such as a freedom from worry and a chance to lead a "normal" life.

Some of the systems tested were designed to be used only at night. "Night is the most dangerous time," Phillip says. Some parents

CREDIT: ROMAN HOVORKA/UNIVERSITY OF CAMBRIDGE METABOLIC RESEARCH LABORATORIES

Published by AAAS

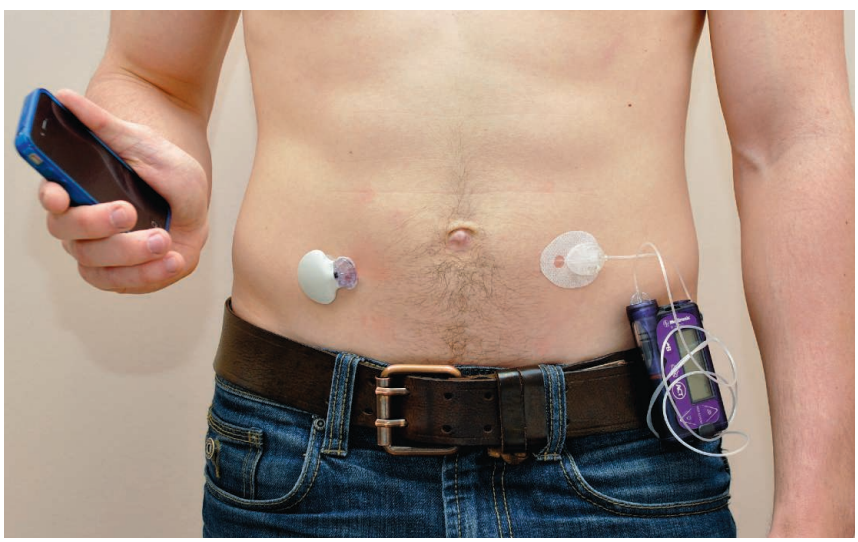
rise several times every night to test a sleeping child's blood sugar. The "Glucositter" system that he and his team are developing "will change the quality of life for parents," he says.

Systems designed to work round the clock, however, still require some input from the user to deal with daytime activities such as eating or exercise. The huge influx of carbohydrate in a meal poses perhaps the biggest challenge. In a nondiabetic person, the β cells in the pancreas are relatively dormant between meals. Other cells known as α cells take charge and produce a hormone called glucagon, a sort of anti-insulin that signals the liver to release stores of glucose to keep the body ticking over. When the person sees and smells food and knows that a meal is on the way, the body starts getting ready. The brain turns off the α cells and sets the β cells producing insulin, which in turn tells the liver to switch from secreting glucose to storing it. Within 10 minutes, the body is primed and ready to digest the meal.

In a diabetic, the body can't prepare in this way. And because injected insulin can take up to 2 hours to reach peak activity, a patient's blood sugar level often rises above the target range in the hours after a meal before leveling off as the insulin takes effect. With an artificial pancreas, the situation is even worse because the CGM takes time to detect the meal: half an hour or more for the carbohydrate to reach the bloodstream, 15 minutes for it to reach the interstitial fluid where it can be detected, and another 6 to 15 minutes for signal processing. Algorithms also have trouble gauging the size of a meal from the scanty information the CGM provides early in the digestive process. So the device could easily administer too much insulin and—because the hormone remains active in the body for up to 4 hours—trigger a hypo hours later.

To get around this problem, some researchers require users to warn the system that a meal is on the way. The artificial pancreas can then either base a dose on a user's estimate of how much carbohydrate he or she is about to eat, or simply administer a starter dose of insulin and then top up as necessary once blood sugar readings begin to rise. Users may soon be able to assist the system by taking a premeal puff from an insulin inhaler. The drug company MannKind Corp. has developed a very quick-acting inhalable insulin called AFREZZA. FDA turned AFREZZA down for approval in 2011 because the agency wanted more information, but MannKind resubmitted the product in October and hopes for approval in April 2014.

Such approaches help reduce postmeal blood sugar peaks and later troughs. Many researchers, however, want to provide a fully hands-free system. "We're trying to do this invisibly and automatically. But we need faster insulin, and we need faster CGMs," says chemical engineer Frank Doyle of the University of California, Santa Barbara. Companies are working on ways to speed insulin into the bloodstream by altering its molecular structure or using drugs or small electric heaters to change the properties of skin and tissue.



Technological fix. In an artificial pancreas, a glucose sensor (on stomach, *left*) transmits readings to a controller (here in a smartphone), which instructs an insulin pump to administer the required dose.

Perhaps the fastest approach is to inject insulin straight into the abdominal cavity near the liver and pancreas, where it can get to work instantly and signal the liver to halt releasing glucose before a meal. "This would speed up considerably what you can do with a fully automatic system," Doyle says. The pharmaceuticals company Roche has developed a permanent injector called DiaPort, but because of the complications of a permanently inserted device, only a tiny number of diabetics now use it.

Others are working on making CGMs faster and especially more reliable. Current systems are not only slow to respond but can also make mistakes. Miscalibration, a dislodged sensor, or a loss of sensor sensitivity can cause spuriously high readings of blood glucose, resulting in a serious hypo. "Outliers are the main problem," says Kowalski, who believes developers will have to use techniques from critical systems engineering, such as redundant sensors and failure analysis, to spot erroneous readings.

Alternatives to the electrochemical signals now used to detect glucose could also yield better CGMs. Some makers are developing sensors that shine light through the skin and look for wavelengths that glucose absorbs. Other systems inject proteins that fluoresce in the presence of glucose and use light sensors to spot the telltale glow. JDRF is now working with several companies to develop a single sensor that uses both electrochemical and optical techniques as a fail-safe.

Another safety mechanism employs a pump that can separately dispense both insulin and the anti-insulin hormone glucagon. When blood glucose readings dip too low, a squirt of glucagon quickly brings them up again. A team at Boston University tested the idea using two pumps in 2013 with "very, very impressive results," Kowalski says. JDRF is working with the device manufacturer Tandem Diabetes Care on a dual-hormone pump. Right now, glucagon is not stable in solution for long periods, but drug companies are working on a reformulated long-lasting version of the hormone.

Whether developers will ever get to a fully automated system that diabetics can insert and forget remains to be seen. But "we shouldn't let perfect be the enemy of good," Kowalski says. Stuart Weinzimer of the Yale University School of Medicine agrees: "We don't need these things to be perfect. It doesn't matter what system is best. Just make them available to market and let clinicians decide." As for those who stand to benefit from an artificial pancreas, Jane says, all that matters is that the devices work. In that case, pump and tubes notwithstanding, "it will feel like not having diabetes."

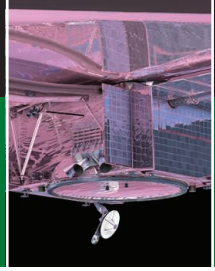
–DANIEL CLERY

CREDIT: © IRCM/MEDTRONIC INC.

Published by AAAS



To the cities for jobs
138



Space Science funding
140

LETTERS | BOOKS | POLICY FORUM | EDUCATION FORUM | PERSPECTIVES

LETTERS

edited by Jennifer Sills

Antibiotics: Call for Real Change

IN HIS EDITORIAL "TIME TO DEAL WITH ANTIBIOTICS" (15 NOVEMBER 2013, p. 777), D. Kennedy mentioned our assessment of the impact of the Pew Commission on Industrial Farm Animal Production (IFAP) (*1*). We support his call to end the misuse of antibiotics in animal agriculture. We believe, however, that finalization of the U.S. Food and Drug Administration (FDA) guidance documents will not have a meaningful impact on the way these life-saving drugs are administered to animals; thus, they will not slow the contribution of IFAP to our rapid progression toward a postantibiotic era.



These guidances—nonbinding pleas for the cooperation of drug companies—do not call for an end to the use of antimicrobials in the absence of a microbial disease or documented disease exposure, as recommended by the Commission (*2*). Instead, they would effectively rebrand uses currently labeled "growth promotion" as "disease prevention." Like growth promotion, prophylactic uses entail low, subtherapeutic doses and can span much of the animal's life span. They apply continuous selective pressure for antibiotic resistance and may even induce new resistance-conferring mutations (*3*). Furthermore, the FDA's proposal for veterinary oversight would eliminate the federal requirement that a valid "veterinarian-client-patient relationship" exist before veterinarians order the use of antibiotics in feed, allowing veterinarians to prescribe antibiotics for use at operations they have not visited recently for administration to animals they have never seen.

The head of a large drug company recently told *The Wall Street Journal* that the guidances will not substantially affect revenues (*4*), implying that minimal changes to antibiotic sales are expected. This explains why companies support voluntary limits on their products: The limits will have little practical effect.

We share Kennedy's assessment of the problem, but instead would call for meaningful regulation—comparable to what he attempted as FDA commissioner almost four decades ago—to curb irresponsible antibiotic use. If such efforts fall short, legislative relief is needed.

KEEVE E. NACHMAN,* TYLER J. S. SMITH, ROBERT P. MARTIN

Environmental Health Sciences, Johns Hopkins Bloomberg School of Public Health, Baltimore, MD 21205, USA.

*Corresponding author. E-mail: knachman@jhsph.edu

References

1. Johns Hopkins Center for a Livable Future, "Industrial Food Animal Production in America: Examining the Impact of the Pew Commission's Priority Recommendations" (Johns Hopkins Bloomberg School of Public Health, Baltimore, MD, 2013); www.jhsph.edu/research/centers-and-institutes/johns-hopkins-center-for-a-livable-future/_pdf/research/clf_reports/CLF-PEW-for%20Web.pdf.
2. Pew Commission on Industrial Farm Animal Production, "Putting Meat on the Table: Industrial Farm Animal Production in America" (Johns Hopkins Bloomberg School of Public Health, Baltimore, MD, 2008); www.ncifap.org/_images/PCIFAPFin.pdf.
3. D. C. Love, M. F. Davis, A. Bassett, A. Gunther, K. E. Nachman, *Environ. Health Perspect.* **119**, 279 (2011).
4. P. Loftus, "Zoetis chief leads animal-health firm following split from Pfizer," *Wall Street Journal* (2013); http://online.wsj.com/news/articles/SB10001424052702303755504579207710851450896.

Antibiotics: Discontinue Low-Dose Use

IN HIS EDITORIAL "TIME TO DEAL WITH ANTIBIOTICS" (15 November 2013, p. 777), D. Kennedy correctly calls again (as he did in the 1970s) for curbs on the overuse of antibiotics on industrial farms, where excessive animal crowding has favored the likelihood of disease and the perceived need to rely on low-dose prophylactic antibiotics to stifle outbreaks.

It is critical to recognize that veterinarians must continue to have access to effective antibiotics to treat animals that are clinically ill from bacterial infections. Such treatment entails the targeted use of therapeutic doses for short periods of time at concentrations that are capable of achieving high bacterial kill rates. However, the practice of routinely administering antibiotics at low-dose concentrations in feed and water for extended periods of time to large populations of animals that lack signs of clinical illness is the surest way to spawn resistant bacteria (*1*). Even more threatening, and many would say unethical, has been the industry's use of low-dose antibiotics for purposes of growth promotion in healthy animals.

Although the FDA has recently determined the use of antibiotics for growth promotion to be injudicious, it continues to condone the use of low-dose antibiotics in feed and water for disease prevention (*2*). Kennedy states that the FDA Guidance for Industry #213 "would end antibiotic use for growth promotion" and restrict prophylactic use in feed and water to veterinary prescriptions, but it must first be recognized that this is a guidance document only and has no enforcement authority. Furthermore, if low-dose concentrations of antibiotics continue to be allowed for preventive use (even by prescription), they provide a "back door" through which growth promotion effects can still be exploited under another name, thereby incentivizing industry to secure the needed prescriptions and essentially continue business as usual. In this respect, Kennedy's enthusiasm for the new FDA guidelines may be overly optimis-

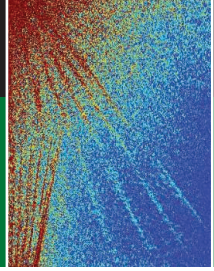
CREDIT: ALVAREZ/ISTOCKPHOTO (MODIFIED BY G. GRULLÓN/*SCIENCE*)

Downloaded from www.sciencemag.org on January 10, 2014

Published by AAAS



Don't blame the Dingo
142



Computing with light waves
144

tic. Rather, to truly deal with antibiotics, we are going to have to find innovative ways to reconfigure the production environments on animal farms that are grounded in sound husbandry principles and obviate the need for low-dose antibiotics in any form.

RAYMOND J. TARPLEY

College of Veterinary Medicine and Biomedical Sciences, Texas A&M University, College Station, TX 77843, USA. E-mail: rtarpley@cvm.tamu.edu

References

1. M. T. Brewer *et al.*, *Am. J. Vet. Res.* **74**, 1078 (2013).
2. FDA Center for Veterinary Medicine, "Guidance for Industry #209: The Judicious Use of Medically Important Antimicrobial Drugs in Food-Producing Animals" (www.fda.gov/downloads/AnimalVeterinary/GuidanceComplianceEnforcement/GuidanceforIndustry/UCM216936.pdf).

Science for Sale: Fair Evaluation Standards

IN HER NEWS FOCUS STORY "CHINA'S PUBLICATION bazaar" (29 November 2013, p. 1035), M. Hvistendahl points out that many scientists and organizations are starting to abandon the use of impact factors to evaluate a single researcher. Science leaders in China are considering new standards as well, such as total paper citations.

The use of the Science Citation Index (SCI) may have some disadvantages, such as the financial incentives to forgery described in the article. However, in China, it may be the fairest standard to assess scientists. Without the SCI standard, the chance of getting research funding in China would be entirely based on the scientist's relations with government. Using total paper citations or number of patents awarded would have similar problems, because both of these metrics can be influenced by money.

Thus, although the SCI or impact factor system has drawbacks, it is still a fair standard. More research is needed to build a system, based on impact factor or SCI, in which cheaters stand to lose more than they gain.

CAI LUO

Department of Automation, Tsinghua University, Beijing, 100084, China. E-mail: luo_cai@tsinghua.edu.cn

Science for Sale: Authorship Confirmed

IN HER NEWS FOCUS STORY "CHINA'S PUBLICATION bazaar" (29 November 2013, p. 1035), M. Hvistendahl highlighted the issue of scientific articles being for sale in China. This problem is not widely known by journal editors outside of China. The article indicated that a meta-analysis published in the *Canadian Journal of Neurological Sciences* (CJNS) was available for sale on 21 August 2012 on Core Editing's blog, before submission of the paper to CJNS. At CJNS, we conducted an investigation of the paper in question. The corresponding author was able to provide detailed information of their data analysis, including screen shots of a list of files used for data analysis from the first author's computer, output from the data analysis program used, copies of handwritten notes used for data analysis, records of discussion between the authors regarding the results, and previous versions of the paper. The authors also provided records of e-mail correspondences from February 2012 between the first author and the author of a paper included in the meta-analysis in which the first author asked and obtained data for the meta-analysis. These e-mail communications were independently verified by the U.S.-based author who provided the additional data. On the basis of this information, we concluded that the paper published in CJNS was the work of the first and the corresponding author of the paper.

ROBERT CHEN

Department of Medicine (Neurology), Toronto Western Hospital, University of Toronto, Toronto, ON M5T 2S8, Canada and Editor-in-Chief, Canadian Journal of Neurological Sciences. E-mail: robert.chen@uhn.ca

Science for Sale: Improve Ethics Education

WE APPLAUD *SCIENCE* FOR ITS INVESTIGATIVE journalism on "China's publication bazaar" (M. Hvistendahl, News Focus, 29 November 2013, p. 1035). This article should stimulate other journals to undertake similar research. Indeed, we would like to suggest that conducting such research become a standard component in the responsible conduct of research courses now required of all National Science Foundation (NSF)–funded students and postdocs.

Unfortunately, the NSF requirement is, at many universities, met with minimalist online courses. Even at our own institution, there has been resistance to making ethics education mandatory for all graduate students. We believe that just as true science and engineering education requires original research or experimental designs rather than simply learning the results of others' work, ethics education should include more than studying classic ethical theory, professional codes, and case studies. This would, however, require turning a one-credit course into a more substantial effort. Such a course would not only enhance ethics education. It could well benefit the fields of science and engineering, as well as the ways in which these fields serve society.

Finally, we would recommend that courses in research ethics be required of all graduate students, not solely those who receive support from NSF or National Institutes of Health grants.

CARL MITCHAM* AND ROEL SNIEDER

Colorado School of Mines, Golden, CO 80401–1887 USA.

*Corresponding author. E-mail: cmitcham@mines.edu

CORRECTIONS AND CLARIFICATIONS

News Focus: "China's publication bazaar" by M. Hvistendahl (29 November 2013, p. 1035). Wang Mouyue, managing director of the *Chinese Medical Journal*, was quoted incorrectly due to an error in transcription from the original Chinese. The article quotes Mr. Wang as saying that "China's paper-selling market is very large, and there's every sort of agency imaginable out there." He actually said: "China's paper-publishing market is very large, and there's every sort of agency imaginable out there." Also, the article stated that the *Journal of Zhejiang University-SCIENCE* is not indexed in SCI. The three journals under the title *Journal of Zhejiang University-SCIENCE* are all listed in SCI Expanded. The PDF and HTML versions online have been corrected to reflect these changes. In addition, the article described how Core Editing had advertised authorship for sale on 12 papers listed on its blog. The corresponding author of one of these papers, later published by the *Canadian Journal of Neurological Sciences*, has since provided documentation to *Science* and to the editor of the *Canadian Journal of Neurological Sciences* indicating that none of the authors paid to have their names added to the paper.

Letters to the Editor

Letters (~300 words) discuss material published in *Science* in the past 3 months or matters of general interest. Letters are not acknowledged upon receipt. Whether published in full or in part, Letters are subject to editing for clarity and space. Letters submitted, published, or posted elsewhere, in print or online, will be disqualified. To submit a Letter, go to www.submit2science.org.

Published by AAAS

DEMOGRAPHY

People Flocking to China's Cities

Xin Meng

China's Urban Billion: The Story Behind the Biggest Migration in Human History

by Tom Miller

Zed, London, 2012. 200 pp. $125.95, £70. ISBN 9781780321424. Paper, $29.95, £16.99. ISBN 9781780321417.

Affecting us all, China's economic growth is reallocating income around the world—cheaper imports for consumers and more competition for local manufacturing, leading to job loss, higher commodity prices, and greater income for commodity exporters. How can we learn more about the second-largest economy in the world? One first step on that fascinating knowledge journey of 1000 li is to read Tom Miller's balanced, insightful, and detailed *China's Urban Billion*.

Journalist Miller (*China Economic Quarterly*) tells the story of the movement of 200 million rural Chinese to the cities, which has fed the extraordinary Chinese growth. He focuses on the past impacts of mass migration and an analysis of policy choices and their likely effects on future migration, Chinese city growth, and Chinese well-being.

Miller believes there are two important political obstacles that must be overcome to ensure a high-growth future with improved social outcomes. The first is the household registration system (*hukou*), which divides the Chinese into two groups: the urban privileged (with higher incomes and better jobs, education, and access to the social welfare system) and the rural disadvantaged (with lower incomes, lower-quality schools, restricted opportunities for urban employment, and no access to the city welfare system). *Hukou* was designed in the early 1950s to reduce the cost of industrialization (through lower costs of raw materials and urban living) and to facilitate affordable full employment and full social welfare for the urban sector. For the following 30 to 40 years, it ensured low geographic mobility.

Two decades ago, the *hukou* system—driven by economic growth and excess labor in rural areas—began to break down in regards to where individuals can work as more rural workers moved to the cities to seek higher incomes in manufacturing and construction. But *hukou* has been retained as a means of restricting access to good city jobs, welfare, and social services. As a result, most rural migrants remain second-class, temporary, and low-paid citizens in cities. They return home to get married, to have children, and when unemployed or ill. Parents often leave their children behind in rural areas, where they receive less parental care and a poor education. The system not only is extremely unfair but also constrains China's future economic growth. It shortens migrants' stay in cities, reduces the supply of much-needed low-skilled labor, and restricts migrant workers' ability to accumulate human capital through on-the-job training.

It seems self-evident that *hukou* must break down. And, as each year passes, the system becomes a little less binding. However, it remains restrictive, and removing it completely will probably require major reform. How and when this reform will take place is the difficult part. Miller explains how such reform goes to the heart of the politics and economics of the Chinese federal system and how some cities have adjusted more than others. His detailed analyses of various experiments in different cities and the public finance implications of *hukou* removal are particularly good.

A second, and related, obstacle to high future growth rates and increasing Chinese well-being is land-tenure reform. Currently, rural land is owned by and can only be sold by the local collective. Individuals have no rights to particular pieces of land. Rural people cannot achieve high incomes across the board when so many still live and work on small land plots. In the long run, large numbers of people must permanently move off the farms, as they have done in most societies as those have become richer. But to move means to give up the income cushion that the land provides. Hence, revising *hukou* to develop a nationwide welfare system intertwines with land reform.

If we look back in time or across many current poorer nations, large population movements to the cities have been accompanied by increasing poverty, rising crime, spreading slums, and poor living conditions. China has largely avoided these outcomes. The issue is whether it can continue to do so through a shift to a migration system without *hukou* and to a deregulated land market. Miller spends a great deal of time discussing that question, and he provides considerable detail as to progress across different cities. There remain, however, many questions without easy answers: How can rural migrants with families move to cities on a permanent basis given that current urban housing prices remain so far above what migrants can afford? Can cheap housing be provided on a large scale in cities without formation of ghettos? Does the future lie in small towns rather than mega cities? For example, recent studies on urbanization in China have found that most Chinese cities are too small to be economically viable. Whereas, if the average size of cities at the prefecture level can be doubled, their value added per worker could be increased by 20 to 35 percent (*1*–*3*).

China's Urban Billion offers something for everyone, lay reader and expert alike, to think about. I do, however, have a quibble. I wonder whether Miller is right when he asks if "Chinese leaders are willing to forgo short-



CREDIT: TRAVELSTOCKCOLLECTION—HOMER SYKES/ALAMY

Heading home. Migrant laborers in Beijing, waiting for their trains back to the country.

The reviewer is at the Research School of Economics, Australian National University, Canberra, ACT 0200, Australia. E-mail: xin.meng@anu.edu.au

Published by AAAS

term economic gains and make the changes needed to create a healthier form of urbanization?" Although China's urbanization seems certain to proceed further along the reform path, I don't see that journey necessarily involving a trade-off of short-term economic gains. Future reforms (some of which were announced at the recent Third Plenum of the 18th Communist Party of China, as part of the next round of changes) could proceed in an experimental manner, with careful evaluation of the effects on potential winners and losers before they are introduced across the whole country (as was done during the previous economic reforms). If that path is followed, I believe that future *hukou* and land reform can lead to better outcomes all around.

References
1. X. Wang, X. Xia, *Jingji Yanjiu [J. Econ. Res.]* **1999** (9), 22 (1999).
2. C.-C. Au, J. V. Henderson, *Rev. Econ. Stud.* **73**, 549 (2006).
3. X. Wang, in *Rising China: Global Challenges and Opportunities*, J. Golley, L. G. Song, Eds. (Australian National Univ. E Press, Canberra, 2011), pp. 315–327.

10.1126/science.1244814

FICTION

Biogeek Catastrophe

Michael A. Goldman

The conclusion to a dystopian trilogy that began ten years ago with *Oryx and Crake* (*1*), Margaret Atwood's *MaddAddam* is an example of what I call firm science fiction—not quite hard, but not quite soft, either. It's grounded in the plausible science of the very near future (or of today) but is by no means didactic about that science. Atwood likes to call it speculative fiction.

I should warn you to read *Oryx and Crake* and *The Year of the Flood* (*2*) before you plunge into *MaddAddam*. But I won't. Atwood provides a superb summary at the start of the novel, a far better synopsis than I could give you. Moreover, reading any of the Canadian author's work is dangerous. It might make you a fan and send you back to earlier works, such as *The Handmaid's Tale* (*3*), which swept up a few science fiction awards in the 1980s. It could make you join her cultlike following on Facebook or Twitter. And it's a good way for scientists to blend in at a cocktail party with their friends in the arts and humanities. Atwood has touched every branch of literature, from poetry to science fiction. It's grand to see her versatility and to have her skill at bringing science into mainstream literary thought.

MaddAddam joins a host of recent dystopian novels. It incorporates overpopulation, climate change, genetic engineering, and a new cyberreality that threatens the future of our species, threats to which we must either adapt in some way or face an ungraceful extinction. The frightening part is that these themes aren't simply fiction. We are assaulted daily with evidence of a deteriorating, unpredictable climate; an ever-growing population; diseases we can't fight; terrorism; and a maturing cybercrimes industry. I think we need to pay attention.

I tend to get lost rapidly in dictionaries of unconventional names, unprecedented creatures, novel biologies, and anthropologies, so I will leave out most of the jargon here. MaddAddam's world is one in which a few biotechnology companies and other firms have come to control the world. There's even a religion built around the petroleum industry (the Church of PetrOleum). Their employees live and work in compounds, seldom mixing with the "pleeblands" beyond, which evokes a picture of life in Los Angeles at the time of *Blade Runner*. The oceans have risen—Santa Monica is now called the "floating world"—and resources have become scarce. Genetically engineered creatures have become the norm. "Chicky knobs," or headless, live chickens, were introduced in *Oryx and Crake*. Pigs with human organ tissue, called pigoons or Pig Ones, frolic among skunk-rats, and it isn't even clear that most of the remaining humans are what we'd recognize as human.

MaddAddam
A Novel

by Margaret Atwood
Doubleday, New York, 2013. 415 pp. $27.95. ISBN 9780385528788. McClelland and Stewart, Toronto. C$32.95. ISBN 9780771008467. Bloomsbury, London. £18.99. ISBN 9781408819708.

The characters inhabit a time of modern gadgetry and a virtual world in which they can meet in secret. One scientist, Glenn (later known as Crake), takes it upon himself to create a new race of humans without the faults of the old. They come to be known as the Crakers. These simple creatures are incapable of war and jealousy and feed on leaves so they don't need agriculture. Satisfied with them, Crake releases a "feel good" pill called BlyssPluss through HelthWyzer that has an untoward side effect—a virus that kills all but a few surviving humans, in what's known as the waterless flood. *MaddAddam* recounts the origins of the oral and then written creation mythology of the new world. The Crakers will inherit the Earth, and one among them, called Blackbeard, is writing its history.

To give you a feel for a typical scene, just after the peaceful Crakers free the Painballers (you can guess they're no fun)

> The Crakers all started talking at once. "Snowman must stay with us! We must put Snowman back into his tree." "That is what he likes, he likes a tree." "Yes, only he can talk with Crake." "Only he can tell the words of Crake, about the Egg." "About the chaos." "About Oryx, who made the animals." "About how Crake made the chaos go away." "Good, kind Crake." They began singing.

The characters Adam and Zeb keep in touch with each other through "a biogeek challenge game called Extinctathon. Monitored by MaddAddam, it said: *Adam named the living animals, MaddAddam names the dead ones. Do you want to play?*" Some of the names used in the book are aliases of people participating in Extinctathon.

Atwood has characterized her novel as hopeful because a few humans are still surviving at the end (*4*). Her narrative imposes a population bottleneck, and we've seen those before in the course of human evolution. But do we really need another flood? Are things really getting that bleak? I like to think not, but I suppose averting the flood wouldn't make much of a story.

Reading *MaddAddam* can be rough going for those accustomed to straightforward science, and it can be disturbing at times. But Atwood, who comes from a family of scientists, is no mindless critic of the scientific enterprise. And the chance to read a great novelist talking about the very science we do every day is far too worthwhile to pass up. Although science themes in mainstream literature sometimes make us practitioners look mad, in the end they foster understanding and form a crucial part of public education about science.

References
1. M. Atwood, *Oryx and Crake* (McClelland and Stewart, Toronto, 2003); reviewed in (*5*).
2. M. Atwood, *The Year of the Flood* (Doubleday, New York, 2009).
3. M. Atwood, *The Handmaid's Tale* (McClelland and Stewart, Toronto, 1985).
4. Interview, "City Arts and Lectures" (San Francisco), 13 October 2013.
5. S. M. Squier, *Science* **302**, 1154 (2003).

10.1126/science.1247253

The reviewer is at the Department of Biology, San Francisco State University, San Francisco, CA 94132–1722, USA. E-mail: goldman@sfsu.edu

Published by AAAS

SPACE SCIENCE

Coping with Uncertainty in Space Science Planning

Decadal surveys should propose financially responsible priorities and standing committees should facilitate their implementation.

Charles Kennel[1]* and Alan Dressler[2]

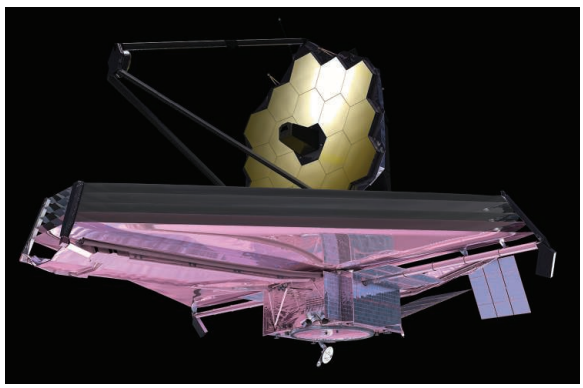
Political gridlock is spreading a miasma of uncertainty over the space sciences in the United States. Neither those who give science advice nor those who receive it have a clear grasp of what the future holds, a reality for the U.S. National Aeronautics and Space Administration (NASA) that was underscored in *NASA's Strategic Direction and the Need for a National Consensus* (*1*). This report concluded that "There is no national consensus on strategic goals and objectives for NASA. Absent such a consensus, NASA cannot reasonably be expected to develop enduring strategic priorities for the purpose of resource allocation and planning."

Given the divergence in political views, consensus is out of the question for the moment. Even if there were clear political direction, the space sciences would still be hostage to NASA's internal struggle to reshape its human exploration program, a struggle that will last the rest of the decade. Major observational projects in both NASA and the National Oceanic and Atmospheric Administration (NOAA) have had serious overruns in the past few years, which have rendered the best-made plans moot. The possibility of unanticipated cost growth is ever-present.

In such circumstances—the combination is unprecedented in our experience—we on the National Research Council's (NRC) Space Studies Board (SSB) are reexamining how we structure and deliver planning advice that preserves essential scientific priorities in a time of unexpected changes in policy, budget, and execution. We have progressed along two paths—to strengthen the stewardship role of the SSB's standing committees (*2*) in coping with short-term program fluctuations and to make more resilient the SSB's "decadal surveys" that develop 10-year research strategies for each of the major space-science disciplines.

Expectations, Reality, Mismatch

Between 2010 and 2012, the SSB carried out decadal surveys in astronomy and astrophysics (*3*), planetary science, solar and space physics (heliophysics), life and physical sciences in space, and a midterm review of Earth sciences and applications from space. Each decadal survey identified the most important scientific goals for the coming decade by soliciting hundreds of white papers and conducting dozens of town hall meetings.



Should high-profile missions such as the James Webb Space Telescope require special treatment by the decadal surveys and NASA?

The survey teams included experienced managers and engineers, as well as scientists, and commissioned independent estimates of cost and technical risk so as to make financially responsible recommendations. Taken together, these surveys may comprise the most complete characterization of the state of the space sciences ever achieved. NASA, by and large, implements the first priority recommendations of such major NRC studies, but this time around, key recommendations, notably for astrophysics and planetary science, were virtually dead before arrival and have had to be reconstructed.

How did the mismatches between expectation and reality emerge during the recent decadal surveys? After all, the government sponsors and the SSB believed the surveys were realistically designed when they began. However, there had been a key breakdown. Both government and NRC rules impeded the flow of information between NASA and the SSB during the conduct of the surveys. During the years that the SSB was managing four decadal surveys and one midterm decadal review, the board's disciplinary standing committees had to stand down because of budget and staff limitations.

Just as the huge cost overruns in the James Webb Space Telescope (JWST) project (*4*) (see the figure) became apparent within a NASA facing budget reductions, the SSB's science communities were sequestered writing the decadal surveys—which they could not discuss with anyone until the surveys had gone through NRC peer review. This is the price of rigor, but just when our colleagues in NASA's Science Mission Directorate wished they could solicit our advice, government rules prevented them from telling the study committees officially of a budget problem that altered the prospects for all the space sciences and would have changed the terms of reference for the surveys. The scientific community had suspected there would be bad news, but there was no way for the decadal studies to adjust in midstream (*5*).

In short, NASA's program managers did not hear from the SSB on the things about which they were most worried. We lost touch. And the decadal surveys' recommendations looked out of touch. The day-by-day ebb and flow of knowledge and intent between NASA and the SSB had been blocked.

Agreeing on Terms, Estimating Costs

How can we improve the next time around? These were the central questions motivating a "lessons learned" workshop convened by the SSB and the NRC Board on Physics and Astronomy that the authors cochaired. Participants from the domestic and international Earth and space science communities debated all aspects of the decadal review process: how each community reviews its past achievements; how each characterizes its present status and identifies future opportunities; how scientific ideas are shaped and reshaped by committee debate into notional (or "placeholder") mission and program concepts; how technical challenges are identified and costs estimated; how cost and technical evaluations influence scientific choices and the committee process; how the survey com-

[1]Scripps Institution of Oceanography, University of California San Diego, La Jolla, CA 92093, USA. [2]Observatories of the Carnegie Institution for Science, Pasadena, CA 91101, USA. *Corresponding author. ckennel@ucsd.edu

Downloaded from www.sciencemag.org on January 10, 2014

CREDIT: NASA

Published by AAAS

mittees interact with NASA and the scientific community during the study phase; what role international and interagency collaborations play in shaping recommendations; and above all, how to cope with policy fluctuations and budgetary uncertainty. Uncertainty was the elephant in the room, permeating all discussions at the workshop.

NRC reports are notable for their rigorous peer review, whose most critical task is to ensure that no report strays beyond its statement of task (SOT). The SOT defines the issues to be considered and the criteria on which they shall be prioritized. Nothing is more important to success than getting the SOT right. You have to do this even before you choose the survey committees.

The SOT negotiations between the NRC and the U.S. agencies that sponsor space science (NASA, National Science Foundation, NOAA, Department of Energy, and U.S. Geological Survey) should develop a common understanding of terms of art that might otherwise be misinterpreted by the various sponsors as well as the other stakeholders in the decadal surveys—the U.S. Office of Management and Budget, the Office of Science and Technology Policy, Congress, and, not least, the Earth and space science community at large. The most important terms of art are the words used to describe notional missions and the meaning of the uncertainty in their cost and technical estimates. To the maximum extent feasible, the SOTs of the decadal surveys should promote commensurate treatments of uncertainty, but disciplines have different kinds of risk. Future SOTs should call for planning formats ("decision rules") that help sponsoring agencies cope with unexpected changes in direction. With all this to think about, the next time around, the SSB, through its standing committees, will need to enlist broad community input before the SOTs are set in stone.

The SSB now makes cost assessment and technical evaluation (CATE) part of every decadal survey and many of its other studies. This means SSB committees delve into the nuts and bolts of choosing one notional mission over another, somewhat like program managers. The question is how study committees should go about it. Some people, both sponsors and scientists, favor "science-only" prioritization, i.e., no notional missions. This group argues that SSB should not talk about missions that may never fly and so risk compromising the priority of the underlying science.

Another group argues that although objective nonadvocate cost estimates enhance credibility, any cost estimate for a mission on the drawing board is nonetheless speculative. Nearly all argue that great care is needed to convey the appropriate sense of uncertainty. Still others worry that even highly approximate cost estimation takes too much time away from science in the study process and "boxing" notional missions into categories (small, medium, or large) would be sufficient.

At the end of the day, however, the scoping of representative missions—however immature—having been tried, now seems essential to making financially responsible recommendations, and the SSB has decided to continue the practice. The problem was not more realistic cost estimations but less realistic expectations. This places a further burden on SOTs—to agree in advance on a range of budget scenarios.

Seizing Golden Moments

The work of the SSB does not end with the completion of the decadal surveys. Large projects tend to come together in golden moments when science, technology, finance, and politics align. No one has learned how to time a golden moment to arrive at the completion of a decadal survey. Someone has to be there to seize the opportunity when it emerges, even if it comes in a different form than visualized.

Then there is the opposite problem: What happens when NASA's plans or SSB's decadal recommendations go awry? Who then looks after the intentions embodied in the decadal surveys? Dealing with such ongoing issues is the job of the SSB's standing committees. The NRC worked closely with NASA to give SSB's standing committees more flexibility to respond to change while preserving the integrity of NRC review processes. Now that the decadal surveys have been completed, the reinstated standing committees are up and running, designing SOTs for new studies, providing feedback on strategies to accomplish some of the surveys' original goals, and evaluating the programmatic significance of the latest developments in science and technology.

Despite these lessons learned, some key questions still have no clear answer. Should high-profile missions such as the JWST and the Mars Science Laboratory (the Curiosity rover) require special treatment by the decadal surveys and NASA? Should they become an agency-wide responsibility, as happened with JWST when it encountered major cost growth? Should other programs be protected by enhanced risk-management practices for missions that are too big or too important to fail? How do you decide which ones are in this category? Could SSB, with its present structure, find ways to resolve priority disputes among the disciplines if it has to agree on one for special treatment?

Should the priority of a mission depend upon the availability of willing partners? Clearly, the larger the mission, the more likely is the need for international collaboration to offload costs. Just as clearly, NASA's budget prospects are not rosy. Furthermore, foreign space programs are developing impressively in scope and sophistication. How can decadal survey teams learn about the opportunities in enough depth to recommend collaborative missions with the same rigor they apply to homegrown initiatives? All in all, future success may depend on both NASA and SSB doing a better job of coordinating planning with international partners. Despite past successes, there remain important challenges in aligning the prioritization processes of partners like the European Space Agency or the Japan Aerospace Exploration Agency. And there are new space powers on the horizon.

In March 2014, all four SSB standing committees, and a fifth committee devoted to life and physical sciences in space, will convene to review the past year's accomplishments and identify emerging scientific opportunities. The SSB will invite representatives of foreign space agencies to brief the standing committees so that, when the time comes to begin the next round of decadal surveys, the U.S. Earth and space science communities will be better informed about prospects for international collaboration.

One of the glories of the American space program has been NASA's pursuit of first-class space science. There have been good times and there have been bad, but despite all that has happened, NASA's science programs have always been based on answering fundamental questions. If the questions are not answered in one decade, the scientific community will pose them again in the next decade, and again if necessary, until it does have an answer. A trusting dialog between government sponsors and the science community is fundamental to the excellence of American space science. It is important to get this dialog right, lest today's severe programmatic turbulence becomes a precursor to tomorrow's decline.

References and Notes

1. National Research Council, *NASA's Strategic Direction and the Need for a National Consensus* (National Academies Press, Washington, DC, 2012); www.nap.edu/catalog.php?record_id=18248.
2. The SSB has four standing committees that act as stewards for their disciplines and associated decadal surveys (see http://sites.nationalacademies.org/SSB/ssb_052296).
3. The Astronomy and Astrophysics Decadal Survey was jointly sponsored by the SSB and the NRC Board on Physics and Astronomy (BPA).
4. JWST was the highest priority of the previous astronomy and astrophysics decadal survey.
5. The SSB's later survey in heliospheric physics did take reduced budget expectations more into account.

10.1126/science.1244231

Published by AAAS

ECOLOGY

A Pardon for the Dingo

The extinction of the thylacine and devil on mainland Australia is best explained not by the arrival of the dingo but by human population growth and climate change.

Richard G. Roberts

The dingo (*Canis lupus dingo*) has grown accustomed to bad press. Dingoes first set paw in Australia a few millennia ago, possibly in association with the spread of Austronesians into the Pacific. They have since been blamed for snatching babies, killing sheep, and forcing the marsupial thylacine (*Thylacinus cynocephalus*) and the related devil (*Sarcophilus harrisii*) into extinction on the Australian mainland. The present-day ecological role of dingoes is still debated (see Ripple *et al*. on page 151 of this issue) (*1*), but in a recent article, Prowse *et al*. (*2*) propose that Australia's favorite scapegoat can be largely absolved of blame for driving the mainland thylacine and devil to extinction.

Dingoes never reached the island of Tasmania. The survival there of the thylacine until 1936—dubbed the Tasmanian "tiger" because of its striped back—and the devil to modern times is generally attributed to the absence of competition and predation from dingoes. However, Prowse *et al*. (*2*) use ecological models to show that the dingo did not play a key role in the extinction of these species on the mainland. Instead, they point the finger at humans, perhaps assisted by increasing aridity. The pivotal role played by humans in this recent extinction event, superimposed on a background of climate change, echoes the earlier extinction of the Australian megafauna and highlights the repeated impacts of hunter-gatherers on Australian ecosystems over the last 50,000 years (*3*).

The Australian megafauna included marsupials, reptiles, and birds weighing more than 44 kg. Most had vanished by ~40,000 years ago (*4*–*6*), but differing views persist about the exact timing and mechanism of extinction. Some form of human impact is widely favored (*3*–*5*), possibly with climate deterioration as an added stressor (*6*). The disappearance of the megafauna left the thylacine and devil as the two largest terrestrial carnivores.

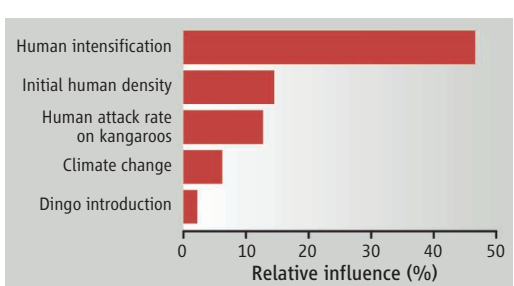
Thylacines were familiar to Aboriginal Australians and are depicted at numerous rock art sites in north and northwest Australia (see the first figure). A radiocarbon date of ~3500 years before present (yr B.P.) has been reported for a desiccated thylacine carcass found in a cave in southern Australia (*3*), but reliably dated sites with fossil remains of the thylacine and devil are scarce, frustrating attempts to establish exactly when and why they went extinct on the mainland.



Australian "tiger." Ancient rock paintings, drawings, and engravings of presumed thylacines have been recorded in north, northwest, and southeast Australia. This 50-cm-wide composition of a possible thylacine being speared or fended off by a person adorns a rock shelter in the far north of Western Australia (*12*).

Enter the dingo. Genetic estimates place its introduction at or before 4600 years ago (*7*), but no dingo fossils of such antiquity have been discovered. An almost complete dingo skeleton dated to ~3400 yr B.P. is one of the few remains older than 3000 years, with the sparse record hinting at dingo arrival shortly after 4000 yr B.P. (*3*).

Given the poorly resolved chronologies for entry of dingoes and exit of thylacines and devils on mainland Australia, Prowse *et al*. (*2*) took a modeling approach to evaluate the processes responsible for the extinction of these two marsupials. They first constructed a stochastic model to simulate the complex interactions among the hunters (humans, thylacines, devils, and dingoes) and the hunted (the herbivorous prey, represented in the model by kangaroos) in a grassland habitat. The goal was to determine which combination of factors was most effective at predicting the extinction of the two native carnivores. A simulation was judged to be successful if it predicted their dual extinction after the arrival of dingoes and before European landfall around 200 years ago.



Extinction drivers. Relative importance of the main model parameters for predicting thylacine and devil extinctions on mainland Australia, estimated from the best-performing boosted regression tree (*2*).

The model allows for competition between predators, the exponential growth in human populations on the mainland from ~5000 yr B.P. (*8*, *9*), and the effect on vegetation and prey populations of a climatic shift toward a drier regime at about the same time (*10*). A wide range of ethnographically, archaeologically, and ecologically plausible values are included in the model, such as predator and prey densities, population growth rates, predation rates, and factors to allow for competition for resources both within and between species. The authors modeled eight scenarios, representing the different permutations of dingo introduction (assumed to have

CREDIT: FIRST FIGURE, MIKE DONALDSON; SECOND FIGURE, ADAPTED FROM (*2*)

Centre for Archaeological Science, School of Earth and Environmental Sciences, University of Wollongong, Wollongong, NSW 2522, Australia. E-mail: rgrob@uow.edu.au

Published by AAAS

occurred 4000 years ago), human intensification (modeled as population growth), and climate change. Ecological extinction was declared when populations dwindled to fewer than 500 individuals.

Such simulation studies will conceal regional and local responses to various parameters, as well as subtle interplay at fine spatial and temporal scales. But the main findings were clear-cut. Human intensification featured in 80% of the successful simulations, compared to the inclusion of climate change (44%) and dingo invasion (16%). Prowse *et al*. then analyzed a subset of these simulations using boosted regression trees (*11*) to assess the importance of different model parameters on the probability of successfully predicting the extinction of mainland thylacines and devils. This analysis confirmed humans as the main driver of the mainland extinctions. Human intensification was the most influential factor, followed by the initial human density and the rate of human predation on kangaroos (see the second figure). Climate change became important when the latter two parameters were at their lowest values, but dingoes had a negligible effect. Predictive success was affected more by human attack rates on kangaroos than on thylacines and devils; thus, human hunting of these native carnivores had less influence than did human predation on their common prey.

Vindication of the dingo for the extirpation of the thylacine and devil on mainland Australia puts people—and perhaps climate change—squarely in the frame. Humans are also implicated in the demise of the Australian megafauna (*3*–*6*). However, searching for prehistoric synergies among extinction drivers is made more difficult by the declines in quantity and quality of evidence further back in time, hampering efforts to resolve the causes of megafaunal extinction from dated fossils, artefacts, and proxy records of climatic and ecological change. Prowse *et al*.'s scenario-testing approach (*2*) offers a new lens through which to study the range of dynamic interactions and impacts responsible for this earlier mass extinction.

References

1. W. J. Ripple *et al*., *Science* **343**, 1241484 (2014).
2. T. A. A. Prowse, C. N. Johnson, C. J. A. Bradshaw, B. W. Brook, *Ecology* 10.1890/13-0746.1 (2013).
3. C. Johnson, *Australia's Mammal Extinctions* (Cambridge Univ. Press, Cambridge 2006).
4. R. G. Roberts, B. W. Brook, *Science* **327**, 420 (2010).
5. S. Rule *et al*., *Science* **335**, 1483 (2012).
6. G. J. Prideaux *et al*., *Proc. Natl. Acad. Sci. U.S.A.* **107**, 22157 (2010).
7. M. C. R. Oskarsson *et al*., *Proc. Biol. Sci.* **279**, 967 (2012).
8. C. N. Johnson, B. W. Brook, *Proc. Biol. Sci.* **278**, 3748 (2011).
9. A. N. Williams, *Proc. Biol. Sci.* **280**, 20130486 (2013).
10. J. M. Reeves *et al*., *Quat. Sci. Rev.* **74**, 21 (2013).
11. J. Elith, J. R. Leathwick, T. Hastie, *J. Anim. Ecol.* **77**, 802 (2008).
12. M. Donaldson, *Kimberley Rock Art,* vol. 2, *North Kimberley* (Wildrocks Publications, Mount Lawley, Australia, 2012).

10.1126/science.1248646

ECOLOGY

Bacterial Vesicles in the Ocean

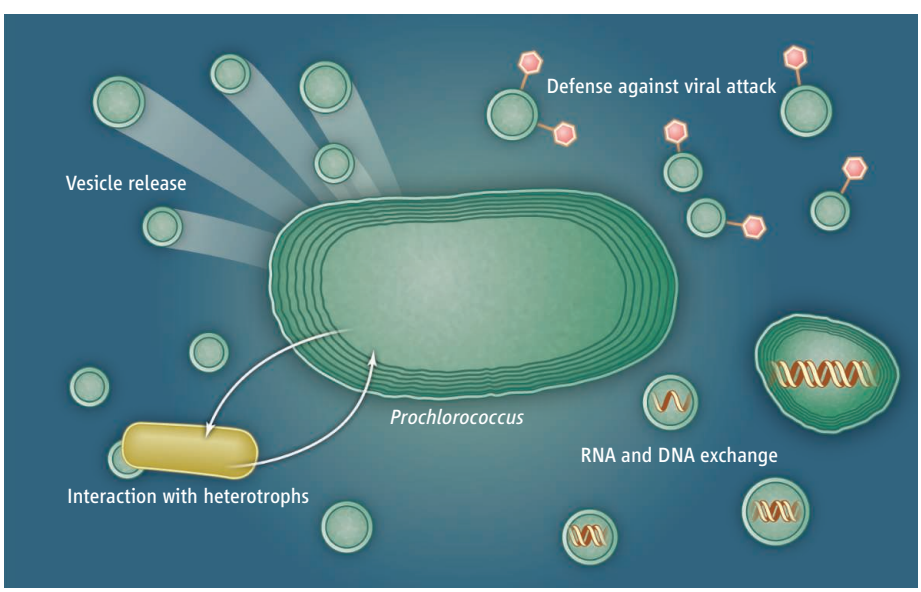
Vesicles released by phytoplankton may play key roles in carbon cycling, viral defense, and gene transfer.

David Scanlan

Marine microbes play a key role in global nutrient cycling (*1*). Phytoplankton account for less than 1% of the photosynthetic biomass on Earth, yet contribute almost half of the world's primary production (*2*). In open oceans between ~45°N and ~40°S, cyanobacteria of the genus *Prochlorococcus* dominate the phytoplankton (*3*). *Prochlorococcus* is the smallest free-living phototroph; its genome is subject to miniaturization (*4*), and distinct ecotypes are adapted to the strong gradients of light and nutrients in the surface ocean (*5*). On page 183 of this issue, Biller *et al*. (*6*) identify a further striking feature of *Prochlorococcus*: the production of extracellular vesicles that may play a role in carbon cycling, gene transfer, and viral defense.

Biological production of extracellular vesicles is widespread, with vesicles produced by species across all three branches of the tree of life (*7*). In Gram-negative bacteria, vesicles are produced when small regions of the outer membrane bulge away from the cell before pinching off and being released (*8*). Biller *et al*. carefully purified 70 to 100 nm-sized membrane-bound extracellular vesicles from exponentially growing *Prochlorococcus* cells. The vesicles contain not only periplasmic and outer-membrane proteins but also proteins characteristic of inner membrane and cytoplasmic compartments, although their relative abundance is unknown. They also contain DNA and RNA.

The authors show that vesicles are produced not only by *Prochlorococcus*, but also



Multipurpose vesicles. Biller *et al*. show that *Prochlorococcus* produce vesicles that may play functional roles in defending against viral attack, interactions between heterotrophs and *Prochlorococcus*, and horizontal gene transfer. This is a schematic presentation and is not to scale.

CREDIT: P. HUEY/SCIENCE

School of Life Sciences, University of Warwick, Coventry, CV8 1FN, UK. E-mail: d.j.scanlan@warwick.ac.uk

Published by AAAS

by a marine *Synechococcus* strain, the sister group to *Prochlorococcus*, potentially extending vesicle production to organisms that are ubiquitous in oceans across the world. Indeed, Biller *et al*. were able to purify structures containing protein and various lipids indicative of vesicles from natural seawater collected at coastal and oligotrophic sites off the American east coast. Thus, vesicles are produced in the open ocean and not only by pathogens and biofilm-inhabiting microbes living at high cell density.

In the cultures and natural samples analyzed by Biller *et al*., the vesicles are as abundant as the organisms themselves (and in some cases up to 10 times more so). They are also relatively stable, with numbers remaining constant for more than 2 weeks. This has important consequences for the nature and origin of dissolved organic carbon (DOC) in the ocean. DOC in turn supports microbial growth and hence plays a key role in the global carbon cycle through the microbial loop.

Why would an organism like *Prochlorococcus*, which is clearly well adapted to the nutrient-poor open ocean, shed vesicles containing large amounts of carbon, nitrogen, and phosphorus that have been hard work to win? The authors speculate on several different avenues (see the figure), all of which are ripe for future research. First, the labile carbon released in such vesicles may stimulate heterotrophic growth. Some marine heterotrophs are known to positively stimulate the growth of *Prochlorococcus*. Indeed, all currently sequenced *Prochlorococcus* strains lack the enzymes for catalase or catalase-peroxidase, making the organism highly susceptible to oxidative damage. Heterotrophic "helper" bacteria can compensate for this loss (*9*), an idea that has been called the Black Queen hypothesis, where gene loss in free-living organisms like *Prochlorococcus* may leave them dependent on co-occurring microbes for lost metabolic functions (*10*).

Second, the extracellular vesicles may transfer DNA fragments between organisms, thereby facilitating horizontal gene transfer. This idea is not new (*9*), but the fact that vesicles from both cultured bacteria and natural marine communities contain DNA hints at a potentially widespread mechanism for moving DNA (and RNA) between cells.

Perhaps the most evocative of the functions put forward by Biller *et al*. is the idea that the vesicles might prevent phage attack by acting as decoys. Viruses, including marine cyanophages, which specifically infect cyanobacteria, are very abundant in marine systems (*11*, *12*). The extracellular vesicles reported by Biller *et al*. are enriched in outer membrane components, suggesting that they harbor phage receptors that can act to directly bind viral particles. Indeed, the authors show that purified vesicles bind phage particles; many of these vesicle-attached phage particles possess an altered morphology suggestive of DNA injection into the vesicles. However, it remains to be shown whether, and if so how, these vesicles affect phage-host infection dynamics at concentrations found in the ocean.

Extracellular vesicle release by the most abundant marine phototroph, and likely many other marine microbes, provides a crucial bridge between microbes and the biotic and abiotic world. The environmental variables that affect production and stability of the vesicles will be important to decipher. High local concentrations of compounds within vesicles, possibly including toxins that deter grazers as well as viral predators, suggest that much remains to be learned about the function of such biologically derived colloids. Given that some eukaryotes are also known to produce extracellular vesicles, it will be interesting to find out whether eukaryotic phytoplankton produce similar structures. If such vesicles are produced by bloom-forming species, this could have further profound implications for carbon release and carbon cycling in marine systems.

References

1. P. G. Falkowski, T. Fenchel, E. F. Delong, *Science* **320**, 1034 (2008).
2. P. Falkowski, *Nature* **483**, S17 (2012).
3. P. Flombaum *et al*., *Proc. Natl. Acad. Sci. U.S.A.* **110**, 9824 (2013).
4. F. Partensky, L. Garczarek, *Annu. Rev. Mar. Sci.* **2**, 305 (2010).
5. Z. I. Johnson *et al*., *Science* **311**, 1737 (2006).
6. S. J. Biller *et al*., *Science* **343**, 183 (2014).
7. B. L. Deatherage, B. T. Cookson, *Infect. Immun.* **80**, 1948 (2012).
8. A. Kulp, M. J. Kuehn, *Annu. Rev. Microbiol.* **64**, 163 (2010).
9. J. J. Morris, Z. I. Johnson, M. J. Szul, M. Keller, E. R. Zinser, *PLOS ONE* **6**, e16805 (2011).
10. J. J. Morris, R. E. Lenski, E. R. Zinser, *mBio.* **3**, e00036-12 (2012).
11. O. Bergh, K. Y. Børsheim, G. Bratbak, M. Heldal, *Nature* **340**, 467 (1989).
12. M. B. Sullivan, J. B. Waterbury, S. W. Chisholm, *Nature* **424**, 1047 (2003).

10.1126/science.1248566

PHYSICS

Enabling Optical Analog Computing with Metamaterials

The manipulation of light with structured materials could allow mathematical operations to be performed with compact optics.

Ari Sihvola

Progress in the development of calculating machines has led to modern computers that represent and treat data digitally. In principle, the physical platform on which computation is done is irrelevant: A digital computer can be realized with vacuum tubes, discrete transistors, integrated circuits, pneumatic valves, or optical logic gates. However, digital optical computing is not the only way in which computing can be done with light. On page 160 of this issue, Silva *et al*. (*1*) show theoretically that the direct manipulation of light waves can offer extraordinary possibilities toward analog computing. Instead of representing quantities by discrete bits, the input and output data are expressed as continuous electric fields of light. The necessary mathematical operations are realized through the interaction of the wave with metamaterials, microstructured composites that respond in ways that cannot be realized in isotropic materials (*2*). Furthermore, the wavelength-scale dimensions of such computing machines make them extremely compact.

Digital computing is exact in the sense that algebraic operations are deterministic; an abacus is a simple example of a computer that keeps track of discrete numbers. On the other hand, the operation of a slide rule comes with finite precision and accuracy because this analog computing process is inherently connected with the mechanical movement of matter. Hence, advances in material technology were essential to progress in the

Department of Radio Science and Engineering, Aalto University School of Electrical Engineering, Otakaari 5A, 02150 Espoo, Finland. E-mail: ari.sihvola@aalto.fi

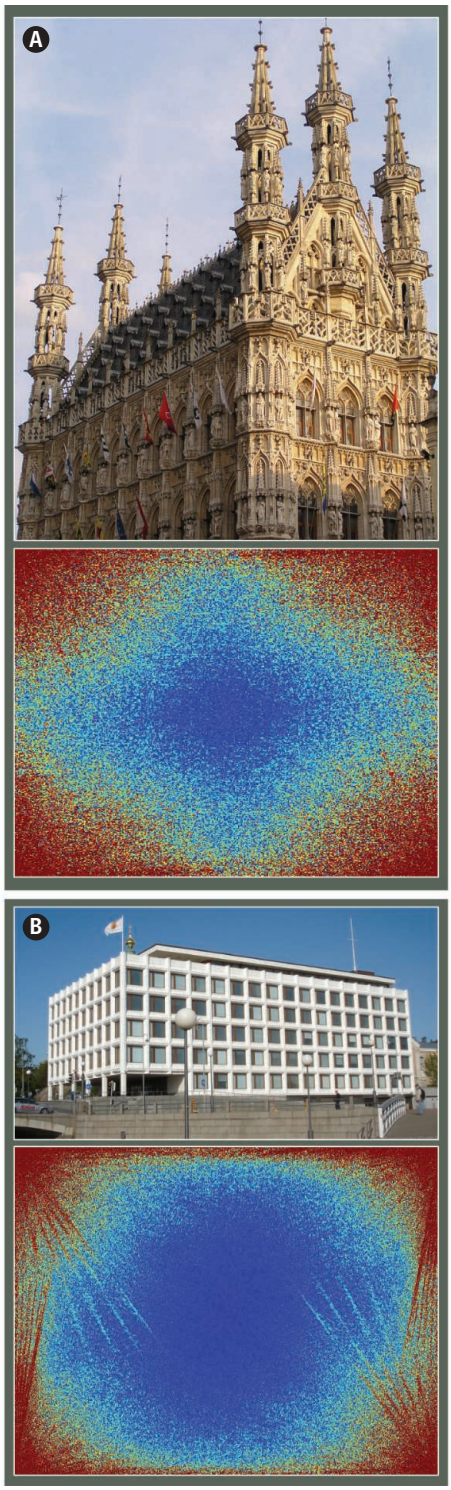
Published by AAAS

accuracy of analog computers, as evidenced by the progression from planispheres and astrolabes for early astronomy to clocks in the great cathedrals of the Middle Ages (*3*) and electromechanical fire-control machines during the Second World War (*4*).

In the optical analog computing scheme of Silva *et al*., both the drawbacks of inertia in mechanical analog computers and transformation delays in digital electronic computers are absent. The complex shape of an electromagnetic wave carries the information of computational operations. The propagation characteristics of this wave are determined by the carefully tailored dielectric and refractive profile of the metamaterial structures. Two important principles are exploited in the design: Fourier transform of signals and the electromagnetic properties of metamaterials.

The Fourier transform is a powerful mathematical operation that represents the variation of a function in one variable in the spectral space of its conjugate variable. For time-dependent signals, the spectral view means that time variation is displayed as a combination of frequencies. The pitch of a sound from a musical instrument corresponds to a frequency (and its harmonics, which give the characteristic color for the sound) that is located from the tens of hertz (10 cycles per second) to kilohertz range. We also feel lower frequencies in our everyday life: The 1-Hz beating of hearts, the daily rhythm of sunrise and sunset, and the yearly variation of seasons (at least in high latitudes of the globe), which have a frequency of a few tens of nanohertz. The spectral view can also be applied in spatial dimensions. Looking at an image, we can focus on its localized details and their variations, but sometimes a picture sends a strong message through its "spatial rhythm"—for example, when features are periodically repeated (see the figure). The Fourier transform is richer in the spatial domain than the temporal one, as it operates on three spatial dimensions.

Operations between functions have strong connections to operations between their Fourier transforms. These mathematical correspondences are exploited in the analog computer proposed by Silva *et al*. by manipulating the spatial waveform of the incident field. In their first design, the structure consists of three blocks—a Fourier transform, a metamaterials-based unit, and the inverse Fourier transform. Propagation through a so-called graded-index (GRIN) dielectric slab produces a Fourier transform of the input function (*5*). The Fourier transform is imaged along a transverse coordinate, which makes it practical to apply multiplication-type operations on the different parts of the spectrum. The manipulation and rephasing of the spectrum in the middle block requires either a thin metasurface or an extended composite metamaterial structure. Finally, the inverse Fourier transform is achieved by either a "complementary" GRIN structure (*6*) or another "ordinary" GRIN, which produces a mirror image of the required output function.



Richer versus sparer Fourier transforms. Two sets of images illustrate how Fourier transformations, which can identify repetitions in time series or spatial images, can vary in richness. (**A**) The ornate Leuven City Hall in Belgium would create a rich spectrum, as it has structural details at many length scales. (**B**) A more functional architecture—like Alvar Aalto's Enso House in Helsinki, Finland, which has a strong "rhythm" at the 5-m scale—results in a sparser spectrum with more flatter regions but with stronger features. Silva *et al*. propose a way to use metamaterial structures to perform Fourier transforms on light waves for use in analog computing.

Metamaterials turn out to be extremely effective for controlling the phase and amplitude of the wavefront in the middle block. An example of a metamaterial is a doublet of materials, with permittivities that have opposite signs, that behaves in an extremely anisotropic manner (*7*, *8*). In infrared frequencies, silicon and aluminum-doped zinc oxide make such a pair. By exploiting this very sensitive response and by varying the relative thicknesses of the two materials in the nanodoublet, Silva *et al*. introduce realistic designs for the metamaterial block to achieve the required mathematical operations, such as taking derivatives and convoluting functions.

The route through the Fourier transform is mathematically efficient, but a GRIN lens can be quite thick. One possibility of "flat" optics is holographic coherent imaging (*9*, *10*). In their desire to compact the computing machine, Silva *et al*. suggest an alternative device that avoids the transverse Fourier transform and leads to an extremely compact structure. However, the design requires a longitudinal distribution of the refractive index of the metamaterial with strict tolerances in the submicrometer scale. Just as access to pure brass during the late Middle Ages led to more accurate mechanical clocks, the smooth operation of the gears and wheels of these analog computers will likely rely on advances in fabrication enabled by nanotechnology.

References

1. A. Silva *et al*., *Science* **343**, 160 (2014).
2. A. Sihvola, *Metamaterials* **1**, 2 (2007).
3. D. de Solla Price, *IEEE Micro* **4**, 22 (1984).
4. *Basic Fire Control Mechanisms* (Navy Department, Bureau of Ordnance, Washington, DC, September 1944); http://hnsa.org/doc/op1140/.
5. J. B. Pendry, S. A. Ramakrishna, *J. Phys. Condens. Matter* **15**, 6345 (2003).
6. J. W. Goodman, *Introduction to Fourier Optics* (Roberts & Co., Englewood, CO, ed. 3, 2005).
7. H. Kettunen *et al*., *J. Appl. Phys.* **103**, 094112 (2008).
8. A. Alù, N. Engheta, *New J. Phys.* **11**, 013026 (2009).
9. D. Gabor, *Nature* **161**, 777 (1948).
10. G. Lipworth *et al*., *J. Opt. Soc. Am. A* **30**, 1603 (2013).

10.1126/science.1248659

CREDITS: (LEUVEN CITY HALL) WIKIMEDIA COMMONS; (ALL OTHERS) ARI SIHVOLA

Published by AAAS

NEUROSCIENCE

Young Neurons Sever Ties to the Parental Niche

Neuronal precursor cells of the vertebrate central nervous system shed an apical end-foot to differentiate.

Samuel Tozer and Xavier Morin

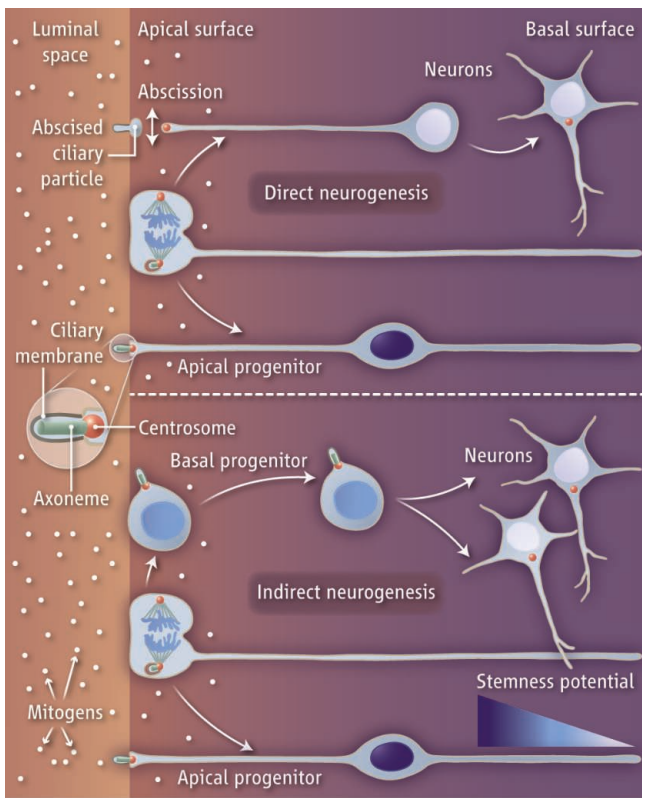
Neurogenesis in the vertebrate embryo involves the production of neurons through asymmetric divisions of neuroepithelial progenitors, also known as apical progenitors. The coordination of intrinsic transcriptional events, reception of external stimuli, and cellular remodeling that accompany neuronal birth is still far from being understood. On page 200 of this issue, Das and Storey (*1*) provide insight into this process and describe an unexpected cell remodeling process called apical abscission.

Apical progenitors reside in the neural tube, the embryonic precursor of the vertebrate central nervous system. They display apical and basal attachments through which they adhere to their neighbors and to the basal lamina, respectively. Mitosis takes place while the nucleus occupies an apical position. After neurogenic divisions, prospective neurons lose their basal attachment but initially retain an apical domain. Differentiation and exit from the cell division cycle correlate with the extension of a new basal process, basal translocation of the nucleus, followed by apical detachment (*2*).

Negative regulation of the cell surface adhesion protein N-cadherin in prospective neurons leads to detachment at the apical surface and differentiation. This occurs in response to activation of the FoxP2/4 transcription factors by the neurogenic factor Neurog2 (*3*). Das and Storey imaged chick neural tube slices in real time and observed that apical detachment involves shedding of a particle composed of the apical and ciliary membrane domains (each cell bears a primary cilium that serves as a sensory "antenna"). The authors demonstrate that apical abscission involves an actin-myosin controlled subapical constriction that leads to severing of the apical particle. This program is initiated by Neurog2 and involves decreasing N-cadherin expression levels. The centrosome, a microtubule organizer that lies at the base of the cilium and nucleates its cytoskeletal inner core (the axoneme), is not included in the apical particle. Instead, it remains in the withdrawing cell and leaves the apical surface (see the figure). By contrast, the ciliary membrane is retained in the abscised particle. This implies that the centrosome is undocked from the base of the ciliary membrane, and suggests that the axoneme is dismantled in the process.

Apical shedding may abruptly blind the cell to mitogenic signals coming from the intraluminal space of the neural tube, such as sonic hedgehog (Shh), to allow exit from the cell cycle. Indeed, Das and Storey noted accumulation of protein constituents of the Shh signaling pathway (Smoothened and Gli2) in the cilium, which indicates that Shh is active until immediately before abscission. In addition, the data support the idea that abscising cells are poised to differentiate but will do so only if abscission can be completed. Thus, abscission could be viewed as a checkpoint that synchronizes basal translocation of the nucleus, exit from the cell cycle, and acquisition of neuronal identity.

The study of Das and Storey provides insights into the timing of neurogenesis, but more generally opens the question of how an epithelial tissue can maintain its integrity while a part of its population undergoes an epithelial-mesenchymal transition. During this process, cells exit from epithelial structures through the basal lamina. The loss of apical-basal polarity and apical adhesion is a key event in both normal developmental situations and cancer (*4*). Classical examples of this transition include situations in which an entire cell population loses its epithelial organization, and cases when individual cells leave an epithelial structure. Although newborn neurons remain within the confine of the basal lamina, their withdrawal from the apical surface can be viewed as a form of the latter scenario, and apical particle shedding provides a remarkable example of how an epithelial-mesenchymal transition may occur without disrupting the surrounding epithelium. In this respect, the fate of the apical particle after abscission has yet to be described. Future studies should explore whether apical shedding occurs in cuboidal epithelia whose larger apical surface may represent a challenge to abscission. Moreover, shedding may provide the cell with an efficient way to transiently lose apical-basal polarity without changing its transcriptional regulation. This may be of particular interest in newborn neurons that reuse many polarity determinants



Remodeling. (**Top**) In the early spinal cord, newborn neurons abscise an apical particle to detach from the apical surface, allowing cell differentiation. (**Bottom**) In the mouse cortex, a ciliary remnant is recycled to the daughter that retains the apical progenitor identity. Its sister produces a new basolateral cilium and becomes a basal progenitor with restricted proliferation.

CREDIT: H. MACDONALD/*SCIENCE*

Ecole Normale Supérieure, Institut de Biologie de l'ENS (IBENS), Paris F-75005, France; Inserm, U1024, Paris F-75005, France; CNRS, UMR 8197, Paris F-75005, France. E-mail: xavier.morin@ens.fr

Published by AAAS

during axonal growth and/or migration (*5*). As neurons of different types and origins adopt different strategies to polarize (*6*), it will be interesting to explore whether apical shedding is a marginal or widespread mechanism in neurogenesis.

During mitosis of apical progenitors in the mouse cortex, a ciliary remnant associates with the centrosome at one pole of the mitotic spindle, resulting in asymmetric inheritance of a ciliary structure (*7*). Thus, the cilium is partly conserved rather than dismantled during cell division. The cell inheriting the ciliary remnant rapidly reconstitutes an apical cilium and is more likely to retain apical progenitor identity. Its sister produces a basolateral cilium, a phenomenon associated with basal progenitor identity. Basal progenitors' restricted capacity to proliferate may result from the reduced exposure of the basolateral cilium to luminal mitogens (*8*). Future research should address whether apical shedding is also present in the developing cortex, where indirect neurogenesis, through basal progenitors, is predominant, and how shedding integrates with asymmetric ciliary recycling and basolateral cilia formation.

The cortex and neural tube appear to have a remarkable plasticity of ciliary structures during neurogenesis. Although mechanistically different, asymmetric recycling of ciliary remnants (*7*), differential positioning of cilia (*8*), and dismantling of the cilium and shedding of the ciliary membrane are many ways for a cell to modulate the timing and dosage of its exposure to environmental signals. These new layers of control in signal reception are independent of the source concentration and may therefore contribute to the diversity of cell fate decisions, allowing progression of neural differentiation and maintenance of a pool of apical progenitors to occur simultaneously in a niche.

References

1. R. M. Das, K. G. Storey, *Science* **343**, 200 (2014).
2. R. M. Das, K. G. Storey, *EMBO Rep.* **13**, 448 (2012).
3. D. L. Rousso *et al*., *Neuron* **74**, 314 (2012).
4. J. P. Thiery, H. Acloque, R. Y. Huang, M. A. Nieto, *Cell* **139**, 871 (2009).
5. P. L. Cheng, M. M. Poo, *Annu. Rev. Neurosci.* **35**, 181 (2012).
6. Y. Hatanaka, K. Yamauchi, F. Murakami, *Dev. Growth Differ.* **54**, 398 (2012).
7. J. T. Paridaen, M. Wilsch-Bräuninger, W. B. Huttner, *Cell* **155**, 333 (2013).
8. M. Wilsch-Bräuninger, J. Peters, J. T. Paridaen, W. B. Huttner, *Development* **139**, 95 (2012).

10.1126/science.1249497

CANCER

Can Cancer Trigger Autoimmunity?

A chronic autoimmune disease sometimes appears coincidently in patients with cancer.

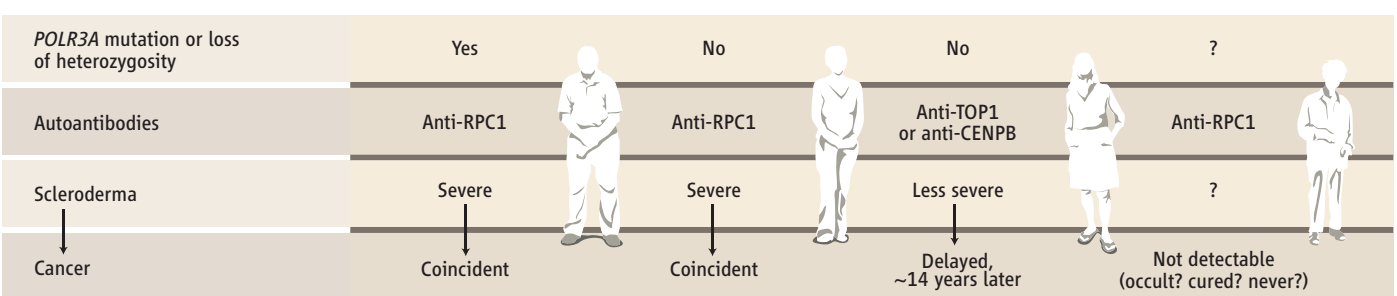
Michele W. L. Teng[1,2] and Mark J. Smyth[1,2]

Autoimmune diseases occur when immune B and T cells fail to distinguish the body's own proteins as self and attack them, ultimately damaging tissues and organs. There are many possible causes of autoimmune diseases, such as chemical exposures, infections, and genetic factors. On page 152 of this issue, Joseph *et al*. (*1*) raise another possibility—nascent growing cancers might express new proteins (neoantigens) whose exposure to the immune system creates the potential for an autoimmune disease to develop.

Systemic sclerosis (scleroderma) is a rare chronic autoimmune rheumatic disease associated with fibrosis of the skin and widespread destruction of blood vessels that affects organs, with life-threatening consequences. Some rheumatic diseases are also paraneoplastic—they are present with cancers—and removal of the tumor or its medical treatment causes regression of the clinical manifestations. Coincidental timing of scleroderma and cancer had been observed in patients with autoantibodies specific for RNA polymerase III subunit (RPC1) (*2*). Joseph *et al*. examined tumor tissue and blood samples from 16 scleroderma patients with various types of cancer. Among the eight patients who had anti-RPC1 autoantibodies and coincident cancer, six had genetic mutations—either somatic mutations or loss of heterozygosity (only one copy of an allele) in *POLR3A* (*polymerase III polypeptide A*, the gene encoding RPC1) (see the figure, below). The other eight patients had autoantibodies to either topoisomerase 1 (anti-TOP1) or centromere protein B (anti-CENPB) and developed delayed cancer.

Interestingly, all the anti-RPC1 antibodies recognized wild-type and mutated RPC1, indicating that the humoral immune response does not directly target the area of the mutation or discriminate between mutant and wild-type versions of RPC1. But some patients with scleroderma who possessed defined *POLR3A* mutations had T cells that reacted to RPC1 protein fragments produced from the mutated gene. The reactivity was specific to the patient and peptide, but the frequencies of these T cells were comparable to those observed in other autoimmune diseases. Given that *POLR3A* mutations are exceedingly rare in cancer (0.7% overall), it is unlikely that the onset

[1]Cancer Immunoregulation and Immunotherapy and Immunology in Cancer and Infection Laboratories, QIMR Berghofer Medical Research Institute, 300 Herston Road, Herston, 4006 Queensland, Australia. [2]School of Medicine, University of Queensland, Herston, 4006 Queensland, Australia. E-mail: mark.smyth@qimrberghofer.edu.au



Coincidence. Four subsets of scleroderma patients are shown (as observed by Joseph *et al*. (*1*)) with different autoantibody profiles, mutations, and coincident cancer.

CREDIT: V. ALTOUNIAN/*SCIENCE*

Published by AAAS

of scleroderma and the cancer genomes of these patients were unrelated, and that the mutations, and T cell responses directed against them, were coincidental. Rather, *POLR3A* mutation in the occasional cancer triggers the scleroderma.

According to cancer immunoediting (*3*), the host can control tumor growth through innate and adaptive immune mechanisms. Genetic instability in the tumor may create neoantigens that are recognized by the immune system, leading to the selection of tumor cells that can escape immune pressure. Neoantigens have been demonstrated in tumors by means of epitope prediction algorithms (*4*). These principles have been demonstrated in mouse models of carcinogenesis and multistage cancer progression (*3*, *4*), but also recently, the importance of a patient's immune reaction with cancer in dictating disease-free survival (immune contexture) has been established (*5*).

The relatively low fraction of neoplastic cells with genetic alterations in the cancers from some of the scleroderma patients studied by Joseph *et al*. suggests that cancer immunoediting had occurred. Cancer cells targeted by T cells appear to selectively lose the mutant allele, and loss of heterozygosity occurred in most of the tumors that were present synchronously with the scleroderma. In some tumors, the loss of heterozygosity was not yet complete (clonal heterogeneity was observed in which a small percentage of the tumor cells still carried the mutation). Presumably, if those tumors had been sampled a few months later, there might not be any detectable mutant cells because loss of heterozygosity would have been complete. The loss of heterozygosity in the other tumors without detectable mutations is quite possibly a "historical" record of the tumors once carrying mutations. Interestingly, no mutant allele or loss of heterozygosity was detected in some patients with anti-RPC1 autoantibodies, suggesting that other mechanisms can induce their production. The etiology of scleroderma development in these patients may resemble that in patients with anti-TOP1 and anti-CENPB autoantibodies. It is also possible that patients with RPC1-specific autoantibodies and no cancer may once have had nascent cancer or harbor cancer in a state of immune-mediated dormancy. The loss of heterozygosity of *POLR3A* in some patients raises the possibility that immunoediting may involve gene copy-number alterations in the cancer. Alternatively, because RPC1 plays a role in sensing and limiting infection by intracellular bacteria and viruses (*6*), cancer may also mutate or lose *POLR3A* to evade activating innate immunity.

The association between cancer and rheumatic diseases has been intriguing for many years (*7*). Paraneoplastic syndromes may be mediated by autoantibodies due either to tumor antigens that are also expressed by cells targeted by the autoimmune disease or to the release of intracellular antigens from apoptotic tumor cells (*8*). However, these responses are directed to the normal protein, and there is yet no evidence that encoding genes were mutated in the tumors. Joseph *et al*. extend causation to include mutant *POLR3A* in human tumors that elicits an immune response against the mutant RPC1 but cross-reacts with the normal RPC1, resulting in autoimmunity. However, the cancer mutation is likely not enough and additional factors (genetic, environmental, or target tissue–specific) may be required to generate damage to normal tissue.

From an epidemiological viewpoint, the study by Joseph *et al*. is underpowered, but these findings may also prompt research into whether antigens other than RPC1 might trigger autoimmunity (e.g., in myositis and lupus). In larger studies, mining exome sequencing data can help identify a patient's specific tumor antigen profile and potential tumor immunity and autoimmunity. However, the findings by Joseph *et al*. raise interesting issues about tumors with high mutation rates (lung, melanoma) or microsatellite DNA instability (colorectal) and their predisposition to cause autoimmunity. Simple analysis of large tissue collections from cancer patients with accompanying "immunoscores" and patient disease history might reveal correlations with autoimmune syndromes.

Very little autoimmunity has been causally linked to cancer mutations and subsequent immune reactions, but these events have only been examined in cancer patients with clinically detectable disease. Do autoimmune patients in general have an undetectable burden or history of cancer? New immunotherapeutic treatments for cancer that break tolerance will help to clarify the underlying natural human immune reaction to cancer and its side effects on normal tissues.

References and Notes

1. C. G. Joseph *et al*., *Science* **343**, 152 (2014); 10.1126/science.1246886.
2. A. A. Shah, A. Rosen, L. Hummers, F. Wigley, L. Casciola-Rosen, *Arthritis Rheum.* **62**, 2787 (2010).
3. R. D. Schreiber, L. J. Old, M. J. Smyth, *Science* **331**, 1565 (2011).
4. H. Matsushita *et al*., *Nature* **482**, 400 (2012).
5. J. Galon *et al*., *Science* **313**, 1960 (2006).
6. A. Ablasser *et al*., *Nat. Immunol.* **10**, 1065 (2009).
7. J. E. Naschitz, *Curr. Opin. Rheumatol.* **13**, 62 (2001).
8. M. L. Albert, R. B. Darnell, *Nat. Rev. Cancer* **4**, 36 (2004)
.

Acknowledgments: M.W.L.T is supported by a CDF1 Fellowship and Project Grant from the National Health and Medical Research Council of Australia (NH&MRC) and Prostate Cancer Foundation of Australia. M.J.S. is supported by a NH&MRC Australia Fellowship and Program Grant, and Program Grant from the Susan G. Komen for the Cure.

10.1126/science.1249486

PLANETARY SCIENCE

Glimpsing Eruptions on Europa

John R. Spencer

Recent observations with the Hubble Space Telescope reveal what are probably eruptions of water vapor from Jupiter's moon Europa.

Second-closest to Jupiter (after Io) of the four large Galilean satellites, icy Europa is one of the strangest objects in the solar system (*1*). On page 171 of this issue, Roth *et al*. (*2*) present strong evidence for ongoing eruptions of plumes of water vapor from Europa's surface. This is a potentially major discovery, making Europa only the fourth object in the solar system known to exhibit ongoing internally powered geological activity, after Earth, Europa's volcanic neighbor moon Io, and Saturn's icy moon Enceladus.

Europa is slightly smaller than our own Moon, with a radius of 1561 km and a density of 3010 kg m^{-3}, implying an interior mostly composed of silicates plus about 10% water by mass. Gravity observations by the Galileo Jupiter orbiter revealed that Europa is strongly differentiated, with the lower-density water component concentrated near the surface (*3*). The surface is dominated by water ice, along with other hydrated species, probably salts. Europa's surface appearance is truly bizarre, crisscrossed with fractures, sometimes global in extent, that on closer inspection turn out to be double ridges (see the fig-

Southwest Research Institute, 1050 Walnut Street, Boulder, CO 80302, USA. E-mail: spencer@boulder.swri.edu

Published by AAAS

ure), and punctuated by aptly named chaos regions where the surface has disintegrated into a mass of jumbled fragments. Impact craters are rare, implying that the surface is only about 50 million years old (*4*), and thus must be replaced at an average rate of about 1 km^2 per year. Europa is too small to retain sufficient primordial or radiogenic heat to power this resurfacing. Instead, activity is almost certainly driven by frictional heating due to the tides raised by Jupiter, which vary diurnally as a result of Europa's slightly eccentric orbit. The same mechanism powers the silicate volcanoes on Io and the water vapor plumes of Enceladus, which resembles Europa in many ways (*5*).



A volatile surface. The strange surface of Europa's ice shell, which overlies a subsurface ocean, as seen from the Galileo Jupiter orbiter in 1998. The cycloid shape of many of the ridges is best explained by the propagation of fractures in the thin ice shell, controlled by the daily variation of tidal stresses from Jupiter (*7*). The recent results from the Hubble Space Telescope, as reported by Roth *et al.*, suggest that similar fractures elsewhere on Europa are actively jetting water vapor into space. The image is about 200 km across.

CREDIT: NASA

Most exciting is what lies beneath Europa's surface. Magnetic field measurements from Galileo showed the interior to be electrically conductive, implying that much of the outer water layer is liquid (*6*). The inference of a massive global ocean, over 100 km deep, beneath the icy surface is strengthened by the apparent presence of surface salts on disrupted regions on the surface. In addition, many of the fracture patterns are best explained by stresses in a thin floating ice shell, decoupled from the interior (*7*). Given the weight of evidence, the existence of an ocean beneath Europa's icy surface is now almost universally accepted. Estimates of the thickness of the overlying ice vary from a few kilometers to tens of kilometers.

This abundance of liquid water, rare in the solar system and essential to life on Earth, makes Europa of great interest to astrobiologists. Could life have developed in that subsurface ocean? One key ingredient for the existence of life is a persistent source of chemical energy, which is not guaranteed in an ocean isolated from sunlight beneath kilometers of ice. Activity in Europa's interior might supply such energy, but its surface, rich in oxidants due to bombardment by magnetospheric particles, is also a potential source of chemical energy (*8*). Whether that energy can power life in the ocean depends on the age, thickness, and nature of activity in the ice shell, which acts as an intermediary between the surface and the ocean beneath.

A mission to Europa to further investigate its potential for life has been a high priority for planetary scientists since the Galileo discoveries and was recommended by the last two Planetary Decadal Surveys (*9*, *10*). NASA's latest mission concept, "Europa Clipper," which would probe Europa with dozens of close flybys, is exciting, but the funding necessary to turn it into reality has been elusive. The only funded plans to return to Europa are two flybys in 2031, by the European Space Agency's Jupiter Icy Moons Explorer (JUICE) spacecraft.

Meanwhile, investigations have continued from Earth. All the Galilean moons have tenuous atmospheres, which are best studied in the far-ultraviolet (UV), at wavelengths between 100 and 200 nm, where auroral emissions are excited by Jupiter's magnetosphere. Because the far-UV is blocked by Earth's atmosphere, the Hubble Space Telescope is a prime tool for atmospheric investigations, and it was Hubble that first revealed Europa's molecular oxygen atmosphere in the 1990s (*11*). And now, it is Hubble that has revealed what is perhaps the most dramatic discovery about Europa since the Galileo era.

Roth *et al*. report the discovery of intermittent bright emissions from a region extending several hundred kilometers above Europa's surface, near the south pole. The wavelength distribution of the emissions implies that they originate from a temporary cloud of water vapor, probably ejected from a source on the surface. It thus appears that Europa, at least some of the time, erupts water vapor from active surface fissures, much like its smaller cousin Enceladus.

This interpretation is the most plausible explanation of the data, but it is not watertight, because the signal-to-noise ratio and spatial resolution of the observations are relatively low, and the environment around Europa is complex. Further observations will be needed to confirm and better understand the discovery. Observations so far suggest a correlation between the presence of the plume and Europa's position in its slightly eccentric orbit around Jupiter. Orbital position is likely to control, via tidal stresses, the opening and closing of the south polar fissures that are probably the source of the plume—such a correlation has recently been seen on Enceladus (*12*). Confirmation of a similar correlation on Europa would tie the UV emissions to geophysically controlled internal activity and would clinch the case for Enceladus-like plume activity on Europa.

If the inferred plumes are real, as seems probable, they only increase Europa's allure. Plumes allow direct sampling of the interior, and perhaps the ocean itself, by passing spacecraft. They pinpoint locations where the ice shell is likely to be thin, perhaps allowing access to the ocean for biologically useful chemical energy. This exciting new window into the interior should provide fresh impetus for continued exploration from Earth and for future missions to Europa.

References

1. R. T. Pappalardo *et al*., *Europa* (Univ. of Arizona Press, Tucson, 2009).
2. L. Roth *et al*., *Science* **343**, 171 (2014).
3. J. D. Anderson *et al*., *Science* **281**, 2019 (1998).
4. K. Zahnle, P. Schenk, H. Levison, L. Dones, *Icarus* **163**, 263 (2003).
5. J. R. Spencer, F. Nimmo, *Annu. Rev. Earth Planet. Sci.* **41**, 693 (2013).
6. K. K. Khurana *et al*., *Nature* **395**, 777 (1998).
7. G. V. Hoppa, B. R. Tufts, R. Greenberg, P. E. Geissler, *Science* **285**, 1899 (1999).
8. C. F. Chyba, *Nature* **403**, 381 (2000).
9. Space Studies Board, *New Frontiers in the Solar System: An Integrated Exploration Strategy* (National Academies Press, Washington, DC, 2003).
10. Space Studies Board, *Visions and Voyages for Planetary Science in the Decade 2013–2022* (National Academies Press, Washington, DC, 2011).
11. D. T. Hall, D. F. Strobel, P. D. Feldman, M. A. McGrath, H. A. Weaver, *Nature* **373**, 677 (1995).
12. M. M. Hedman *et al*., *Nature* **500**, 182 (2013).

10.1126/science.1248879

Published by AAAS

RETROSPECTIVE

Nelson R. Mandela (1918–2013)

A great world leader and humanitarian fought for racial equality, human rights, science education, and the rights of AIDS patients.

Salim S. Abdool Karim

When Nelson Rolihlahla Mandela died on 5 December, the world lost one of its greatest leaders. Lawyer. Protester. Revolutionary. Anti-apartheid leader. Prisoner. Negotiator. President. Statesman. Anti-AIDS campaigner. Philanthropist. These 10 stages of his life capture his historic long walk to freedom and his legacy as a great humanitarian.

Born on 18 July 1918 in the rural Thembu village of Mveso in Transkei, South Africa, Mandela was named Rolihlahla, which in Xhosa means "tugging a tree branch." He was given the Christian name "Nelson" on his first day at a local missionary school in Qunu. At the age of 21, Nelson enrolled at the University of Fort Hare, the only South African residential higher education institution for blacks at the time. After student protests, he was expelled in his third year of study. But he completed his law degree at the University of Witwatersrand in Johannesburg and, with Oliver Reginald Tambo, established the first black law firm that mostly provided free or low-cost legal counsel to blacks victimized by the country's discriminatory laws.

Mandela joined the African National Congress at age 24 and rose to its leadership as he directed nonviolent acts of defiance against the South African government's racist policies for two decades. After the 1961 Sharpeville massacre, when police killed 69 peaceful protesters, Mandela established the armed wing of the African National Congress, becoming its first commander-in-chief. In 1963, he was tried by the apartheid government for treason and sentenced to life imprisonment, at the age of 44, for political offenses, including sabotage.

Mandela was released unconditionally on 11 February 1990 at age 71 by President Frederik W. de Klerk, paving the way for negotiations between the government and anti-apartheid organizations. He was a formidable negotiator and charted a power-sharing deal with the architects of apartheid, the National Party. In 1993, Mandela and de Klerk received the Nobel Peace Prize.

Mandela became president of South Africa after the first democratic elections in 1994. At that time, 1 in 13 pregnant women



was HIV positive (national prenatal HIV prevalence was 7.6%). One of his first acts as president was to proclaim free health care for pregnant women and children. Mandela's government gave due consideration to AIDS, making it a Presidential Lead Program. His government also appointed a leading local AIDS scientist as the country's National AIDS Program Director.

Despite his recognition of AIDS as a serious health problem during his tenure, Mandela was focused on building a democratic, nonracial, nonsexist nation as a priority. He raised the bar on forgiveness by his benevolent tea invitation to the prosecutor who was responsible for his 27-year imprisonment. He set up the Truth and Reconciliation Commission under the leadership of Archbishop Desmond Tutu (1984 recipient of the Nobel Peace Prize) to help the country deal with and purge its apartheid past. One of Mandela's greatest achievements was to convince whites in South Africa that blacks would not oppress or treat them in the same way that they had treated blacks during apartheid. By voluntarily stepping down after his first term as president, an act seldom seen in Africa, where dictators frequently cling to power as lifetime presidents, Mandela confirmed that South Africa had indeed been set on the path of democracy.

By the end of his presidency in 1999, when almost one in four pregnant women was HIV positive (national prenatal HIV prevalence was 22.4%), Mandela had provided little personal leadership or contribution in the fight against AIDS, as a consequence of his competing nation-building priorities. He later spoke of his regret in not speaking out more forcefully about AIDS and set about making amends. Mandela is well known for saying, "Unlike some politicians, I can admit to a mistake." He established the Nelson Mandela Children's Fund, which supported community programs for preventing mother-to-child transmission of HIV and caring for AIDS orphans.

His successor, President Thabo Mbeki, promoted AIDS denialism, which opposed the scientific consensus that AIDS was caused by a viral infection that could be treated by antiretroviral drugs. During this time, the Nelson Mandela Foundation sponsored a national household AIDS survey to focus the country's attention on the urgent need to act against AIDS. Perhaps Mandela's most important act regarding AIDS was to speak out at the 13th International AIDS Conference in 2000 in Durban, when he roused the audience to 17 standing ovations as he declared that South Africa and the world had to make AIDS treatment accessible to all who needed it. Mandela did not stop there; he fought AIDS stigma and discrimination by symbolically wearing a Treatment Action Campaign "HIV Positive" T-shirt. In his foreword to the book *HIV/AIDS in South Africa* (for which I was a coeditor) he highlighted that "we will not succeed until we appreciate the gender dimension of vulnerability to HIV" and "until we have addressed the stigmatisation and discrimination." In 2005, he focused attention on AIDS-related stigma when he announced to the world, "My son has died of AIDS." Nelson Mandela had effectively extended his fight for freedom to the fight for human rights in dealing with AIDS and soon thereafter to the fight against tuberculosis.

His philanthropy reached beyond AIDS to education as he pronounced that "Education is the most powerful weapon which you can use to change the world." In establishing the Mandela Rhodes Foundation for educational scholarships in 2002, he became one of the country's major contributors to postgraduate training in the sciences. Mandela saw this as central to creating the next generation of leaders for South Africa and the world.

Mandela set humankind on the paths of truth, selflessness, and freedom. His long walk was the first step toward freedom from oppression, freedom from want, and freedom from disease. With his passing, his legacy is in each of us as we follow in his footsteps in the enduring quest to make our world a better place for all.

10.1126/science.1249822

CAPRISA, University of KwaZulu-Natal, Durban 4013, South Africa. E-mail: karims1@ukzn.ac.za

CREDIT: ERIC MILLER/DOCTORS WITHOUT BORDERS/MSF

Published by AAAS

Status and Ecological Effects of the World's Largest Carnivores

William J. Ripple,* James A. Estes, Robert L. Beschta, Christopher C. Wilmers, Euan G. Ritchie, Mark Hebblewhite, Joel Berger, Bodil Elmhagen, Mike Letnic, Michael P. Nelson, Oswald J. Schmitz, Douglas W. Smith, Arian D. Wallach, Aaron J. Wirsing

Background: The largest terrestrial species in the order Carnivora are wide-ranging and rare because of their positions at the top of food webs. They are some of the world's most admired mammals and, ironically, some of the most imperiled. Most have experienced substantial population declines and range contractions throughout the world during the past two centuries. Because of the high metabolic demands that come with endothermy and large body size, these carnivores often require large prey and expansive habitats. These food requirements and wide-ranging behavior often bring them into conflict with humans and livestock. This, in addition to human intolerance, renders them vulnerable to extinction. Large carnivores face enormous threats that have caused massive declines in their populations and geographic ranges, including habitat loss and degradation, persecution, utilization, and depletion of prey. We highlight how these threats can affect the conservation status and ecological roles of this planet's 31 largest carnivores.

Advances: Based on empirical studies, trophic cascades have been documented for 7 of the 31 largest mammalian carnivores (not including pinnipeds). For each of these species (see figure), human actions have both caused declines and contributed to recovery, providing "natural experiments" for quantifying their effects on food-web and community structure. Large carnivores deliver economic and ecosystem services via direct and indirect pathways that help maintain mammal, avian, invertebrate, and herpetofauna abundance or richness. Further, they affect other ecosystem processes and conditions, such as scavenger subsidies, disease dynamics, carbon storage, stream morphology, and crop production. The maintenance or recovery of ecologically effective densities of large carnivores is an important tool for maintaining the structure and function of diverse ecosystems.

Outlook: Current ecological knowledge indicates that large carnivores are necessary for the maintenance of biodiversity and ecosystem function. Human actions cannot fully replace the role of large carnivores. Additionally, the future of increasing human resource demands and changing climate will affect biodiversity and ecosystem resiliency. These facts, combined with the importance of resilient ecosystems, indicate that large carnivores and their habitats should be maintained and restored wherever possible. Preventing the extinction of these species and the loss of their irreplaceable ecological function and importance will require novel, bold, and deliberate actions. We propose a Global Large Carnivore Initiative to coordinate local, national, and international research, conservation, and policy.



Ecologically important carnivores. Seven species of large carnivores with documented ecological effects involving (**A**) "tri-trophic cascades" from large carnivores to prey to plants, (**B**) "mesopredator cascades" from large carnivores to mesopredators to prey of mesopredators, and (**C**) both tri-trophic and mesopredator cascades. [Photo credits: sea otter (N. Smith), puma (W. Ripple), lion (K. Abley), leopard (A. Dey), Eurasian lynx (B. Elmhagen), dingo (A. McNab), gray wolf (D. Mclaughlin)]

READ THE FULL ARTICLE ONLINE
http://dx.doi.org/10.1126/science.1241484

Cite this article as W. J. Ripple *et al.*, *Science* **343**, 1241484 (2014). DOI: 10.1126/science.1241484

ARTICLE OUTLINE

Ecological Effects of Large Carnivores
Ecosystem and Economic Services
Anthropogenic Impacts
Climate Change
Outlook
A Final Word

SUPPLEMENTARY MATERIALS

Figs. S1 to S4
Tables S1 to S3

ADDITIONAL RESOURCES

"Lords of nature: Living in a land of great predators"; www.youtube.com/watch?v=PagO3gmwmA0

George Monbiot, TED "For more wonder, rewild the world"; www.youtube.com/watch?v=8rZzHkpyPkc

Trophic Cascades Program, www.cof.orst.edu/cascades/

Large Carnivore Initiative for Europe, www.lcie.org/Home.aspx

RELATED ITEMS IN *SCIENCE*

J. A. Estes *et al.*, "Trophic downgrading of planet Earth." *Science* **333**, 301–306 (2011).

The list of author affiliations is available in the full article online.
*Corresponding author. E-mail: bill.ripple@oregonstate.edu

Status and Ecological Effects of the World's Largest Carnivores

William J. Ripple,[1]* James A. Estes,[2] Robert L. Beschta,[1] Christopher C. Wilmers,[3] Euan G. Ritchie,[4] Mark Hebblewhite,[5] Joel Berger,[6] Bodil Elmhagen,[7] Mike Letnic,[8] Michael P. Nelson,[1] Oswald J. Schmitz,[9] Douglas W. Smith,[10] Arian D. Wallach,[11] Aaron J. Wirsing[12]

Large carnivores face serious threats and are experiencing massive declines in their populations and geographic ranges around the world. We highlight how these threats have affected the conservation status and ecological functioning of the 31 largest mammalian carnivores on Earth. Consistent with theory, empirical studies increasingly show that large carnivores have substantial effects on the structure and function of diverse ecosystems. Significant cascading trophic interactions, mediated by their prey or sympatric mesopredators, arise when some of these carnivores are extirpated from or repatriated to ecosystems. Unexpected effects of trophic cascades on various taxa and processes include changes to bird, mammal, invertebrate, and herpetofauna abundance or richness; subsidies to scavengers; altered disease dynamics; carbon sequestration; modified stream morphology; and crop damage. Promoting tolerance and coexistence with large carnivores is a crucial societal challenge that will ultimately determine the fate of Earth's largest carnivores and all that depends upon them, including humans.

The order Carnivora consists of 245 terrestrial species inhabiting nearly every major habitat on Earth (*1*). These mammalian species, which we call carnivores, are generally unified by a shared heritage of subsisting largely on other animals and are naturally rare because of their position at the top of the food web. These are also some of the world's most revered and iconic species. Ironically, they are also some of the most threatened. During the previous two centuries, many carnivores have experienced substantial population declines, geographic range contractions, and fragmentation of their habitat (*2*, *3*).

Carnivores of various sizes play an important role in regulating ecosystems (*4*–*7*). These roles, moreover, may not be redundant among carnivore species, because the strength and nature of their impacts are influenced by factors such as the carnivore's size, metabolic demands, density, sociality, and hunting tactics. The larger carnivores especially tend to have large energetic constraints, slow life histories, and low population densities and roam widely in search of larger prey (*8*–*10*). This conflation of low population densities and reproductive rates with high food requirements and wide-ranging behavior, bringing them into conflict with humans and livestock, is what makes them vulnerable and poorly able to respond to persecution.

Large carnivores can exert ecological effects despite existing at low densities (*11*), but persecution can affect their social structure and influence their ecological role (*12*). Classically, the effects of large carnivores are thought to extend down the food web to herbivores and to plants, but we are learning that their cascading influences propagate broadly to other species as mediated by their controlling effects on mesocarnivores (*4*, *13*, *14*). Large carnivores have the dual role of potentially limiting both large herbivores through predation and mesocarnivores through intraguild competition, thus structuring ecosystems along multiple food-web pathways. Together, these controls influence the nature and strength of ecosystem functioning. What makes the conservation of large carnivores exceptionally important, therefore, is both their vulnerability to extinction and their ability to structure ecosystems. With this in mind, our focus here is on the largest carnivores.

We review the conservation status and ecological effects of the 31 largest (average adult body masses ≥15 kg) species of Carnivora (not including pinnipeds). Although most of these species are obligate meat eaters, some are omnivorous and one is herbivorous (Table 1). The remaining 214 carnivore species with body masses <15 kg are not considered here, but we acknowledge they also can play important and varied roles in communities (*4*, *13*). The 31 largest carnivores belong to five families: Canidae, Felidae, Mustelidae, Ursidae, and Hyaenidae. They generally have small population sizes (Fig. 1 and table S1), often due to high levels of range loss (Table 1). Many of these species (61%) are listed by the International Union for the Conservation of Nature (IUCN) as threatened (vulnerable, endangered, or critically endangered) and are at risk of local or total extinction. Most (77%) are undergoing continuing population declines (Table 1). Estimates of range contractions for 17 of the 31 species revealed that they currently occupy on average only 47% (minimum <1%, maximum 73%) of their historical ranges (Table 1). These range losses can result in local population extinctions, which have implications for the maintenance of ecosystem and socioeconomic services. Thus, many of these species are gradually disappearing just as we are beginning to understand and appreciate their roles in ecosystems and the many societal benefits that accrue from their preservation (*5*, *15*).

We report our current understanding of the substantial ecological roles large-carnivore species play in ecosystems and how their population declines, extirpations, and recoveries stand to influence ecological communities and ecosystems across the globe. We further consider how those roles may change as environmental conditions become altered when humans cause habitat loss and climate change. We end by addressing the outlook for the future and the looming uncertainties motivating an urgent need for more research on carnivore interactions in food webs and the conservation of these species.

Ecological Effects of Large Carnivores

Seven of the 31 species of large carnivores are associated with documented trophic cascades. Therefore, we focus on these seven species with analysis and discussion. Each of the seven species is well studied in comparison to other large carnivores (fig. S2). In all cases, these seven species of large carnivores clearly have cascading influences on ecological communities and ecosystems. We assessed the general strength of these effects using available data to calculate the $\log_{10}(X_a/X_p)$ effect magnitudes, where X_a and X_p are the values for the response variables with the large-carnivore species absent and present, respectively [for methods, see (*6*)]. The effect magnitude of large-carnivore removal on the abundance of prey, plants, and mesopredators ranged from –2.3 to 2.3 (Fig. 2). These are considered large effects. For example, an effect size of 2 or –2 represents a difference of two orders of magnitude (100 times) in the effect

[1]Trophic Cascades Program, Department of Forest Ecosystems and Society, Oregon State University, Corvallis, OR 97331, USA. [2]Department of Ecology and Evolutionary Biology, University of California, Santa Cruz, CA 95060, USA. [3]Center for Integrated Spatial Research, Department of Environmental Studies, University of California, Santa Cruz, CA 95064, USA. [4]Centre for Integrative Ecology and School of Life and Environmental Sciences, Deakin University, Burwood, Victoria 3125, Australia. [5]Wildlife Biology Program, Department of Ecosystem and Conservation Sciences, College of Forestry and Conservation, University of Montana, Missoula MT, 59812, USA, and Department of Biodiversity and Molecular Ecology, Research and Innovation Centre, Fondazione Edmund Mach, Via Mach 1, 38010 San Michele all'Adige (TN), Italy. [6]Department of Organismic Biology and Ecology, University of Montana, Missoula, MT 59812, and Wildlife Conservation Society, Bronx, NY 10460, USA. [7]Department of Zoology, Stockholm University, SE-106 91 Stockholm, Sweden. [8]School of Biological, Earth and Environmental Sciences, University of New South Wales, Sydney, New South Wales 2052, Australia. [9]School of Forestry and Environmental Studies, Yale University, New Haven, CT 06511, USA. [10]Yellowstone Center for Resources, Yellowstone National Park, Post Office Box 168, Mammoth, WY 82190, USA. [11]School of Marine and Tropical Biology, James Cook University, Townsville, Queensland 4811, Australia. [12]School of Environmental and Forest Sciences, University of Washington, Seattle, WA 98195, USA.

*Corresponding author. E-mail: bill.ripple@oregonstate.edu

between when carnivores are absent as compared to present. These values also rank relatively high when compared to a meta-analysis of 114 case studies of predators from both aquatic and terrestrial systems, where effects, expressed in $\log_{10}$ ratios, ranged from −0.3 to 1.0 (*16*). With the exception of the sea otter, all of the aquatic and terrestrial predators included in that study were ≤2 kg in body mass, suggesting a potential link between carnivore size and ecological influence. Below we provide a brief synthesis for each of the seven large-carnivore species. Following these species accounts is a general discussion of other large-carnivore species, for which less is known about their ecological effects.

Lions and Leopards

The African lion (*Panthera leo*) occupies 17% of its historical range and is listed as vulnerable by the IUCN. Its abundance has declined dramatically in recent decades because of habitat loss and indiscriminate killing in defense of humans and livestock (*17*). The leopard (*Panthera pardus*) is near threatened and occupies 65% of its historical range. When sympatric, lions and leopards exert control on mesopredators. In West Africa, olive baboons (*Papio anubis*) increased in abundance at rates most closely correlated with declines in these apex predators relative to seven other environmental variables that might explain baboon abundance and range occupancy (*18*). Increases in baboons correlated with accelerated declines in small ungulates and primates. Among large mammals, baboons pose the greatest threat to livestock and crops and they use many of the same sources of animal protein and plant foods as humans in sub-Saharan Africa. In some areas, baboon raids in agricultural fields require families to keep children out of school so they can help guard planted crops (*18*).

Dingoes

The dingo (*Canis dingo*), thought to have arrived in Australia around 5000 years ago (*19*), became the sole remaining mammalian apex predator on the continent after the extinction of the Tasmanian tiger (*Thylacinus cynocephalus*). With European settlement, dingo populations have been affected across the continent, notably by the erection of a 5500-km dingo-proof fence designed to keep dingoes out of Australia's major sheep-grazing region. The presence and absence of dingoes on either side of the fence, along with variation in dingo management practices among properties, has produced a continental-scale experiment. The most significant and well-understood effects of dingoes are in the control of populations of native

Table 1. Large-carnivore species list, body mass (in kilograms), diet, endangerment status, population trend, and percent of historical range occupied. Body masses are from Gittleman (*15*), Mammalian Species Accounts, and the Animal Diversity Web. Diet categories are from Hunter (*1*) as follows: M, meat eater; V, vegetation and/or fruit eater; O, omnivore. Species status and trend are from the IUCN Red List (*16*): LC, least concern; NT, near threatened; VU, vulnerable; EN, endangered; CR, critically endangered.

Family/species*	Common name	Mass, diet	IUCN status (trend)	% of historical range	Reference for % of historical range
Canidae					
Canis lupus	Gray wolf	33, M	LC (stable)	67	(*1*)
Canis rufus	Red wolf	25, M	CR (increasing)	<1	(*91*)
Chrysocyon brachyurus	Maned wolf	23, O	NT (unknown)	68	(*2*)
Lycaon pictus	African wild dog	22, M	EN (decreasing)	10	(*17*)
Cuon alpinus	Dhole	16, M	EN (decreasing)	–	–
Canis dingo†	Dingo	15, M	VU (decreasing)	84	(*20*)
Canis simensis	Ethiopian wolf	15, M	EN (decreasing)	2	(*17*)
Felidae					
Panthera tigris	Tiger	161, M	EN (decreasing)	18	(*3*)
Panthera leo	Lion	156, M	VU (decreasing)	17	(*17*)
Panthera onca	Jaguar	87, M	NT (decreasing)	57	(*3*)
Acinonyx jubatus	Cheetah	59, M	VU (decreasing)	17	(*17*)
Panthera pardus	Leopard	53, M	NT (decreasing)	65	(*3*)
Puma concolor	Puma	52, M	LC (decreasing)	73	(*3*)
Panthera uncia	Snow leopard	33, M	EN (decreasing)	–	–
Neofelis nebulosa	Clouded leopard	20, M	VU (decreasing)	–	–
Neofelis diardi	Sunda clouded leopard	20, M	VU (decreasing)	–	–
Lynx lynx	Eurasian lynx	18, M	LC (stable)	–	–
Mustelidae					
Enhydra lutris	Sea otter	28, M	EN (decreasing)	–	–
Pteronura brasilliensis	Giant otter	24, M	EN (decreasing)	–	–
Aonyx capensis	Cape clawless otter	19, M	LC (stable)	–	–
Ursidae					
Ursus maritimus	Polar bear	365, M	VU (decreasing)	–	–
Ursus arctus	Brown bear	299, O	LC (stable)	68	(*3*)
Ailuropoda melanoleuca	Giant panda	134, V	EN (decreasing)	–	–
Ursus americanus	American black bear	111, O	LC (increasing)	59	(*35*)
Tremarctos ornatus	Andean black bear	105, O	VU (decreasing)	–	–
Ursus thibetanus	Asiatic black bear	104, O	VU (decreasing)	–	–
Melursus ursinus	Sloth bear	102, O	VU (decreasing)	–	–
Helarctos malayanus	Sun bear	46, O	VU (decreasing)	–	–
Hyaenidae					
Crocuta crocuta	Spotted hyena	52, M	LC (decreasing)	73	(*17*)
Hyaena brunnea	Brown hyena	43, O	NT (decreasing)	62	(*17*)
Hyaena hyaena	Striped hyena	27, O	NT (decreasing)	62	(*17*)

*Changes to taxonomic status have influenced the number of species included in this group, and some less-known and taxonomically ambiguous carnivores may be missing from this analysis because they have yet to be listed by the IUCN. †Currently incorporates the New Guinea singing dog, *C. hallstromi*, whose taxonomic and conservation status is yet to be elucidated.

herbivores, introduced herbivores, and the exotic mesopredator the red fox (*Vulpes vulpes*). The suppression of these species by dingoes reduces total herbivory and predation pressure, in turn benefiting plant communities and smaller native prey (*12*, *14*, *20*, *21*). The dingo's social stability and associated behavior are thought to be key to its ecological effectiveness (*12*). Overall, the suppression of dingoes has probably contributed to the endangerment and extinction of small marsupials and rodents over much of the continent (*21*, *22*).

Eurasian Lynx

The Eurasian lynx (*Lynx lynx*) maintains an extensive distribution in eastern and northern Eurasia, but it has been extirpated from large parts of Western Europe (*23*). At the continental scale, the effects of lynx predation increase with harsh winter conditions (*23*, *24*). Lynx may limit both prey (roe deer *Capreolus capreolus*) and mesocarnivore (red fox) abundance, so changes in lynx status may trigger cascading effects along two pathways, of which the mesocarnivore-mediated cascade is the more explored (*25*). The recent recovery and enhanced conservation protection of Eurasian lynx in Finland were accompanied by a decline in red fox abundance and a commensurate recovery in the abundance of forest grouse (*Tetrao tetrix and T. urogallus*) and mountain hare (*Lepus timidus*) (*7*, *25*). Moreover, where lynx density had recovered to "ecologically effective" levels, the controlling effects of lynx on red foxes and prey increased with ecosystem productivity, indicating that the strength of predator control may vary as a function of the net primary productivity of the ecosystem (*26*, *27*).

Sea Otters

Sea otters (*Enhydra lutris*) were hunted to near-extinction during the Pacific maritime fur trade in the 18th and 19th centuries (*28*). Sea otter populations are presently stable or increasing from about Kodiak Island eastward, deeply depleted [presumably because of killer whale predation (*29*)] from about Kodiak Island westward through the Aleutian archipelago, and largely recovered in Russia. The earlier recovery of these populations and the more recent decline of recovered populations in southwest Alaska (*29*) offer natural experiments to study the sea otter's influences on coastal ecosystems. The best-documented cascade of effects involves sea otters limiting herbivorous sea urchins and, in turn, enhancing the abundance and distribution of kelp and other fleshy macroalgae in coastal inshore ecosystems (Fig. 3A) (*30*). As sea otter populations recover and decline, shifts between the kelp-dominated and urchin-dominated conditions can be abrupt (*31*). Once reached, these different ecological states tend to persist (*32*) unless the system is pushed strongly to the other state by substantial increases or reductions in otter abundance. The follow-on effects of these shifts influence numerous other species and ecological processes in coastal ecosystems through three basic mechanisms: the creation of biogenic habitat (i.e., created by living organisims), the enhancement of primary production, and the influence of kelp forests in dampening coastal waves and currents [reviewed in (*31*)].

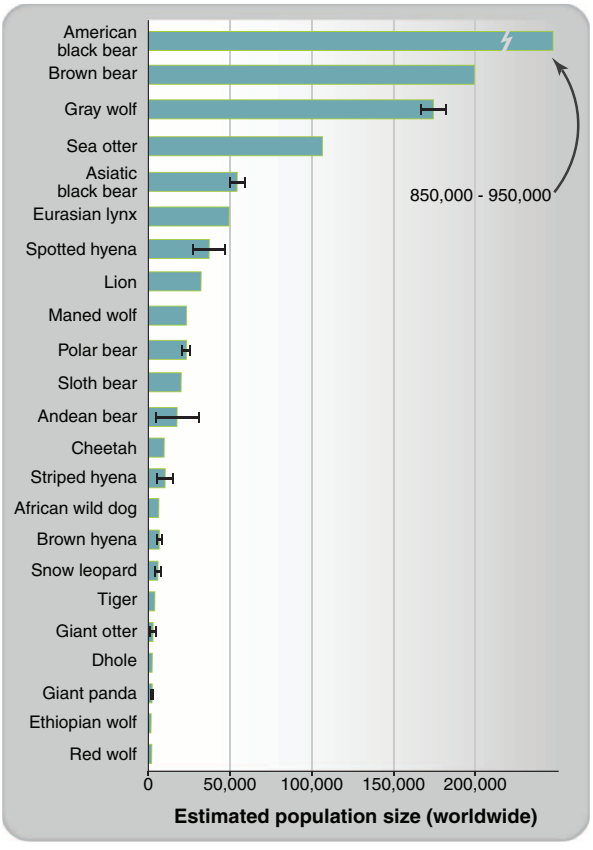


Fig. 1. Worldwide population estimates of large-carnivore species. Error bars represent the low and high range of the estimates when available. Population estimates were not available for all species. Species ranges vary widely, and range sizes can have a strong influence on species population levels (table S1). Sources: Gray wolf (*90*), all other species IUCN (*91*).

Gray Wolves

The gray wolf (*Canis lupus*) is one of the world's most widely distributed mammals and the most studied large carnivore (fig. S2). It has been extirpated from much of Western Europe, the United States, and Mexico, and its overall range has been reduced by approximately one-third because of persecution by humans and habitat fragmentation (*1*). In recent decades, wolf population declines have been arrested because of enhanced legal protection, reintroduction programs, and natural recolonization, resulting in population recoveries in portions of the Rocky Mountains, Great Lakes, and southwestern regions of North America, as well as in various parts of Europe. Other than humans, gray wolves, by virtue of their widespread geographic distribution, group hunting, and year-round activity, are the most important predator of cervids in the Northern Hemisphere (*33*). Predation by wolves with sympatric bears (*Ursus* spp.) generally limits cervid densities (*33*). In North America and Eurasia, cervid densities were, on average, nearly six times higher in areas without wolves than in areas with wolves (*34*). As early as the 1940s, cervid irruptions, after wolf and other predator declines, were first documented in various ecosystems of western North America (*35*). The shifts in plant communities consequent to the cascading effects of wolf extirpations and of recoveries have been found across a variety of areas of North America, representing a wide range of productivity (*6*). In Yellowstone National Park, wolves were reintroduced in 1995–1996, making this park one of the most predator-rich areas in North America. This reintroduction triggered various direct and indirect effects, as mediated by both mesopredators and cervid prey (Figs. 3B and 4).

Pumas

The range of the puma (*Puma concolor*) in the Western Hemisphere remains larger than that of any other terrestrial mammal, even though they have been extirpated from most of the eastern United States (*36*). In the absence of pumas and sometimes other large carnivores, hyperabundant cervids [such as the white-tailed deer (*Odocoileus virginianus*)] in the eastern United States and Canada now affect many aspects of ecosystem function, including plant recruitment and survival, endangered species status, forest stand structure, nutrient dynamics, and socioeconomics through vehicle collisions (*37*). Where pumas are present, they can be important drivers of cervid populations and associated trophic relations, as in canyon settings in western North America, where they locally limit mule deer (*O. hemionus*) densities, releasing woody plants from browsing suppression (*38*, *39*). Pumas also appear to influence processes affecting terrestrial and aquatic species, including hydrophytic plants, wildflowers, amphibians,

lizards, and butterflies. Their presence may also help to stabilize stream banks and channels (*38*). Pumas may induce their prey to engage in "human shielding" as an antipredator strategy. Deer at risk from pumas, for example, associated themselves with human development at high densities, in turn causing plant damage (*38*, *39*).

Other Large Carnivores

Little is known about the ecological effects of the other large-carnivore species listed in Table 1, and questions remain about their potential roles in controlling food webs and ecosystem functioning, especially in the tropics and subtropics (Fig. 5). However, some valuable lessons come from the flooding of a forest region in Venezuela to generate hydroelectric power. This once-intact, productive tropical system was composed of a species-rich food web with multiple linkages among species. Flooding fragmented the region to produce mountaintop islands—the Lago Guri islands—resulting in the loss of an entire predator guild of jaguars (*Panthera onca*), pumas, lesser mammalian predators, large raptors, and snakes (*40*). This loss of predators had cascading effects on species of pollinators, seed dispersers, seed predators, folivores, and mesopredators, as well as on woody plant recruitment, bird abundance, and soil carbon/nitrogen ratios (*41*).

Predator species often co-occur, requiring consideration of their joint effects. Multiple predator effects on prey species and on ecosystems can be synergistic (*15*). Thus, in some cases, the strength of a trophic cascade may be due to synergisms owing to complementarity among species in the top carnivore guild of communities. This implies that the combined effects of predator species may need to be conserved to fully ensure control over communities and ecosystem functioning. For example, bears of northern latitudes (*Ursus* spp.) may control the recruitment of juveniles into populations of their prey species (*42*). Because bears are opportunistic omnivores and eat a variety of foods, their effects may complement those of gray wolves (*34*). In North America, both black (*U. americanus*) and brown (*U. arctos*) bears commonly prey on neonatal cervids, taking a large percentage of the annual offspring that are less than 1 month old, and these effects could be additive. In Yellowstone National Park, bears killed more elk (*Cervus elaphus*) calves than did gray wolves, coyotes (*Canis latrans*), and pumas combined (*43*). In Europe, roe deer densities were significantly lower in areas with sympatric wolves and lynx than in areas with wolves alone or areas where both predators were absent (*24*, *34*). The effect of multiple predators on prey, however, need not always be synergistic. Adult female elk mortality was similar in areas of western North America with pumas alone as compared to areas with sympatric pumas and wolves (*44*).

Questions persist about how large-carnivore effects interact with habitat productivity. Theory

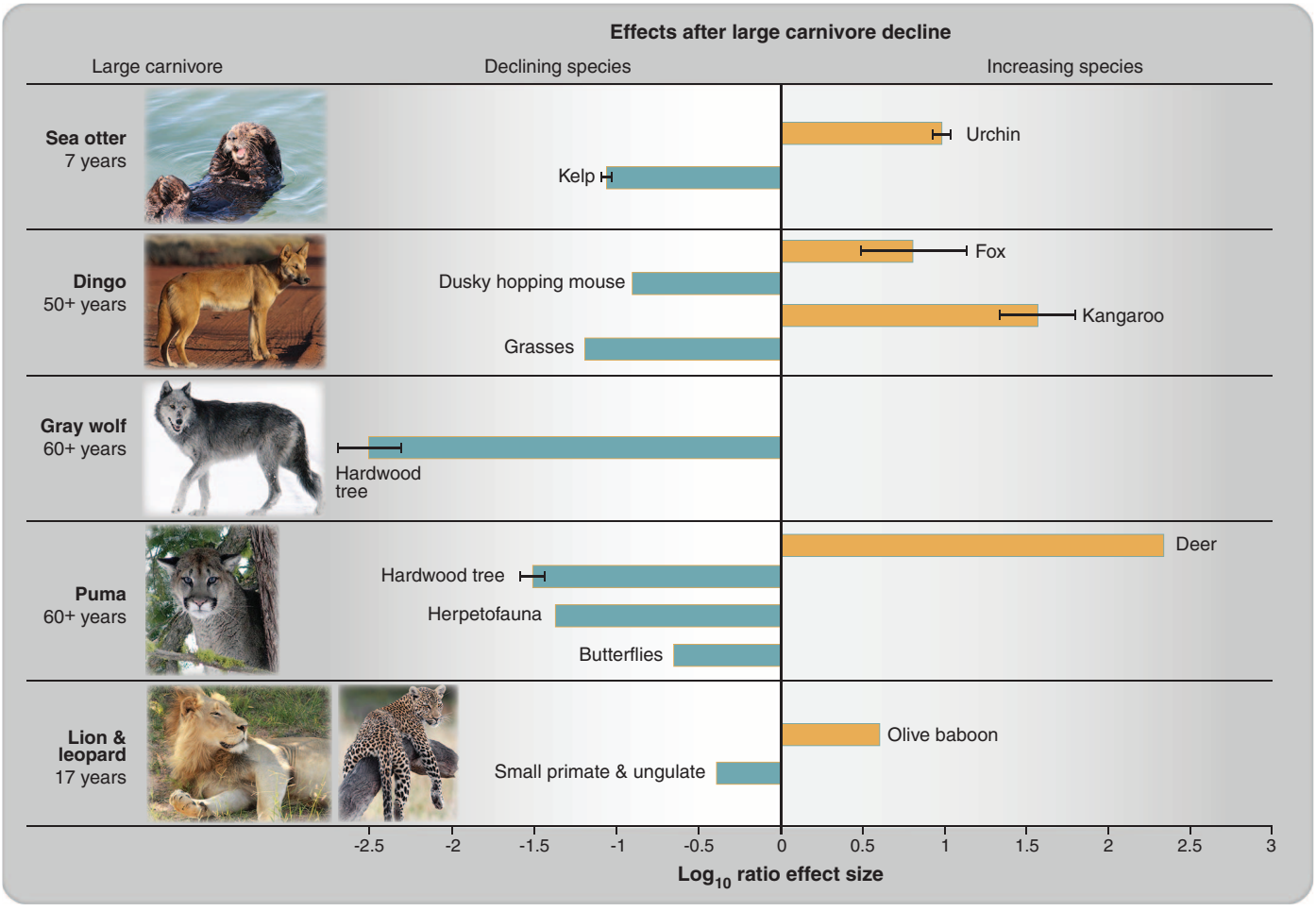


Fig. 2. Examples of effect sizes, shown as $\log_{10}$ ratios, after the removal of large-carnivore species. Sea otters (*29*, *92*), dingoes-foxes and dingoes-kangaroo (*21*, *93*), dingoes-mice (*Notonmys fuscus*) (*93*), dingoes-grasses (*20*), gray wolves–hardwood trees (*94*, *95*), pumas–hardwood trees (*38*, *39*), pumas-deer-herpetofauna-butterflies (*38*), and lions and leopards (*18*). The number of years refers to the time since large-carnivore extirpation. The $\log_{10}$ ratios were calculated by dividing the values of each response variable without predator by those with predator and then taking the $\log_{10}$ of that ratio. Positive log ratios$_{10}$ indicate a positive effect, and negative $\log_{10}$ ratios indicate a negative effect of removing large carnivores. For studies using time-series data, we used the final sampling date in our analysis. The orange bars indicate direct effects and the blue bars indicate indirect effects. Error bars represent standard errors and were only available in some cases. [Photo credits: sea otter (N. Smith), dingo (A. McNab), gray wolf (Yellowstone National Park), puma (Washington Department of Fish and Wildlife), lion (K. Abley), leopard (A. Dey)]

predicts that the strength of cascading effects may vary with the productivity of ecosystems and should show a "humped relationship" with ecosystem productivity (*26*, *27*). That is, we might not expect to see strong trophic cascades in ecosystems such as extreme deserts, high elevations, or high latitudes, where low primary productivity limits herbivore populations and where there is insufficient energy available to support populations of large carnivores (*27*). The trophic effects of single carnivore species might also be diminished in extremely productive environments, because prey species diversity may also be high in such systems and, consequently, the strength of interspecific interactions is diffused across a greater number of interaction pathways (*20*, *41*, *45*). For example, in a productive tropical forest, Sunda clouded leopards (*Neofelis diardi*) had no measurable effect on the abundance of the main large ungulate prey species (*46*). Conversely, there is also empirical evidence indicating that some canids consistently limit prey densities regardless of ecosystem productivity (*34*, *47*). Accordingly, more analyses of how productivity interacts with trophic interactions are needed. To this end, regions harboring large-carnivore populations with different conservation statuses, including places without them, can be used as broad bioclimatic contexts for natural experiments.

Ecosystem and Economic Services

Large carnivores deliver economic and ecosystem services in a variety of direct and indirect ways. Because of their iconic and charismatic nature, large carnivores provide direct economic benefits associated with tourism. In both Minnesota and Yellowstone (*48*, *49*) and the African photo-safari industry (*50*), the opportunity to simply observe large carnivores can drive tourism revenue. In Yellowstone alone, wolf-related tourism expenditures range from $22 million to $48 million (in U.S. dollars) per year (*49*).

Large carnivores also have strong potential to indirectly deliver ecosystem services, such as carbon storage to buffer climate change, biodiversity enhancement, reestablishment of native plant diversity, riparian restoration, and even regulation of diseases. In some ecosystems, large carnivores may enhance carbon storage by limiting the numbers of their herbivore prey, thus allowing plants (all of which absorb and store CO_2) to flourish. Carnivore conservation and restoration might reverse declines in forests stands and production, thereby aiding carbon storage, especially in the highly productive tropics, where declines in plant biomass occur after predator extirpation (*40*, *41*). Maintaining gray wolf populations and their interactions with moose is estimated to help store significant amounts of carbon in boreal ecosystems (*51*). The restoration of sea otter populations can reduce sea urchin herbivores, thereby allowing kelp ecosystems to flourish at levels that can, in the North American range, lead to a 4.4- to 8.7-teragram increase in stored carbon valued at $205 million to $408 million (in U.S. dollars) on the European Carbon Exchange (*52*). Predators may enhance scavenger diversity (*53*) and thereby contribute to nutrient cycling, in addition to myriad other documented cascading and ramifying pathways (*15*). In riparian systems, large carnivores may reduce stream bank erosion through the growth of woody plants and enhance water quality and flood control through the restoration of beaver that benefit from the restored plants (*54*–*57*). Large carnivores help reduce disease prevalence in ungulate prey populations, thereby mitigating agricultural costs because of spillover effects on domestic livestock (*58*). Perhaps counterintuitively, large carnivores may also provide crucial services for the very industry they are perceived to be at most in conflict with: pastoralism. By limiting the density of wild herbivores and promoting productivity, large carnivores may enable pastoral activities that are sustainable (*12*, *59*). This is not to deny that large carnivores also have direct costs, often associated with livestock losses (*60*), and balancing these costs against potential benefits for human-dominated ecosystems as a whole is a pressing challenge (*61*). Regardless, the potentially widespread beneficial ecosystem and economic services associated with large carnivores are underappreciated by society.

Anthropogenic Impacts

Large-carnivore population declines are typically precipitated by multiple, and sometimes concurrent, human threats, including habitat loss and degradation, persecution, utilization (such as for traditional medicine, trophy hunting, or furs), and depletion of prey. Globally, the strength of these threats varies substantially by region (Fig. 6 and table S2). These threats are sometimes localized to only parts of a carnivore's range and, in some cases, may extend beyond its range, thus acting to limit reoccupation of former habitats.

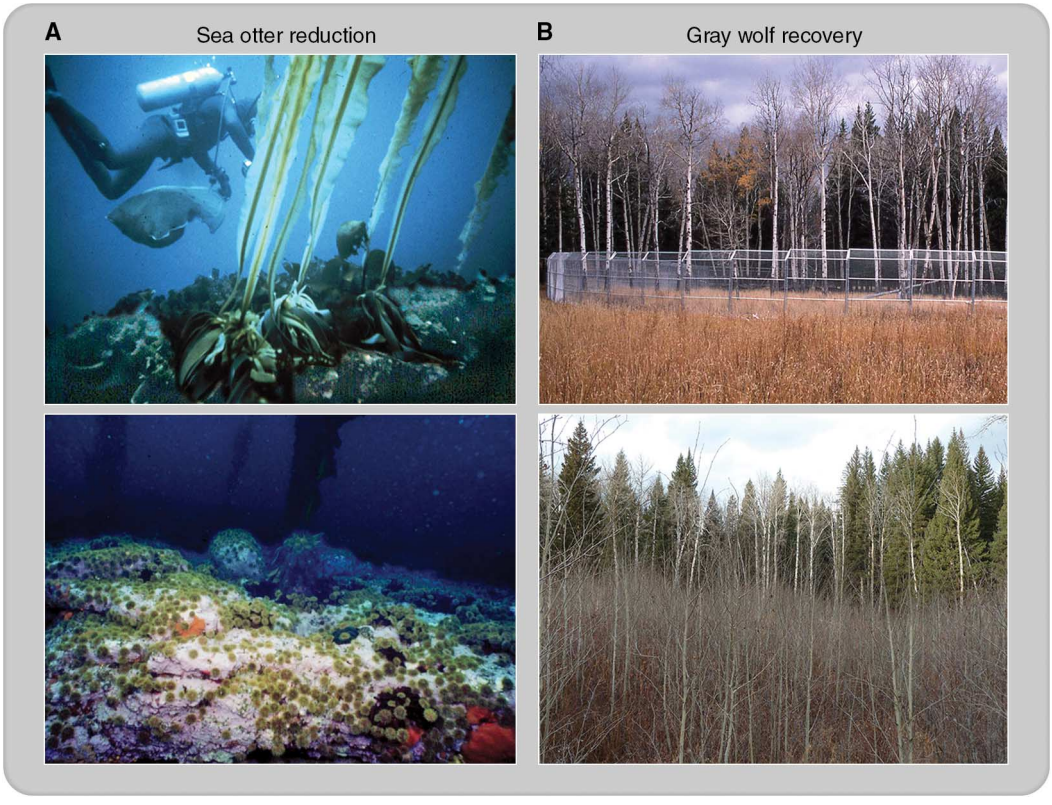


Fig. 3. Examples of plant response after sea otter reduction and after gray wolf recovery. (**A**) An area of seafloor near Kirilof Point, Amchitka Island, Alaska, in 1971 (upper left, photo by P. Dayton), at which time sea otters were abundant, and in 2001 (lower left, photo by M. Kenner) at which time sea otter numbers had been reduced by more than 90% by killer whale predation. (**B**) Photos of the Yellowstone Northern Range taken in October 1994 (top right, photo by National Park Service) and November 2012 (bottom right, photo by D. Mclaughlin), showing increased recruitment of aspen since wolf reintroduction in 1995–1996 at the site of the Crystal Creek gray wolf holding pen, which was removed in 1998. Young aspen in the 1994 photo were mostly less than 1 m tall and those in the 2012 photo were typically 3 to 4 m tall.

Human actions may dampen or even eliminate cascading effects. For example, Mexican gray wolves in southwestern North America have not yet been restored to an ecologically effective density in relation to that of their main prey, elk, because of ongoing conflicts with livestock grazing and repeated management translocations (*62*). Likewise, recent wide-scale hunting of recovering gray wolf populations in parts of the Great Lakes region and the western United States may reduce wolf populations below sizes at which they are able to exert their effects on communities and ecosystems (*63*–*65*). Furthermore, wolves and other carnivores may have little influence on other species in areas where human hunters have disproportionate effects on prey densities (*66*). Few large carnivores can persist in parts of Latin America, Asia, and Africa because of the loss of wild ungulate prey species caused by activities such as hunting for bushmeat. The extraction of bushmeat, in turn, has created "empty forests" (*1*). Conversely, hyperabundant exotic ungulates (domestic livestock) are present in much of the world. These livestock are a potential prey base and thus a continuing source of conflict between humans and large carnivores (*17*).

Hunting by humans, whether legal as in North America and Europe or illegal as in the pantropical bushmeat trade, may itself cause trophic cascades, because humans are also predators with the potential for ecological impacts. Indeed, human hunting pressure on moose (*Alces alces*) has led to the release of control on willow (*Salix* spp.) shrub production and hence encouraged increases in neotropical migrant bird abundances (*42*). Although it is often claimed that human hunting substitutes for predators, it remains doubtful whether such substitution actually leads to the same functional consequences for communities and ecosystems. Effects may be different because of differences in the intensity and timing of predation by humans versus predators, as well as hunting effects on the behavior, age, and sex of prey (*67*). Many carnivores hunt year-round, day or night, and away from human access points. The behavioral responses of prey to predation risk caused by carnivores may create an "ecology of fear" with myriad cascading effects on ecosystems (*68*). In the end, it is not surprising that various human activities in Australia (*12*), North America (*13*, *34*), and Eurasia (*24*) have been unsuccessful in substituting for large carnivores to control populations of native and nonnative herbivores and mesopredators. The huge importance of carnivores is exemplified by the fact that humans typically cannot replicate the effects of carnivores on ecosystems.

Habitat fragmentation, and more generally the intensity of human uses of landscapes, continue to be persistent threats to larger-bodied carnivores, with the potential for cascading impacts on species diversity (*5*, *38*). There exists, therefore, an increasing need to understand the interacting effects of anthropogenic land-use changes and altered large-carnivore guilds on community structure and function. Because of differences in their ecology and human tolerance, pumas are able to persist in areas with much higher levels of human land use than are gray wolves, even though these two carnivores are of similar size. Such differential predator species loss in the face of landscape changes may be especially critical if synergism among multiple large carnivores within predator guilds is required to maintain control over prey populations (*34*, *43*). These and other carnivore species make kills in different habitats, or scavenge to supplement their diets, which can determine the nature and rates of prey kills and consumption (*53*, *69*). In addition to altering predator communities, increased human land use can alter nutrient and water availability, thereby mitigating natural controls over ecological communities and ecosystem functioning (*70*).

Perhaps one of the most insidious threats to carnivores is global human population size and its associated resource consumption, which are expected to continue rising significantly through at least 2050 (Fig. 7). Increased human population size can lead to increased demand for meat. Interestingly, human carnivory competes with

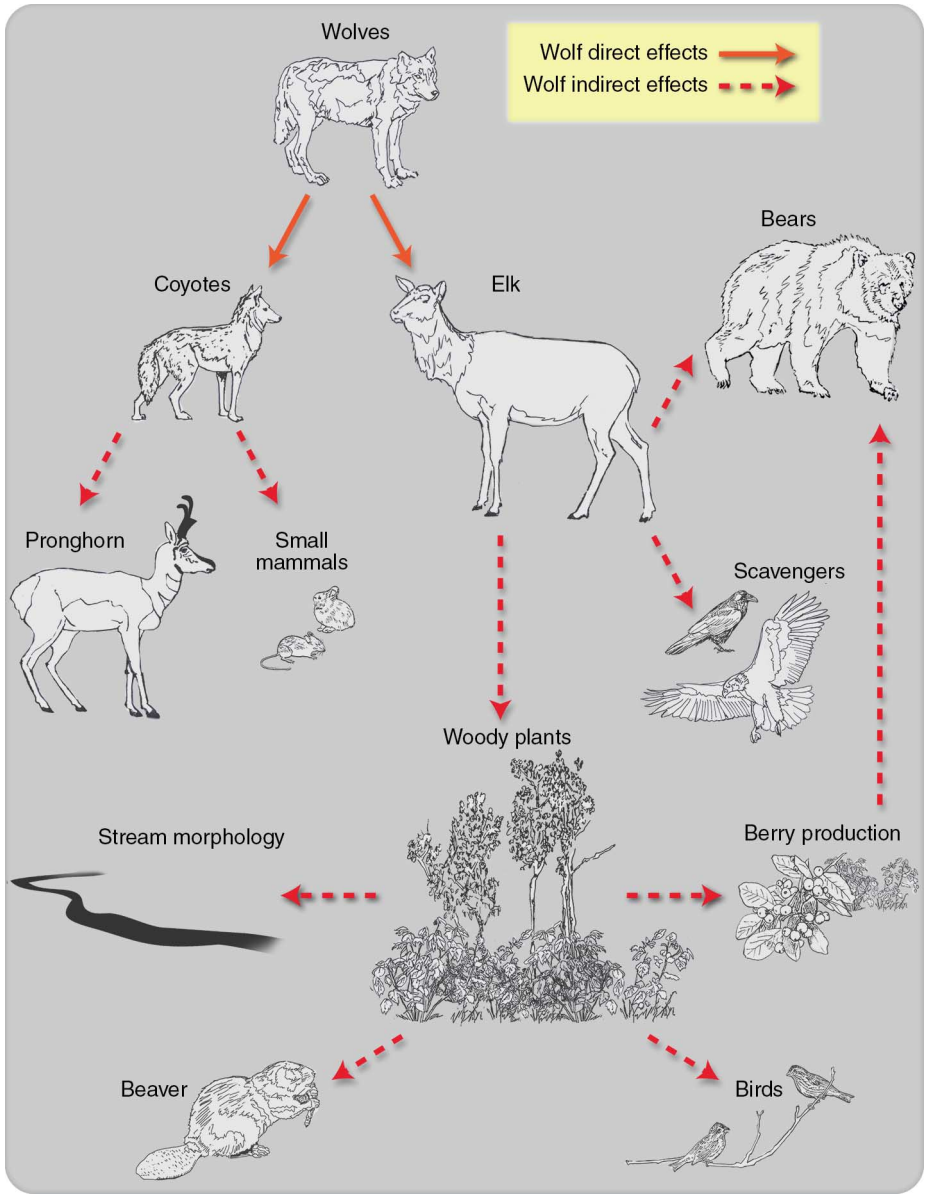


Fig. 4. Conceptual diagram showing direct (solid lines) and indirect (dashed lines) effects of gray wolf reintroduction into the Greater Yellowstone ecosystem. Wolf direct effects have been documented for elk (*96*) and coyotes (*97*), whereas indirect effects have been shown for pronghorn (*98*), small mammals (*99*), woody plants (*100*), stream morphology (*54*), beaver (*55*), birds (*101*), berry production (*63*), scavengers (*53*), and bears (*56*, *63*). This is a simplified diagram, and not all species and trophic interactions are shown. For example, the diagram does not address any potential top-down effects of pumas, bears, and golden eagles (*Aquila chrysaetos*), which are all part of the Yellowstone predator guild where juvenile or adult elk are prey.

large carnivores. For example, the need for humans to either produce meat through livestock production or to exploit wild sources necessarily puts extra pressure on large carnivores on multiple fronts, including ongoing habitat loss from land conversion, depletion of prey, and direct persecution due to conflicts with livestock. In light of their slow life histories and requirement for large continuous habitat, such trends exacerbate the vulnerability of large carnivores to extinction (*9*). Increases in both human population and meat consumption can also affect biodiversity, greenhouse gas emissions, food security, deforestation, desertification, and water quality and quantity (*71*, *72*). Therefore, policy for carnivore conservation needs to be joined up with policy addressing these other converging issues having implications at the global scale (*71*, *72*). Ideally, discussions regarding potential decreases in both human fertility rates and per-capita meat consumption would be part of a long-term strategy for overcoming these concurrent challenges.

Climate Change

Looking forward, the status of large carnivores will influence the extent to which individual species, biotic communities, and ecosystems respond to climate change. For example, mesopredators that have been released from control by the loss of their carnivore predators may increase further in abundance wherever climate change relaxes limitations on their own prey (*23*). Large carnivores may instrumentally determine resilience against invading species, because both native and introduced species are less likely to become invasive in ecosystems in which food-web interdependencies remain intact (*7*). These potential buffering capacities remain both poorly appreciated and poorly understood. Widespread modeling approaches forecasting climate change effects on species still simplistically assume that such interactions and interdependencies do not require consideration, let alone quantification (*73*). Furthermore, climate change is already causing species geographic range shifts that stand to disrupt existing species interactions (*74*, *75*). As species move at different rates and in different directions, novel communities are likely to be created as new combinations of predator and prey species assemble on landscapes. The recently documented change in hunting locations and food habits among polar bears (*Ursus maritimus*) is a case in point. With receding sea ice, polar bears have more difficulty hunting seals, their traditional prey, and are now feeding onshore on the eggs of migratory waterfowl (*76*).

As climate change progresses, large carnivores might serve as important buffers or amplifiers of effects on ecosystems (*77*). In Yellowstone National Park, reintroduced gray wolves control the timing and abundance of ungulate carrion resources, on which a suite of scavenger species, ranging in size from grizzly bears to magpies (*Pica hudsonia*), depend for winter survival and reproduction. The return of wolves has buffered the influence of climate change on late-winter carrion availability (*77*) by shifting the dynamics of carrion availability from a boom–and-bust cycle, linked to climate variability, to a more dependable resource based on shifting patterns of wolf pack size (*53*). Large carnivores might also help augment ecosystem carbon storage by suppressing herbivores, thereby allowing plants to flourish (*34*). For instance, the decline of large carnivores in western North America was followed by a decline in hardwood tree recruitment in riparian areas of over two orders of magnitude (*6*). In northern North America, gray wolves limiting moose populations may be responsible for increased net ecosystem uptake of carbon due to decreased browsing and increased net primary productivity (*51*). Likewise, the presence of sea otters in nearshore environments suppresses sea urchins, allowing macroalgael kelp to thrive and thereby

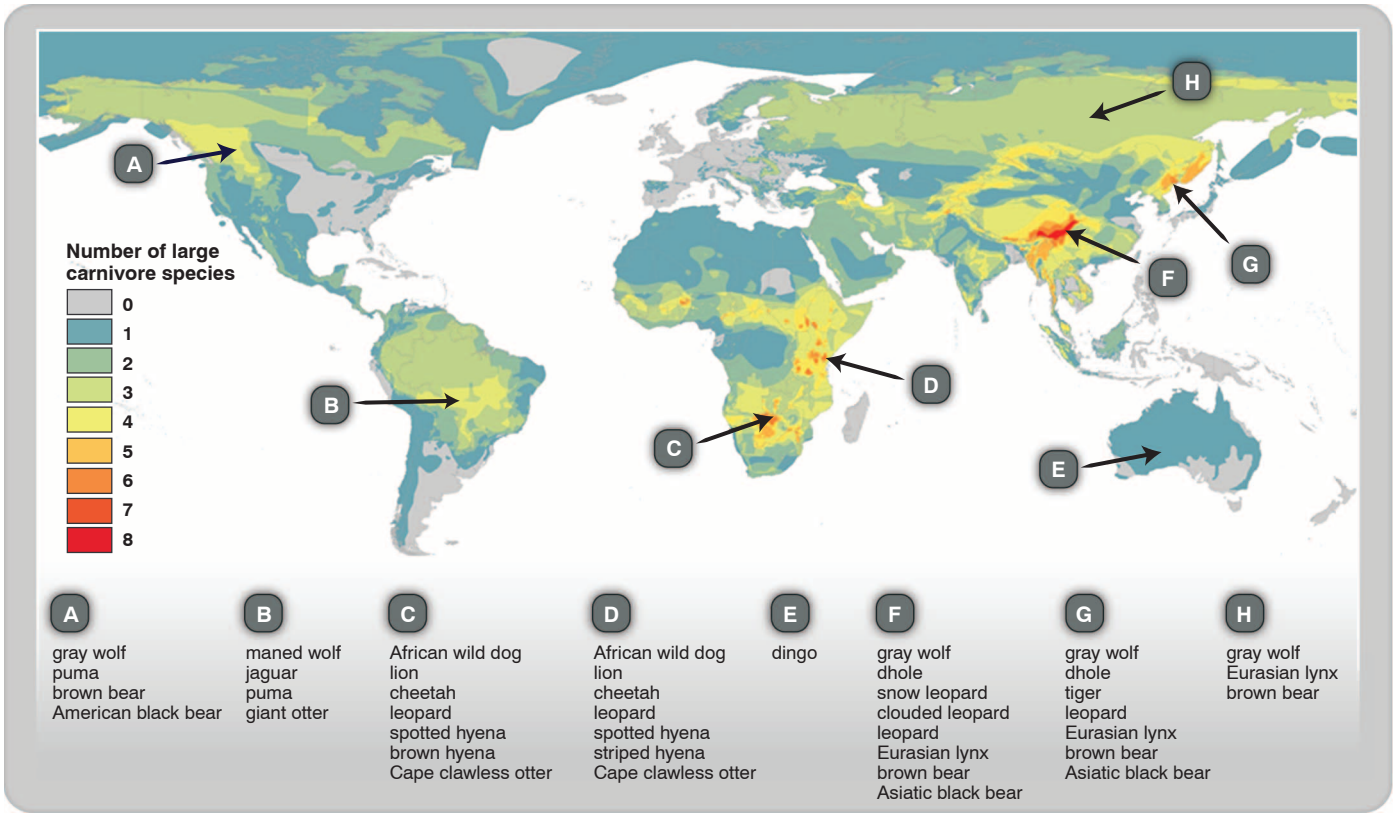


Fig. 5. Contemporary overlap of large carnivore ranges throughout the world. Compared to historical times, large-carnivore range contractions have been most extensive in Europe, southeastern North America, and western and central Africa. The areas with the highest number of species and with intact large-carnivore guilds are some of the best regions for research and conservation (e.g., southeastern Asia, eastern and southern Africa, and northwestern North America). Northern Eurasia is the region with the most expansive range for a three-species guild (gray wolves, Eurasian lynx, and brown bear). The percent of the total terrestrial land area in each of the eight classes in the map includes 0, 13.3%; 1, 29.1%; 2, 23.5%; 3, 20.5%; 4, 9.1%; 5, 2.8%; 6, 1.1%; 7, 0.4%; 8, 0.1%. Only ~5% of Earth's land surface currently contains more than four overlapping large-carnivore species. See fig. S4 for individual range maps. Source: IUCN (*91*).

increasing ecosystem carbon production and storage by one to two orders of magnitude (*52*). Globally, several billion head of ruminating livestock affect global climate change by contributing significant amounts of methane, nitrous oxide, and carbon dioxide (~5.7 gigatons of CO_2 equivalent per year) to the atmosphere, making domestic ruminants a significant contributor to climate change (11.6% of all anthropogenic emissions of greenhouse gases) (*72*). Decreasing global livestock numbers to reduce greenhouse gas emissions would both mitigate climate change and benefit large-carnivore conservation by reducing ongoing worldwide conflict between large carnivores and livestock.

Outlook

The loss of large carnivores across global ecosystems is predicted to lead to two general outcomes. First, as apex predators are lost, we should expect continued change in cascading controls over communities and ecosystem function. Although these effects will differ with the variation in precipitation, temperature, productivity, diversity, and overall landscape features, the continued loss of carnivores nonetheless will be accompanied by changes in plant species diversity, biomass, and productivity. In forest and arid ecosystems, the loss of palatable perennial plant species may interact with global warming to increase the rate of desertification. Because plants are the trophic foundation of all ecosystems, these vegetation changes can be expected to have wide-ranging influences on virtually all other species. The growing list of case studies, some of which we presented above, may well represent the tip of the proverbial iceberg. Changes in species abundance resulting from the loss of large carnivores can be expected to influence numerous other ecological processes, including disease dynamics (*78*, *79*), wildfire (*80*), and carbon sequestration (*51*). Furthermore, the effects of large carnivores are now known to have wide ramifications through highly interconnected food-web networks within their associated ecosystems (*81*). Second, we should expect surprises, because we have only just begun to understand the influences of these animals in the fabric of nature (*82*).

The classic conception of large-carnivore influences on ecosystems held that predators were responsible for depleting resources such as fish, wildlife, and domestic livestock. This assumption is still used to justify wildlife management practices aiming to limit or eradicate predators in some regions (*83*, *84*). This conception of carnivore ecology is now outdated and in need of fundamental change. Indeed, evidence shows that their roles are far more complex and varied, and their myriad social and economic effects on humans include many benefits. Conservation decisions must begin to account for these integral roles and the attendant economic costs of carnivore species losses.

Currently, the IUCN Species Survival Commission (SSC) action plan series represents perhaps the most comprehensive attempt to establish priorities for individual species or taxa (*84*, *85*). These action plans not only provide assessments of threats but recommend conservation monitoring and actions for each large-carnivore species (table S3). Action plans are compiled by the taxonomically organized SSC's Specialist Groups (for example, the Canid Specialist Group compiles action plans for all canid species). Large carnivores, however, also share common conservation challenges that cross taxonomic boundaries: slow life histories, requirement for extensive and continuous habitat, low densities, complex

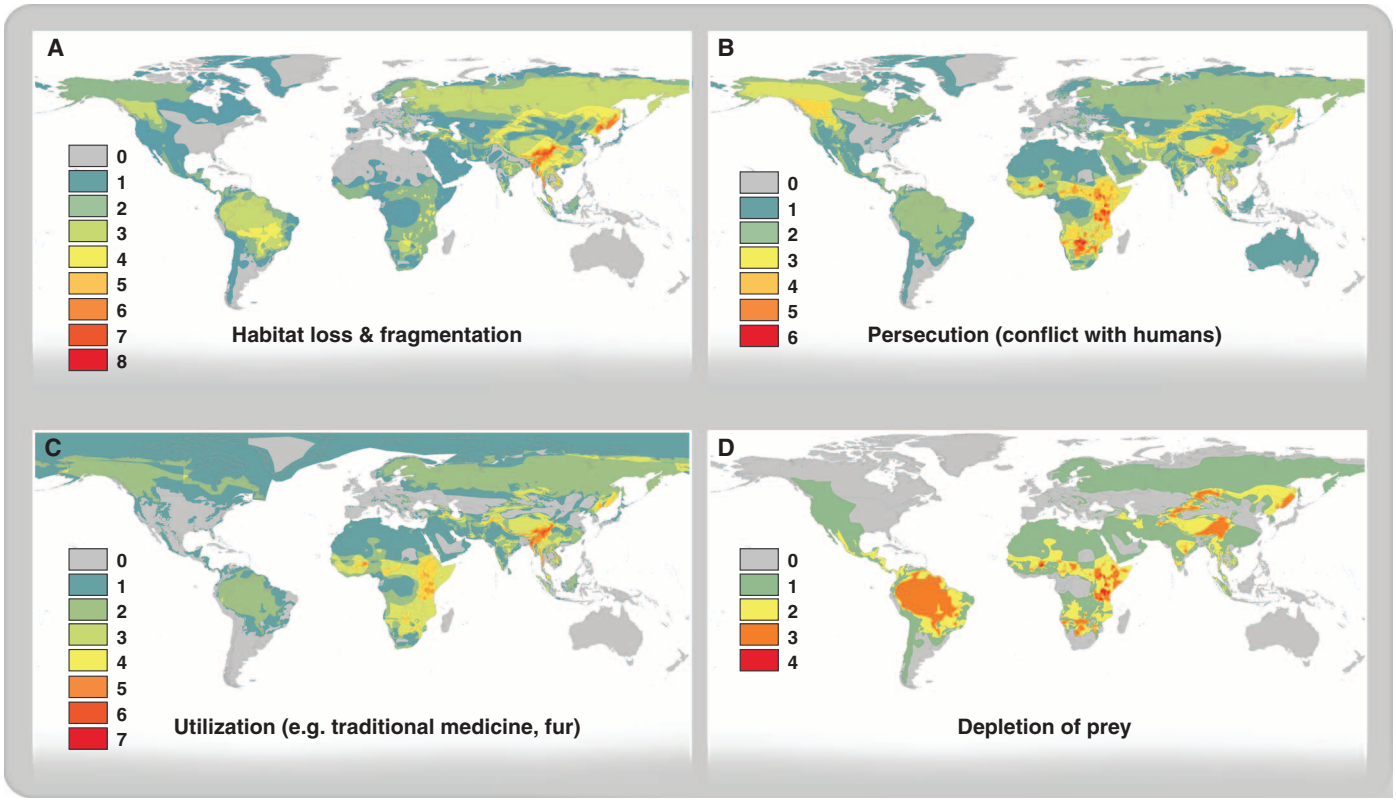


Fig. 6. Maps showing the the spatial overlap for the ranges of large-carnivore species by threat category for habitat loss and fragmentation, persecution, utilization, and depletion of prey. The number of large-carnivore species affected by specific threats is shown in the map legend. Threat catgories include: (**A**) Habitat loss and fragmentation. Forest logging and/or the development of urban, agricultural, and road infrastructure reduces land available to large carnivores and creates barriers between and within populations. (**B**) Persecution. Culling (poison baiting, trapping, and shooting) for the purpose of removal or reduction, in some cases reinforced with a government-subsidized bounty system, in response to real or perceived threat to pastoral and agricultural activities and human lives. (**C**) Utilization. Large carnivores are killed for sport, body parts for traditional medicine, fur, and meat for human consumption, and live animals are captured and sold. (**D**) Depletion of prey. The decline of prey populations due to human hunting, competition with livestock, habitat loss, and other factors reduces the prey base for large carnivores. See table S2 for raw data. Source: IUCN (*91*).

social structures, importance to ecological function, and conflict with humans. These common traits and challenges have given rise to the creation of the Large Carnivore Initiative for Europe, a Specialist Group whose vision is "to maintain and restore, in coexistence with people, viable populations of large carnivores as an integral part of ecosystems and landscapes across Europe" (86). We propose the expansion of this initiative, to establish a Global Large Carnivore Initiative (GLCI).

There is now a substantial body of research demonstrating that, alongside climate change, eliminating large carnivores is one of the most significant anthropogenic impacts on nature (5). Unlike climate change, however, large-carnivore conservation has yet to become a focus of widespread public recognition, possibly because they are rare, remote, and in some cases perceived to be dangerous and a threat to economic prosperity. The formation of a GLCI would be an important step for the advancement of international public recognition of the ecological role and inherent value of large carnivores, and for developing and coordinating strategies for conservation actions that promote human/large-carnivore coexistence. Such an organization could be modeled, in part, after the Global Tiger Initiative, which is coordinating local, national, and international tiger conservation policy across their distribution and was endorsed in 2010 by the leaders of all 13 tiger-range countries, with funding from the World Bank (87). These 13 countries and partners have moved well beyond words to accomplishments on the ground, including securing funding, establishing new tiger reserves, passing laws on tiger conservation, creating high-level commissions to improve wildlife law enforcement, addressing habitat loss and fragmentation, promoting connectivity, and more (87). The success of any future GLCI would probably include these types of authoritative actions, orchestrated by politically bold commitments from nations around the world.

A Final Word

One of the main ecological arguments for the conservation of large carnivores is that they are often capable of exerting strong regulatory effects on ecosystems (5, 15). Although we present evidence that seven of the top carnivore species we reviewed here have such trophic effects, we know much less about the trophic impacts of the 24 other species of large carnivores. More research directed at these species is needed. Also, we need a better understanding of minimum required densities for large carnivores to maintain trophic cascades in different ecosystems, and when and where the strength of those effects is likely to be large versus small. It is also important to understand which human activities are most in conflict with the conservation of specific large carnivores.

A crucial societal challenge is finding creative solutions to maintain viable populations of large carnivores in the face of alternative land uses (7, 59). This is most urgent because global livestock production continues to encroach on land needed by large carnivores, particularly in the developing world, where livestock production tripled between 1980 and 2002 (88). If the world continues to transition into one that replaces top carnivores with livestock and mesopredators, it is incumbent on us to understand more about the ecological effects of such a downward ratcheting on ecosystems. More large and livestock-free protected areas are needed, especially in regions such as southeastern Asia, where large-carnivore richness (Fig. 5) remains the highest in the world. Yet even in these regions, carnivore populations are decreasing (Table 1) and few large reserves exist (fig. S3). More protected areas alone will not be sufficient, so strategies are also needed to facilitate human coexistence with these animals across working landscapes (59).

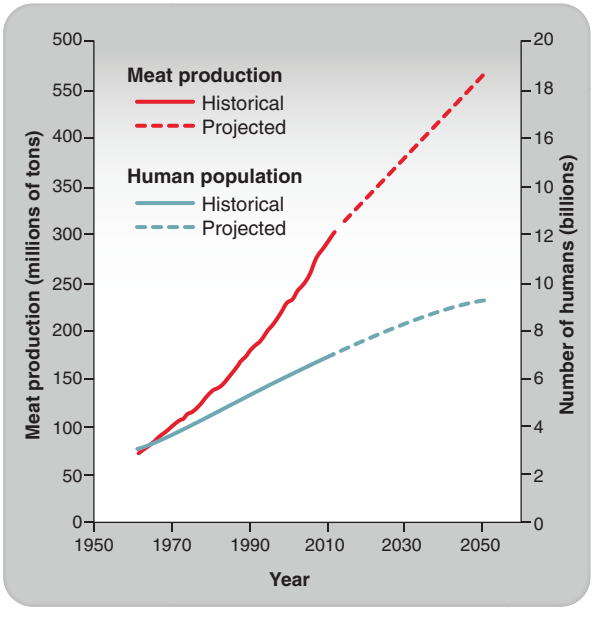


Fig. 7. Historical and projected global human population and global meat production from 1961 to 2050. Source: FAOSTAT (102) and (103) for projected meat production.

Large-carnivore conservation might best be served by a two-pronged approach. First, there is a need for increased recognition of and focus on conserving the full range of the potential effects provided by large carnivores, because this may lead to broader biodiversity, as well as social and economic benefits (5, 15, 89). In areas where large carnivores have been displaced or locally extirpated, their reintroduction may represent a particularly effective approach for passively restoring those ecosystems. However, harnessing the positive effects of large carnivores while (i) minimizing their impacts on humans and (ii) getting humans to adapt to large-carnivore presence, represents a major sociopolitical challenge. Biodiversity conservation programs intended to retain or reintroduce large carnivores must ultimately address both of these challenges if they are to succeed. Second, large-carnivore conservation might also be seen as a moral obligation—the recognition of the intrinsic value of all species. A 40-year history of the field of environmental ethics has both rigorous and systematic rationales for valuing species and nature itself. Large-carnivore conservation, therefore, might benefit greatly from a more formal relationship with practitioners of environmental ethics. It will probably take a change in both human attitudes and actions to avoid imminent large-carnivore extinctions. A future for these carnivore species and their continued effects on planet Earth's ecosystems may depend upon it.

References and Notes

1. L. Hunter, *Carnivores of the World* (Princeton Univ. Press, Princeton, NJ, 2011).
2. G. Ceballos, P. R. Ehrlich, Mammal population losses and the extinction crisis. *Science* **296**, 904–907 (2002). doi: 10.1126/science.1069349; pmid: 11988573
3. J. C. Morrison, W. Sechrest, E. Dinerstein, D. S. Wilcove, J. F. Lamoreux, Persistence of large mammal faunas as indicators of global human impacts. *J. Mammal.* **88**, 1363–1380 (2007). doi: 10.1644/06-MAMM-A-124R2.1
4. L. R. Prugh *et al.*, The rise of the mesopredator. *Bioscience* **59**, 779–791 (2009). doi: 10.1525/bio.2009.59.9.9
5. J. A. Estes *et al.*, Trophic downgrading of planet Earth. *Science* **333**, 301–306 (2011). doi: 10.1126/science.1205106; pmid: 21764740
6. R. L. Beschta, R. J. Ripple, Large predators and trophic cascades in terrestrial ecosystems of the western United States. *Biol. Conserv.* **142**, 2401–2414 (2009). doi: 10.1016/j.biocon.2009.06.015
7. E. G. Ritchie *et al.*, Ecosystem restoration with teeth: What role for predators? *Trends Ecol. Evol.* **27**, 265–271 (2012). doi: 10.1016/j.tree.2012.01.001; pmid: 22321653
8. C. Carbone, G. M. Mace, S. C. Roberts, D. W. Macdonald, Energetic constraints on the diet of terrestrial carnivores. *Nature* **402**, 286–288 (1999). doi: 10.1038/46266; pmid: 10580498
9. M. Cardillo *et al.*, Human population density and extinction risk in the world's carnivores. *PLOS Biol.* **2**, e197 (2004). doi: 10.1371/journal.pbio.0020197; pmid: 15252445
10. M. Cardillo *et al.*, Multiple causes of high extinction risk in large mammal species. *Science* **309**, 1239–1241 (2005). doi: 10.1126/science.1116030; pmid: 16037416
11. C. Carbone, J. L. Gittleman, A common rule for the scaling of carnivore density. *Science* **295**, 2273–2276 (2002). doi: 10.1126/science.1067994; pmid: 11910114
12. A. D. Wallach, C. N. Johnson, E. G. Ritchie, A. J. O'Neill, Predator control promotes invasive dominated ecological

states. *Ecol. Lett.* **13**, 1008–1018 (2010). pmid: 20545732
13. W. J. Ripple, A. J. Wirsing, C. C. Wilmers, M. Letnic, Widespread mesopredator effects after wolf extirpation. *Biol. Conserv.* **160**, 70–79 (2013). doi: 10.1016/j.biocon.2012.12.033
14. E. G. Ritchie, C. N. Johnson, Predator interactions, mesopredator release and biodiversity conservation. *Ecol. Lett.* **12**, 982–998 (2009). doi: 10.1111/j.1461-0248.2009.01347.x; pmid: 19614756
15. O. J. Schmitz, D. Hawlena, G. C. Trussell, Predator control of ecosystem nutrient dynamics. *Ecol. Lett.* **13**, 1199–1209 (2010). doi: 10.1111/j.1461-0248.2010.01511.x; pmid: 20602626
16. E. T. Borer *et al.*, What determines the strength of a trophic cascade? *Ecology* **86**, 528–537 (2005). doi: 10.1890/03-0816
17. J. C. Ray, L. Hunter, J. Zigouris, *Setting Conservation and Research Priorities for Larger African Carnivores* (Report No. 24, Wildlife Conservation Society, New York, 2005).
18. J. S. Brashares, P. R. Prugh, C. J. Stoner, C. W. Epps, in *Trophic Cascades: Predators, Prey, and the Changing Dynamics of Nature*, J. Terborgh, J. A. Estes, Eds. (Island Press, Washington, DC, 2010), pp. 221–240.
19. P. Savolainen, T. Leitner, A. N. Wilton, E. Matisoo-Smith, J. Lundeberg, A detailed picture of the origin of the Australian dingo, obtained from the study of mitochondrial DNA. *Proc. Natl. Acad. Sci. U.S.A.* **101**, 12387–12390 (2004). doi: 10.1073/pnas.0401814101; pmid: 15299143
20. M. Letnic, E. G. Ritchie, C. R. Dickman, Top predators as biodiversity regulators: The dingo *Canis lupus dingo* as a case study. *Biol. Rev. Camb. Philos. Soc.* **87**, 390–413 (2012). doi: 10.1111/j.1469-185X.2011.00203.x; pmid: 22051057
21. M. Letnic, M. S. Crowther, F. Koch, Does a top-predator provide an endangered rodent with refuge from an invasive mesopredator? *Anim. Conserv.* **12**, 302–312 (2009). doi: 10.1111/j.1469-1795.2009.00250.x
22. C. N. Johnson, J. L. Isaac, D. O. Fisher, Rarity of a top predator triggers continent-wide collapse of mammal prey: Dingoes and marsupials in Australia. *Proc. Biol. Sci.* **274**, 341–346 (2007). doi: 10.1098/rspb.2006.3711; pmid: 17164197
23. M. Pasanen-Mortensen, M. Pyykönen, B. Elmhagen, Where lynx prevail, foxes will fail – regulation and limitation of a mesopredator in Eurasia. *Glob. Ecol. Biogeogr.* **22**, 868–877 (2013). doi: 10.1111/geb.12051
24. C. Melis *et al.*, Predation has a greater impact in less productive environments: Variation in roe deer, *Capreolus capreolus*, population density across Europe. *Glob. Ecol. Biogeogr.* **18**, 724–734 (2009). doi: 10.1111/j.1466-8238.2009.00480.x
25. B. Elmhagen, G. Ludwig, S. P. Rushton, P. Helle, H. Lindén, Top predators, mesopredators and their prey: Interference ecosystems along bioclimatic productivity gradients. *J. Anim. Ecol.* **79**, 785–794 (2010). pmid: 20337755
26. O. J. Schmitz, Exploitation in model food chains with mechanistic consumer-resource dynamics. *Theor. Popul. Biol.* **41**, 161–183 (1992). doi: 10.1016/0040-5809(92)90042-R
27. L. Oksanen, T. Oksanen, The logic and realism of the hypothesis of exploitation ecosystems. *Am. Nat.* **155**, 703–723 (2000). doi: 10.1086/303354; pmid: 10805639
28. K. W. Kenyon, The sea otter in the eastern Pacific Ocean. *North Am. Fauna* **68**, 1–352 (1969). doi: 10.3996/nafa.68.0001
29. J. A. Estes, M. T. Tinker, T. M. Williams, D. F. Doak, Killer whale predation on sea otters linking oceanic and nearshore ecosystems. *Science* **282**, 473–476 (1998). doi: 10.1126/science.282.5388.473; pmid: 9774274
30. J. A. Estes, J. F. Palmisano, Sea otters: Their role in structuring nearshore communities. *Science* **185**, 1058–1060 (1974). doi: 10.1126/science.185.4156.1058; pmid: 17738247
31. J. A. Estes, C. H. Peterson, R. Steneck, in *Trophic Cascades: Predators, Prey, and the Changing Dynamics of Nature*, J. Terborgh, J. A. Estes, Eds. (Island Press, Washington, DC, 2010), pp. 37–54.
32. B. Konar, J. A. Estes, The stability of boundary regions between kelp beds and deforested areas. *Ecology* **84**, 174–185 (2003). doi: 10.1890/0012-9658(2003)084[0174:TSOBRB]2.0.CO;2
33. R. O. Peterson, J. A. Vucetich, R. E. Page, A. Chouinard, Temporal and spatial aspects of predator–prey dynamics. *Alces* **39**, 215–232 (2003).
34. W. J. Ripple, R. L. Beschta, Large predators limit herbivore densities in northern forest ecosystems. *Eur. J. Wildl. Res.* **58**, 733–742 (2012). doi: 10.1007/s10344-012-0623-5
35. A. Leopold, L. K. Sowls, D. L. Spencer, A survey of over-populated deer ranges in the United States. *J. Wildl. Manage.* **11**, 162–183 (1947). doi: 10.2307/3795561
36. A. S. Laliberte, W. J. Ripple, Range contractions of North American carnivores and ungulates. *Bioscience* **54**, 123–138 (2004). doi: 10.1641/0006-3568(2004)054[0123:RCONAC]2.0.CO;2
37. S. D. Côté, T. P. Rooney, J. P. Tremblay, C. Dussault, D. M. Waller, Ecological impacts of deer overabundance. *Annu. Rev. Ecol. Evol.* **35**, 113–147 (2004).
38. W. J. Ripple, R. L. Beschta, Linking a cougar decline, trophic cascade, and catastrophic regime shift in Zion National Park. *Biol. Conserv.* **133**, 397–408 (2006). doi: 10.1016/j.biocon.2006.07.002
39. W. J. Ripple, R. L. Beschta, Trophic cascades involving cougar, mule deer, and black oaks in Yosemite National Park. *Biol. Conserv.* **141**, 1249–1256 (2008). doi: 10.1016/j.biocon.2008.02.028
40. J. Terborgh *et al.*, Ecological meltdown in predator-free forest fragments. *Science* **294**, 1923–1926 (2001). doi: 10.1126/science.1064397; pmid: 11729317
41. J. Terborgh, K. Freeley, in *Trophic Cascades: Predators, Prey, and the Changing Dynamics of Nature,* J. Terborgh, J. A. Estes, Eds. (Island Press, Washington, DC, 2010), pp. 125–140.
42. J. Berger, P. B. Stacey, L. Bellis, M. P. Johnson, A mammalian predator-prey imbalance: Grizzly bear and wolf extinction affect avian neotropical migrants. *Ecol. Appl.* **11**, 947–960 (2001).
43. S. M. Barber-Meyer, L. D. Mech, P. J. White, Elk calf survival and mortality following wolf restoration to Yellowstone National Park. *Wildl. Monogr.* **169**, 1–30 (2008).
44. J. Brodie *et al.*, Relative influence of human harvest, carnivores, and weather on adult female elk survival across western North America. *J. Appl. Ecol.* **50**, 295–305 (2013). doi: 10.1111/1365-2664.12044
45. G. A. Polis, D. R. Strong, Food web complexity and community dynamics. *Am. Nat.* **147**, 813–846 (1996). doi: 10.1086/285880
46. J. F. Brodie, A. Giordano, Lack of trophic release with large mammal predators and prey in Borneo. *Biol. Conserv.* **163**, 58–67 (2013). doi: 10.1016/j.biocon.2013.01.003
47. M. Letnic, M. S. Crowther, Patterns in the abundance of kangaroo populations in arid Australia are consistent with the exploitation ecosystems hypothesis. *Oikos* **122**, 761–769 (2013). doi: 10.1111/j.1600-0706.2012.20425.x
48. C. M. Chambers, J. C. Whitehead, A contingent valuation estimate of the benefits of wolves in Minnesota. *Environ. Resour. Econ.* **26**, 249–267 (2003). doi: 10.1023/A:1026356020521
49. L. Richardson, J. Loomis, The total economic value of threatened, endangered and rare species: An updated meta-analysis. *Ecol. Econ.* **68**, 1535–1548 (2009). doi: 10.1016/j.ecolecon.2008.10.016
50. R. Naidoo *et al.*, Effect of diversity of large wildlife species on financial benefits to local communities in northwest Namibia. *Environ. Resour. Econ.* **48**, 321–335 (2011). doi: 10.1007/s10640-010-9412-3
51. O. J. Schmitz *et al.*, Animating the carbon cycle. *Ecosystems* 10.1007/s10021-013-9715-7 (2013). doi: 10.1007/s10021-013-9715-7
52. C. C. Wilmers, J. A. Estes, M. Edwards, K. L. Laidre, B. Konar, Do trophic cascades affect the storage and flux of atmospheric carbon? An analysis for sea otters and kelp forests. *Front. Ecol. Environ* **10**, 409–415 (2012). doi: 10.1890/110176
53. C. C. Wilmers, R. L. Crabtree, D. W. Smith, K. M. Murphy, W. M. Getz, Trophic facilitation by introduced top predators: Gray wolf subsidies to scavengers in Yellowstone National Park. *J. Anim. Ecol.* **72**, 909–916 (2003). doi: 10.1046/j.1365-2656.2003.00766.x
54. R. L. Beschta, R. J. Ripple, The role of large predators in maintaining riparian plant communities and river morphology. *Geomorphology* **157-158**, 88–98 (2012). doi: 10.1016/j.geomorph.2011.04.042
55. D. W. Smith, D. B. Tyers, The history and current status and distribution of beavers in Yellowstone National Park. *Northwest Sci.* **86**, 276–288 (2012). doi: 10.3955/046.086.0404
56. M. Hebblewhite, D. Smith, in *The World of the Wolves: New Perspectives on Ecology, Behaviour, and Management*, M. P. C. Musiani, P. C. Paquet, Eds. (Univ. of Calgary Press, Calgary, Alberta, Canada, 2010), pp. 69–120.
57. M. Hebblewhite *et al.*, Human activity mediates a trophic cascade caused by wolves. *Ecology* **86**, 2135–2144 (2005). doi: 10.1890/04-1269
58. C. Packer, R. D. Holt, P. J. Hudson, K. D. Lafferty, A. P. Dobson, Keeping the herds healthy and alert: Implications of predator control for infectious disease. *Ecol. Lett.* **6**, 797–802 (2003). doi: 10.1046/j.1461-0248.2003.00500.x
59. L. van Bommel, C. N. Johnson, Good dog! Using livestock guardian dogs to protect livestock from predators in Australia's extensive grazing systems. *Wildlife Res.* **39**, 220–229 (2012).
60. T. B. Muhly, M. Musiani, Livestock depredation by wolves and the ranching economy in the northwestern US. *Ecol. Econ.* **68**, 2439–2450 (2009). doi: 10.1016/j.ecolecon.2009.04.008
61. E. Nelson *et al.*, Modeling multiple ecosystem services, biodiversity conservation, commodity production, and tradeoffs at landscape scales. *Front. Ecol. Environ* **7**, 4–11 (2009). doi: 10.1890/080023
62. R. L. Beschta, R. J. Ripple, Mexican wolves, elk, and aspen in Arizona: Is there a trophic cascade? *For. Ecol. Manage.* **260**, 915–922 (2010). doi: 10.1016/j.foreco.2010.06.012
63. W. J. Ripple, R. L. Beschta, J. K. Fortin, C. T. Robbins, Trophic cascades from wolves to grizzly bears in Yellowstone. *J. Anim. Ecol.* **83**, 223–233 (2014). doi: 10.1111/1365-2656.12123; pmid: 24033136
64. T. Levi, C. C. Wilmers, Wolves-coyotes-foxes: A cascade among carnivores. *Ecology* **93**, 921–929 (2012). doi: 10.1890/11-0165.1; pmid: 22690642
65. R. Callan, N. P. Nibbelink, T. P. Rooney, J. E. Wiedenhoeft, A. P. Wydeven, Recolonizing wolves trigger a trophic cascade in Wisconsin (USA). *J. Ecol.* **101**, 837–845 (2013). doi: 10.1111/1365-2745.12095
66. C. Wikenros, thesis, Swedish University of Agricultural Sciences, Uppsala, Sweden (2011).
67. J. Berger, in *Large Carnivores and the Conservation of Biodiversity*, J. Ray, K. H. Redford, R. Steneck, J. Berger, Eds. (Island Press, Washington, DC, 2005), pp. 315–341.
68. W. J. Ripple, R. L. Beschta, Wolves and the ecology of fear: Can predation risk structure ecosystems? *Bioscience* **54**, 755–766 (2004). doi: 10.1641/0006-3568(2004)054[0755:WATEOF]2.0.CO;2
69. L. M. Elbroch, H. U. Wittmer, Nuisance ecology: Do scavenging condors exact foraging costs on pumas in Patagonia? *PLOS ONE* **8**, e53595 (2013). doi: 10.1371/journal.pone.0053595; pmid: 23301093
70. S. H. Faeth, P. S. Warren, E. Shochat, W. A. Marussich, Trophic dynamics in urban communities. *Bioscience* **55**, 399–407 (2005). doi: 10.1641/0006-3568(2005)055[0399:TDIUC]2.0.CO;2
71. P. Smith *et al.*, How much land-based greenhouse gas mitigation can be achieved without compromising food security and environmental goals? *Glob. Change Biol.* **19**, 2285–2302 (2013). doi: 10.1111/gcb.12160; pmid: 23505220
72. W. J. Ripple *et al.*, Ruminants, climate change, and climate policy. *Nat. Clim. Change* **4**, 2–5 (2014).
73. T. P. Dawson, S. T. Jackson, J. I. House, I. C. Prentice, G. M. Mace, Beyond predictions: Biodiversity conservation in a changing climate. *Science* **332**, 53–58 (2011). doi: 10.1126/science.1200303; pmid: 21454781

74. C. Parmesan, G. Yohe, A globally coherent fingerprint of climate change impacts across natural systems. *Nature* **421**, 37–42 (2003). doi: 10.1038/nature01286; pmid: 12511946
75. C. Parmesan, Ecological and evolutionary responses to recent climate change. *Annu. Rev. Ecol. Evol. Syst.* **37**, 637–669 (2006). doi: 10.1146/annurev.ecolsys.37.091305.110100
76. L. J. Gormezano, R. F. Rockwell, What to eat now? Shifts in polar bear diet during the ice-free season in western Hudson Bay. *Ecol. Evol* **3**, 3509–3523 (2013). pmid: 24223286
77. C. C. Wilmers, W. M. Getz, Gray wolves as climate change buffers in Yellowstone. *PLOS Biol.* **3**, e92 (2005). doi: 10.1371/journal.pbio.0030092; pmid: 15757363
78. R. S. Ostfeld, R. D. Holt, Are predators good for your health? Evaluating evidence for top-down regulation of zoonotic disease reservoirs. *Front. Ecol. Environ* **2**, 13–20 (2004). doi: 10.1890/1540-9295(2004)002[0013:APGFYH]2.0.CO;2
79. T. Levi, A. M. Kilpatrick, M. Mangel, C. C. Wilmers, Deer, predators, and the emergence of Lyme disease. *Proc. Natl. Acad. Sci. U.S.A.* **109**, 10942–10947 (2012). doi: 10.1073/pnas.1204536109; pmid: 22711825
80. R. M. Holdo *et al.*, A disease-mediated trophic cascade in the Serengeti and its implications for ecosystem *C. PLOS Biol.* **7**, e1000210 (2009). doi: 10.1371/journal.pbio.1000210; pmid: 19787022
81. J. A. Estes, J. S. Brashares, M. E. Power, Predicting and detecting reciprocity between indirect ecological interactions and evolution. *Am. Nat.* **181**, S76–S99 (2013). doi: 10.1086/668120; pmid: 23598361
82. D. F. Doak *et al.*, Understanding and predicting ecological dynamics: Are major surprises inevitable? *Ecology* **89**, 952–961 (2008). doi: 10.1890/07-0965.1; pmid: 18481520
83. J. L. Gittleman, Carnivore body size: Ecological and taxonomic correlates. *Oecologia* **67**, 540–554 (1985). doi: 10.1007/BF00790026
84. R. Woodroffe, S. Thirgood, A. Rabinowitz, *People and Widlife. Conflict or Co-existence?* (Cambridge Univ. Press, Cambridge, 2005).
85. J. L. Gittleman, S. M. Funk, D. MacDonald, R. K. Wayne, *Carnivore Conservation* (Cambridge Univ. Press, Cambridge, 2001).
86. Large Carnivores Initiative for Europe, http://www.lcie.org/Home.aspx; accessed 18 August 2013.
87. Global Tiger Initiative, http://globaltigerinitiative.org/; accessed 10 October 2013.
88. World Bank, *Minding the Stock: Bringing Public Policy to Bear on Livestock Sector Development* (Report no. 44010–GLB, The World Bank, Washington, DC, 2009).
89. F. Sergio *et al.*, Top predators as conservation tools: Ecological rationale, assumptions and efficacy. *Annu. Rev. Ecol. Syst.* **39**, 1–19 (2008). doi: 10.1146/annurev.ecolsys.39.110707.173545
90. L. D. Mech, L. Boitani, Eds., *Wolf-Prey Relations. Wolves: Behavior, Ecology, and Conservation* (Univ. of Chicago Press, Chicago, 2003).
91. IUCN, The IUCN Red List of Species, Version 2012.2, http://www.iucnredlist.org; downloaded April 2013.
92. J. A. Estes, D. O. Duggins, Sea otters and kelp forests in Alaska: Generality and variation in a community ecological paradigm. *Ecol. Monogr.* **65**, 75–100 (1995). doi: 10.2307/2937159
93. M. Letnic, F. Koch, Are dingoes a trophic regulator in arid Australia? A comparison of mammal communities on either side of the dingo fence. *Austral Ecol.* **35**, 167–175 (2010). doi: 10.1111/j.1442-9993.2009.02022.x
94. W. J. Ripple, R. L. Beschta, Linking wolves to plants: Aldo Leopold on trophic cascades. *Bioscience* **55**, 613–621 (2005). doi: 10.1641/0006-3568(2005)055[0613:LWAPAL]2.0.CO;2
95. R. L. Beschta, W. J. Ripple, Wolves, trophic cascades, and rivers in the Olympic National Park, USA. *Ecohydrology.* **1**, 118–130 (2008). doi: 10.1002/eco.12
96. P. J. White, K. M. Proffitt, T. O. Lemke, Changes in elk distribution and group sizes after wolf restoration. *Am. Midl. Nat.* **167**, 174–187 (2012). doi: 10.1674/0003-0031-167.1.174
97. K. M. Berger, E. M. Gese, Does interference competition with wolves limit the distribution and abundance of coyotes? *J. Anim. Ecol.* **76**, 1075–1085 (2007). doi: 10.1111/j.1365-2656.2007.01287.x pmid: 17922704
98. K. M. Berger, E. M. Gese, J. Berger, Indirect effects and traditional trophic cascades: A test involving wolves, coyotes, and pronghorn. *Ecology* **89**, 818–828 (2008). doi: 10.1890/07-0193.1; pmid: 18459344
99. B. J. Miller, H. J. Harlow, T. S. Harlow, D. Biggins, W. J. Ripple, Trophic cascades linking wolves (*Canis lupus*), coyotes (*Canis latrans*), and small mammals. *Can. J. Zool.* **90**, 70–78 (2012). doi: 10.1139/z11-115
100. W. J. Ripple, R. L. Beschta, Trophic cascades in Yellowstone: The first 15 years after wolf reintroduction. *Biol. Conserv.* **145**, 205–213 (2012). doi: 10.1016/j.biocon.2011.11.005
101. L. M. Baril, A. J. Hansen, R. Renkin, R. Lawrence, Songbird response to increased willow (*Salix* spp.) growth in Yellowstone's northern range. *Ecol. Appl.* **21**, 2283–2296 (2011). doi: 10.1890/10-0169.1; pmid: 21939061
102. F. A. O. Statistical Database, http://faostat.fao.org; accessed 12 August 2013.
103. H. Steinfeld, *et al.*, *Livestock's Long Shadow: Environmental Issues and Options* (Food and Agriculture Organization of the United Nations, Rome, 2006).

Acknowledgments: We thank S. Arbogast, J. Batchelor, A. Cloud, R. Comforto, A. Comstock, T. Newsome, L. Painter, L. Petracca, and C. Wolf for assisting in this project.

Supplementary Materials

www.sciencemag.org/content/343/6167/1241484/suppl/DC1
Figs. S1 to S4
Tables S1 to S3

10.1126/science.1241484

Association of the Autoimmune Disease Scleroderma with an Immunologic Response to Cancer

Christine G. Joseph,[1]* Erika Darrah,[2]* Ami A. Shah,[2]* Andrew D. Skora,[1]* Livia A. Casciola-Rosen,[2] Fredrick M. Wigley,[2] Francesco Boin,[2] Andrea Fava,[2] Chris Thoburn,[3] Isaac Kinde,[1] Yuchen Jiao,[1] Nickolas Papadopoulos,[1] Kenneth W. Kinzler,[1]† Bert Vogelstein,[1]† Antony Rosen[2]†

Autoimmune diseases are thought to be initiated by exposures to foreign antigens that cross-react with endogenous molecules. Scleroderma is an autoimmune connective tissue disease in which patients make antibodies to a limited group of autoantigens, including RPC1, encoded by the *POLR3A* gene. As patients with scleroderma and antibodies against RPC1 are at increased risk for cancer, we hypothesized that the "foreign" antigens in this autoimmune disease are encoded by somatically mutated genes in the patients' incipient cancers. Studying cancers from scleroderma patients, we found genetic alterations of the *POLR3A* locus in six of eight patients with antibodies to RPC1 but not in eight patients without antibodies to RPC1. Analyses of peripheral blood lymphocytes and serum suggested that *POLR3A* mutations triggered cellular immunity and cross-reactive humoral immune responses. These results offer insight into the pathogenesis of scleroderma and provide support for the idea that acquired immunity helps to control naturally occurring cancers.

Systemic sclerosis (scleroderma) is a chronic autoimmune rheumatic disease associated with widespread obliterative vasculopathy and tissue fibrosis (*1*, *2*). A striking feature of this disease is the temporal clustering of scleroderma and cancer that has been observed in patients with autoantibodies to RNA polymerase III subunit (RPC1) but not in patients with autoantibodies to topoisomerase 1 (TOP1) or centromere protein B (CENPB) (*3*). A variety of potential mechanisms could explain the occurrence of cancers in scleroderma patients with autoantibodies to RPC1 (*4*). For example, it is possible that a defective immune system responsible for the autoimmune disease predisposes to neoplasia, and that this effect is more prominent in patients with antibodies to RPC1 than in the other subgroups. Alternatively, it is possible that the cytotoxic, mutagenic therapies used to treat scleroderma patients with more fulminant disease leads to cancer in these individuals; patients with antibodies to RPC1 tend to have more severe disease than those with other antibodies. Finally, the reverse scenario is possible: Cancer might trigger scleroderma in patients with antibodies to RPC1. In particular, we considered whether occasional cancers might harbor missense mutations in the polymerase III polypeptide A (*POLR3A*) gene. If the altered protein encoded by the mutant *POLR3A* gene were recognized by the patient's immune system, an immune response against the tumor could theoretically be generated. If cross-reactive with the normal RPC1 protein, this immune response could in turn injure selected tissues, thereby inducing scleroderma. Experiments to test this hypothesis were performed, as described below.

[1]Ludwig Center, the Howard Hughes Medical Institutions, and the Department of Pathology, Johns Hopkins University School of Medicine, Baltimore, MD 21287, USA. [2]Division of Rheumatology, Johns Hopkins University School of Medicine, Baltimore, MD 21224, USA. [3]Division of Immunology, The Johns Hopkins Sidney Kimmel Comprehensive Cancer Center, Baltimore, MD 21287, USA.

*These authors contributed equally to this work.
†Corresponding author. E-mail: kinzlke@jhmi.edu (K.W.K.); vogelbe@jhmi.edu (B.V.); arosen@jhmi.edu (A.R.)

Genetic Analysis

We began by searching for missense mutations in the *POLR3A* gene in tumors from scleroderma patients. We collected tumor and normal tissue samples from eight scleroderma patients who had autoantibodies to RPC1. We also evaluated eight scleroderma patients who had autoantibodies to TOP1 or to CENPB and developed cancers (Table 1). Five of the patients with antibodies to RPC1 developed cancer before scleroderma (median of 0.4 years before scleroderma onset), whereas the remaining three developed cancer 0.3 to 2.5 years after the onset of scleroderma (Table 1). In contrast, patients with autoantibodies to CENPB or TOP1 who developed cancers only did so a median of 14.2 years after the onset of their scleroderma (Table 1). The characteristics of the 16 scleroderma patients, including tumor type, age of diagnosis of cancer, cancer-scleroderma interval, and autoantibody status, are listed in Table 1; additional clinical information is provided in table S1 and (*5*).

Formalin-fixed, paraffin-embedded tumors from each of the 16 patients were microdissected to enrich for neoplastic cell content, and DNA was purified, blunt-ended, and ligated to adapters suitable for library preparation (*5*). Libraries from peripheral blood cells of each patient were similarly prepared. After amplification of the 32 libraries (16 tumor, 16 matched normal), the polymerase chain reaction (PCR) products were captured by using PCR-generated fragments containing all coding sequences of the *POLR3A*, *TOP1*, and *CENPB* genes (*5*). The captured fragments were evaluated by sequencing on an Illumina instrument, achieving an average coverage of 516 reads per base of the 53 coding exons of the three genes (range: 95- to 2011-fold).

This sequence revealed three somatic, missense variants in *POLR3A* and none in *TOP1* or *CENPB* (Table 1). All three variants were in the patients with autoantibodies to RPC1. The three somatic mutations were each validated by massively parallel sequencing of PCR products generated from the regions surrounding the mutations (*5*). Notably, both the capture approach and the direct-PCR sequencing approach showed that one of the three somatic mutations was decidedly subclonal, that is, was present in only a subset of the neoplastic cells: The fraction of mutant alleles in the lung cancer from patient SCL-2 was only 4.3%, far less than the estimated fraction of neoplastic cells in the microdissected sample used for DNA purification (Table 1) (*5*).

Given the subclonal nature of one of these mutations, we considered whether cells containing these mutations were selected against during tumor growth, perhaps even disappearing as a result of an immune response. The most frequent way to lose a mutant allele in human cancers is through a gross chromosomal event that results in loss of the entire gene and the surrounding chromosomal region (loss of heterozygosity, LOH) (*6*). To search for evidence of such losses, we designed 19 primer pairs that could each amplify a small fragment containing at least one common single-nucleotide polymorphism (SNP) within or surrounding the *POLR3A* gene (table S2). These primer pairs were used in a multiplexed protocol to evaluate all 16 tumors (*5*). Five of the eight tumors from scleroderma patients with autoantibodies to RPC1 exhibited LOH (Table 2). These five tumors included three that did not contain a detectable somatic mutation of *POLR3A* (Table 1). The fraction of neoplastic cells that had undergone LOH could be estimated from the allelic ratios of the SNP data, and in four of the five cases, was subclonal (Table 2). Notably, none of the tumors from patients with antibodies to TOP1 or CENPB exhibited LOH of the region containing *POLR3A* (Table 2). As an additional control, we evaluated 21 SNPs within or surrounding the *TOP1* locus on chromosome 20 (table S2) and found that none of the 16 tumors from scleroderma patients, regardless of autoantibody status, had undergone LOH of this region (table S3).

In summary, six of eight tumors from scleroderma patients with autoantibodies to RPC1 harbored genetic alterations affecting the *POLR3A* locus compared to zero of eight tumors from scleroderma patients without anti-RPC1 antibodies ($P < 0.01$, Fisher exact probability test, two-tailed).

Immunological Analysis

We began the immunological analysis of these patients by addressing whether RPC1 autoanti-

bodies recognized the mutated protein differently from the wild type (WT) form of the protein. Each of the three abnormal forms of the protein found in scleroderma patients was synthesized by in vitro transcription-translation (IVTT) (*5*). Wild-type and patient-matched mutant RPC1 were then subjected to immunoprecipitation analysis with sera from patients or from normal individuals (control sera). In each case, mutant and WT proteins were precipitated similarly by patient serum, but not precipitated by control sera (fig. S1), demonstrating that the autoantibodies do not discriminate between WT and mutant versions of the antigen.

We next constructed a custom peptide microarray to comprehensively identify linear antigenic regions of the RPC1 protein. We synthesized 276 overlapping peptides of 15 amino acids in length, each offset by five amino acids from the previous peptide and covering the entire length of RPC1 (table S4). Peptides that contained each of the three somatic mutations described above were also synthesized (three peptides for each mutant; table S4). These peptides were printed on microarrays and used to assess serum from the three patients with antibodies to RPC1 (SCL-02, SCL-04, and SCL-42) whose cancers harbored *POLR3A* mutations, and four control patients (SCL-200, SCL-201, SCL-202, SCL-203) who had scleroderma and antibodies to RPC1 but who did not have cancers. Each of the seven serum samples displayed reactivity with at least two of the peptides on the array (fig. S2). Notably, there was no reactivity to the mutant peptides or their wild type counterparts (i.e., WT amino acids in place of mutant amino acids) in sera from the patients whose cancers harbored these mutations (or in the other patients).

Having shown that there was no demonstrable humoral immune response specific to the mutant RPC1 proteins, we sought to determine whether there was a cellular immune response directed against the mutants. We first performed high-resolution class I and II human leukocyte antigen (HLA) typing on the three scleroderma patients in whom somatically mutated *POLR3A* genes were identified (table S5). IEDB analysis resource Consensus tools (*7*–*9*) were then used to determine whether peptides containing the specific mutations in individual patients were likely to bind with high affinity to that patient's HLA alleles. In patient SCL-42, both WT and mutant epitopes were predicted to bind with high affinity to both alleles of the patient's class II DR HLA (table S6). This was particularly pronounced for HLA-DR*0701, where the predicted median inhibitory concentration (IC_{50}) was <1 nM for both the mutant (FHVGYFRAVIG**T**LQMI) and WT peptides (FHVGYFRAVIG**I**LQMI; table S6). High-affinity binding of the WT and mutant peptides to this patient's other DR allele (HLA-DR*1001) was also predicted (table S6). In patient SCL-4, the mutant peptide was predicted to bind to this patient's HLA-DR*0101 allele with an affinity of 4 nM, 18-fold higher than the affinity of the WT peptide (table S6). The WT peptide in this region was also predicted to bind, albeit less strongly, to this patient's second allele (26 nM to HLA-DR*1101). Neither WT nor mutant peptides were predicted to bind with high affinity to the class II molecules of patient SCL-2 (table S6). The algorithms also predicted binding of patient-matched WT and mutant peptides to a single HLA class I allele in each patient, though the binding affinities were only moderate (27 to 78 nM, table S6).

CD4 cells are known to recognize peptides presented by HLA class II alleles and play central roles in both tumor immunity and autoimmunity (*10*, *11*). Given this knowledge and our finding that the predicted affinities for class II

Table 1. Selected clinical and genetic characteristics of the scleroderma patients evaluated in this study. NA, not applicable.

Patient no.	Scleroderma duration at diagnosis of cancer (years)	Auto-antibodies to:	Age at diagnosis of cancer	Cancer type	Cancer subtype	Cancer stage	*POLR3A* mutation (% mutant alleles)	*POLR3A* mutation (genomic position on chr. 10)	*POLR3A* mutation (amino acid change)	*POLR3A* loss of heterozygosity (LOH)
SCL-1	−0.2	RPC1	51	Breast cancer	Invasive ductal	IA	ND†	NA	NA	LOH
SCL-2	−0.1	RPC1	42.3	Lung cancer	Small cell carcinoma	I or II*	26%	79414962C>G	p.E1072Q	LOH
SCL-4	−0.4	RPC1	44	Ovarian cancer	Adenocarcinoma	IIIC	4.3%	79407320C>G	p.K1365N	No LOH
SCL-13	0.3	RPC1	51.1	Breast cancer	Invasive ductal	IIB	No mutation detected	NA	NA	LOH
SCL-35	−2	RPC1	50.9	Breast cancer	Ductal carcinoma in situ	0	No mutation detected	NA	NA	No LOH
SCL-42	1.5	RPC1	47.5	Breast cancer	Invasive ductal	IIA	31%	79455393A>G	p.I104T	LOH
SCL-81	−4.2	RPC1	54.6	Colorectal cancer	Adenocarcinoma	III	No mutation detected	NA	NA	LOH
SCL-82	2.5	RPC1	51.1	Breast cancer	Ductal carcinoma in situ	0	No mutation detected	NA	NA	No LOH
SCL-5	9.2	TOP1	74.6	Lung cancer	Adenocarcinoma	IB	No mutation detected	NA	NA	No LOH
SCL-8	0.4	TOP1	65.1	Breast cancer	Infiltrating lobular	IIIA	No mutation detected	NA	NA	No LOH
SCL-11	13.4	TOP1	55.7	Breast cancer	Infiltrating lobular	IIIC	No mutation detected	NA	NA	No LOH
SCL-12	34	CENPB	68.6	Anal cancer	Squamous cell carcinoma	I	No mutation detected	NA	NA	Uninformative‡
SCL-19	34	TOP1	74.1	Breast cancer	Ductal carcinoma in situ	0	No mutation detected	NA	NA	No LOH
SCL-24	36.9	CENPB	64.2	B cell lymphoma	Extranodal, mantle cell	IV	No mutation detected	NA	NA	No LOH
SCL-32	−2.5	CENPB	43.1	Breast cancer	Invasive ductal	I	No mutation detected	NA	NA	Uninformative‡
SCL-85	15	TOP1	52.1	Breast cancer	Invasive ductal	IIA	No mutation detected	NA	NA	No LOH

*Patient records indicate only that the disease was localized. †No mutation detected. ‡"Uninformative" indicates that none of the evaluated SNPs were heterozygous in the normal cells of the patient.

peptides were much higher than for class I peptides, we searched for CD4 T cells recognizing the predicted peptides in peripheral blood mononuclear cells (PBMCs) from patients whose tumors contained *POLR3A* mutations. CD154 expression at 18 hours after peptide stimulation was used to identify peptide-activated $CD4^+$ T cells (*12*, *13*). In patient SCL-4, CD4 T cell activation was observed in response to the patient-matched mutant peptide but not to the WT peptide (Fig. 1, A and C). Moreover, no CD4 T cell responses to these peptides were observed in T cells from a healthy control matched with SCL-4 at HLA-DR*1101 (Fig. 1A). Thus, the experimental data confirmed the in silico predictions.

The experimental data also confirmed the predicted reactivity of T cells from patient SCL-42, with a twofold increase in the number of $CD4^+$ $CD154^+$ T cells in response to both the WT and mutant SCL-42 peptides over control conditions. The frequency of responding cells was about a log lower in SCL-42 compared to SCL-4, with ~1:5000 CD4 T cells responding (Fig. 1, B and C). The CD4 T cell responses to WT and mutant SCL-42 peptides were abolished by treatment with anti–HLA-DR antibodies but not by an isotype control (fig. S3). As in patient SCL-4, no response to RPC1 peptides was observed in T cells from a healthy control matched with SCL-42 at HLA-DR*0701 (Fig. 1B). As predicted by the in silico binding algorithms (table S6), patient SCL-2 did not respond to either WT or mutant peptides, but did express CD154 in response to the positive control stimulus, demonstrating that her cells were immune competent (fig. S5).

These data document the existence of CD4 T cells reactive with peptides containing the RPC1 mutations in two of the three patients studied. The reactivity was patient, peptide, and HLA-type specific. The frequencies of mutant peptide–reactive CD4 T cells observed in these scleroderma patients (~1:600 to ~1:5000, Fig. 1) were in the range observed for antigen-specific $CD4^+$ T cells observed in other autoimmune processes (*14*).

SCL-4 responded only to the mutant peptide, whereas patient SCL-42 responded to the mutant as well as to the WT peptides (Fig. 1C). It was possible that the CD4 T cells that were activated in response to the mutant peptide in SCL-42 were the same as those responding to the WT peptide. To evaluate this issue, we performed T cell receptor (TCR) spectratyping of T cells stimulated by either WT or mutant peptides. Out of the 22 Vβ families analyzed, 12 displayed a similar distribution of their CDR3 lengths in response to WT and mutant peptides, including Vβ8, Vβ17, and Vβ20 (Fig. 2, A to C). In contrast, significant differences in the distribution of CDR3 lengths were observed for several other Vβs (Vβ3, Vβ5, Vβ7, Vβ12, Vβ16, and Vβ24) (Fig. 2, D to F). For some Vβs, marked skewing in CDR3 lengths was observed, with >25% of TCRs from cells treated with either the mutant or the WT form of the peptide represented by a single CDR3 length. These data suggested that the T cells responding to the mutant peptides were not, in general, those responding to the WT peptides.

To characterize the TCRs in more detail, we determined the sequence of the CDR3 regions in the Vβ7, Vβ12, and Vβ24 PCR products (*5*). Two notable findings were revealed by massively parallel sequencing of these regions. First, the sequences of the dominant TCRs generated from T cells stimulated with the WT peptide were completely distinct from those stimulated by the mutant peptide (Table 3). In five of six dominant TCRs identified by sequencing, the WT- and mutant-specific CDR3 sequences were precisely the lengths predicted by the spectratype analysis (Table 3). The sequencing results therefore strongly supported the conclusion from spectratyping that the mutant and WT peptides had stimulated many distinct T cell clones. Second,

Table 2. Allelic ratios of SNP loci within and closely surrounding the *POLR3A* gene. NI: Noninformative; i.e., the SNP was not heterozygous in the normal cells of the patient (see supplementary materials and methods).

		Patients with RPC-1 antibodies									Patients without RPC-1 antibodies						
Chr. 10 position	SNP ID	SCL-1	SCL-2	SCL-4	SCL-13	SCL-35	SCL-42	SCL-81	SCL-82	SCL-5	SCL-8	SCL-11	SCL-12	SCL-19	SCL-24	SCL-32	SCL-85
79,213,314	rs1054608	**55%**	**88%**	102%	NI	NI	**68%**	**83%**	NI	NI	NI	99%	NI	99%	103%	NI	NI
79,222,098	rs2165046	**52%**	**88%**	99%	NI	NI	**69%**	**76%**	NI	NI	NI	99%	NI	94%	102%	NI	NI
79,222,113	rs1058203	NI	NI	NI	NI	100%	NI	**78%**	NI	NI	102%	NI	NI	NI	99%	NI	99%
79,222,157	rs1058202	**50%**	NI	102%	NI	NI	NI	NI	NI	NI	102%	NI	NI	NI	NI	NI	97%
79,230,809	rs10762763	**53%**	**86%**	103%	NI	NI	**69%**	**85%**	NI	NI	NI	102%	NI	102%	104%	NI	NI
79,235,661	rs2289311	**55%**	**91%**	103%	NI	NI	**66%**	**88%**	NI	97%	NI	104%	NI	100%	103%	NI	NI
79,260,691	rs10824579	NI	**93%**	97%	NI	NI	**70%**	**73%**	NI	NI	NI	96%	NI	97%	103%	NI	NI
79,323,400	rs1248888	**80%**	NI	NI	NI	102%	NI	**87%**	NI	101%	102%	NI	NI	NI	101%	NI	96%
79,406,970	rs2241547	**78%**	NI	NI	NI	104%	NI	NI	NI	NI	NI	NI	NI	NI	NI	NI	102%
79,415,741	rs12241228	NI	NI	NI	NI	NI	NI	NI	NI	100%	NI	NI	NI	NI	NI	NI	NI
79,415,795	rs3815891	**70%**	NI	NI	NI	NI	NI	NI	NI	103%	NI	NI	NI	NI	NI	NI	102%
79,419,810	rs7094028	**79%**	NI	NI	NI	NI	NI	NI	NI	98%	NI	NI	NI	NI	NI	NI	104%
79,424,105	rs2818827	**75%**	NI	104%	NI	100%	NI	NI	NI	NI	102%	NI	NI	NI	NI	NI	102%
79,424,140	rs12267816	NI	NI	NI	NI	NI	NI	NI	NI	104%	NI	NI	NI	NI	NI	NI	NI
79,442,860	rs2493568	**76%**	NI	96%	**44%**	101%	NI	**91%**	NI	NI	103%	NI	NI	NI	NI	NI	101%
79,514,037	rs67287610	NI	NI	NI	**45%**	100%	NI	95%	NI	99%	NI	NI	NI	NI	NI	NI	NI
79,514,072	rs4979801	**85%**	NI	NI	**46%**	101%	NI	95%	NI	NI	96%	NI	NI	NI	NI	NI	104%
79,546,360	rs2253909	NI	NI	94%	**40%**	102%	NI	**76%**	NI	102%	99%	NI	NI	NI	NI	NI	NI
79,549,686	rs2253513	**78%**	NI	102%	**41%**	102%	NI	**88%**	NI	NI	100%	NI	NI	NI	NI	NI	**90%**
79,573,735	rs2114907	**82%**	NI	103%	**43%**	104%	NI	**78%**	96%	NI	104%	100%	NI	NI	NI	NI	NI
79,615,946	rs1249134	**86%**	**90%**	98%	**44%**	102%	NI	**85%**	NI	NI	NI	99%	NI	104%	NI	NI	NI
79,618,728	rs1249126	**75%**	**91%**	103%	**46%**	101%	NI	**74%**	NI	NI	NI	NI	NI	98%	NI	NI	NI
79,654,802	rs2434123	NI	NI	NI	**46%**	NI	**67%**	NI	102%	NI	104%	NI	NI	NI	NI	NI	NI
Allelic ratio average* (%)		71%	88%	99%	44%	101%	69%	83%	99%	99%	101%	100%	NI	99%	102%	NI	100%
Allelic ratio SD (%)		13%	4%	6%	2%	4%	3%	7%	4%	5%	3%	2%	NI	3%	2%	NI	4%

*Entries represent the allelic ratios of the indicated SNPs. The values in normal individuals were 100% ± 3.10%. Allelic ratios less than 2 SDs from the mean (i.e., <94%) are highlighted in bold. A tumor was considered to exhibit LOH if more than 3/4 of the informative SNPs exhibited alleic ratios <94%.

there was a high degree of redundancy among the amino acid sequences—but not the nucleotide sequences—of the TCRs identified in this experiment. For example, we identified 17 different nucleotide sequences (represented by 2066 clusters on the sequencing instrument) that encoded the identical CDR3 amino acid sequence in T cells stimulated by the mutant peptide (Table 3). As T cells, unlike B cells, do not undergo continued evolution once a successful V(D)J rearrangement has occurred (*15*, *16*), these data document the existence of multiple, independent T cell clones responding, and presumably binding, to the same mutant peptide–HLA complex.

Finally, we developed CDR3-specific Taqman assays to verify that distinct populations of WT and mutant-specific T cells were present in the peripheral blood of SCL-42 before the short-term cultures used in the experiments described above. The Vβ24 TCRs were chosen for this experiment because their CDR3 sequences were the most abundant in the sequencing analysis and were each encoded by multiple distinct nucleotide sequences (Table 3). The TCRs expected to bind the mutant and WT peptides were detected in uncultured SCL-42 PBMCs (fig. S4). Neither TCR was detectable in the PMBCs of patient SCL-4, used as a control.

Discussion

A subset of patients with scleroderma and other autoimmune rheumatic diseases manifest cancer around the time of autoimmune disease diagnosis, suggesting that the two processes might be linked mechanistically (*3*, *4*, *17*). In scleroderma, this temporal clustering of scleroderma and cancer appears limited to the subgroup of patients with antibodies to RPC1 (*3*). In the current work, we demonstrated that the *POLR3A* locus is genetically altered (by somatic mutation or LOH) in six of eight cancers of patients with antibodies to RPC1, but not in cancers from scleroderma patients with other autoantibody specificities. Moreover, T cells reactive with the mutant forms of RPC1 could be identified in the peripheral blood of two of the three patients tested. These T cells did not simply cross-react with the WT form of the peptides, because T cells from patient SCL-4 were not stimulated by the WT form, and the sequences of the TCRs conferring responsiveness to the WT and mutant peptides in SCL-42 were largely unrelated.

These genetic and immunologic findings suggest mutation in *POLR3A* as the initiator of the immune response to RPC1 in an important subset of scleroderma patients. The alternative to this conclusion—that the onset of scleroderma and the cancer genomes of these patients were unrelated and that the missense mutations and T cell responses directed against the same mutations were coincidental—is unlikely given the rarity of *POLR3A* mutations in cancer in general (0.7%, $P < 10^{-20}$) (*18*) and the absence of alterations at this locus in scleroderma patients without antibodies to RPC ($P < 0.01$). Additionally, in patient SCL-42, there were multiple different nucleotide sequences encoding TCRs with the identical amino acid sequence in T cells stimulated by the mutant peptide (Table 3). This provides strong support for the conclusion that the mutant *POLR3A* gene product acted as an immunogen initiating the anti-RPC1 immune response in vivo.

Antibodies from all patients with *POLR3A* mutations recognized WT and mutant versions of RPC1 to a similar extent, and no antibodies directed specifically against the WT versus mutant peptides could be demonstrated. This suggests that the humoral response does not directly target the area of the mutation or discriminate between mutant and WT versions of RPC1. The inability of autoantibodies to discriminate between the mutant and WT forms of the antigen is consistent with previous studies showing that a cross-reactive humoral response is typical when a novel form of an antigen initially stimulates T cells that specifically recognize the modified antigen (*19*, *20*). The antibody cross-reactivity might contribute to B cell–mediated diversification of autoimmunity, spreading T cell responses to the WT autoantigen (*21*, *22*).

Our data therefore suggest that the "foreign" antigen triggering the autoimmune response in scleroderma patients is actually a tumor antigen. This complements previous observations indicating that cancers can elicit immune responses. Some cases of paraneoplastic syndrome are

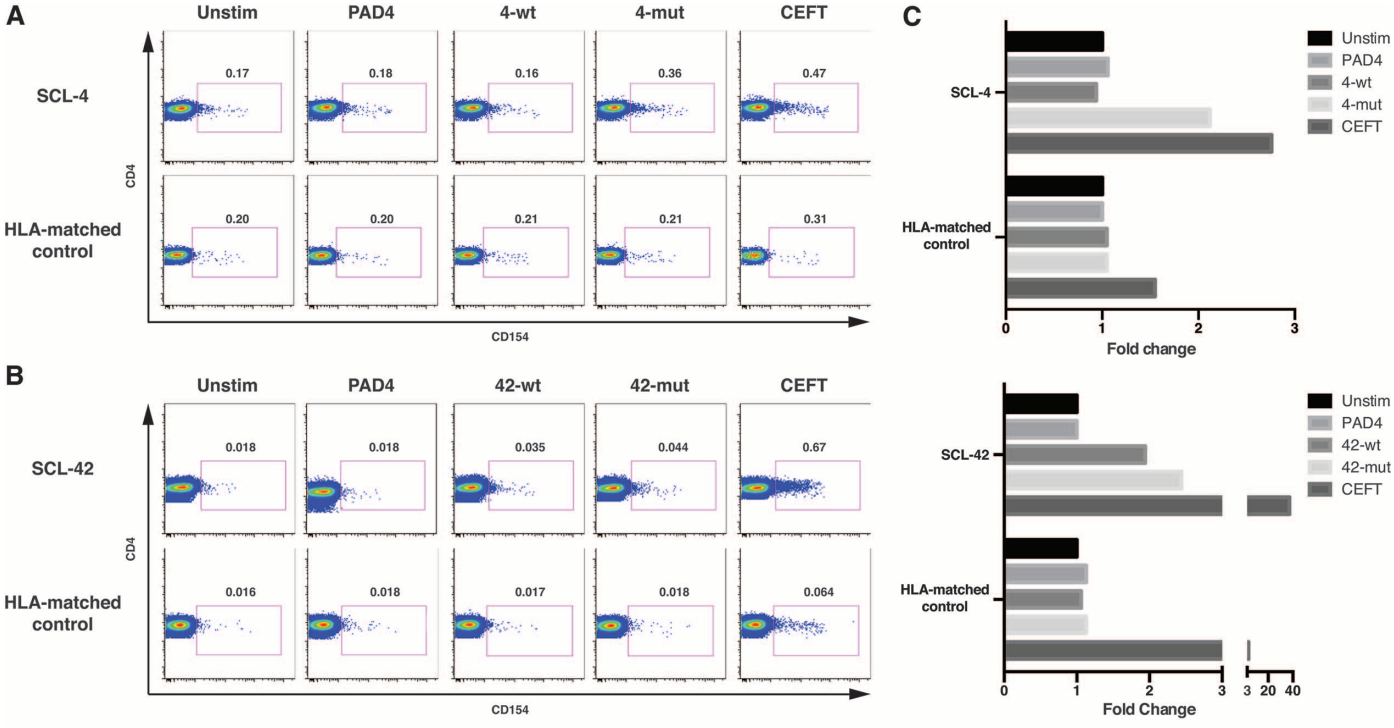


Fig. 1. Mutant and WT peptide-specific CD4$^+$ T cells in patients SCL-4 and SCL-42. CD154 expression on CD4$^+$ T cells was assayed after stimulation (18 hours) with patient-specific WT or mutant RPC1 peptides, PAD4 peptide (negative control), or a pool of peptides from infectious agent antigens (CEFT, positive control). Healthy donors matched for one HLA-DR allele were used as controls. Experiments on SCL-4 (**A**) and SCL-42 (**B**) were repeated on separate blood draws, three and two times, respectively, with similar results. Gate frequencies are expressed as percentage of CD4$^+$ T cells. (**C**) Frequency of peptide-reactive CD4 T cells expressed as fold change over CD154$^+$ CD4 T cells in the unstimulated negative control.

caused by autoimmunity to proteins expressed in tumors (*23*); these responses are directed exclusively to the normal protein, and there is no evidence that the gene(s) are mutated in the tumors. Conversely, mutant genes in human tumors can elicit an immune response against the mutant gene product (*24*–*26*); these immune responses have not been shown to elicit a cross-reactive response to the normal gene product that could result in autoimmunity. Finally, an in vitro–generated protein containing multiple (but not single) mutations, when injected into mice, can elicit a broad, cross-reactive immune response against the normal protein that results in autoimmunity (*27*). In these mice, tumor cells expressing only the WT protein can also be targeted by the subsequent immune response. Our results show that an analogous situation appears to occur in humans when a single, strongly immunogenic epitope is created by somatic mutation in a patient with an appropriate MHC type. However, the generation of an autoreactive immune response alone may not be sufficient to generate the self-sustaining tissue injury seen in scleroderma, and additional factors (genetic, environmental, or target tissue–specific) may be required (*28*).

Our cohort included cancer patients without anti-RPC1 antibodies (Table 1). Although the interval between scleroderma and cancer onset in these patients was long (median of 14.2 years), two patients (SCL-8 and SCL-32) had relatively short intervals. We did not identify genetic alterations of *TOPO1 or CENPB* in these two patients. Whether their cancers were adventitious, related to therapy, or due to mutations in genes encoding homologs of *TOPO1* or *CENPB* or proteins that interact with them is unknown but are intriguing hypotheses for future study. Similar factors could also explain the absence of genetic alterations of *POLR3A* in two of the eight patients with antibodies to RPC1.

The relatively low fraction of neoplastic cells with genetic alterations in the cancers from some of these patients (Tables 1 and 2) suggests that immunoediting of the cancer had occurred, with cells containing these mutations selected against during tumor growth (*29*). The emergence of cancer in RPC1-positive scleroderma patients

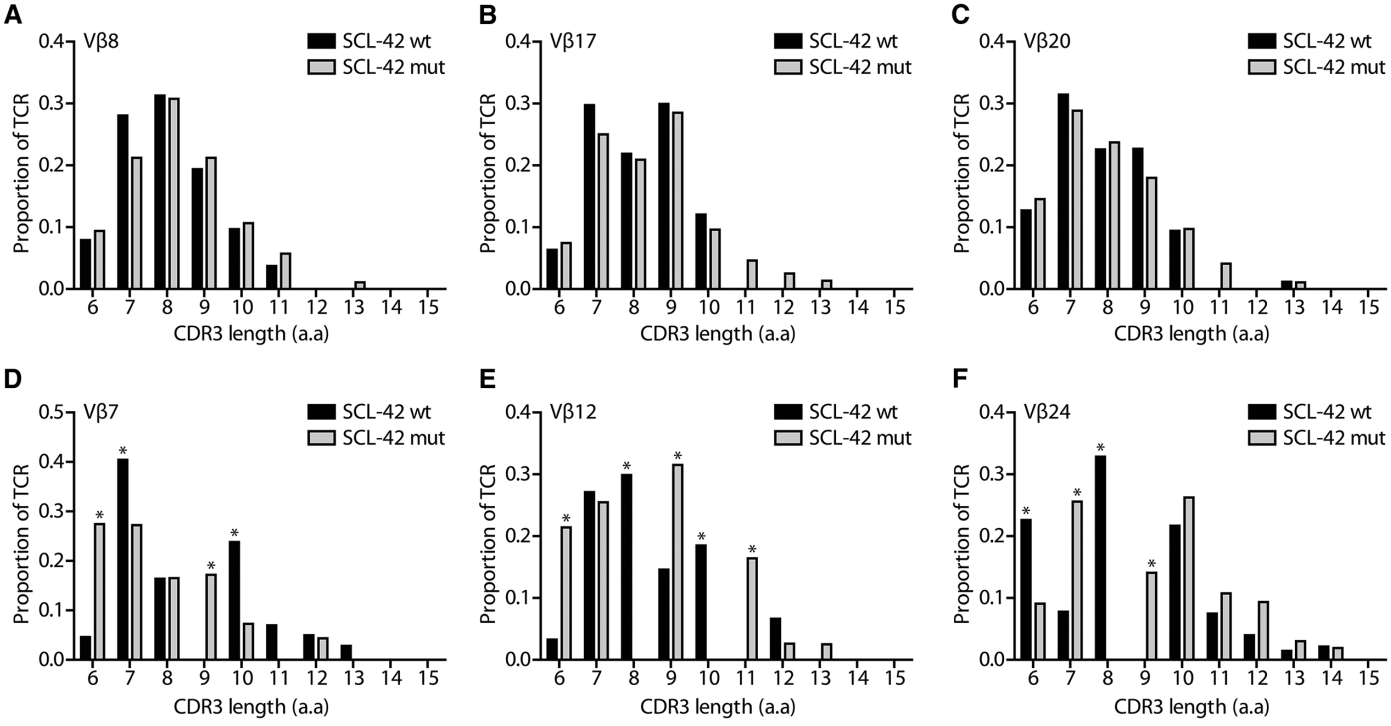


Fig. 2. Vβ-family usage and CDR3 length in patient SCL-42 PBMCs stimulated with WT or mutant peptides. SCL-42 PBMCs were stimulated for 6 days with patient-specific mutant (gray bars) and corresponding WT (black bars) RPC1 peptides. No appreciable differences in TCR diversity were observed in Vβ8 (**A**), Vβ17 (**B**), and Vβ20 (**C**) TCR families. Skewing of the CDR3 length distribution in Vβ7 (**D**), Vβ12 (**E**), and Vβ24 (**F**) TCR families was observed, and CDR3 lengths that differed by >15% between WT and mutant stimulated PBMCs are indicated (*). CDR3 length is expressed in amino acids (a.a).

Table 3. Dominant TCR sequences identified by massively parallel sequencing after stimulation with WT or mutant peptides. Abbreviations for the amino acid residues are as follows: A, Ala; C, Cys; D, Asp; E, Glu; F, Phe; G, Gly; H, His; I, Ile; K, Lys; L, Leu; M, Met; N, Asn; P, Pro; Q, Gln; R, Arg; S, Ser; T, Thr; V, Val; W, Trp; and Y, Tyr.

Vβ	CDR3			Jβ	CDR3 length (amino acids)	Total no. of sequences	No. of unique sequences
			SCL-42 WT-stimulated TCRs				
Vβ7	LCASS	PNELGQGSAF	FGQGT	Jβ1.1	10*	160	1
Vβ12	FCASS	DEVNTEAF	FGQGT	Jβ1.1	8*	18	1
Vβ24	LCATS	TGTVMNTEAF	FGQGT	Jβ1.1	10	1332	6
			SCL-42 mutant-stimulated TCRs				
Vβ7	LCASS	ESWTDYGYT	FGSGT	Jβ1.2	9*	97	1
Vβ12	FCASS	DGGTRHEQF	FGPGT	Jβ2.1	9*	160	2
Vβ24	LCATS	RDTVNQPQH	FGDGT	Jβ1.5	9*	2066	17

*Corresponds to the expected length based on TCR spectratyping.

in much smaller volumes and, in some cases, over subwavelength thicknesses, ensuring controlled manipulation and processing of the incoming signal.

We introduce two approaches to computational metamaterials: (i) a metasurface (MS) approach, in which thin planar metamaterial blocks perform mathematical operations in the spatial Fourier domain and (ii) a Green's function (GF) approach, in which multilayered metamaterial slabs realize a desired GF (i.e., spatial impulse response) at the output, allowing the synthesis of mathematical operations of interest. For simplicity, we focus on metamaterials that realize linear, shift-invariant operations on transverse spatial variables, assuming $\exp(-i\omega t)$ monochromatic signals. Without loss of generality, we assume two-dimensional scenarios in which wave signals and the metamaterial parameters depend only on the longitudinal direction of propagation x and one transverse coordinate y.

We base our first (MS) approach on the fact that the linear convolution $g(y) = \int f(u)G(y-u)du$ between an arbitrary field distribution $f(y)$ and the GF $G(y)$ associated with the operator of choice may be expressed in the spatial Fourier space as $\tilde{g}(k_y) = \tilde{G}(k_y)\tilde{f}(k_y)$, where the tilde indicates Fourier transform. In this approach, our metamaterial system consists of three cascaded subblocks: (i) a Fourier transform subblock, (ii) a suitably tailored MS spatial filter that applies the $\tilde{G}(k_y)$ operation in the Fourier domain, and (iii) an inverse Fourier transform subblock (Fig. 2A). For the first subblock, we consider a two-dimensional graded-index (GRIN) dielectric slab with permeability $\mu = \mu_0$ and a parabolic variation of permittivity

$$\varepsilon(y) = \varepsilon_c \left[1 - \left(\frac{\pi}{2L_g}\right)^2 y^2\right] \qquad (1)$$

where ε_c is the permittivity at the central plane of the GRIN and L_g is the characteristic length (*24*). In Fig. 2A, GRIN(+) indicates a conventional GRIN, with (+) referring to permittivity and permeability being positive. In the paraxial approximation, the GRIN(+) slab operates as a Fourier transformer at the "focal" length L_g along the direction of propagation (*24*). For the inverse Fourier transform [subblock GRIN(–)], we use an ideal GRIN structure with negative parameters: permeability $\mu = -\mu_0$ and permittivity $\varepsilon = -\varepsilon(y)$. Following the concept of complementary materials (*25*), the GRIN(–) has the inverse functionality of the GRIN(+); that is, it acts as an inverse Fourier transformer.

The metastructure screen is designed using two different approaches (insets in Fig. 2A): (i) a "conceptual" thin MS with volumetric parameters $\varepsilon_{ms}(y)/\varepsilon_0 = \mu_{ms}(y)/\mu_0$ (left inset) and (ii) a realistic three-layered thin metamaterial

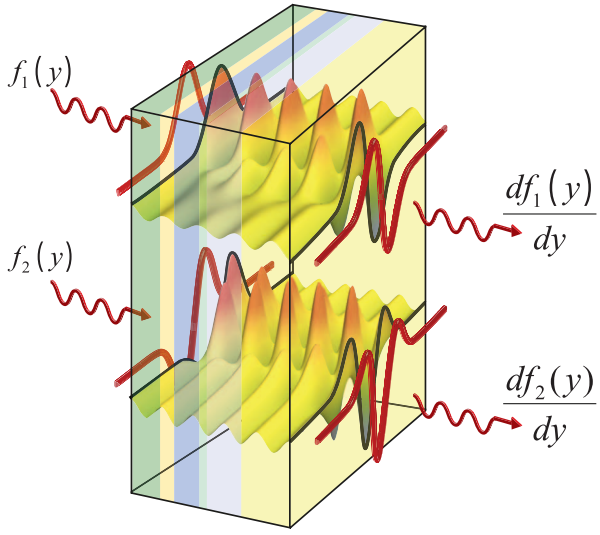


Fig. 1. Wave-based metamaterial computing. A conceptual sketch of a suitably designed metamaterial block that may perform a desired mathematical operation on arbitrary wave signals as they propagate through it.

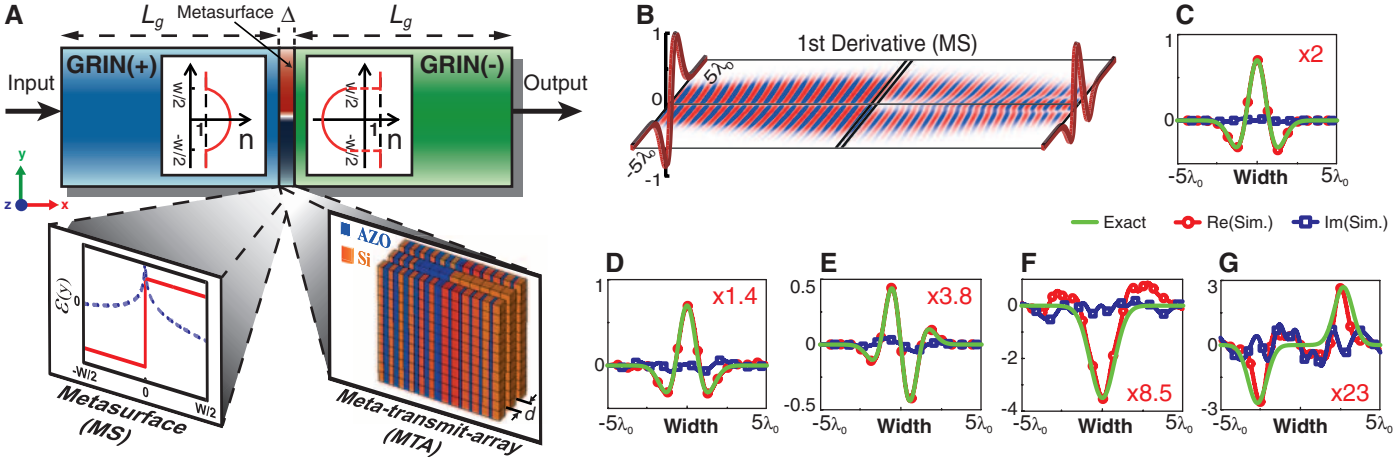


Fig. 2. Metamaterial computing using metasurfaces. (**A**) A thin, properly designed metastructure screen with thickness $\Delta = \lambda_0/3$ and width $W \approx 10\lambda_0$, sandwiched between two GRIN structures with positive and negative parameters, can perform mathematical operations in the Fourier domain. The GRIN(+) and GRIN(–), each with length $L_g \approx 12\lambda_0$, act as Fourier and inverse Fourier transformers. Two designs are proposed for the middle metastructure: a thin MS formed by a single layer with prescribed permittivity and permeability [left inset, with real (red) and imaginary (blue) parts of material parameters] and a realistic meta-transmit-array (MTA) formed by three sublayers made of two alternating materials (here, Si and AZO) with properly prescribed inhomogeneous distribution of their volume filling fractions, and with required loss to impart the desired attenuation (right inset) (*28*). This system forms a computational metamaterial unit that can perform mathematical operations of choice on the input function as the wave propagates through it. (**B**) Perspective view of the input function is shown at left, along with a snapshot of our simulation results for the *z*-component of the electric field throughout the metamaterial system functioning as first differentiator using MS. The output profile is shown at right. (**C** to **G**) Simulation results [real (red) and imaginary (blue) parts] at the output of our computational metastructures for (C) first differentiation, (E) second differentiation, (F) integration, and (G) convolution operators, all using MS; and (D) first differentiation using MTA [with both GRIN sections being GRIN(+)]. All simulated outputs are compared with the expected analytical results (green). For easy comparison, output results in each panel are multiplied by a constant factor (shown in each plot) and proper phase adjustments (*28*) are applied: (C) 8°, (D) –15°, (E) 0°, (F) –8°, (G) 18°.

based on an appropriate alternation of two materials—in this case, aluminum-doped zinc oxide (AZO) (*26*) and silicon (Si)—with different levels of loss (right inset). Our "meta-transmit-array" (MTA) design is inspired by (*27*) and is extended to the present case (*28*) so as to control both phase and magnitude of the transmitted wave according to the desired local transfer function $\tilde{G}(k_y)$ while minimizing reflections. We apply these concepts to realize some fundamental mathematical operators.

First-order derivative: $g(y) \propto df(y)/dy$. In this case, $\tilde{G}(k_y) \propto (ik_y)$ and we first consider a transversely inhomogeneous MS with thickness $\Delta < \lambda_0$ (where λ_0 is the free-space wavelength), in which the transverse coordinate y plays the role of k_y. The relative permittivity and permeability of such a MS (laterally limited to $|y| \le W/2$), required to achieve the normalized transfer function proportional to $iy/(W/2)$, are (*28*)

$$\frac{\varepsilon_{ms}(y)}{\varepsilon_0} = \frac{\mu_{ms}(y)}{\mu_0} = i\left(\frac{\lambda_0}{2\pi\Delta}\right)\ln\left(\frac{-iW}{2y}\right) \quad (2)$$

Once this subblock is sandwiched between a GRIN(+) and a GRIN(–), each one with length L_g, we obtain a first-differentiator metamaterial system. Figure 2B shows our numerical simulation for the input function $f(y) = ay\exp(-y^2/b)$ with $a = 0.7\ \mu m^{-1} = 2.1\lambda_0^{-1}$ and $b = 10\ \mu m^2 = \lambda_0^2/0.9$, used to test all the operators in Fig. 2. In this set of simulations, we assume $\lambda_0 = 3\ \mu m$, $W = 29.75\ \mu m \approx 10\lambda_0$, $L_g = 35\ \mu m \approx 12\lambda_0$, $\varepsilon_c = 2.01\varepsilon_0$, and $\Delta = 1\ \mu m = \lambda_0/3$. Although this design principle can be applied to any wavelength, here we have chosen to operate at infrared frequencies, which are of interest for various applications; this allows us to use realistic CMOS (complementary metal-oxide semiconductor)–compatible materials. The input function, depicted in perspective at the left of Fig. 2B, is the z-component of the electric field distribution at the entrance of this metamaterial system. We also show the distribution (snapshot in time) of this field component as the wave propagates through the entire system. At the output plane ($2L_g + \Delta$), we obtain the electric field distribution $g(y)$ shown also in Fig. 2C, which is indeed closely proportional to the first spatial derivative of the input function (green line).

To get closer to a practical realization, we also consider the more realistic MTA design and replace the ideal GRIN(–) subblock with a GRIN(+), exploiting the relation $\mathcal{F}\{\mathcal{F}[g(y)]\} \propto g(-y)$, with $\mathcal{F}(\cdot)$ denoting Fourier transform, thereby expecting the output function to be proportional to a "mirror image" of the desired result. Simulation results for this scenario (Fig. 2D) are clearly proportional to the analytical result.

Second-order derivative: $g(y) \propto d^2f(y)/dy^2$. A metamaterial that performs second spatial differentiation could be designed as a cascade of two first-differentiator blocks. However, to demonstrate the generality of our concept, we design a MS that directly performs the second differentiation. Thanks to our "modular" scheme, we simply replace the MS subblock by another one with the desired transfer function $[iy/(W/2)]^2$, which requires volumetric permittivity and permeability functions

$$\frac{\varepsilon_{ms}(y)}{\varepsilon_0} = \frac{\mu_{ms}(y)}{\mu_0} = i2\left(\frac{\lambda_0}{2\pi\Delta}\right)\ln\left(\frac{-iW}{2y}\right) \quad (3)$$

for $|y| \le W/2$. Figure 2E presents our numerical simulation for this case, confirming excellent functionality.

Integration: $g(y) \propto \int f(y)dy$. For this operation, the MS subblock needs to implement the transfer function $(iy/d)^{-1}$, where $d = 1\ \mu m$ is an arbitrary normalizing length. To avoid gain requirements for transmission coefficients with magnitude larger than unity for $|y| < d$, we truncate the required transfer function at $|y| = d$ and assume its magnitude to be unity within this range. Therefore, the MS has volumetric constitutive parameters

$$\frac{\varepsilon_{ms}(y)}{\varepsilon_0} = \frac{\mu_{ms}(y)}{\mu_0} = i\left(\frac{\lambda_0}{2\pi\Delta}\right)\ln\left(\frac{iy}{d}\right) \quad (4)$$

for $|y| > d$, and

$$\frac{\varepsilon_{ms}(y)}{\varepsilon_0} = \frac{\mu_{ms}(y)}{\mu_0} = -\left(\frac{\lambda_0}{4\Delta}\right)\mathrm{sgn}\left(\frac{y}{d}\right) \quad (5)$$

for $|y| < d$. Figure 2F presents the simulation results for the integral operation performed by this structure compared with the expected result, again demonstrating good functionality.

Convolution: $g(y) = \int f(u)G(y-u)du$. We also design a MS that performs convolution with a rectangular kernel of width $W_k = 16\ \mu m = 5.33\lambda_0$. As before, our MS realizes a transfer function

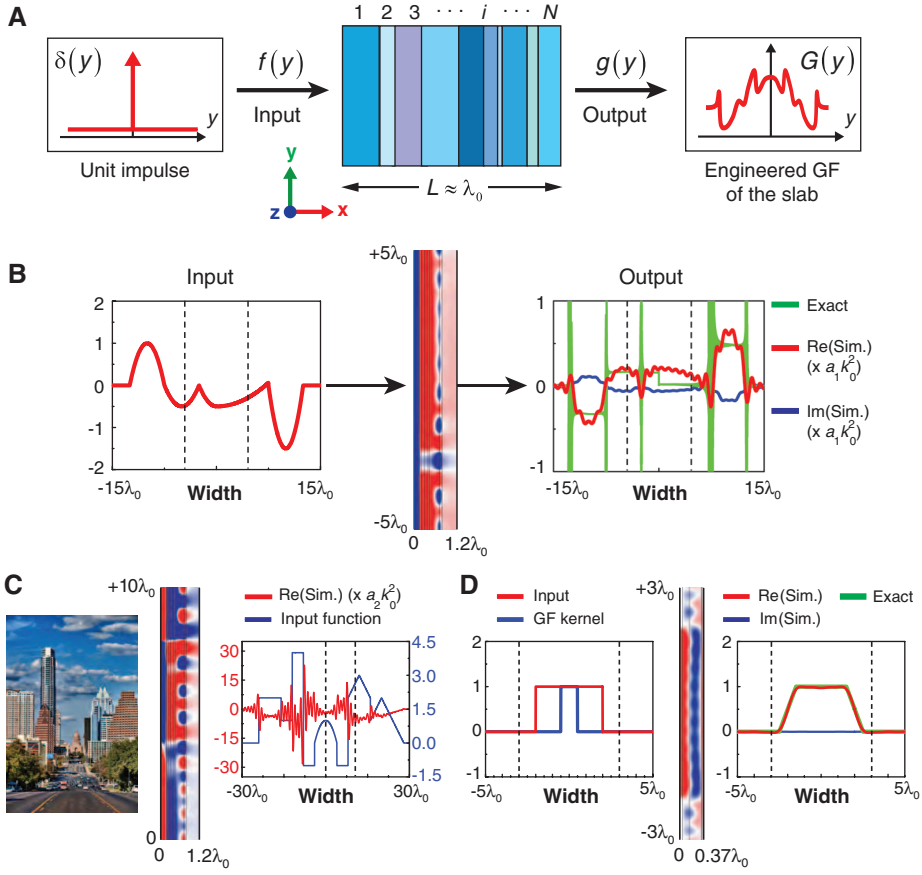


Fig. 3. Metamaterial computing using Green's function slabs. (**A**) A multilayered slab is designed to exhibit the desired GF kernel associated with a mathematical operation of choice. (**B** and **C**) Ten-layered nonmagnetic GF slab designed to perform second spatial differentiation (*28*). Simulated wave propagation (z-component of the magnetic field) throughout the slab for two different input functions: (B) a set of quadratic polynomial functions, and (C) Austin city skyline. The right panel in (B) shows the comparison between simulated output (red, real part; blue, imaginary part) and the analytical (green) results, whereas in (C) the real part of the simulated output (red) is directly compared to the input function (blue) to highlight the correspondence between the input edges and the sharp peaks at the output. In each panel, the simulation result is multiplied by a constant factor (noted in parentheses) for easy comparison. (**D**) Five-layered GF slab (*28*) designed to perform the convolution with a rectangular kernel of width λ_0, shown in blue in the left panel, for a rectangular input function of width $4\lambda_0$ (red line). In (B) to (D), the snapshots of field distributions are shown in a limited lateral region for clarity, indicated by the dashed lines. [Austin city skyline photo courtesy of Tod Grubbs of Bee Creek Photography, reproduced with permission]

may thereby represent escape of the tumor from immune pressure. We speculate that cancers harboring *POLR3A* mutations had stimulated scleroderma in most patients with the RPC1 form of the disease. However, in the majority of these patients, the immune response had eradicated the cancer by the time scleroderma developed. Patients with a short cancer–autoimmune disease interval have also been described for other autoimmune rheumatic disease phenotypes (e.g., myositis, vasculitis, systemic lupus erythematosus), and similar mechanisms may be operative in these diseases (*17*, *30*, *31*). Given the ubiquitous presence of somatic mutations in solid tumors (*32*), these new data add credence to the idea that immunoediting could play a major role in limiting the incidence of human cancer—an old hypothesis (*33*, *34*) that has recently garnered more attention (*35*–*37*). The data also suggest that this family of autoantigens might be used to generate biologically effective antitumor immunity.

References and Notes

1. A. Gabrielli, E. V. Avvedimento, T. Krieg, *N. Engl. J. Med.* **360**, 1989–2003 (2009).
2. M. L. Harris, A. Rosen, *Curr. Opin. Rheumatol.* **15**, 778–784 (2003).
3. A. A. Shah, A. Rosen, L. Hummers, F. Wigley, L. Casciola-Rosen, *Arthritis Rheum.* **62**, 2787–2795 (2010).
4. A. A. Shah, A. Rosen, *Curr. Opin. Rheumatol.* **23**, 530–535 (2011).
5. Materials and methods are available as supplementary materials on *Science* Online.
6. A. G. Knudson, *J. Cancer Res. Clin. Oncol.* **122**, 135–140 (1996).
7. Y. Kim *et al.*, *Nucleic Acids Res.* **40** (W1), W525–W530 (2012).
8. P. Wang *et al.*, *PLOS Comput. Biol.* **4**, e1000048 (2008).
9. P. Wang *et al.*, *BMC Bioinformatics* **11**, 568 (2010).
10. Z. C. Ding, G. Zhou, *Clin. Dev. Immunol.* **2012**, 890178 (2012).
11. I. Mellman, G. Coukos, G. Dranoff, *Nature* **480**, 480–489 (2011).
12. P. K. Chattopadhyay, J. Yu, M. Roederer, *Nat. Med.* **11**, 1113–1117 (2005).
13. M. Frentsch *et al.*, *Nat. Med.* **11**, 1118–1124 (2005).
14. G. T. Nepom *et al.*, *Arthritis Rheum.* **46**, 5–12 (2002).
15. K. J. Jackson, M. J. Kidd, Y. Wang, A. M. Collins, *Front. Immunol.* **4**, 263 (2013).
16. M. G. McHeyzer-Williams, M. M. Davis, *Science* **268**, 106–111 (1995).
17. R. Buchbinder, A. Forbes, S. Hall, X. Dennett, G. Giles, *Ann. Intern. Med.* **134**, 1087–1095 (2001).
18. S. A. Forbes *et al.*, *Nucleic Acids Res.* **39** (Database), D945–D950 (2011).
19. H. A. Doyle, M. J. Mamula, *Ann. N. Y. Acad. Sci.* **1050**, 1–9 (2005).
20. M. J. Mamula *et al.*, *J. Biol. Chem.* **274**, 22321–22327 (1999).
21. R. H. Lin, M. J. Mamula, J. A. Hardin, C. A. Janeway Jr., *J. Exp. Med.* **173**, 1433–1439 (1991).
22. M. J. Mamula, S. Fatenejad, J. Craft, *J. Immunol.* **152**, 1453–1461 (1994).
23. M. L. Albert, R. B. Darnell, *Nat. Rev. Cancer* **4**, 36–44 (2004).
24. C. Gaudin, F. Kremer, E. Angevin, V. Scott, F. Triebel, *J. Immunol.* **162**, 1730–1738 (1999).
25. R. F. Wang, X. Wang, A. C. Atwood, S. L. Topalian, S. A. Rosenberg, *Science* **284**, 1351–1354 (1999).
26. T. Wölfel *et al.*, *Science* **269**, 1281–1284 (1995).
27. M. E. Engelhorn *et al.*, *Nat. Med.* **12**, 198–206 (2006).
28. L. Casciola-Rosen *et al.*, *J. Exp. Med.* **201**, 591–601 (2005).
29. R. D. Schreiber, L. J. Old, M. J. Smyth, *Science* **331**, 1565–1570 (2011).
30. S. Bernatsky *et al.*, *Arthritis Rheum.* **52**, 1481–1490 (2005).
31. E. Tatsis, E. Reinhold-Keller, K. Steindorf, A. C. Feller, W. L. Gross, *Arthritis Rheum.* **42**, 751–756 (1999).
32. B. Vogelstein *et al.*, *Science* **339**, 1546–1558 (2013).
33. M. Burnet, *BMJ* **1**, 841–847 (1957).
34. F. M. Burnet, *Prog. Exp. Tumor Res.* **13**, 1–27 (1970).
35. S. A. Quezada, K. S. Peggs, *Br. J. Cancer* **108**, 1560–1565 (2013).
36. M. DuPage, C. Mazumdar, L. M. Schmidt, A. F. Cheung, T. Jacks, *Nature* **482**, 405–409 (2012).
37. H. Matsushita *et al.*, *Nature* **482**, 400–404 (2012).

Acknowledgments: We thank J. Ptak, N. Silliman. L. Dobbyn, J. Schaeffer, and M. Sampedro for expert technical assistance and J. Wu for advice on capturing. These studies were supported by The Virginia and D. K. Ludwig Fund for Cancer Research, The Donald B. and Dorothy L. Stabler Foundation, the Scleroderma Research Foundation, the Rheumatology Research Foundation Career Development Bridge Funding Award, and NIH grants K23 AR061439, P30-AR053503, CA43460, CA 57345, and CA 62924.

Supplementary Materials

www.sciencemag.org/content/343/6167/152/suppl/DC1
Materials and Methods
Supplementary Text
Figs. S1 to S5
Tables S1 to S6
References (*38*–*44*)

7 October 2013; accepted 25 November 2013
Published online 5 December 2013;
10.1126/science.1246886

Giant Spin Oscillations in an Ultracold Fermi Sea

J. S. Krauser,[1]* U. Ebling,[2]* N. Fläschner,[1] J. Heinze,[1] K. Sengstock,[1,3]† M. Lewenstein,[2,4] A. Eckardt,[5] C. Becker[1,3]

Collective behavior in many-body systems is the origin of many fascinating phenomena in nature, ranging from the formation of clouds to magnetic properties of solids. We report on the observation of collective spin dynamics in an ultracold Fermi sea with large spin. As a key result, we observed long-lived and large-amplitude coherent spin oscillations driven by local spin interactions. At ultralow temperatures, Pauli blocking stabilizes the collective behavior, and the Fermi sea behaves as a single entity in spin space. With increasing temperature, we observed a stronger damping associated with particle-hole excitations. Unexpectedly, we found a high-density regime where excited spin configurations are collisionally stabilized. Our results reveal the intriguing interplay between microscopic processes either stimulating or suppressing collective effects in a fermionic many-body system.

A fundamental question in many-body physics is how the collective behavior of many microscopically interacting particles gives rise to macroscopic properties such as superconductivity, giant magnetoresistance, or superfluidity. Ultracold quantum gases are ideal candidates to address these questions because they offer a high control over crucial experimental parameters, such as the interaction strength and the dimensionality of the system. Collective behavior of ultracold fermions is of particularly high interest because of its analogy to other systems in nature, like electrons in solids, neutron stars, or baryonic matter. Recent experiments on the crossover between a Bose-Einstein condensate and a Bardeen-Cooper-Schrieffer superfluid (*1*, *2*), Mott physics (*3*, *4*), thermodynamic and transport properties (*5*–*7*), collective excitations (*8*–*10*), and magnetic ordering (*11*, *12*) used spin ½ fermions. However, fermionic high-spin systems with more than two spin components constitute a completely new class of many-body systems, yielding collective effects involving the spin degree of freedom (*13*–*20*). For bosonic atoms with a total spin of $f = 1, 2, 3,$ spin-dependent phenomena have been intensively studied [(*21*, *22*) and references therein]. In these experiments, the macroscopic occupation of a common single-particle wave function, which is inherent to Bose-Einstein condensation, strongly favors collective behavior. For fermions, in contrast, every single-particle state can be occupied with no more than one particle, and hence many of these states are occupied in a macroscopic system forming a Fermi sea. This naturally raises the following questions: Can the whole Fermi sea exhibit collective and coherent dynamics of its internal spin degree of freedom (Fig. 1A)? Do these dynamics preserve the spatial structure, or do emerging spin components populate new spatial modes? Recent experiments with high-spin fermions allowed the study of ground-state and dynamical properties in the regime of deep

[1]ILP (Institut für Laserphysik), Universität Hamburg, Luruper Chaussee 149, 22761 Hamburg, Germany. [2]ICFO (Institut de Ciències Fotòniques), Avenida Carl Friedrich Gauss 3, 08860 Castelldefels, Spain. [3]ZOQ (Zentrum für Optische Quantentechnologien), Universität Hamburg, Luruper Chaussee 149, 22761 Hamburg, Germany. [4]ICREA (Institució Catalana de Recerca i Estudis Avançats), Lluís Companys 23, 08010 Barcelona, Spain. [5]MPI-PKS (Max-Planck-Institut für Physik komplexer Systeme), Nöthnitzer Straße 38, 01187 Dresden, Germany.

*These authors contributed equally to this work.
†Corresponding author. E-mail: klaus.sengstock@physnet.uni-hamburg.de

optical lattices (*23*, *24*), few-body physics (*25*), and also the emergence of spatial spin waves (*26*), but left the questions raised above largely unanswered. Here, we report on the observation of coherent spin dynamics in an ultracold Fermi sea. Our detailed studies reveal three fundamental findings: (i) giant collective spin oscillations lasting for seconds at ultralow temperatures, (ii) a continuous suppression of the collective behavior for increasing temperatures, and (iii) stable excited spin configurations at high densities, which we attribute to a collision-induced stabilization mechanism.

The experiments were performed with a quantum degenerate gas of ^{40}K in an optical dipole trap (*27*), an ideal candidate for the investigation of spin-changing dynamics because of its particular high-spin scattering properties (*23*). The hyperfine ground state of ^{40}K has a total spin $f = -9/2$, which gives rise to 10 spin states with magnetic quantum numbers $m = -9/2, ..., 9/2$. To record the population of these different spin components, we released the atoms from the trap and subsequently measured the spin occupations after expansion in a Stern-Gerlach field (*27*). To understand collective spin-changing dynamics, we first consider the underlying microscopic collisions, well described by s-wave scattering: Two fermionic atoms collide and change their spin configuration ($m_1, m_2 \rightarrow m_3, m_4$), conserving the total magnetization ($m_1 + m_2 = m_3 + m_4$) and obeying the Pauli exclusion principle ($m_1 \neq m_2$ and $m_3 \neq m_4$). The interplay between different quadratic Zeeman energies and differential spin-dependent interaction energies for the different spin configurations determines whether spin oscillations can occur or not (*21*). At large magnetic fields, spin-changing collisions are suppressed energetically, and the Fermi sea remains in its initial spin configuration. For low magnetic fields, the two energy scales become comparable, and resonant spin oscillations are induced. As a key result, Fig. 1B demonstrates this kind of coherent spin oscillations for time scales as long as 2s for an ultracold atomic Fermi ensemble. In the following, we show that this peculiar behavior can be theoretically described via a mean-field approach (*26*). Furthermore, all key observations are explained unexpectedly well within a single-spatial-mode approximation; that is, the whole Fermi sea evolves in time as a single spin entity.

The high-spin Fermi sea is described by the single-particle density matrix in Wigner representation $w_{ij}(x,p)$, which depends on position and momentum, whereas i and j account for the spin states. The diagonal elements of this matrix describe the spin occupations, whereas off-diagonal terms reflect the single-particle spin coherences. Its time (t) evolution obeys the Boltzmann equation (*27*)

$$\partial_t w_{ij}(x,p) = \partial_0 w_{ij}(x,p) + [V(x) + qS_z^2, w(x,p)]_{ij} + I_{ij}(x,p) \quad (1)$$

Here, $\partial_0 w_{ij}(x,p)$ accounts for the spin-independent center-of-mass motion of the atoms in the trap, and $I_{ij}(x,p)$ is the collisional integral accounting for particle-hole excitations. Spin-changing dynamics are driven by the commutator, including the mean-field potential $V_{ij}(x) = \int dp \sum_{kl}(U_{klji} - U_{kjil}) w_{kl}(x,p)$ with the interaction tensor U_{klji} and the quadratic Zeeman shift qS_z^2. The commutator drives the spin-changing dynamics in the presence of coherences, which are reflected in finite off-diagonal matrix elements of w_{ij} (*27*). In Fig. 1B, the system is prepared with very small initial coherences sufficient to initialize a spin instability followed by collective spin oscillations, a behavior also observed for Bose-Einstein condensates (*28*).

The interplay between the kinetic and interaction energy in Eq. 1 can lead to a fascinating effect: If the spatial dynamics of the trapped atoms, given by ω_{trap}, are reasonably faster than the spin-changing dynamics, given by $V_{ij}|_{i\neq j}/\hbar$, then the spatially dependent interactions are averaged out, leading to an effective long-range interaction potential (*29*). For our experiments, typically $\hbar\omega_{trap}/V_{ij}|_{i\neq j} \gtrsim 5$, which justifies the above-mentioned single-mode approximation and leads to collective spin-changing behavior of the whole Fermi ensemble despite the underlying complex spatial structure (*27*). Figure 1C shows coherent spin oscillations at ultralow temperatures for an

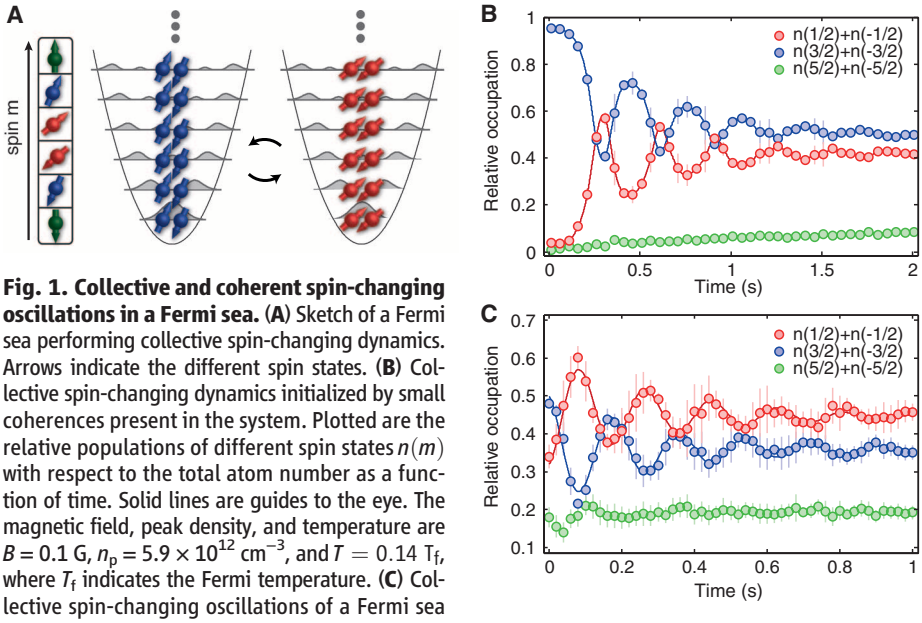


Fig. 1. Collective and coherent spin-changing oscillations in a Fermi sea. (**A**) Sketch of a Fermi sea performing collective spin-changing dynamics. Arrows indicate the different spin states. (**B**) Collective spin-changing dynamics initialized by small coherences present in the system. Plotted are the relative populations of different spin states $n(m)$ with respect to the total atom number as a function of time. Solid lines are guides to the eye. The magnetic field, peak density, and temperature are $B = 0.1$ G, $n_p = 5.9 \times 10^{12}$ cm^{-3}, and $T = 0.14\ T_f$, where T_f indicates the Fermi temperature. (**C**) Collective spin-changing oscillations of a Fermi sea prepared with coherences generated by radio-frequency pulses corresponding to a spin rotation of $\vartheta = 0.44$ (*27*). Plotted is $n(m)$ as a function of time. Solid lines are fits to the data, from which we extract the oscillation amplitude and frequency (*27*). The experimental parameters are $B = 0.12$ G, $n_p = 5.9 \times 10^{12}$ cm^{-3}, and $T = 0.13\ T_f$. Error bars indicate one standard deviation.

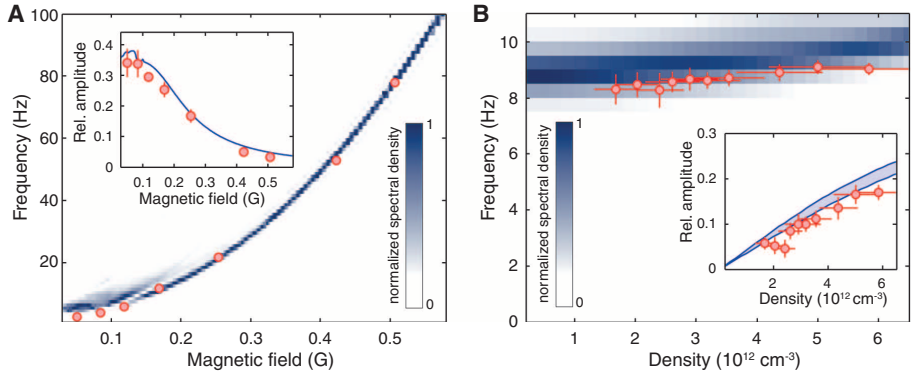


Fig. 2. Collective behavior at ultralow temperatures. Frequency (main graphs) and amplitude (insets) of collective spin oscillations versus magnetic field (**A**) and density (**B**), both for an initial state as in Fig. 1C. Experimental parameters are $n_p = 1.0 \times 10^{13}$ cm^{-3} and $T = 0.22\ T_f$ for (A) and $B = 0.17$ G and $T = 0.18\ T_f$ for (B). Data (red points) are deduced from fits (*27*). Solid lines in insets correspond to the amplitude and the shading in the main graph to a Fourier spectrum, both deduced from calculations within a single-mode approximation without free parameters (*27*). The shaded area in (B) inset reflects uncertainties in particle number and temperature. Vertical error bars indicate two standard deviations; horizontal error bars indicate systematic experimental uncertainties.

ensemble prepared with radio-frequency pulses. This generates an initial state with substantial spin coherences corresponding to a rotation of the density matrix in spin space (*27*). In contrast to the instability-induced oscillations shown in Fig. 1B, this state immediately exhibits spin oscillations and can thus be systematically compared to theoretical calculations.

At high magnetic fields, we found low-amplitude and high-frequency oscillations, in contrast to slow and giant spin oscillations at low magnetic fields (Fig. 2A). By varying the density and thereby the interaction energy within the Fermi sea (Fig. 2B), we found an increase in amplitude and a rather constant frequency for increasing interaction. The system precisely follows the mean-field description within the single-mode approximation without free parameters. As one key result of this work, we therefore conclude that spin-changing collisions can induce collective behavior in a Fermi sea of trapped atoms preserving the spatial structure for long time scales, even for macroscopic systems with particle numbers on the order of 10^5 and a spatial extent larger than 100 μm.

A fundamental question is how finite temperature affects the observed collective behavior. Figure 3A shows the strong impact of increasing temperature on the spin-changing dynamics in our experiment, revealing long-lived oscillations at low temperatures and a nearly full suppression of coherent evolution at higher temperatures. Again we found good agreement for the observed frequencies and amplitudes with the single-mode approximation (Fig. 3B). However, for higher temperatures we observe substantially stronger damping of the coherent oscillations (Fig. 3C). We attribute this to an enhanced rate of particle-hole excitations, which are described by the collisional integral $I_{ij}(x,p)$ in Eq. 1. These "incoherent" collisions are characterized by a finite momentum exchange of the colliding particles and reduce single-particle coherences. In contrast, the "coherent" collisions inducing collective spin oscillations conserve the individual momenta and are captured by the mean-field potential. At ultralow temperatures, the Fermi statistics do not provide any free momentum states because of the Pauli exclusion principle; hence collisions involving momentum exchange are strongly suppressed (*30*). For increasing temperatures, however, free momentum states become available in the Fermi sea and allow for increased particle-hole excitations. In a relaxation approximation (*31*), we estimate the corresponding damping rate. Despite the fair agreement in the low-temperature regime (Fig. 3C), this simplified model does not catch the full behavior at higher temperatures. For an explanation, see (*27*). In general, the observed temperature-dependent damping rate is in contrast to experiments with thermal gases in the Knudsen regime at low interactions, where independent of temperature a suppression of incoherent collisions arises because of the large separation of the trap levels ($\hbar\omega_{\mathrm{trap}} \gg V_{ii}$) (*32*, *33*). In our system, incoherent collisions are energetically possible ($\hbar\omega_{\mathrm{trap}} \approx V_{ii}$) but suppressed at ultralow temperatures because of Pauli blocking. This is crucial for collective spin-changing dynamics in a Fermi sea at moderate interactions.

Lastly, we investigated the occurrence of spin instabilities like the one presented in Fig. 1B as a function of the density and the magnetic field. As a particularly unexpected feature, we found a regime at high densities where magnetically excited initial states remain stable for seconds. We studied this effect by investigating the emergence of spin instabilities, which is depicted in the stability diagram in Fig. 4A. Here, we initially prepared the system in the magnetically excited spin states $m = \pm 3/2$ and mapped out the $m = \pm 1/2$

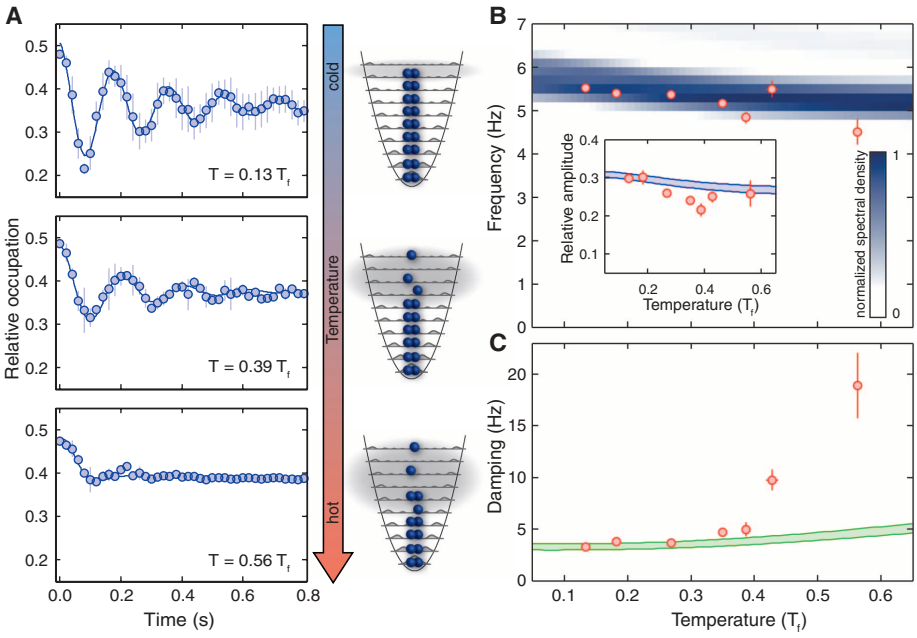


Fig. 3. Temperature influence on collective spin dynamics. The initial state is prepared as in Fig. 1C, and the experimental parameters are $B = 0.12$ G and $n_p = 5.2 \times 10^{12}$ cm^{-3}. (**A**) Time evolution of the occupations $n(\pm 3/2)$ for three different temperatures (experimental data and fitted curves). (**B**) Frequency (main graph) and amplitude (inset) for different temperatures. (**C**) Damping rate versus temperature. Data (red points) are deduced from fits. Amplitude and frequency calculations in (B) are performed within a single-mode approximation; damping calculations in (C) within a relaxation approximation, both without free parameters (*27*). The shaded areas reflect the uncertainties in particle number and temperature. Error bars of occupation and temperature indicate one standard deviation, error bars of frequency, amplitude, and damping indicate two standard deviations.

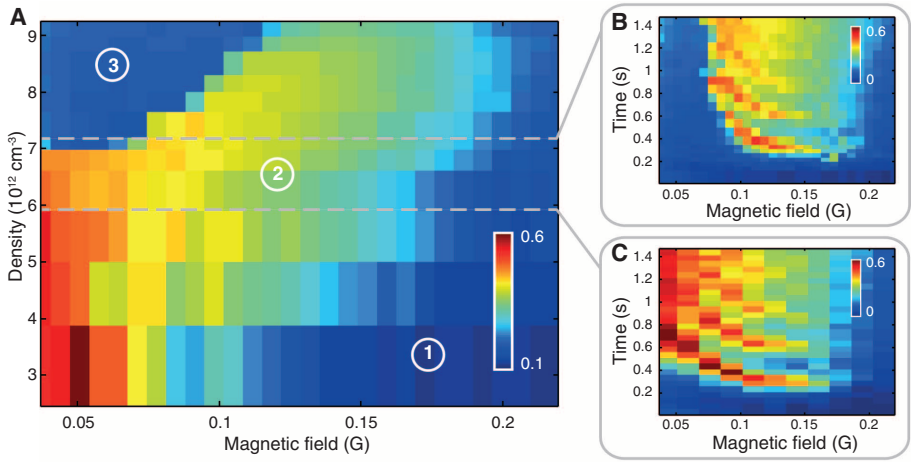


Fig. 4. Stability diagram of a magnetically excited Fermi sea. (**A**) Occupation of $n(\pm 1/2)$ after a time evolution of 2 s, dependent on the magnetic field and the density for an initial state as in Fig. 1B. Three regions are identified: a Zeeman-protected regime (labeled 1), a spin-oscillation regime, 2; and a high-density regime, 3. (**B** and **C**) The time evolution for different magnetic fields at a density of $n_p = 7.2 \times 10^{12}$ cm^{-3} and $n_p = 5.9 \times 10^{12}$ cm^{-3}, respectively.

occupation after a time evolution of 2 s, when collective spin oscillations have been damped out already and the system is in a quasi-equilibrium configuration. We identify three different regions: (i) the Zeeman-protected regime, where spin-changing collisions are off-resonant and the spin configuration remains constant; (ii) the spin-oscillation regime, where spin-changing collisions are resonant and spin instabilities occur; and (iii) a stable high-density regime, where the spin configuration does not change, despite the fact that coherent spin-changing oscillations would be resonant, thus possible. To illustrate the behavior in regime (iii) more clearly, we show time evolutions at different magnetic fields for two slightly different densities (Fig. 4, B and C), revealing an abrupt spin stabilization at small magnetic fields for the larger density. We attribute this stabilization to an increased rate of incoherent collisions at large densities. In terms of the single-particle density matrix formalism, these incoherent collisions project the initial state onto the diagonal elements, which is similar to the measurement projection associated with the quantum-Zeno effect. In further analogy, any coherent evolution is suppressed. In the experiments presented here, this mechanism is highly sensitive to slight changes of the experimental parameters and leads to a completely different macroscopic behavior of the Fermi sea.

We have investigated the intriguing interplay between several microscopic spin-changing processes in ultracold high-spin Fermi gases. The high experimental control as well as the obtained understanding of our model system, opens the path to studying exotic phenomena, such as the creation of topological structures and textures in superfluid Fermi gases with high spin.

References and Notes

1. C. A. Regal, M. Greiner, D. S. Jin, *Phys. Rev. Lett.* **92**, 040403 (2004).
2. M. W. Zwierlein, J. R. Abo-Shaeer, A. Schirotzek, C. H. Schunck, W. Ketterle, *Nature* **435**, 1047–1051 (2005).
3. U. Schneider *et al.*, *Science* **322**, 1520–1525 (2008).
4. R. Jördens, N. Strohmaier, K. Günter, H. Moritz, T. Esslinger, *Nature* **455**, 204–207 (2008).
5. N. Navon, S. Nascimbène, F. Chevy, C. Salomon, *Science* **328**, 729–732 (2010); 10.1126/science.1187582.
6. A. Sommer, M. Ku, G. Roati, M. W. Zwierlein, *Nature* **472**, 201–204 (2011).
7. M. Koschorreck, D. Pertot, E. Vogt, M. Köhl, *Nat. Phys.* **9**, 405–409 (2013).
8. L. A. Sidorenkov *et al.*, *Nature* **498**, 78–81 (2013).
9. X. Du, L. Luo, B. Clancy, J. E. Thomas, *Phys. Rev. Lett.* **101**, 150401 (2008).
10. M. J. Martin *et al.*, *Science* **341**, 632–636 (2013).
11. G.-B. Jo *et al.*, *Science* **325**, 1521–1524 (2009).
12. D. Greif, T. Uehlinger, G. Jotzu, L. Tarruell, T. Esslinger, *Science* **340**, 1307–1310 (2013); 10.1126/science.1236362.
13. T.-L. Ho, S. Yip, *Phys. Rev. Lett.* **82**, 247–250 (1999).
14. P. Lecheminant, E. Boulat, P. Azaria, *Phys. Rev. Lett.* **95**, 240402 (2005).
15. C. Wu, *Phys. Rev. Lett.* **95**, 266404 (2005).
16. A. Rapp, G. Zaránd, C. Honerkamp, W. Hofstetter, *Phys. Rev. Lett.* **98**, 160405 (2007).
17. M. A. Cazalilla, A. F. Ho, M. Ueda, *New J. Phys.* **11**, 103033 (2009).
18. A. V. Gorshkov *et al.*, *Nat. Phys.* **6**, 289–295 (2010).
19. K. Rodríguez, A. Argüelles, M. Colomé-Tatché, T. Vekua, L. Santos, *Phys. Rev. Lett.* **105**, 050402 (2010).
20. Y. Dong, H. Pu, *Phys. Rev. A* **87**, 043610 (2013).
21. D. M. Stamper-Kurn, M. Ueda, *Rev. Mod. Phys.* **85**, 1191–1244 (2013).
22. Y. Kawaguchi, M. Ueda, *Phys. Rep.* **520**, 253–381 (2012).
23. J. S. Krauser *et al.*, *Nat. Phys.* **8**, 813–818 (2012).
24. S. Taie, R. Yamazaki, S. Sugawa, Y. Takahashi, *Nat. Phys.* **8**, 825–830 (2012).
25. T. Lompe *et al.*, *Science* **330**, 940–944 (2010).
26. J. Heinze *et al.*, *Phys. Rev. Lett.* **110**, 250402 (2013).
27. Supplementary materials are available on *Science* Online.
28. C. S. Gerving *et al.*, *Nat. Commun.* **3**, 1169 (2012).
29. U. Ebling, A. Eckardt, M. Lewenstein, *Phys. Rev. A* **84**, 063607 (2011).
30. C. Lhuillier, F. Laloë, *Phys. Rev. Lett.* **54**, 1207 (1985).
31. T. Nikuni, J. E. Williams, C. W. Clark, *Phys. Rev. A* **66**, 043411 (2002).
32. H. K. Pechkis *et al.*, *Phys. Rev. Lett.* **111**, 025301 (2013).
33. C. Deutsch *et al.*, *Phys. Rev. Lett.* **105**, 020401 (2010).

Acknowledgments: We acknowledge stimulating discussions with N. Cooper, W. Hofstetter, L. Mathey, and L. Santos. This work has been funded by Deutsche Forschungsgemeinschaft (DFG) grant FOR 801, DFG excellence cluster The Hamburg Centre for Ultrafast Imaging - Structure, Dynamics, and Control of Matter on the Atomic Scale, European Research Council AdG QUAGATUA, Spanish Ministerio de Ciencia e Innovación [grant TOQATA (FIS2008-00784) and Formación de Personal Investigador fellowship], and European Union Integrated Project Simulators and Interfaces with Quantum Systems.

Supplementary Materials

www.sciencemag.org/content/343/6167/157/suppl/DC1
Materials and Methods
Supplementary Text
Figs. S1 to S3
Reference (*34*)

31 July 2013; accepted 4 December 2013
10.1126/science.1244059

Performing Mathematical Operations with Metamaterials

Alexandre Silva,[1]* Francesco Monticone,[2]* Giuseppe Castaldi,[3] Vincenzo Galdi,[3] Andrea Alù,[2] Nader Engheta[1]†

We introduce the concept of metamaterial analog computing, based on suitably designed metamaterial blocks that can perform mathematical operations (such as spatial differentiation, integration, or convolution) on the profile of an impinging wave as it propagates through these blocks. Two approaches are presented to achieve such functionality: (i) subwavelength structured metascreens combined with graded-index waveguides and (ii) multilayered slabs designed to achieve a desired spatial Green's function. Both techniques offer the possibility of miniaturized, potentially integrable, wave-based computing systems that are thinner than conventional lens-based optical signal and data processors by several orders of magnitude.

Metamaterials—artificially engineered structures designed to exhibit unconventional wave properties—have recently opened exciting venues for unprecedented control and manipulation of electromagnetic fields, as well as other forms of waves, such as acoustic, elastic, mechanical, and matter waves (*1*–*5*). The spatial and/or temporal engineering of their bulk parameters, such as the permittivity and permeability of an artificial material, enables shaping of local and global field distributions to achieve a desired functionality. Transformation optics (*6*, *7*), for instance, has shown that by locally tailoring the electric and magnetic response of a material, one may be able to achieve functionalities of interest, such as cloaking (*6*–*8*), field concentration or rerouting (*9*–*14*), and optical illusions (*15*).

Here, we introduce the concept of "computational metamaterials" that can be used to perform mathematical operations—such as spatial differentiation, integration, or convolution—as electromagnetic waves propagate through them. Traditional analog computers, or "calculating machines" in the form of mechanical, electronic, and hybrid analog computers, have been designed in the past to perform such mathematical computations (*16*–*18*), but these solutions have suffered from substantial limitations, including relatively large size and slow response. Mechanical deformation of arrays of bars and pivots to achieve a certain functional response (*19*) and construction of linkages to synthesize a portion of an algebraic curve (*20*) have also been explored. Our idea for metamaterial-based computing is conceptually sketched in Fig. 1, in which metamaterial blocks produce a wave profile at their output proportional to the desired operation performed on an arbitrary input wave profile by suitably manipulating the impinging wave as it propagates through them. Although a selected set of these functionalities may be achieved with well-known optical signal processing or Fourier optics using conventional lenses (*21*–*23*), our approaches provide the possibility of highly compact, potentially integrable architectures with-

[1]Department of Electrical and Systems Engineering, University of Pennsylvania, Philadelphia, PA 19104, USA. [2]Department of Electrical and Computer Engineering, University of Texas, Austin, TX 78712, USA. [3]Waves Group, Department of Engineering, University of Sannio, Benevento I-82100, Italy.

*These authors contributed equally to this work.
†Corresponding author. E-mail: engheta@ee.upenn.edu

corresponding to the Fourier transform of the kernel

$$\tilde{G}(y) = \mathrm{sinc}\left(\frac{W_k y}{2s^2}\right) \quad (6)$$

where

$$s = \sqrt{\frac{\lambda_0 L_g}{\pi^2 \sqrt{\varepsilon_c/\varepsilon_0}}} \quad (7)$$

is a GRIN scale factor defined in (*24*). For such a transfer function, the required constitutive parameters are

$$\frac{\varepsilon_{ms}(y)}{\varepsilon_0} = \frac{\mu_{ms}(y)}{\mu_0} = i\left(\frac{\lambda_0}{2\pi\Delta}\right)\ln\left[\frac{1}{\mathrm{sinc}(W_k y/2s^2)}\right] \quad (8)$$

The results of our simulation are shown in Fig. 2G, demonstrating good agreement with the analytical results.

In our second (GF) approach, we design a multilayered metamaterial slab, transversely homogeneous but longitudinally inhomogeneous, that realizes an output field distribution $g(y)$ to an input function $f(y)$, consistent with the GF $G(y)$ associated with a desired operator of choice (Fig. 3A). In this approach, we avoid the need of going into the Fourier domain, hence avoiding the GRIN subblocks that perform Fourier and inverse Fourier transforms. Because this GF slab is transversely symmetric, it can in principle realize an arbitrary GF with even symmetry, such as the second spatial derivative $g(y) \propto d^2f(y)/dy^2$, which can be written in terms of an even kernel as $g(y) \propto \int f(u)\delta''(y-u)du$ [where the required GF is proportional to the second spatial derivative of the Dirac delta function $\delta''(y)$]. Our goal is then to tailor the transmission coefficient for impinging plane waves as a function of the transverse wavenumber k_y to be $\tilde{G}(k_y) \propto -k_y^2$. In (*29*), we addressed this problem within the framework of nonlocal transformation optics, assuming infinite media. Here, we consider a finite longitudinal thickness divided into N parallel layers with subwavelength thicknesses d_i, $i = 1, 2, \ldots, N$ (Fig. 3A). We developed a fast synthesis approach to obtain the permittivity, permeability, and thickness of each layer required to tailor the overall plane-wave transmission coefficient to match $\tilde{G}(k_y)$ for all impinging angles (*28*). It is also possible to obtain the same result using nonmagnetic layered metamaterials by suitably increasing the number of layers, arguably simplifying the design and bringing it closer to practical realization. The 10-layered design (*28*) in Fig. 3B is a GF slab with nonmagnetic ($\mu = \mu_0$) constitutive parameters and an overall thickness comparable to λ_0.

Our numerical results confirm that the designed metamaterial provides a GF kernel that resembles, given the unavoidable limited resolution, the desired $\delta''(y)$ at the output plane when the input is an approximate delta function. In Fig. 3, B and C, we apply a set of quadratic polynomial functions and the Austin city skyline borders, respectively, as inputs for our second-spatial-derivative GF slab, showing the evolution of the z-component of the magnetic field distribution along the slab, and demonstrating that the designed structure indeed approximately performs the second-derivative operation as the wave propagates through it. Edge-detection spatial analog filters [e.g., Laplace filters (*30*)] and image-processing devices may largely benefit from this system. We also design a five-layered GF slab (with overall thickness of $0.37\lambda_0$) that performs the convolution operation of an input function with a one-wavelength rectangular spatial kernel (*28*). Figure 3D shows the simulation results using another rectangular function as input.

Our proposed computational metastructures are smaller than conventional lens-based optical signal-processing systems by several orders of magnitude. Moreover, with no analog-to-digital conversion or other systematic delays, here mathematical operations get processed as the electromagnetic signals propagate through the highly miniaturized and compact computational metamaterials. Such designs may potentially lead to direct, ultrafast, wave-based analog computation, equation solving, and signal processing at the hardware level.

References and Notes

1. N. Engheta, R. W. Ziolkowski, Eds., *Metamaterials—Physics and Engineering Explorations* (IEEE-Wiley, New York, 2006).
2. G. V. Eleftheriades, K. G. Balmain, *Negative-Refraction Metamaterials* (IEEE, New York, 2005).
3. D. R. Smith, J. B. Pendry, M. C. K. Wiltshire, *Science* **305**, 788–792 (2004).
4. C. Caloz, T. Itoh, *Electromagnetic Metamaterials—Transmission Line Theory and Microwave Applications* (IEEE-Wiley, New York, 2006).
5. W. Cai, V. Shalaev, *Optical Metamaterials: Fundamentals and Applications* (Springer, New York, 2010).
6. J. B. Pendry, D. Schurig, D. R. Smith, *Science* **312**, 1780–1782 (2006).
7. U. Leonhardt, *Science* **312**, 1777–1780 (2006).
8. A. Alù, N. Engheta, *Phys. Rev. E* **72**, 016623 (2005).
9. A. Vakil, N. Engheta, *Science* **332**, 1291–1294 (2011).
10. E. F. Kuester, M. A. Mohamed, M. Piket-May, C. L. Holloway, *IEEE Trans. Antenn. Propag.* **51**, 2641–2651 (2003).
11. N. Yu *et al.*, *Science* **334**, 333–337 (2011).
12. X. Ni, N. K. Emani, A. V. Kildishev, A. Boltasseva, V. M. Shalaev, *Science* **335**, 427 (2012).
13. Y. Zhao, M. A. Belkin, A. Alù, *Nat. Commun.* **3**, 870 (2012).
14. A. Pandey, N. M. Litchinitser, *Opt. Lett.* **37**, 5238–5240 (2012).
15. Y. Lai *et al.*, *Phys. Rev. Lett.* **102**, 253902 (2009).
16. D. de Solla Price, *IEEE Micro.* **4**, 22–52 (1984).
17. A. B. Clymer, *IEEE Ann. Hist. Comput.* **15**, 19 (1993).
18. Computer History Museum, www.computerhistory.org/revolution/analog-computers/3.
19. G. W. Milton, *J. Mech. Phys. Solids* **61**, 1543–1560 (2013).
20. A. B. Kempe, *Proc. London Math. Soc.* **7**, 213 (1876).
21. A. Weiner, *Rev. Sci. Instrum.* **71**, 1929 (2000).
22. D. Casasent, *Proc. IEEE* **65**, 143–157 (1977).
23. J. Goodman, *Introduction to Fourier Optics* (Roberts & Co., Englewood, CO, ed. 3, 2005).
24. H. M. Ozaktas, D. Mendlovic, *J. Opt. Soc. Am. A* **10**, 2522 (1993).
25. J. B. Pendry, S. A. Ramakrishna, *J. Phys. Condens. Matter* **15**, 6345–6364 (2003).
26. G. V. Naik, J. Kim, A. Boltasseva, *Opt. Mater. Express* **1**, 1090 (2011).
27. F. Monticone, N. M. Estakhri, A. Alù, *Phys. Rev. Lett.* **110**, 203903 (2013).
28. See supplementary materials on *Science* Online.
29. G. Castaldi, V. Galdi, A. Alù, N. Engheta, *Phys. Rev. Lett.* **108**, 063902 (2012).
30. R. C. Gonzalez, R. E. Woods, *Digital Image Processing* (Prentice Hall, New York, 2008).

Acknowledgments: Supported in part by U.S. Office of Naval Research Multidisciplinary University Research Initiative (MURI) grant N00014-10-1-0942.

Supplementary Materials

www.sciencemag.org/content/343/6167/160/suppl/DC1
Materials and Methods
Supplementary Text
Figs. S1 to S23
Tables S1 and S2
References (*31*–*35*)

5 July 2013; accepted 12 November 2013
10.1126/science.1242818

Heteroepitaxial Growth of Two-Dimensional Hexagonal Boron Nitride Templated by Graphene Edges

Lei Liu,[1]* Jewook Park,[2]* David A. Siegel,[3] Kevin F. McCarty,[3] Kendal W. Clark,[2] Wan Deng,[1] Leonardo Basile,[2,4] Juan Carlos Idrobo,[2] An-Ping Li,[2]† Gong Gu[1]†

By adapting the concept of epitaxy to two-dimensional space, we show the growth of a single-atomic-layer, in-plane heterostructure of a prototypical material system—graphene and hexagonal boron nitride (h-BN). Monolayer crystalline h-BN grew from fresh edges of monolayer graphene with atomic lattice coherence, forming an abrupt one-dimensional interface, or boundary. More important, the h-BN lattice orientation is solely determined by the graphene, forgoing configurations favored by the supporting copper substrate.

In conventional heteroepitaxial growth, an extended single-crystal film, or epilayer, forms on a two-dimensional (2D) surface of a single crystal of a different material, as exemplified by the growth of GaAs on Si (*1*). In general, if the lattice constants of the different materials are similar, the atomic lattice of the surface can act as a template for the initial growth of the

epilayer and ensure that it forms a single crystal. Because of the interactions in 3D space between the 2D seed crystal and the surroundings, it is not a trivial question whether a purely 2D heteroepitaxial crystal would grow from the 1D edge of a 2D seed crystal, with the crystallography of the epitaxial crystal solely determined by the seed. Here, we implement heteroepitaxy in a 2D material system by growing monolayer hexagonal boron nitride (h-BN; BN hereafter) from the edges of existing graphene crystals, which have a close lattice match (1.7%). We demonstrate abrupt zigzag boundaries as well as lattice coherence between the graphene "substrate" and the BN "epilayer."

The growth method is schematically illustrated in Fig. 1A and described in detail in the supplementary materials (*2*). First, monolayer graphene single crystals (fig. S1) were grown by atmospheric-pressure chemical vapor deposition (APCVD) (*3*, *4*) on a Cu foil, providing the substrate in 2D space. Immediately before BN growth, we performed a hydrogen etch (*4*–*6*) to obtain fresh edges, or "surfaces" in 2D. Graphene island edges were etched back, and equiangular hexagon etch holes with zigzag edge sides (*5*) formed, which exhibited distinctive 120° angles, as revealed by scanning electron microscopy (SEM) (Fig. 1B). This step is analogous to the common practice of obtaining fresh starting surfaces for conventional epitaxy and is critical to the formation of the BN epilayer here. For controlled BN epilayer formation, we ensure that (i) the growth is indeed confined in a 2D space—the Cu surface—and (ii) the growth is sufficiently slow to allow for epitaxial growth. A low precursor (BH_3–NH_3) supply rate satisfies both requirements and was achieved with APCVD exploiting process kinetics (*7*), analogous to graphene APCVD using highly diluted CH_4 precursor that yields crystallites with zigzag edges (*3*, *4*).

The early stage of BN-"on"-graphene heteroepitaxy in 2D shown in Fig. 1C revealed several BN islands, with a distinct contrast in the SEM image, forming at the graphene edges. Figure 1D shows the formation of BN epilayers in 2D, which we refer to as "epistrips." The growth of the epistrip, which is a 2D crystal, is different from seeded lateral epitaxy (*8*) of 3D crystalline films. Figure 1E shows graphene islands enclosed by continuous epistrips. Eventually, all etch holes in graphene were filled by BN (Fig. 1F). No second-layer formation was observed in SEM. Atomic resolution scanning tunneling microscopy (STM) revealed atomic-level details of graphene-BN boundaries (*2*), with the assignment of graphene and BN regions made by their distinctive scanning tunneling spectra (STS), as discussed in detail below. Figure 1G shows an abrupt boundary as well as lattice coherence between graphene and BN. Electron diffraction experiments to be discussed below confirm lattice coherence on larger length scales and, more important, show that the BN epistrip crystalline orientation is solely determined by the graphene seed, independent of the underlying Cu lattice.

These results differ fundamentally from those of the previous demonstrations of graphene-BN heterostructure growth. In-plane graphene-BN heterostructures were demonstrated (*9*, *10*) on Cu foils by top-down patterning and regrowth, without or agnostic of graphene-BN lattice coherence, which is unnecessary for the intended ultrathin circuit board or passive component applications. Also, on polycrystalline Cu foils by chemical vapor deposition (CVD), a variety of hybrid vertical/in-plane heterostructures were synthesized (*11*). On single-crystal metal substrates in ultrahigh vacuum chambers, two-step growth methods resulted in patchworks of graphene and BN domains, which exhibited lattice coherence that is coincident with epitaxy in the third dimension because the graphene and the BN are both epitaxial to the single-crystal supporting substrates (*12*, *13*). This coincidence masks possible heteroepitaxy in 2D, especially for the case (*13*) where BN nucleated at graphene edges.

We examined the heterostructure by STM after annealing the Cu foil sample in the STM system at 430°C for 48 hours to relax strain (*14*). The 2D heterostructure did not need to be transferred from the Cu foil, thus avoiding transfer-induced contamination (*2*). The STM image in Fig. 2A shows the seamless connection between lower graphene and higher BN regions, which have an apparent height difference. Although electronic properties contribute to apparent heights, the observed difference is considerably smaller than the interlayer spacings of graphene (3.37 Å) and BN (3.33 Å) (*15*), confirming the in-plane connection between graphene and BN and the absence of additional layers. Notably, each segment of the boundary is zigzag oriented, consistent with the formation of zigzag graphene edges by the hydrogen etch (*4*, *5*). Furthermore, enlarged images (fig. S3, B and C) of the graphene and BN regions in fig. S3A, along with their 2D fast Fourier transforms (insets to figs. S2, B and C), show no discernible rotational misalignment between the two, corroborated by Z-contrast scanning transmission electron microscopy (STEM) (fig. S10). The measured lattice constants of graphene (2.46 ± 0.04 Å) and BN (2.50 ± 0.04 Å) are consistent with reported values (2.46 Å and 2.50 Å) (*15*). Moreover, the STEM results also indicate that the interface boundary is formed by monolayer graphene and BN (fig. S11A) and that it is sharp, with a transition width of ~0.5 nm (fig. S11B).

Graphene and BN regions can be identified by simultaneously acquiring STM images and STS. Differential tunneling conductance (*dI/dV*) maps (Fig. 2B and fig. S3F) clearly show two distinct regions, with segments of the boundary forming distinctive 120° angles. To elucidate the assignment of graphene and BN regions, we show in Fig. 2D a series of STS curves obtained along a line across a boundary. Figure 2C marks the location where each curve was obtained. The top curves (yellow, magenta, and cyan) are characteristic of graphene (*16*), with the Dirac point ~300 mV below the Fermi level. The black curve displays metallic behavior, which we attribute to an interface band between BN and Cu, following the analysis of Joshi *et al*., who considered the BN transparent at these low biases (*17*). Noticeably, the zero-bias differential conductance was lower in the BN region. Thus, in the *dI/dV* map obtained at a low sample bias $V = 0.1$ V shown in fig. S3F, we assigned the low differential conductance region to BN. At a high bias $V = 1$ V, the differential conductance map is reversed (Fig. 2B).

To show lattice coherence between the graphene substrate and the BN epistrip over larger length scales than atomic-resolution images and, more important, the overriding of the influence of the underlying Cu lattice, we investigated a sample by low-energy electron microscopy (LEEM) and micro low-energy electron diffraction (μ-LEED). Preserving the Cu support allowed us to study the heterostructure crystallography with regard to the underlying Cu surface, which consists predominantly of (100)-oriented grains (*18*). The LEEM image in Fig. 3A shows the graphene cores, the BN epistrips, and the bare Cu with bright, dim, and dark contrasts, respectively. The μ-LEED patterns acquired at eight locations are shown in Fig. 3, B to I (corresponding to locations labeled B to I in Fig. 3A). The four first-order diffraction spots arising from the Cu(100) surface [marked by blue circles with one connected to the (00) spot with a blue arrow] in all eight patterns show the same orientation, indicating that the imaged area is a single Cu grain. The graphene and BN spots are circled, with one connected to the (00) spot by an arrow, in red and green, respectively. Comparing diffraction patterns of the graphene cores and their corresponding BN epistrips, we notice that all BN epistrips are orientationally aligned to their graphene cores, regardless of the rotation angle between the graphene-BN lattice and the underlying Cu(100) surface lattice. The rotation is labeled for each LEED pattern. The top, middle, and bottom panels of Fig. 3J depict real-space structures corresponding to the three rotations, +16°, −6°, and 0°, respectively.

Whereas graphene does not align to the underlying Cu(100) at particular rotation angles (*18*), BN exhibits a definitive alignment when grown on a bare Cu foil (with 0° rotation; see the supplementary materials). Here, grown as the epistrip, or epilayer in 2D, the BN adopts the orientation of the graphene, because the in-plane interaction is much stronger than and thus overrides the out-of-plane interaction with the Cu. This observation is the best manifestation of epitaxy in 2D, in contrast to graphene-BN lattice coherence mediated by an underlying metal

[1]The University of Tennessee, Knoxville, TN 37996, USA. [2]Center for Nanophase Materials Sciences, Oak Ridge National Laboratory, Oak Ridge, TN 37831, USA. [3]Sandia National Laboratories, Livermore, CA 94550, USA. [4]Departamento de Física, Escuela Politécnica Nacional, Quito, Ecuador.

*These authors contributed equally to this work.
†Corresponding author. E-mail: ggu1@utk.edu (G.G.); apli@ornl.gov (A.-P.L.)

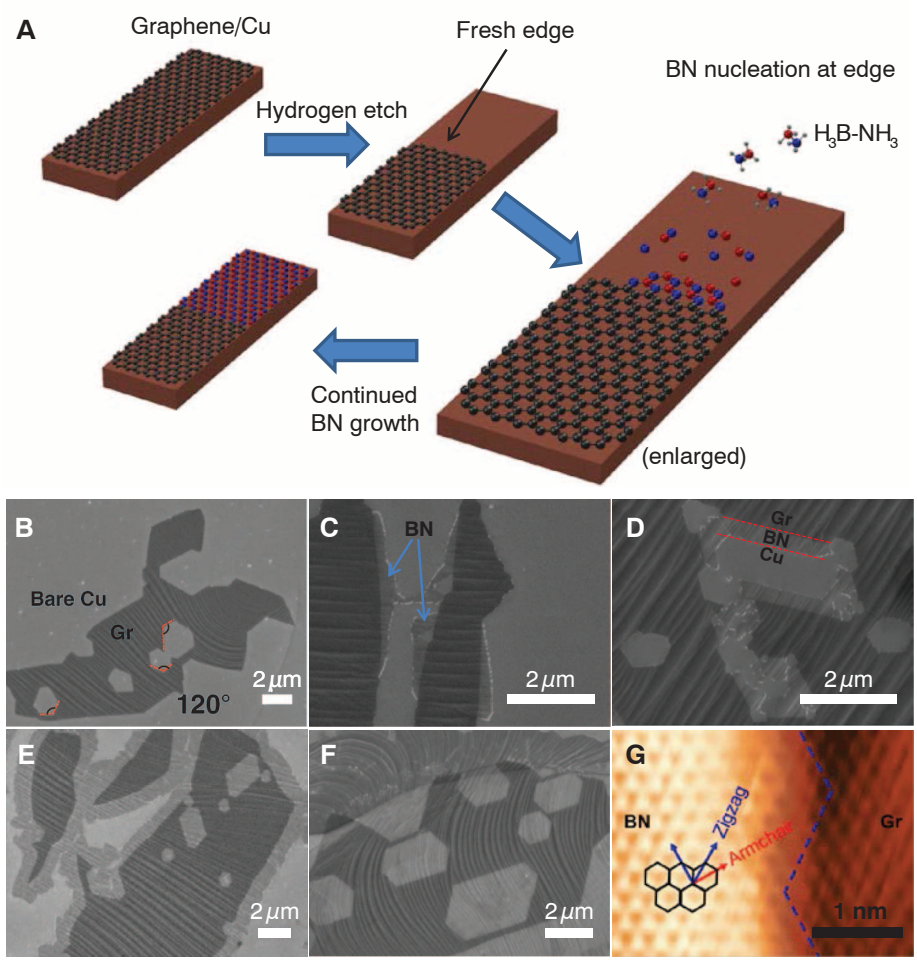


Fig. 1. Heteroepitaxy in 2D space. (**A**) Cartoon illustration of epitaxial growth of BN onto graphene edges. Black, blue, red, and small gray spheres visualize C, N, B, and H atoms, respectively. The reliance on the catalytic Cu surface for precursor (H_3B–NH_3) decomposition confines the growth to 2D. (**B**) SEM image of a hydrogen-etched graphene (Gr) island with equiangular hexagon etch holes. (**C**) Nucleation of BN at graphene edges during initial growth. (**D**) Formation of BN epistrips at graphene edges. (**E**) Continuous BN epistrips enclosing graphene islands. (**F**) Full coverage of the etch holes in a graphene island by BN. (**G**) Atomic-resolution STM image (3.5 nm by 2.5 nm) of a graphene-BN boundary. A honeycomb lattice and zigzag boundaries are overlaid on the image.

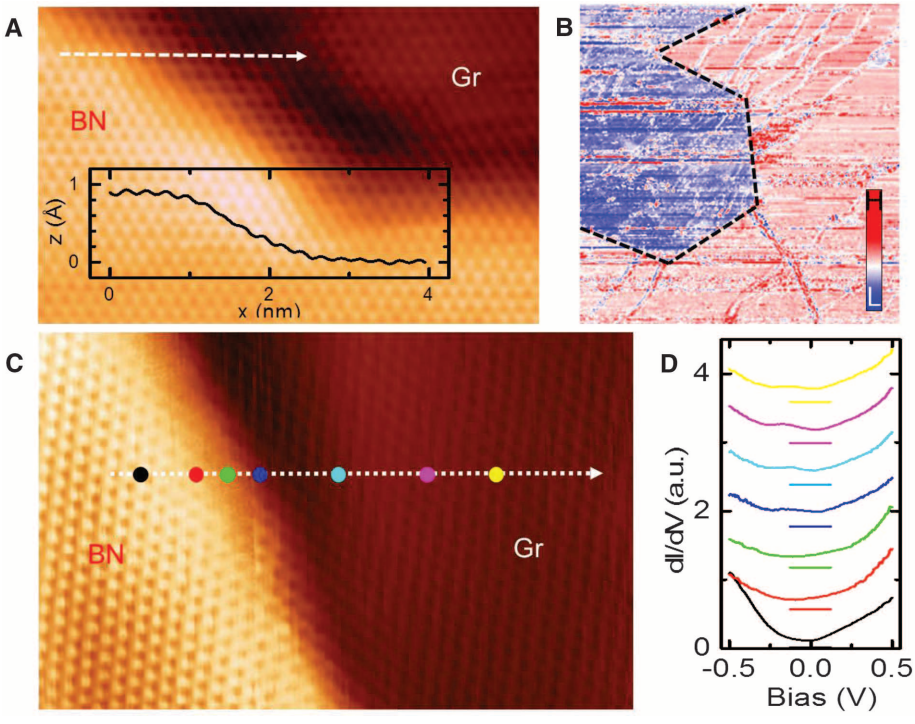


Fig. 2. Graphene-BN boundary structure at atomic scale. (**A**) STM image at a graphene-BN boundary (7.5 nm by 5 nm, sample bias 0.5 V). (Inset) Height profile along the white dashed arrow across the boundary. (**B**) Differential tunneling conductance map simultaneously obtained in the same region as fig. S3E (1 μm by 1 μm; 1 V sample bias voltage; 200 pA tunneling current). (**C**) STM image (8 nm by 5 nm) of a graphene-BN boundary, with colored dots marking locations of STS acquisition. (**D**) *dI/dV* curves color coded by location and offset for clarity, with horizontal lines indicating zero differential conductance.

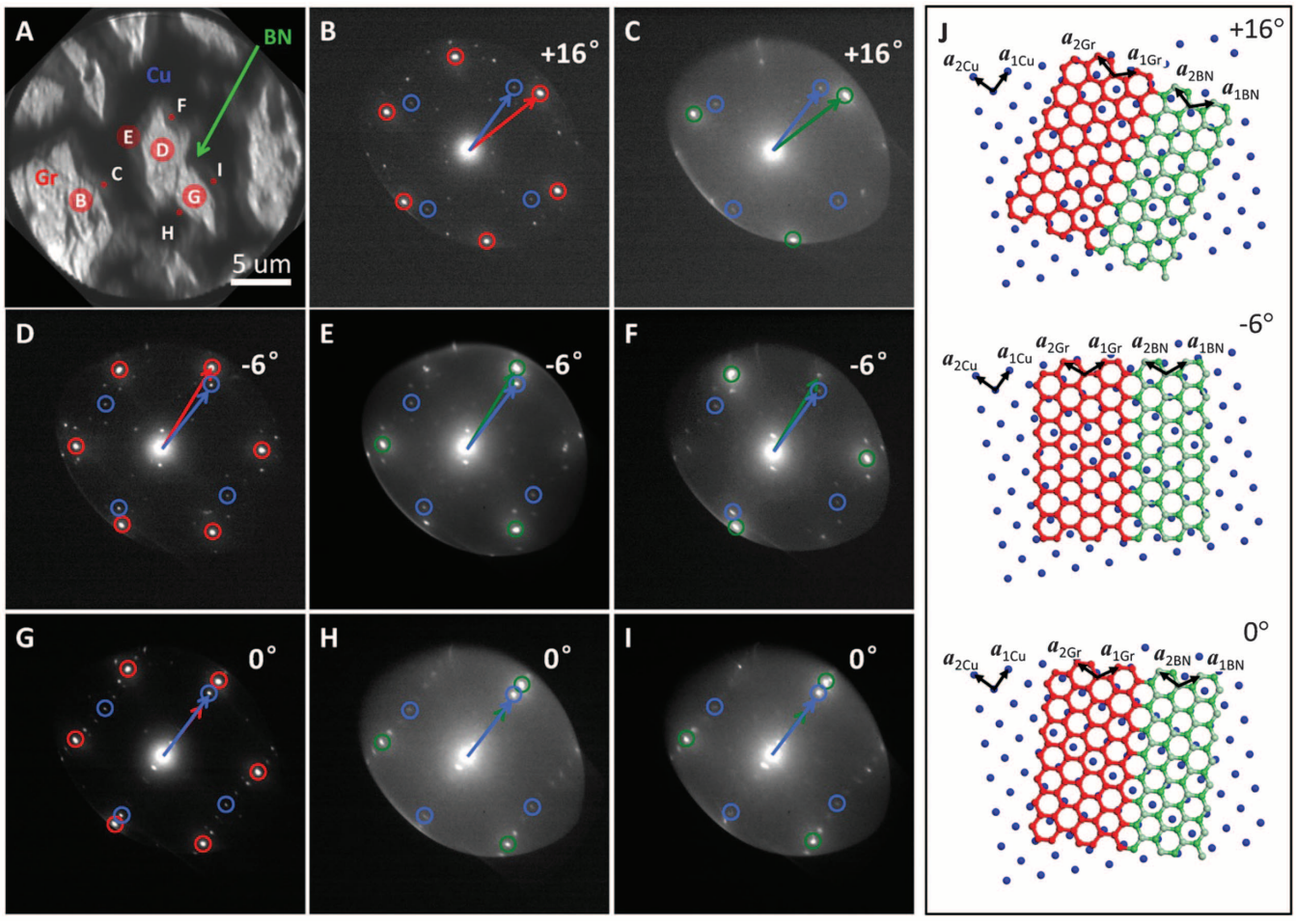


Fig. 3. Graphene-BN boundary structure at mesoscopic scale. (**A**) LEEM image of BN epistrips grown onto edges of graphene (Gr), the brightest regions. The darkest and the medium gray regions are bare Cu and BN, respectively. The labeled circles show the locations and sizes (0.5 or 2 μm diameter) of the regions analyzed in the μ-LEED patterns of (B) to (I). (**B** to **I**) LEED patterns acquired at locations marked in (A). The first-order diffraction spots and reciprocal lattice vectors of Cu, graphene, and BN are distinguished by blue, red, and green colors, respectively. Each BN epistrip and the corresponding graphene substrate have the same in-plane orientation with respect to the underlying Cu lattice: rotations of +16° [(B) and (C)], −6° [(D) to (F)], and 0° [(G) to (I)]. (**J**) Real-space structure models corresponding to the three rotations. Following (B) to (I), blue, red, and green represent Cu, graphene, and BN, respectively; B and N atoms are symbolized by two shades of green. Lattice vectors are shown.

lattice (*12*, *13*). The epistrip is purely 2D and is not necessarily epitaxial to the support in the third dimension. Thus, epitaxy in 2D is not to be confused with the Frank–van der Merwe film growth mode (sometimes referred to as 2D growth) (*8*).

As expected, the BN patterns exhibit threefold symmetry, a feature besides LEEM contrast distinguishing it from the six-fold symmetric graphene. Interestingly, the BN spots in Fig. 3, E and F, acquired on BN epistrips of the same graphene core, are mirror images of each other, whereas those in Fig. 3, H and I, are the same. This observation relates to the well-known antiphase phenomenon in polar-on-nonpolar epitaxy (*1*) and has implications in the spin and magnetic properties of the boundaries (*19*, *20*).

Now we discuss the rationale behind heteroepitaxy in 2D space. Although the growth of 2D crystals has been extensively studied (*15*, *21*–*25*) and 2D heterostructures have been synthesized recently (*9*–*13*), it has until now been unclear whether a purely 2D heterostructure (criterion 1) can form by the growth of an epistrip from the 1D edge of a seed 2D crystal (criterion 2) with the crystallography of the epistrip solely determined by the seed (criterion 3). Because of the complex interactions in 3D space that involve the 2D crystal, the supporting substrate, and the feed gas, the three criteria closely intertwine. To meet criterion 1, the supporting substrate must at the same time serve as a constraint that confines the growth process on its surface to avoid the formation of multiple stacked sheets. We achieved confinement by limiting the precursor feed rate, leveraging the catalytic property of Cu (*2*, *22*, *23*). Criterion 2 can be met if the supporting substrate surface is sufficiently uniform to suppress nucleation (which results from interactions between the supporting substrate and feed gas) away from the seed 2D crystal edge. Simultaneously meeting criteria 2 and 3 is subtle, however, because of the interaction between BN and the Cu support. In the absence of graphene seeds, BN definitively aligns with the underlying Cu lattice (*2*). In contrast, graphene itself exhibits a wide distribution of orientations relative to the underlying Cu lattice (*18*). For intended heteroepitaxy in 2D, therefore, it is not obvious whether the BN epistrip will preferably nucleate at the graphene edge, adopting its orientation, or elsewhere aligning to the Cu lattice. This work demonstrates that, at least in one prototypical material system, the epistrips indeed nucleate at the seed crystal edge to form a 2D heterostructure. The growth of other 2D crystals, such as metal dichalcogenides (*24*, *25*), has been established, providing the foundation to explore heteroepitaxy in 2D space based on those materials. There, the three criteria intertwine in different ways and need to be met by leveraging different mechanisms.

References and Notes

1. H. Kroemer, *J. Cryst. Growth* **81**, 193–204 (1987).
2. Supplementary materials are available on *Science* Online.
3. Q. Yu *et al.*, *Nat. Mater.* **10**, 443–449 (2011).
4. I. Vlassiouk *et al.*, *ACS Nano* **5**, 6069–6076 (2011).

5. Y. Zhang, Z. Li, P. Kim, L. Zhang, C. Zhou, *ACS Nano* **6**, 126–132 (2012).
6. S. Choubak, M. Biron, P. L. Levesque, R. Martel, P. Desjardins, *J. Phys. Chem. Lett.* **4**, 1100–1103 (2013).
7. J. D. Plummer *et al.*, *Silicon VLSI Technology: Fundamentals, Practices and Modeling* (Prentice Hall, Upper Saddle River, NJ, 2000).
8. M. Ohring, *Materials Science of Thin Films* (Academic Press, Waltham, MA, ed. 2, 2002).
9. M. P. Levendorf *et al.*, *Nature* **488**, 627–632 (2012).
10. Z. Liu *et al.*, *Nat. Nanotechnol.* **8**, 119–124 (2013).
11. S. M. Kim *et al.*, *Nano Lett.* **13**, 933–941 (2013).
12. Y. B. Gao *et al.*, *Nano Lett.* **13**, 3439–3443 (2013).
13. P. Sutter, R. Cortes, J. Lahiri, E. Sutter, *Nano Lett.* **12**, 4869–4874 (2012).
14. J. Tian *et al.*, *Nano Lett.* **12**, 3893–3899 (2012).
15. C. Oshima, A. Nagashima, *J. Phys. Condens. Matter* **9**, 1–20 (1997).
16. Y. Zhang *et al.*, *Nat. Phys.* **4**, 627–630 (2008).
17. S. Joshi *et al.*, *Nano Lett.* **12**, 5821–5828 (2012).
18. J. M. Wofford, S. Nie, K. F. McCarty, N. C. Bartelt, O. D. Dubon, *Nano Lett.* **10**, 4890–4896 (2010).
19. J. M. Pruneda, *Phys. Rev. B* **81**, 161409 (2010).
20. S. Bhowmick, A. K. Singh, B. I. Yakobson, *J. Phys. Chem. C* **115**, 9889–9893 (2011).
21. J. Wintterlin, M.-L. Bocquet, *Surf. Sci.* **603**, 1841–1852 (2009).
22. X. Li *et al.*, *Science* **324**, 1312–1314 (2009).
23. K. K. Kim *et al.*, *Nano Lett.* **12**, 161–166 (2012).
24. S. Najmaei *et al.*, *Nat. Mater.* **12**, 754–759 (2013).
25. A. M. van der Zande *et al.*, *Nat. Mater.* **12**, 554–561 (2013).

Acknowledgments: This work was partially supported by NSF (ECCS-1231808), the Defense Advanced Research Projects Agency (approved for public release; distribution is unlimited), and the National Secretariat of Higher Education, Science, Technology and Innovation of Ecuador (SENESCYT). A portion of this research was conducted at the Center for Nanophase Materials Sciences (CNMS), which is sponsored at Oak Ridge National Laboratory by the Scientific User Facilities Division, Office of Basic Energy Sciences, U.S. Department of Energy. Work at Sandia was supported by the Office of Basic Energy Sciences, Division of Materials and Engineering Sciences, U.S. Department of Energy, under contract DE-AC04-94AL85000. We thank R. M. Feenstra for discussions on LEEM. Authors declare no conflicts of interest.

Supplementary Materials
www.sciencemag.org/content/343/6167/163/suppl/DC1
Materials and Methods
Supplementary Text
Figs. S1 to S11
Reference (*26*)

18 September 2013; accepted 3 December 2013
10.1126/science.1246137

Self-Accelerating CO Sorption in a Soft Nanoporous Crystal

Hiroshi Sato,[1,2] Wataru Kosaka,[1,2] Ryotaro Matsuda,[1,2]* Akihiro Hori,[2] Yuh Hijikata,[3] Rodion V. Belosludov,[4] Shigeyoshi Sakaki,[3] Masaki Takata,[2,5] Susumu Kitagawa[1,2,6]*

Carbon monoxide (CO) produced in many large-scale industrial oxidation processes is difficult to separate from nitrogen (N_2), and afterward, CO is further oxidized to carbon dioxide. Here, we report a soft nanoporous crystalline material that selectively adsorbs CO with adaptable pores, and we present crystallographic evidence that CO molecules can coordinate with copper(II) ions. The unprecedented high selectivity was achieved by the synergetic effect of the local interaction between CO and accessible metal sites and a global transformation of the framework. This transformable crystalline material realized the separation of CO from mixtures with N_2, a gas that is the most competitive to CO. The dynamic and efficient molecular trapping and releasing system is reminiscent of sophisticated biological systems such as heme proteins.

Carbon monoxide (CO) is a central resource for carbon-based chemical products such as polymer fibers, plastics, and medicines (*1*–*4*). Although huge amounts of CO are produced in industrial processes such as steel manufacturing, CO is mixed with other gases (such as unburned N_2 from air). This exhaust gas cannot be used as a carbon resource and is burned to produce a huge amount of CO_2. For effective separation, the selective uptake and ready release of CO are inseparable; however, these objectives often conflict because the trade-off for the increase in interaction with CO is some loss of ease in subsequent CO release. To date, CO separation has been limited to processes that strongly chemisorb CO on transition metal ions such as monovalent Cu^+ (*5*), but high temperatures are required to release CO. A synergistic system that makes use of a weak local interaction and subsequent global structural change could overcome this limitation in a manner similar to allosteric effects in the binding and release of O_2 by heme proteins (*6*).

Despite their crystalline form, porous coordination polymers (PCPs) or metal-organic frameworks (*7*–*10*) can provide a nanometer-sized soft space that is transformable in response to guest accommodation (*11*–*17*). This feature encouraged us to create a synergy system in a PCP solid to achieve the ultimate separation of mixed gases. Herein, we report on a PCP that has specific but weak CO adsorption and recognition sites and a reversibly transformable framework. Weak adsorption of CO on the Cu^{2+} site induces marked global structural changes in a positive cooperative manner, which produces additional space and allows further adsorption of CO as so-called reversible self-accelerating CO adsorption (fig. S1 and movie S1) (*18*). As a result, this crystalline porous compound achieved unprecedented highly effective trapping of CO from a gas mixture with N_2.

We prepared the PCP **1** composed of 5-azidoisophthalate (aip) (*19*) and divalent Cu^{2+} ions. In the as-synthesized crystal of PCP **1** {[Cu(aip)(H_2O)](solvent)$_n$, (where n is the number of solvent molecules)}, the Cu^{2+} and aip ligands form Cu^{2+} paddle-wheel units, the axial positions of which are occupied by water molecules (Fig. 1A). An infinite kagomé-type two-dimensional (2D) sheet structure (*20*, *21*) is formed through the connection between the paddle-wheel units by the aip ligands (Fig. 1B). The 2D sheets are stacked with a separation distance of 6.7 Å, creating two types of 1D infinite channels with cross-section sizes of 9 × 9 Å^2 (channel *L*; hexagonal larger channel) and 4 × 4 Å^2 (channel *S*; triangular smaller channel), respectively, along the *c* axis (Fig. 1, B to D). The total solvent-accessible volume was estimated to be 38% (766 Å^3) of the unit cell volume. The contributions by channels *L* and *S* to the total solvent-accessible volume were estimated as 65% (498 Å^3) and 35% (268 Å^3), respectively.

Thermogravimetric analysis (fig. S2) (*18*) indicated that the guest molecules were easily removed by heating at 80°C to give a dried PCP **2** [Cu(aip)] that is thermally stable up to ~180°C. We determined the crystal structure of the dried PCP **2** by Rietveld analysis using synchrotron powder x-ray diffraction data (fig. S3) (*18*). The removal of water molecules from the axial site of the Cu^{2+} paddle-wheel unit caused one of the carboxylate oxygen atoms in the adjacent layer to coordinate to this site to form the paddle-wheel chains along the *c* axis (Fig. 1, E and H, and fig. S5) (*18*). We observed marked changes in the shape and volume of channels upon the removal of the guest molecules (Fig. 1, F and G). The total solvent-accessible volume was reduced from 38% of the unit cell to 25%. In the structure of the dried PCP **2**, the carboxylates twisted against the Cu-Cu axis, and the aromatic planes further inclined to the pores to make the channels narrower than those of the as-synthesized PCP **1**. We noted distinct shape changes in channel *S*. Channel *S* was squeezed at the neck, causing a structural change from a bellows-like shape (Fig. 1C) to a garlic-like shape (Fig. 1G) (each pore is almost separated). We expected that access of

[1]Institute for Integrated Cell-Material Sciences (WPI-iCeMS), Kyoto University, Kyoto 615-8510, Japan. [2]RIKEN SPring-8 Center, Hyogo 679-5148, Japan. [3]Fukui Institute for Fundamental Chemistry, Kyoto University, Kyoto 606-8103, Japan. [4]Institute for Materials Research, Tohoku University, Sendai 980-8577, Japan. [5]Japan Synchrotron Radiation Research Institute/SPring-8, Hyogo 679-5198, Japan. [6]Department of Synthetic Chemistry and Biological Chemistry, Graduate School of Engineering, Kyoto University, Kyoto 615-8510, Japan.

*Corresponding author. E-mail: rmatsuda@icems.kyoto-u.ac.jp (R.M.); kitagawa@icems.kyoto-u.ac.jp (S.K.)

the guest molecules would be greatly hindered. In addition, the dried PCP **2** easily recovered to the original PCP **1** configuration when it was exposed to air containing moisture, indicating that the structural transformation between PCP **1** and **2** is completely reversible upon water introduction and removal.

It is generally considered very difficult to distinguish and separate CO from N_2 in industrial processes, because their electronic structures, sizes, and physicochemical properties (boiling points, critical temperatures, etc.) are quite similar (table S1) (*18*). However, we deduced from the above-mentioned structural viewpoints that PCP **2** would show a contrasting sorption be-

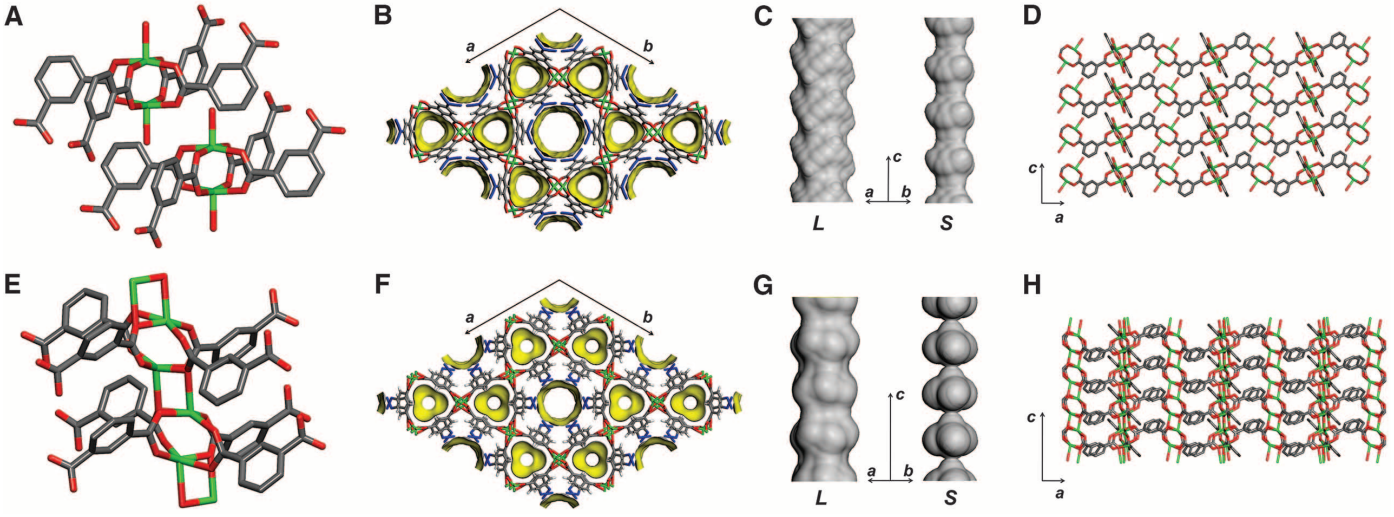
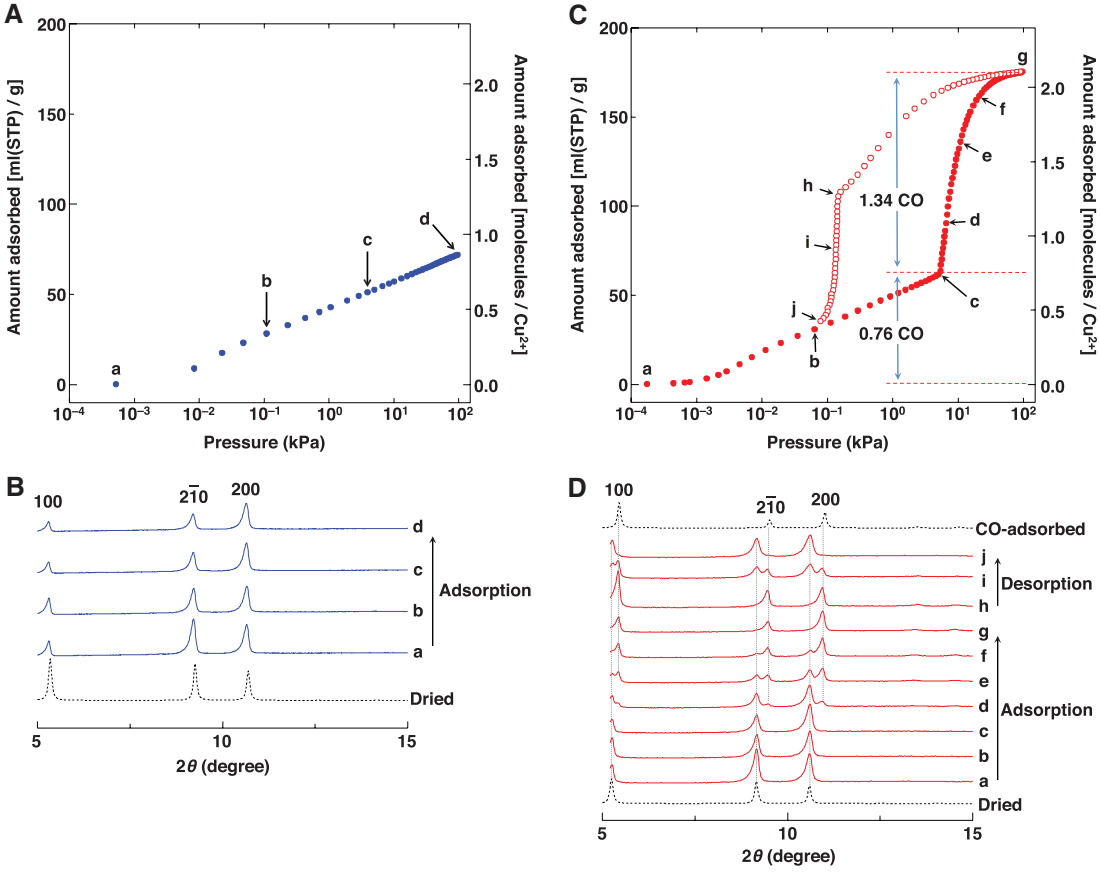


Fig. 1. Crystal structures and channel shapes of PCP 1 (A to D) and 2 (E to H). Atoms are colored as follows: Cu, green; C, gray; N, blue; O, red; H, white. Azide moieties and hydrogen atoms are omitted for clarity, except for in (B) and (F). (A) Coordination environment of Cu^{2+} in **1**. (B) Porous structure of **1** with Connoly surfaces. (C) Connolly surfaces of channels *L* and *S* in **1**. (D) Stacking of the kagomé-type 2D structures. (E) Coordination environment of Cu^{2+} in **2**. (F) Porous structure of **2** with Connoly surfaces. (G) Connolly surfaces of channels *L* and *S* in **2**. (H) Interconnection of the kagomé-type 2D sheets in **2**. The Connoly surfaces are calculated with a probe radius of 1.88 Å (a radius of CO).

Fig. 2. Coincident XRPD and sorption measurements of PCP 2. (**A**) N_2 sorption isotherms at 120 K. (**B**) XRPD patterns measured at each point (a to d) shown in the N_2 sorption isotherms. The simulated pattern for the dried PCP **2** is shown at the bottom. (**C**) CO sorption isotherms at 120 K. Adsorption and desorption profiles are shown in solid and open circles, respectively. (**D**) XRPD patterns measured at each point (a to j) shown in the CO sorption isotherms. The simulated patterns for the dried PCP **2** and CO-adsorbed PCP **3** are shown at the bottom and top, respectively.



havior for each of these two gases. We studied the sorption behavior of CO and N_2 on PCP **2** and its structural changes upon sorption by in situ x-ray powder diffraction (XRPD) and sorption coincident measurements (*22*) (Fig. 2). In the adsorption isotherm of N_2 at 120 K (Fig. 2A), the adsorbed amount of N_2 was gradually increased up to 71 ml [at standard temperature and pressure (STP)] g^{-1} (0.85 molecules per Cu^{2+}) at 80 kPa. In contrast, the adsorption isotherm of CO for PCP **2** at 120 K showed clear steps at ~5 kPa (c in Fig. 2C). At the first step, PCP **2** adsorbed 63 ml (STP) g^{-1} of CO (0.76 molecules per Cu^{2+}), then 112 ml (STP) g^{-1} of additional CO (1.34 molecules per Cu^{2+}) was adsorbed up to 80 kPa. The total adsorbed amount of CO [175 ml (STP) g^{-1} at 80 kPa, 2.10 molecules per Cu^{2+}] was much greater than that of N_2 [71 ml (STP) g^{-1} at 80 kPa].

The difference between the isotherms of N_2 and CO on PCP **2** is quite exceptional. Indeed, various porous materials—including a material with specific recognition sites, such as accessible metal sites (AMSs) {$[Cu_3(btc)_2(H_2O)_3]$, where btc is benezene-1,3,5-tricarboxylate (*23*); one of the most popular PCPs with AMSs}—show almost the same isotherms for both adsorbates (figs. S6 to S8) (*18*). The most notable features of CO sorption on PCP **2** are the very steep adsorption (c to f in Fig. 2C) and desorption (h to j in Fig. 2C), which are indicative of highly cooperative sorption events. To examine the degree of cooperativity, we applied Hill model analysis for the CO sorption isotherm on PCP **2** (fig. S9) (*18*). The Hill model is used to evaluate the cooperativity in the binding of substrates to proteins, such as oxygen in hemoglobin (*24*). Surprisingly, the Hill coefficient in the second step of the CO adsorption isotherm was estimated to be 20.3, indicating that PCP **2** adsorbs CO molecules in a highly positive cooperative manner, and CO binding accelerates further accommodation of CO molecules.

During the N_2 adsorption process, we did not observe any appreciable positional changes in the peaks of the XRPD patterns, indicative of few structural changes (Fig. 2B). However, upon CO adsorption and desorption, we noted pronounced changes in the XRPD patterns (Fig. 2D). Although the XRPD pattern of PCP **2** did not change markedly in the initial CO adsorption (points a to c in the isotherm), after point c, the original peaks of PCP **2** gradually diminished and new peaks appeared in the higher-angle region, indicative of structural contraction. These results show that the steep uptake after point c accompanied a structural change. The XRPD pattern finally obtained at point g was similar to the profile obtained from the as-synthesized PCP **1** before desolvation. This profile change indicates that the dried PCP **2** returned to a similar structure to that of PCP **1** during the second step. Similarly, the XRPD patterns did not show any notable change up to point h in the desorption isotherm. Thereafter, clear structural changes occurred after point h, and the peaks finally appeared at similar positions to those obtained from the dried PCP **2** and, thus, were indicative of reversible sorption and structural change.

No crystal structure of the Cu^{2+}–CO complex has been reported so far. Previously, divalent Cu ion was not expected to form stable coordination bonds with CO molecules, because the interaction between Cu^{2+} and CO is usually very weak. Theoretical analyses also showed that the Cu^{2+}–CO bond in a discrete complex is too weak to form a stable bond because of the small contribution of the π back-donation (see supplementary materials). However, via Rietveld analysis with the synchrotron XRPD data of PCP **2** in a CO atmosphere (50 kPa) at 100 K, we successfully obtained the crystal structure of PCP **3** containing a Cu^{2+}–CO complex module (Fig. 3 and figs. S4 and S5) (*18*). The connection between the paddle-wheel units through the oxygen atoms of the carboxylates was uncoupled by the coordination of CO molecules (fig. S5D) (*18*). The coordination of CO induces a global structural change that creates a suitable compartment for

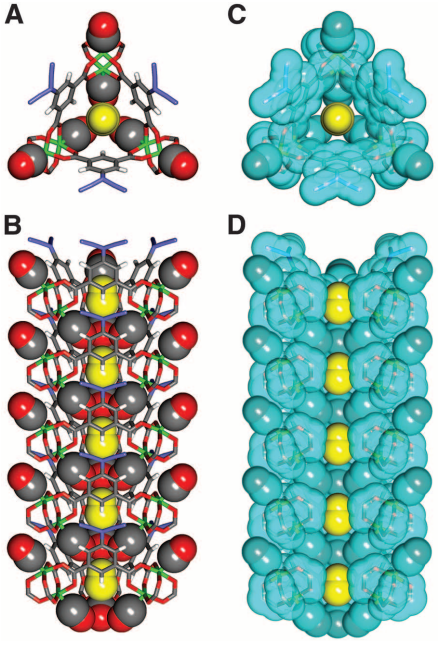


Fig. 3. X-ray crystal structures of CO-adsorbed PCP 3. (**A** and **B**) Top and side views of CO-adsorbed channel *S*. (**C** and **D**) Top and side views of CO-adsorbed channel *S* with van der Waals surfaces depicted in light blue. Atoms are colored as follows: Cu, green; C, gray; N, blue; O, red; H, white. Coordinated (gray and red) and noncoordinated (yellow) CO molecules are shown in a CPK model. In (D), part of the aryl moieties have been omitted for clarity.

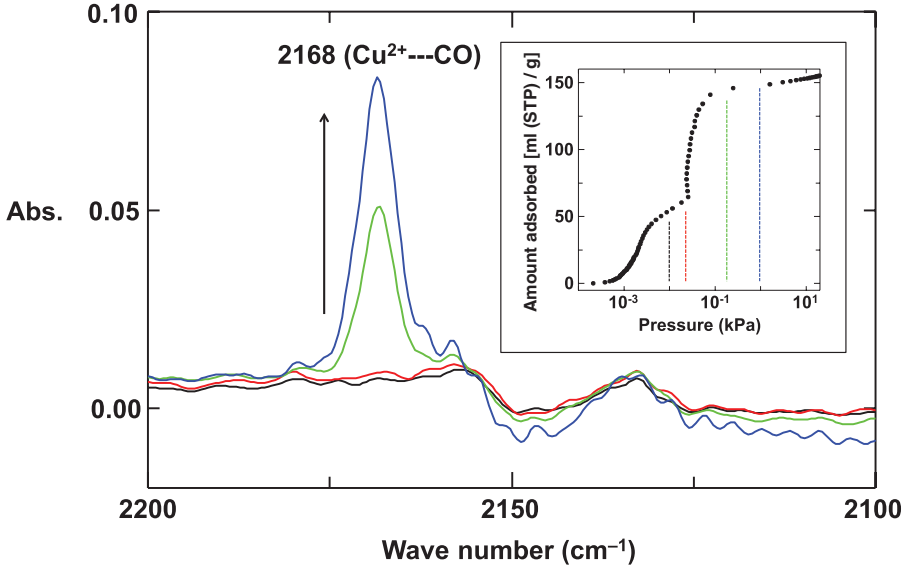


Fig. 4. Infrared spectra of CO adsorbed on PCP 2 at 81.7 K. The spectra were recorded upon increasing CO pressure (10 Pa; black, 30 Pa; red, 150 Pa; green, 1 kPa; blue). The peak at 2168 cm^{-1} can be assigned to the stretching vibration mode of CO interacting with Cu^{2+} sites. Abs., absorbance (arbitrary unit). (**Inset**) CO adsorption isotherm measured at 81.7 K. The dashed vertical lines show the pressures at each measurement.

further accommodation of CO molecules in the center of channel *S*. The one CO molecule per three Cu^{2+} ions (0.333 CO molecules per Cu^{2+}) is accommodated in the compartments and those CO molecules align in a 1D fashion in channel *S* (Fig. 3). Thus, the total number of CO molecules adsorbed in channel *S* is calculated to be 1.333 per Cu^{2+}. We also found CO molecules in channel *L* (0.76 molecules per Cu^{2+}), which shows disorder in two positions with an occupancy of 0.38 (fig. S5E) (*18*).

The mechanism for the stepwise sorption of CO can be explained as follows (fig. S1 and movie S1) (*18*): In the first step in the isotherm, CO molecules are physically adsorbed exclusively in the larger channel *L* without marked structural change to the framework because of poor accessibility to the highly constricted channel *S*. After filling channel *L*, CO molecules start to form a Cu^{2+}–CO bond, inducing a global structural transformation with the expansion of the squeezed paths. This expansion promotes additional CO adsorption in the center of channel *S*, which is the so-called self-accelerating gas adsorption. The adsorption event in the channel *S* is reminiscent of hemoglobin efficiently trapping O_2 through allosteric effects.

In situ infrared spectra, which were recorded from PCP **2** for various pressures of CO atmosphere at 81.7 K, support the suggested mechanism that the structural transformation was induced by Cu^{2+}–CO bond formation (Fig. 4). We assigned the peak that appeared at 2168 cm^{-1} to the stretching vibration mode of CO interacting with Lewis acid metal sites (*25*, *26*). In the spectra, although the characteristic vibrational mode did not appear at the pressure below the flex point (0.03 kPa at 81.7 K), a clear increase in intensity of the peak was seen over the second-step pressure region, indicative of the formation of the Cu^{2+}–CO bond. These results suggest that weak coordination of CO molecules on the Cu^{2+} sites induced the global structural change. From the theoretical calculation, the adsorption energy for CO adsorption on a discrete paddle-wheel–type model complex was calculated to be –20.4 kJ mol^{-1} (exothermic process), which corresponds to a weak chemisorption. We also used adsorption data collected at 120, 130, and 140 K to evaluate the isosteric heat of CO adsorption, q_{st}, for PCP **2** from the Clausius-Clapeyron equation (fig. S10) (*18*). The q_{st} was estimated to be –19 kJ mol^{-1} at 87 ml (STP) g^{-1} of CO adsorbed (= 1.0 molecules per Cu^{2+}).

We tested PCP **2** for its CO separation ability with various compositions of CO mixtures with N_2 (percent CO: 10 to 80%) (figs. S11 to S13) (*18*). While the dried PCP **2** was exposed to mixtures of CO and N_2 in 100 kPa, an equilibrium state was achieved by gradually decreasing the temperature from 300 to 81.7 K, and the adsorbed gas ratios were examined by gas chromatography analysis. For example, a surprising enrichment of CO of 85 and 94% was achieved after the first and second cycles starting from a 1:1 mixture of CO and N_2, respectively. Furthermore, PCP **2** has a much higher separation ability than various types of porous materials over a wide range of CO concentrations (fig. S14) (*18*). In the adsorption events of CO-N_2 mixtures in PCP **2**, it might be possible that N_2 molecules were also incorporated in the center of channel *S* instead of CO. However, the 1D small channel *S* of PCP **2** with an open-close system can enhance the selectivity by the following kinetic mechanism (fig. S19) (*18*): Because of the size restriction, neither CO nor N_2 molecule can diffuse into the channel *S* without expansion of the narrow path. CO can expand the path when it breaks a coordination bond between Cu and O atoms (from carboxylates) and forms a coordination bond with Cu, realizing the diffusion of CO into the channel. However, N_2 cannot expand the path because of extremely weak coordination ability. In addition, even after the expansion of narrow path by CO, N_2 cannot diffuse into the channel because the path is surrounded by the coordinated three CO molecules that sterically refuse the access of N_2 (Fig. 1G and fig. S17) (*18*). Thermodynamic preference of CO inclusion in channel *S* might also contribute to the effective separation. The results of first-principles calculations indicated that N_2 inclusion in channel *S* is less favorable. Regardless of CO or N_2 in channel *L*, full occupation of channel *S* with CO is much more favorable than that with N_2. For example, when the N_2 molecules are introduced in the center of channel *S* instead of CO, the adsorbed phase becomes unstable in the total binding energy (entries 1 and 8 in table S7) (*18*).

Our material is potentially applicable to processes enabling the separation of CO from mixtures with N_2, a gas that is the most competitive to CO, with a low-energy requirement. However, it may be necessary to use this process in combination with a precleanup of the exhaust gases to remove contaminants (such as water) that have a stronger coordinative affinity toward Cu^{2+} than CO. We believe that the concept of self-accelerating sorption in a soft nanoporous crystal (*27*, *28*) will not only lead to a new approach for the separation and storage of valuable gases without consuming large amounts of energy, but will also open up a new field of study intersecting with both crystalline porous materials and soft cooperative biomolecules.

References and Notes

1. K. Weissermel, H.-J. Arpe, *Industrial Organic Chemistry* (Wiley-VCH, Weinheim, Germany, ed. 5, 2008).
2. F. E. Paulik, J. F. Roth, *Chem. Commun.* **1968**, 1578a (1968).
3. A. Haynes, in *Advances in Catalysis*, B. Gates, H. Knoezinger, F. Jentoft, Eds. (Academic Press, Waltham, MA, 2010), vol. 53, pp. 1–45.
4. K. C. Waugh, *Catal. Today* **15**, 51–75 (1992).
5. J. A. Hogendoorn, W. P. M. van Swaaij, G. F. Versteeg, *Chem. Eng. J. Bioch. Eng.* **59**, 243–252 (1995).
6. G. A. Petsko, D. Ringe, *Protein Structure and Function* (Sinauer Associates, Sunderland, MA, 2003).
7. O. M. Yaghi *et al.*, *Nature* **423**, 705–714 (2003).
8. S. Kitagawa, R. Kitaura, S. Noro, *Angew. Chem. Int. Ed.* **43**, 2334–2375 (2004).
9. K. Sumida *et al.*, *Chem. Rev.* **112**, 724–781 (2012).
10. J.-R. Li, J. Sculley, H.-C. Zhou, *Chem. Rev.* **112**, 869–932 (2012).
11. L. C. Tabares, J. A. R. Navarro, J. M. Salas, *J. Am. Chem. Soc.* **123**, 383–387 (2001).
12. G. J. Halder, C. J. Kepert, B. Moubaraki, K. S. Murray, J. D. Cashion, *Science* **298**, 1762–1765 (2002).
13. R. Kitaura, K. Seki, G. Akiyama, S. Kitagawa, *Angew. Chem. Int. Ed.* **42**, 428–431 (2003).
14. C. Serre *et al.*, *Science* **315**, 1828–1831 (2007).
15. D. Bradshaw, J. E. Warren, M. J. Rosseinsky, *Science* **315**, 977–980 (2007).
16. B. D. Chandler *et al.*, *Nat. Mater.* **7**, 229–235 (2008).
17. J. Rabone *et al.*, *Science* **329**, 1053–1057 (2010).
18. Supplementary materials are available on *Science* Online.
19. H. Sato, R. Matsuda, K. Sugimoto, M. Takata, S. Kitagawa, *Nat. Mater.* **9**, 661–666 (2010).
20. B. Moulton, J. Lu, R. Hajndl, S. Hariharan, M. J. Zaworotko, *Angew. Chem. Int. Ed.* **41**, 2821–2824 (2002).
21. M. I. H. Mohideen *et al.*, *Nat. Chem.* **3**, 304–310 (2011).
22. S. Bureekaew *et al.*, *Angew. Chem. Int. Ed.* **49**, 7660–7664 (2010).
23. S. S.-Y. Chui, S. M.-F. Lo, J. P. H. Charmant, A. G. Orpen, I. D. Williams, *Science* **283**, 1148–1150 (1999).
24. A. V. Hill, *Proc. Phys. Soc.* **40**, 4–7 (1910).
25. E. Garrone, C. Otero Areán, *Chem. Soc. Rev.* **34**, 846–857 (2005).
26. S. Bordiga *et al.*, *Phys. Chem. Chem. Phys.* **9**, 2676–2685 (2007).
27. The pore sizes of PCP **1**, **2**, and **3** are in the region of micropores (less than 2 nm in diameter), which is defined by the International Union of Pure and Applied Chemistry (*28*).
28. J. Rouquerol *et al.*, *Pure Appl. Chem.* **66**, 1739–1758 (1994).

Acknowledgments: This work was supported by Exploratory Research for Advanced Technology, Japan Science and Technology Agency. H.S. and S.K. acknowledge the financial support of KAKENHI, a Grant-in-Aid for Specially Promoted Research (grant no. 25000007) by the Japan Society of the Promotion of Science. S.S. and Y.H. are thankful for a Grant-in-Aid for Specially Promoted Research (grant no. 22000009). R.V.B. would like to express sincere thanks to the staff of the Center for Computational Materials Science of the Institute for Materials Research, Tohoku University, for their continuous support of the SR16000-M1 supercomputing facilities and also to the Integrated Materials Research Center for a Low-Carbon Society and the Ministry of Education, Culture, Sports, Science, and Technology of Japan (grant no. 23241027) for financial support. The x-ray crystallographic coordinates for structures reported in this paper have been deposited at the Cambridge Crystallographic Data Centre under deposition numbers CCDC 973391, 973449, and 973450. These data can be obtained free of charge from the Cambridge Crystallographic Data Centre (www.ccdc.cam.ac.uk/Community/Requestastructure/Pages/DataRequest.aspx).

Supplementary Materials

www.sciencemag.org/content/343/6167/167/suppl/DC1
Materials and Methods
Supplementary Text
Figs. S1 to S21
Tables S1 to S7
References (*29*–*56*)
Movie S1

25 September 2013; accepted 3 December 2013
Published online 12 December 2013;
10.1126/science.1246423

Transient Water Vapor at Europa's South Pole

Lorenz Roth,[1,2]*† Joachim Saur,[2]† Kurt D. Retherford,[1] Darrell F. Strobel,[3,4] Paul D. Feldman,[4] Melissa A. McGrath,[5] Francis Nimmo[6]

In November and December 2012, the Hubble Space Telescope (HST) imaged Europa's ultraviolet emissions in the search for vapor plume activity. We report statistically significant coincident surpluses of hydrogen Lyman-α and oxygen OI 130.4-nanometer emissions above the southern hemisphere in December 2012. These emissions were persistently found in the same area over the 7 hours of the observation, suggesting atmospheric inhomogeneity; they are consistent with two 200-km-high plumes of water vapor with line-of-sight column densities of about 10^{20} per square meter. Nondetection in November 2012 and in previous HST images from 1999 suggests varying plume activity that might depend on changing surface stresses based on Europa's orbital phases. The plume was present when Europa was near apocenter and was not detected close to its pericenter, in agreement with tidal modeling predictions.

Europa's exceptional surface morphology suggests the existence of a layer of liquid water under the icy crust (*1*, *2*), which has been confirmed independently by magnetometer measurements (*3*). Despite signs of active resurfacing in chaos terrains (*4*) and the existence of a subsurface ocean, current geologic activity has not been observed directly in Voyager and Galileo observations (*2*, *5*, *6*) or in any other data. Europa also possesses a tenuous atmosphere generated by sputtering and radiolysis (*7*–*9*) that was detected in 1995 through Hubble Space Telescope (HST) ultraviolet (UV) observations of O emissions at 130.4 nm and 135.6 nm (*10*, *11*). Spatially revolved images of these atmospheric emissions obtained by the HST Space Telescope Imaging Spectrograph (STIS) revealed an irregular emission pattern at the two O multiplets, which originates from an inhomogeneous neutral gas abundance across the surface (*12*, *13*) or Europa's highly variable plasma environment, or both. An enhanced emission near 90°W longitude detected by the HST Advanced Camera for Surveys (ACS) was associated with a possible existence of plumes in a region where high shear stresses are expected, but an unambiguous correlation was not possible because of low data quality (*14*).

We report STIS spectral images of Europa's trailing/anti-jovian hemisphere and leading hemisphere obtained in November and December 2012, respectively. Previous observations, in 1999, targeted Europa's trailing hemisphere (Table 1). The observations in 2012 were timed to coincide with the maximum variation of Jupiter's magnetic field orientation at Europa. With this configuration, spatially inhomogeneous yet time-variable emissions originating from the periodically changing magnetospheric conditions can be separated from time-stationary emission inhomogeneities due to atmospheric anomalies.

After correction of the images for instrumental and background noise (*15*), the remaining emission sources are solar reflectance from Europa's surface, solar resonance scattering by atmospheric H and O atoms (negligible for OI 135.6 nm), and electron impact (dissociative) excitation of atmospheric species, such as O_2, O, and H_2O. To subtract the light reflected from the surface, we generated model spectral images by convolving normalized inverted visible images with a solar UV spectrum (*15*). Whereas the surface reflectance–corrected Lyman-α brightness is mostly consistent with a zero signal for the 1999 and November 2012 observations, a pronounced 400- to 600-rayleigh (R) (*16*) region is found above the limb near the south pole in the residual Lyman-α emission in the December 2012 image (Fig. 1I).

The residual atmospheric O emissions at 130.4 and 135.6 nm, in contrast, cover most of Europa's disk (Fig. 1, J to O). The 135.6/130.4 ratios of 1.6 ± 0.1 (both 1999 and November 2012) and 2.1 ± 0.2 (December 2012) are consistent with previous measurements and an O_2 atmosphere with a low mixing ratio of O (*10*, *11*). The O aurora morphologies underwent considerable variations during the ~7 hours of all observations (Fig. 2 and figs. S1 and S2). Bright OI 135.6-nm patches are found close to the poles, which appear to rock toward and away from Jupiter in correlation with the varying magnetic field orientation at Europa. The OI 130.4-nm aurora pattern roughly resembles the OI 135.6-nm pattern (I and N in figs. S1 and S2, respectively), as expected if both OI multiplets originate from electron-impact–dissociated O_2. Apparent deviations of the OI 130.4-nm morphology from the OI 135.6 emission can be attributed in part to the inhomogeneity of the higher surface reflectance at 130.4 nm. This becomes most apparent in the combined images (Fig. 1, J to L), because the time-variable atmospheric contributions are smoothed through the superposition. The generally patchy OI 130.4-nm morphology is additionally affected by the low signal-to-noise ratio (SNR) of the 130.4-nm emission (*15*).

We focus our analysis on the emission above the limb of Europa, which is only marginally influenced by the surface reflectance due to instrument-scattered light from the on-disk features. Above the south polar limb in the December 2012 composite images, an OI 130.4-nm enhancement of similar appearance was found in the same region as the Lyman-α enhancement (compare Fig. 1, I and L). Detectable Lyman-α and OI 130.4-nm emissions were persistently found above the southern anti-jovian limb during all five HST orbits of the December 2012 observations (Fig. 2, A to J). Bright OI 135.6-nm emissions across the entire south polar region shifted from the sub-jovian to the anti-jovian hemisphere between the first and last orbits (Fig. 2, K to O). A persistent or significant above-limb OI 135.6-nm emission surplus was not detected.

In a next step, we subdivided the region between 1 R_E (Europa radius, 1561 km) and 1.25 R_E (corresponding to an above-limb altitude of 390 km) into 18 bins spanning angles of 20° around the disk of Europa in all images (Fig. 3). The December 2012 Lyman-α image brightnesses of all pixels in limb bins 12 and 13 are 420 ± 136 R and 604 ± 140 R, which exceed the faint average limb emission of 46 R (outside the anomaly) by 2.8 and 4.0 times the propagated uncertainty (σ), respectively. The OI 130.4 emission of 59 ± 18 R in bin 13 is also significantly (2.4σ) higher than the average limb emission of 16 R, and bin 12

[1]Southwest Research Institute, San Antonio, TX, USA. [2]Institute of Geophysics and Meteorology, University of Cologne, Germany. [3]Department of Earth and Planetary Science, The Johns Hopkins University, Baltimore, MD, USA. [4]Department of Physics and Astronomy, The Johns Hopkins University, Baltimore, MD, USA. [5]NASA Marshall Space Flight Center, Huntsville, AL, USA. [6]Department of Earth and Planetary Sciences, University of California Santa Cruz, CA, USA.

*Corresponding author. E-mail: lorenz.roth@swri.edu
†These authors contributed equally to this work.

Table 1. HST/STIS G140L observations of Europa's UV emissions.

Observation start date and time	HST orbits/ exposures	Total exp. time (min)	Spatial resolution (km/pixel)	Sub-observer W long. (°)	System III longitude (°)	Mag. lat. range (°)	True anomaly *f* (°)	Water vapor detected
5 Oct. 1999 8:39*	5/9	156	71.5	245–274	300–158	−9.5 to 6.8	343–13	No
8 Nov. 2012 20:41†	5/10	183	73.9	209–238	25–243	−9.3 to 9.5	289–318	No
30 Dec. 2012 18:49†	5/9	164	74.9	79–108	0–218	−9.5 to 9.5	185–218	Yes

*PI M. A. McGrath. †PI J. Saur.

shows a slight enhancement (35 ± 17 R). At both lines, the emission anomaly appears to have two individual peaks in bins 12 and 13, which cannot, however, be clearly separated within the measurement uncertainties. No significant emission surplus is found in either of the bins at 135.6 nm (Fig. 3E). In 1999 and November 2012, all of the Lyman-α bins are consistent with zero signal within 2σ (*17*).

Detectable Lyman-α emission is not expected for the generally assumed abundance of H-bearing molecules ($\leq 10^{17}$ m^{-2}) in the global sputtered atmosphere (*7*–*9*). Lyman-α emission from a global atomic H corona that is not gravitationally bound as observed at Ganymede (*18*) would be isotropic. Lyman-α solar resonant scattering on atomic H also would require optically thick columns (>10^{17} m^{-2}) to produce brightnesses >400 R and can be excluded. In contrast, H_2O freezes (*19*), and any enhancement must be localized to its source. In addition, electron impact on H_2O ($e + H_2O$) yields HI 121.6 nm and OI 130.4 nm, but has a lower cross section at 135.6 nm (*20*). Hence, the emission surplus at HI 121.6 nm and OI 130.4 nm in an area, where no remarkable enhancement of OI 135.6 nm is found, suggests a local atmospheric H_2O enhancement.

We derived average H_2O and O_2 column densities using measured cross sections for electron-impact dissociative excitation and the standard plasma parameters for Europa (*15*). Neglecting presumably small contributions from e + O or $e + H_2O$, the observed OI 135.6-nm brightness of bin 13 requires a line-of-sight O_2 column of ~5×10^{19} m^{-2}. The Lyman-α brightness in bin 13 implies an optically thin H_2O column density of 1.5×10^{20} m^{-2}. In this case, excitation of O_2 and H_2O would contribute 27 and 29 R, respectively, to the OI 130.4-nm emission, which is consistent with the measured brightness of 59 ± 18 R in bin 13. Thus, the Lyman-α/OI 130.4-nm/OI 135.6-nm ratios are diagnostic of $e + H_2O$ in an approach similar to the average OI 135.6-nm/OI 130.4-nm ratio being diagnostic of $e + O_2$ (*10*, *11*).

We generated model images for two three-dimensional plume distributions, taking into account H_2O continuum absorption and resonant scattering. We started by generating a standard model for an average background atmosphere by adjusting the density of an exponentially decreasing O_2 atmosphere with low O and H_2O mixing ratios (*15*) to the observed OI 135.6-nm limb brightness for all observations (Fig. 3, E and F, dotted gray line). The fitted vertical O_2 column density of $N_{O2} = 3.5 \times 10^{18}$ m^{-2} agrees well with the observed OI 130.4 limb brightness and is consistent with previous results (*7*–*11*, *21*). Deviations from the model in several bins for both O aurora lines are probably attributable to the variable plasma environment.

We then generated model images with two local H_2O plumes (*15*). We adjusted the plume height of 200 km and the latitudinal expansion of 10° (or ~270 km on the surface) to the observed spatial profile of the Lyman-α emissions. The implemented density profile resembles an intermediate case between Io's shock-dominated Pele-type plumes (*22*) and the low-gravity outgassing of the Enceladus plumes (*23*). Because the surface source locations cannot be determined from the images, the plumes were arbitrarily centered on the anti-jovian meridian (180°W) and in the center of bins 12 and 13 at 55° and 75°S, respectively. The densities of the plumes were fit to the observed Lyman-α bin brightness, yielding total contents of 4.9×10^{31} and 8.2×10^{31} H_2O molecules for the plumes at 55° and 75°S, respectively. The combined plume content is one to two orders of magnitude higher than the H_2O abundance in global atmosphere models without plumes (*7*–*9*). The derived H_2O plume densities independently match the observed OI 130.4-nm emission surplus, if resonant scattering and electron impact on O with an estimated mixing ratio of O/H_2O ~ 0.2% are taken into account (*15*).

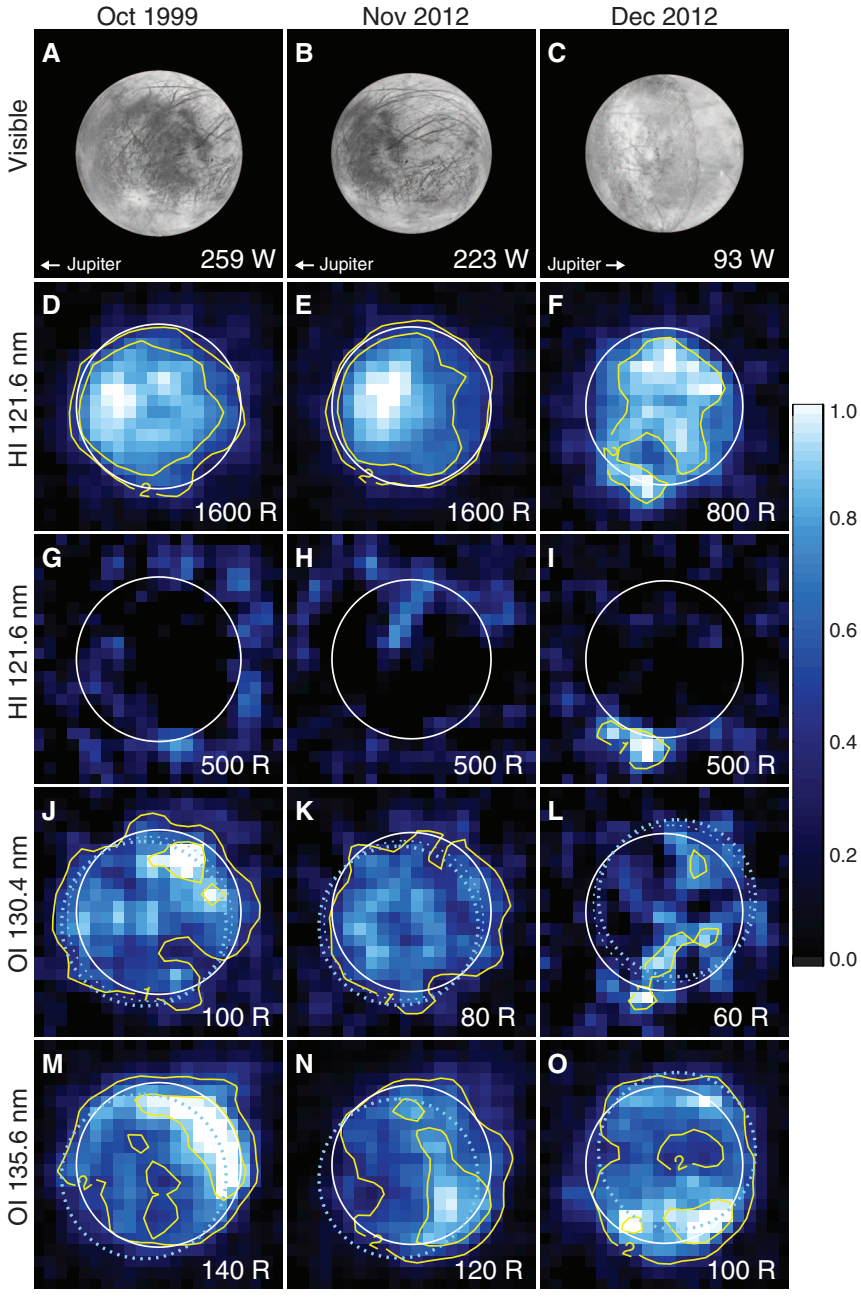


Fig. 1. Visible images of the observed hemispheres (A to C) with sub-observer longitudes listed and combined STIS images of the H and O emissions (D to O) (Table 1). The Lyman-α morphology [(D) to (F)] reveals an anticorrelation with the brightness in the visible (*15*). (G) to (O) Same Lyman-α images and OI 130.4-nm and OI 135.6-nm images with solar disk reflectance subtracted. 3 × 3 pixels are binned, and the STIS images are smoothed to enhance the visibility of the significant features. The dotted light blue circles indicate the multiplet lines (*15*). The color scale is normalized to the respective brightness, and the scale maximum (corresponding to 1.0 on the scale) is listed in each image. Oversaturated pixels with intensities above maximum are white. The contours show SNR ratios of the binned pixels [and contours for SNR = 1 are omitted here in (D) to (F) and (M) to (O)].

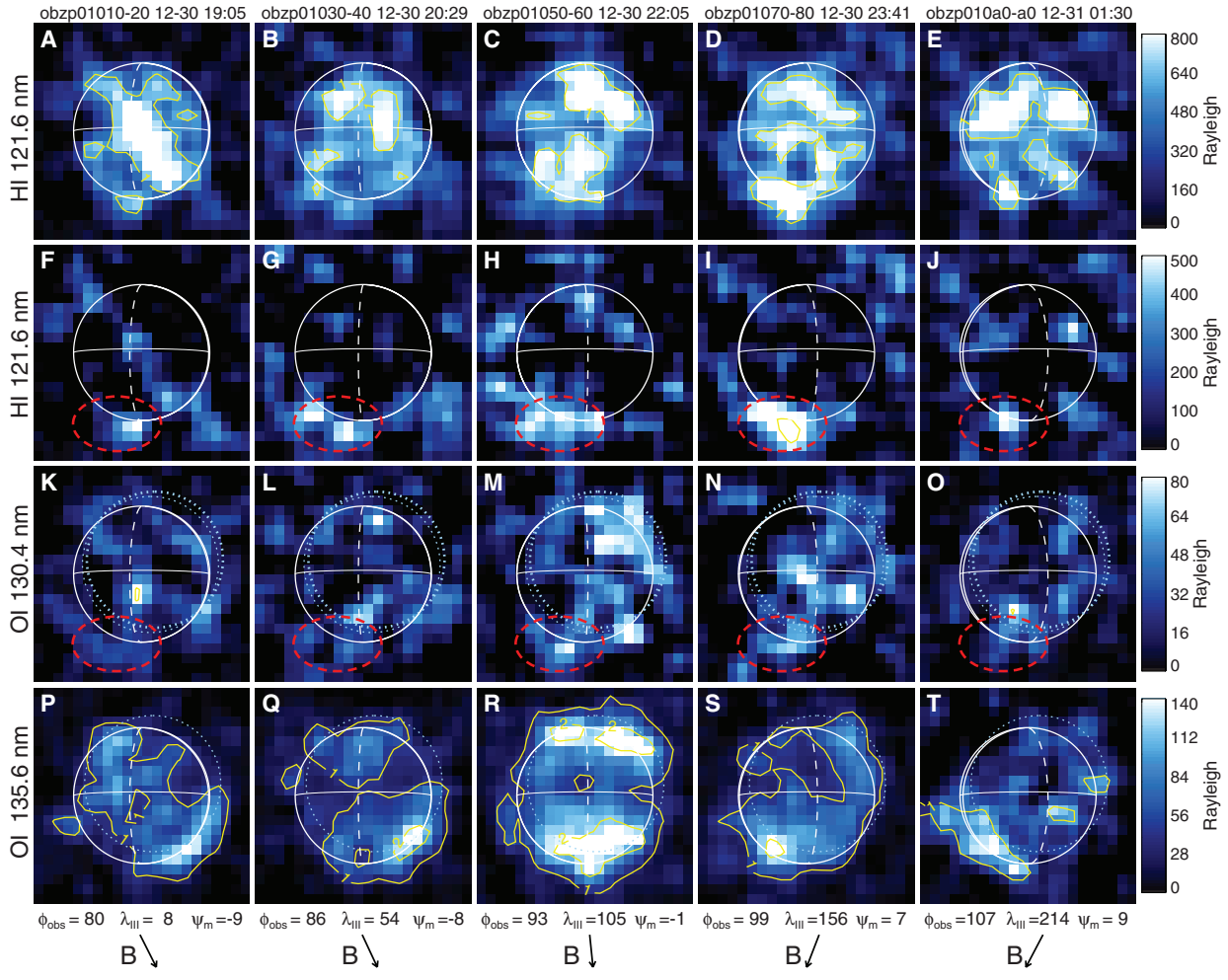


Fig. 2. Individual STIS images of the five HST orbits from December 2012. Lyman-α emissions before disk-reflectance subtraction (**A** to **E**) and reflectance-subtracted Lyman-α and O emissions (**F** to **T**). The persistent plume emission is highlighted by the dashed red circles. Sub-observer longitude ϕ_{obs}, jovian system III longitude λ_{III}, magnetic latitude ψ_m, and projected magnetic field line *B* are listed at the bottom of the figure. The leading meridian (90°W) is shown by a dashed white line, and the equator shown by a solid white line. Other details are as in Fig. 1.

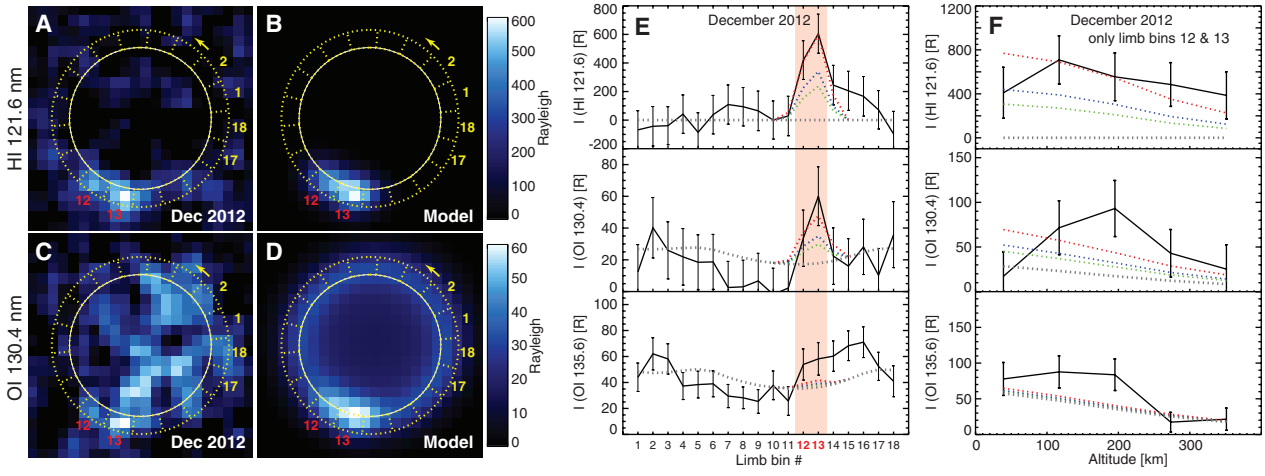


Fig. 3. Comparison of December 2012 observations and atmosphere plume model results. (**A** to **D**) Lyman-α and OI 130.4-nm STIS images (as in Fig. 1) and model aurora images from a global atmosphere with two H_2O plumes. The south polar above-limb emission is found in bins 12 and 13 (vertical shaded bar) of the 18 20° bins illustrated by the dotted yellow lines. The patchiness of the 130.4-nm on-disk emissions might originate from surface reflectance or atmospheric or plasma inhomogeneities, but it is also consistent with statistically expected variations across a uniform disk (*15*). (**E**) Measured (solid black line) and modeled (dotted lines) brightnesses of each 20°-wide limb bin around Europa's disk. The best-fit plume model atmosphere is shown in red, and plume densities decreased by a factor 2 and 3 are shown in blue and green, respectively. (**F**) Radial profiles of measured and modeled brightness versus altitude in bins 12 + 13.

The model reasonably reproduces the Lyman-α plume morphology and brightness decrease with altitude (Fig. 3). At low altitudes (<100 km), the measured brightness decreases for both the Lyman-α and OI 130.4-nm emission. Because bright OI 135.6-nm emission is also detected up to altitudes of 200 km, the OI 130.4-nm profile might be best explained by a peak in O abundance at higher altitudes. Also, the derived plume height of 200 km is higher than expected from model results (*24*) and would require large supersonic eruption velocities of ~700 m/s. However, interpretation of the derived height and radial profile requires caution because of the systematic uncertainties of the disk location by one or two pixels or ~100 km. Moreover, a local density enhancement within a smooth global atmosphere would substantially alter the plasma environment, which in turn modifies the aurora morphology and brightness (*25*).

The high plume velocities and relatively low number densities we inferred are consistent with vapor emission from narrow fractures (*15*), as occurs at Enceladus (*23*, *26*). The surface area of Europa's fractures is too small to produce a thermal anomaly detectable by the Galileo Photopolarimeter-Radiometer instrument (*27*). Plume fallback could produce terrain softening in the near-polar regions, which might be detectable in suitable high-resolution images (*15*).

The modeled Lyman-α limb brightnesses for the 1999 and November 2012 geometries are not consistent with persistent plumes. Also, no striking surplus of OI 130.4-nm emission was detected. The model indicates that the plumes were less dense by at least a factor of 2 and 3 during the 1999 and November 2012 observations, respectively, if present (fig. S3). Thus, the plume activity appears to undergo considerable variability.

Recently, the plumes at Enceladus' south pole have been shown to be more active near the apocenter than at the pericenter (*28*). Similar tidal stress variability for Europa is expected to open and close its Linea features [fig. S4 (*15*)]. Europa was very close to its apocenter during the December 2012 observations and was shortly before and at the pericenter during the 1999 and November 2012 observations (Table 1). This causal relationship might explain the observed variability and the lack of detections in 1999 and November 2012. The plume variability, if real, verifies a key prediction of tidal-flexing models based on the existence of a subsurface ocean.

References and Notes

1. M. H. Carr *et al.*, *Nature* **391**, 363–365 (1998).
2. R. T. Pappalardo *et al.*, *J. Geophys. Res.* **104**, 24015–24055 (1999).
3. K. K. Khurana *et al.*, *Nature* **395**, 777–780 (1998).
4. B. E. Schmidt, D. D. Blankenship, G. W. Patterson, P. M. Schenk, *Nature* **479**, 502–505 (2011).
5. C. B. Phillips *et al.*, *J. Geophys. Res.* **105**, 22579–22597 (2000).
6. S. A. Fagents, *J. Geophys. Res.* **108**, 5139 (2003).
7. V. I. Shematovich, R. E. Johnson, J. F. Cooper, M. C. Wong, *Icarus* **173**, 480–498 (2005).
8. W. H. Smyth, M. L. Marconi, *Icarus* **181**, 510–526 (2006).
9. C. Plainaki *et al.*, *Icarus* **218**, 956–966 (2012).
10. D. T. Hall, D. F. Strobel, P. D. Feldman, M. A. McGrath, H. A. Weaver, *Nature* **373**, 677–679 (1995).
11. D. T. Hall, P. D. Feldman, M. A. McGrath, D. F. Strobel, *Astrophys. J.* **499**, 475–481 (1998).
12. M. A. McGrath, C. J. Hansen, A. R. Hendrix, in *Europa*, R. T. Pappalardo, W. B. McKinnon, K. K. Khurana, Eds. (Univ. of Arizona Press, Tucson, AZ, 2009), pp. 485–505
13. T. A. Cassidy, R. E. Johnson, M. A. McGrath, M. C. Wong, J. F. Cooper, *Icarus* **191**, 755–764 (2007).
14. J. Saur *et al.*, *Astrophys. J.* **738**, 153 (2011).
15. See the supplementary materials for more information.
16. Rayleigh (R) is the column emission rate of 10^{10} photons per square meter per column per second, 1 R = $10^{10}/4\pi$ photons m^{-2} sr^{-1} s^{-1}.
17. The 1999 Lyman-α image might hint at a plume feature in the south polar region (Fig. 1G), but is not statistically significant and is therefore not considered further.
18. C. A. Barth *et al.*, *Geophys. Res. Lett.* **24**, 2147–2150 (1997).
19. J. R. Spencer, L. K. Tamppari, T. Z. Martin, L. D. Travis, *Science* **284**, 1514–1516 (1999).
20. O. P. Makarov *et al.*, *J. Geophys. Res.* **109**, A09303 (2004).
21. J. Saur, D. F. Strobel, F. M. Neubauer, *J. Geophys. Res.* **103**, 19947–19962 (1998).
22. J. Zhang *et al.*, *Icarus* **163**, 182–197 (2003).
23. F. Tian, A. I. F. Stewart, O. B. Toon, K. W. Larsen, L. W. Esposito, *Icarus* **188**, 154–161 (2007).
24. S. A. Fagents *et al.*, *Icarus* **144**, 54–88 (2000).
25. L. Roth, J. Saur, K. D. Retherford, D. F. Strobel, J. R. Spencer, *Icarus* **214**, 495–509 (2011).
26. C. J. Hansen *et al.*, *Geophys. Res. Lett.* **38**, L11202 (2011).
27. J. A. Rathbun, N. J. Rodriguez, J. R. Spencer, *Icarus* **210**, 763–769 (2010).
28. M. M. Hedman *et al.*, *Nature* **500**, 182–184 (2013).

Acknowledgments: This work is based on HST observations available at the NASA Mikulski Archive for Space Telescopes. Support for program number GO-13040 was provided by NASA through a grant from the Space Telescope Science Institute, which is operated by the Association of Universities for Research in Astronomy, under contract NAS5-26555; and by Verbundforschung Astronomie und Astrophysik.

Supplementary Materials

www.sciencemag.org/content/343/6167/171/suppl/DC1
Materials and Methods
Supplementary Text
Figs. S1 to S10
Tables S1 to S2
References (*29*–*70*)

10 October 2013; accepted 2 December 2013
10.1126/science.1247051

Strong Sensitivity of Pine Island Ice-Shelf Melting to Climatic Variability

Pierre Dutrieux,[1]* Jan De Rydt,[1] Adrian Jenkins,[1] Paul R. Holland,[1] Ho Kyung Ha,[2] Sang Hoon Lee,[2] Eric J. Steig,[3] Qinghua Ding,[3] E. Povl Abrahamsen,[1] Michael Schröder[4]

Pine Island Glacier has thinned and accelerated over recent decades, significantly contributing to global sea-level rise. Increased oceanic melting of its ice shelf is thought to have triggered those changes. Observations and numerical modeling reveal large fluctuations in the ocean heat available in the adjacent bay and enhanced sensitivity of ice-shelf melting to water temperatures at intermediate depth, as a seabed ridge blocks the deepest and warmest waters from reaching the thickest ice. Oceanic melting decreased by 50% between January 2010 and 2012, with ocean conditions in 2012 partly attributable to atmospheric forcing associated with a strong La Niña event. Both atmospheric variability and local ice shelf and seabed geometry play fundamental roles in determining the response of the Antarctic Ice Sheet to climate.

Austral summer observations in the Amundsen Sea, West Antarctica, show that lightly modified, warm (0.5° to 1.2°C) and saline (>34.6) Circumpolar Deep Water (CDW), 2° to 4°C above the in situ freezing point, pervades a network of glacially scoured seabed troughs (*1*) (Fig. 1A). The CDW reaches nearby Antarctic glaciers and delivers heat to the base of their 200- to 1000-m-thick ice shelves (*2*–*4*). It is overlain by a 200- to 300-m-thick layer of cold (–1.5°C) and fresh (salinity <34.4) Winter Water (WW, Fig. 2A) that is seasonally replenished by interaction with the atmosphere and sea ice.

Pine Island Glacier (PIG), a major outlet glacier feeding one such ice shelf, has shown apparently continuous thinning (*5*, *6*) and intermittent acceleration (*7*–*9*) from 1973 to 2009. During this period, its ice shelf has also thinned (*6*, *10*–*12*), and the reduction in buttressing driven by oceanic melting is believed to be responsible for the changes inland. Earlier analysis indicated that a higher CDW volume and temperature in Pine Island Bay (PIB) in January 2009 caused an increase in ice-shelf melting and in the associated meltwater-driven circulation, relative to 1994 (*2*). The lack of subannual variability in CDW temperature during 1-year-long measurement in PIB (*1*) and the long-term correlation between the oceanic melting and the mass loss required to sustain thinning of the ice shelf gave the impression that the ice-ocean system had shown progressive change over the last two decades. This is consistent with a positive geometrical feedback, with oceanic melt enlarging the cavity under the ice shelf, allowing stronger circulation and further melting.

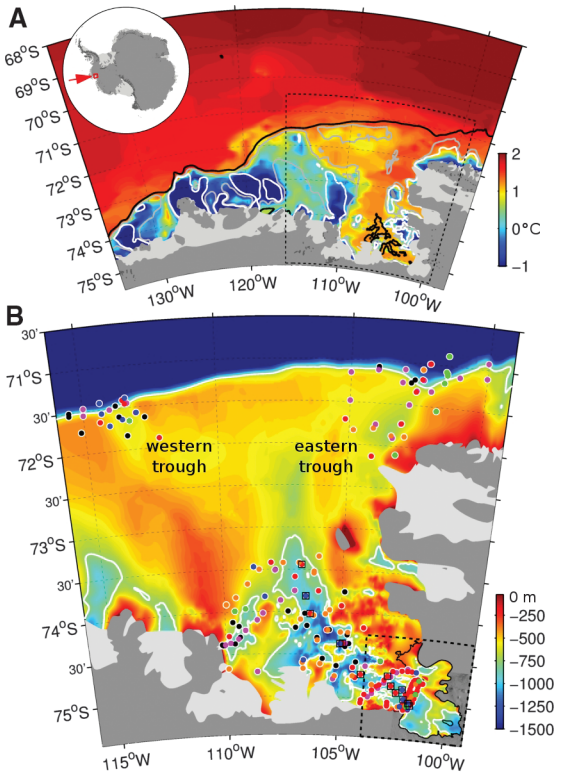
However, such ice-ocean systems are likely to be more complex. The glacier's rapid change

[1]British Antarctic Survey, Natural Environment Research Council (NERC), Cambridge, UK. [2]Korea Polar Research Institute, Korea Institute of Ocean Science and Technology (KIOST), Incheon, Korea. [3]Department of Earth and Space Sciences and Quaternary Research Center, University of Washington, Seattle, WA, USA. [4]Alfred-Wegener-Institute for Polar and Marine Research, Bremerhaven, Germany.

*Corresponding author. E-mail: pierre.dutrieux@bas.ac.uk

over the last few decades was probably triggered by its ungrounding from the top of a seabed ridge transverse to the ice flow at some time before the 1970s (*4*). Subsequent migration of the glacier's grounding line (*13*) down the seabed slope upstream from the ridge crest was probably an inevitable response (*14*), which had a major impact on cavity geometry, but projections of future evolution remain unclear (*15*–*17*). In this context, climate-driven variability of the delivery of heat to the ice-sheet margin may be important (*18*). To understand the relative roles of glacier dynamics and climate variability in driving past, present, and future glacier evolution requires knowledge of the spatial (*19*, *20*) (Fig. 1C) and temporal variability of ocean-driven melting.

Ocean simulations with a varying degree of horizontal resolution and using poorly constrained seabed and ice geometry produce a broad spectrum of variability in CDW volume in PIB (*21*) and oceanic melt of PIG (*22*). Some studies suggest that basal melt is sensitive to the strength of the circulation in the Amundsen Sea (*22*). Others associate its variability with changing wind-driven inflow of warm CDW at the continental shelf edge and temperature variability at the calving front of the glacier (*21*, *23*) influ-



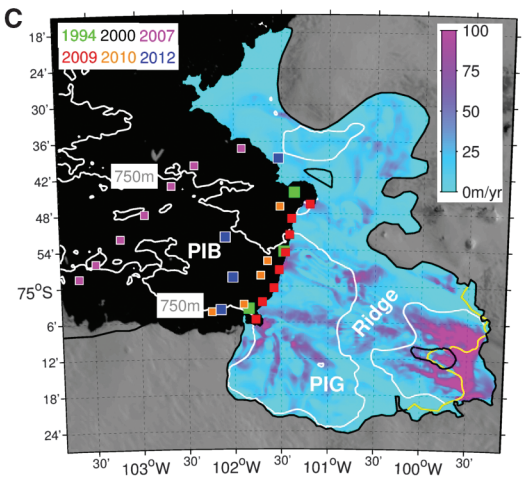


Fig. 1. Temperature maximum, seabed elevation, and selected observation locations in the Amundsen Sea. (**A**) Maximum subsurface temperature deduced from a climatology of observations taken between 1994 and 2012 (supplementary materials). Black, gray, and white contours indicate seabed elevations (*33*) of −1000, −500, and −400 m, respectively. The dashed black box shows the area in (B). (**B**) Detailed bathymetry on the eastern Amundsen Sea continental shelf. The white line shows −750-m seabed elevation. Color-coded dots (squares) show ocean station positions used in Fig. 2 (Fig. 3, A and B). The dashed black box shows the area in (C). The PIG ice shelf has been removed to show the seabed elevation beneath (supplementary materials). (**C**) The 2009 coastline and ice-shelf grounding line (*9*) are indicated by the black line. The yellow line shows the position of the grounding line in 1996 (*7*). Color-coded squares indicate ocean stations used to compute PIG ice shelf melt budgets. Simulated freshwater flux into the ocean (color) for 2009 boundary conditions.

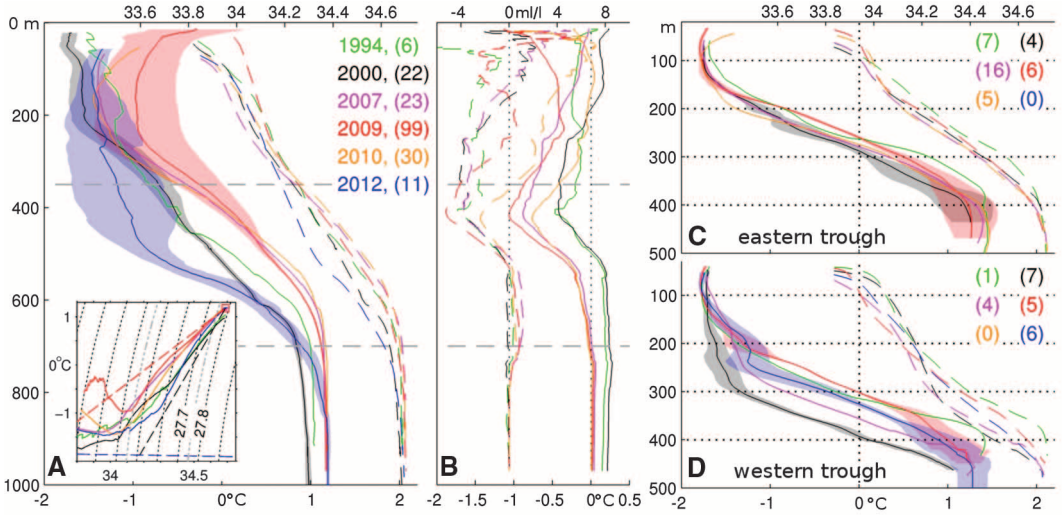


Fig. 2. Hydrographic properties in PIB. (**A**) Cruise-average, 25-dbar averaged temperature (continuous lines; shading indicates 1 SD for selected years) and salinity (dashed lines) profiles from January to March 1994, 2000, 2007, 2009, 2010, and 2012 in the wider Pine Island Bay (individual profile locations are shown in Fig. 1B; number of profiles per year is indicated in parentheses). Averages are performed in density-space and the resulting profiles re-gridded into pressure-space using the average stratification for each year. Dashed gray lines roughly indicate the 2009 ice-front draft and the seabed ridge crest, respectively. Inset: the same data in potential temperature-salinity space, with the surface freezing line indicated in dashed blue, the 2009 CDW-glacial-ice melt line in dashed red, and the 2009 CDW-WW mixing line in dashed black. Black-dotted contours of potential density anomaly are also shown, with the isopycnals corresponding to the 2009 ice-front draft and seabed ridge crest indicated in dotted gray. (**B**) Mean 2012 offset from other years in potential temperature (continuous) and meltwater concentration (dashed) for all other observed summers [color-coded as in (A)]. The difference is computed in density-space and then plotted in pressure-space using the mean 2009 stratification. (**C**) Same as (A), but for the near-shelf edge area to the east (see Fig. 1B). (**D**) Same as (A), but for the near-shelf edge area to the west (see Fig. 1B).

enced by far-field forcing of the atmospheric circulation (*18*). All these ocean-atmosphere sensitivities are linked dynamically, but a clear consensus on the most important driver of melt variability is lacking.

Hydrographic observations made in January 2012 in the eastern Amundsen Sea complement previous surveys from 1994, 2000, 2007, 2009 (*2*), and 2010 (*24*) (Fig. 1B) and offer a new perspective. Indeed, though near-bottom 2012 CDW temperatures of 1.2°C are very similar to the warmest records (2007, 2009, and 2010), the available heat reaching the PIG calving front is significantly reduced. The top of the thermocline (the depth at which temperature first increases sharply with increasing depth) is about 250 m deeper compared with that of any other year for which measurements exist (Figs. 2A and 3, A and B). Furthermore, the 2012 thermocline is sharpened such that the temperature increases from –0.8° to 0.8°C over only 180 m, compared with 250 to 350 m for other summers (Fig. 2A).

The temperature change occurring between 2010 and 2012 is largely associated with a salinity change, implying either that anomalies in the regional surface buoyancy or wind forcing cooled the upper thermocline through diapycnal exchanges (*25*) or that remote modifications in the atmosphere-ocean system led to decreased isopycnal advection of CDW from the continental shelf edge (*21*), or both. Thermocline depth changes in PIB are generally expected to occur at intraseasonal to interannual time scales (*21*, *22*), but the few synoptic summer observations available do not allow assessment of the origin, magnitude, frequency, or duration of such variability. Hydrographic profiles taken at the continental shelf edge in the troughs leading to PIB (Fig. 2, C and D) show that the western trough has a deeper and more variable thermocline than the eastern trough, consistent with the warmest inflows being found in the east (Fig. 1A), but heavy sea ice prevented sampling in the eastern trough in 2012.

Another observation is that a temperature decrease of 0.4° to 1°C occurred in 2012 at the location of previously identified meltwater outflows (*2*) (around 400-m depth, Fig. 2B), and this must be associated with changes in the ice shelf–ocean interaction. Derived ice-shelf meltwater concentrations (see supplementary materials) were 30 to 50% lower at these locations than during previous warm summers, and a weaker secondary meltwater maximum developed at around 600-m depth (Fig. 2B and fig. S3). The reduced meltwater concentration is identifiable in temperature-salinity space (Fig. 2A, inset), where previous warm summer observations depart far less from a two-component mixture of CDW and meltwater. Geostrophic budgets of dissolved oxygen, temperature, and salinity at the ice front (*26*) show that meltwater production dropped

Table 1. Balanced-transport estimates. For each set of observations, transports are estimated by balancing geostrophic fluxes of temperature, salinity, and dissolved oxygen budgets at the calving front of the ice shelf (see supplementary materials), allowing for a barotropic adjustment of the geostrophic velocity profiles (last column). Seawater transport into the cavity ("In") and net transport out of the cavity ("Diff", positive outward) are given in mSv (1 mSv = 10^3 m^3 s^{-1}) and in equivalent of ice (Iceq), using a water density of 1030 kg m^{-3} and an ice density of 920 kg m^{-3}. Meltwater transports are also shown, using the calculated meltwater fraction and balanced geostrophic velocity. Both transports do not depart significantly from each other, providing a consistency check. The 2007 observations were taken farther away from the ice front and thus are reflective of the entire ice shelf (*27*), whereas other years probably represent only the fast-flowing southern part of the ice shelf (see supplementary materials). Transport estimates are typically subject to a methodological uncertainty of about 10% (*2*).

Year	Seawater transport			Meltwater transport		Maximum (mean) correction
	mSv		km^3 $year^{-1}$ (Iceq)	km^3 $year^{-1}$ (Iceq)		cm s^{-1}
	In	Diff	Diff	In	Diff	
1994	–245	1.45	51.3	–36.4	49.1	2.8 (2.1)
2007	–355	3.13	110.6	–61.3	107.3	2.6 (0.8)
2009	–401	2.26	79.7	–36.8	79.4	2.4 (1.4)
2010	–401	2.13	75.2	–43.4	69.2	2.8 (2.1)
2012	–357	1.06	37.3	–71	34.7	1.6 (1.3)

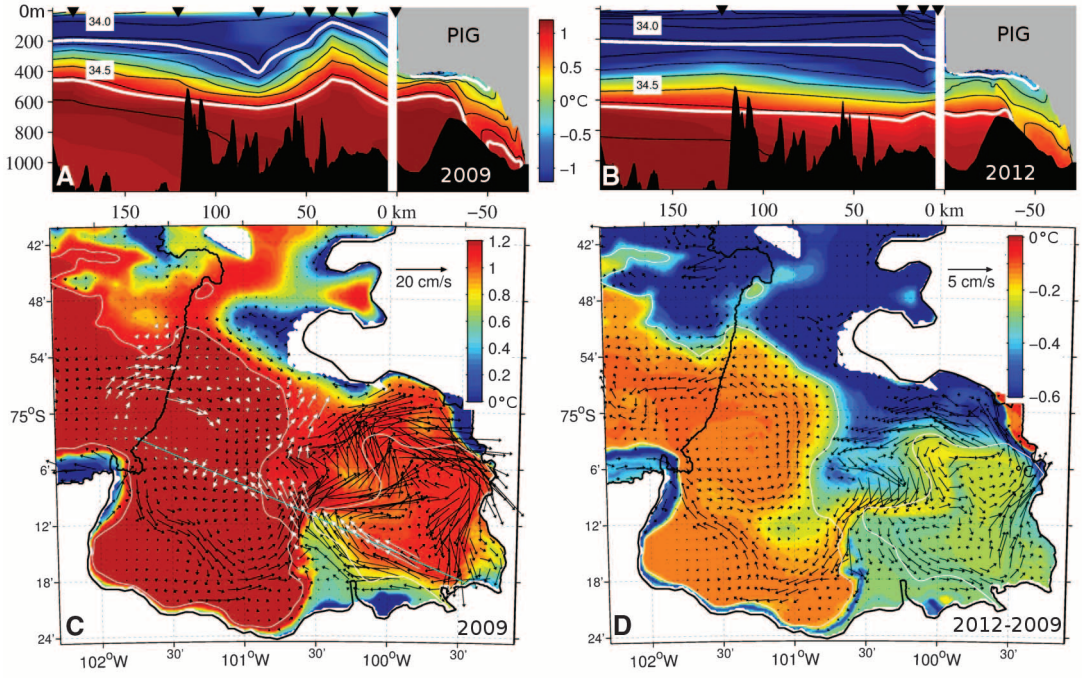


Fig. 3. Observed and simulated hydrography and circulation in 2009 and 2012. (**A**) Section of observed and simulated 2009 potential temperatures (color) and salinity (black contours) along the eastern Amundsen Sea trough and underneath the PIG ice shelf. White lines show the surface-referenced 27.47 and 27.75 isopycnals. The panel shows observations outside the PIG cavity, and simulation results within it. Observations are linearly interpolated from profiles (black triangles) indicated in Fig. 1B. (**B**) Same as (A) but for the 2012 observations and simulation. (**C**) Modeled potential temperature (color) and velocity (black vectors; every fifth vector is shown) averaged within 50 m of the seabed for the 2009 simulation. White vectors show the corresponding velocity observed by Autosub (binned on the model grid, see also fig. S2A). The cyan line indicates the position of the section used in (A) and (B). The white line indicates 750-m seabed depth. (**D**) Same as (C), but for the difference between the 2012 and the 2009 simulations.

from ~80 km^3 year^{-1} in 2009 (*2*) and 2010 (*24*) to 37 km^3 year^{-1} in 2012 (Table 1), assuming that synoptic sections are representative of a short-term balanced state. This amounts to a 53% decrease in meltwater production, making the basal melting of PIG in summer 2012 the lowest on record, even below that estimated in 1994, when the warmest, deepest waters were ~0.2°C cooler at the glacier front.

To clarify links between ocean and basal melt variability, we use a state-of-the-art regional ocean–ice shelf model at 400-m resolution with the latest ice and seabed geometry (see supplementary materials). When 2009 hydrographic conditions are imposed at its lateral boundaries (Fig. 3A), the model reproduces the main oceanographic features observed under the ice shelf by an autonomous submarine (*4*). The ocean circulation and water properties are divided in two by the ridge (Fig. 3, A and C). Offshore of the ridge, warm CDW circulates cyclonically after entering the cavity from the north, and then meanders back toward the ridge. Only the upper part of the CDW can flow over the ridge and reach the ice-shelf grounding line. This CDW melts the ice, creating a colder, fresher, buoyant meltwater plume that rises along the ice-shelf base (Fig. 3A). The vorticity created by this process and the cavity geometry impose a vigorous cyclonic circulation on the inshore side of the ridge, with near-seabed velocity reaching 0.2 m s^{-1} (Fig. 3C). The boundary between the inner and outer cavities is therefore marked by a dynamical front, further emphasizing (*2*, *4*) the crucial role played by the ridge in controlling the ocean circulation and its interaction with the ice shelf. For 2009, the model simulates reasonable basal melt patterns (Fig. 1C) compared with observations (*19*, *20*), producing 105 km^3 year^{-1} of meltwater over the entire ice shelf (*27*, *28*) and 86 km^3 year^{-1} over its more commonly quoted fast-flowing southern part (*2*, *19*, *24*) (see also supplementary materials).

In sensitivity experiments, 1994 and 2012 hydrographic conditions were imposed at the lateral boundaries while all other features (including ice geometry) were kept the same. For 2012, the simulated cooling of the sub-ice cavity and diminished basal melting are consistent with the observed decrease in meltwater production. The lowered thermocline in 2012 reduces the amount of heat flowing over the ridge and cools the water that reaches the grounding line by 0.3°C (Fig. 3B). In turn, melting is less pronounced and the buoyancy-driven circulation is concurrently decreased, particularly in the inner cavity (Fig. 3D). Overall, the model estimates a 31 to 38% decrease in meltwater flux from the ice shelf in response to the cooling at its boundaries (table S1). For 1994, when deepest waters are cooler than in 2012 but mid-depth waters are warmer, the model estimates only an 8 to 10% decrease in melting. These simulations neglect surface forcing and are limited by the imperfect seabed and constant ice geometry, which may explain the smaller reduction in melting than that observed. However, the model confirms the large sensitivity of the present ice-ocean system to the depth of the thermocline relative to the ridge that is implied by the observations. The inability of the simulation to proportionally reproduce the 1994 melting level also suggests the importance of unresolved changes in cavity geometry between 1994 and 2009 (*13*).

If prolonged, the ocean conditions observed in January 2012 would have profound implications for the PIG ice shelf. Continuation of a deep thermocline would reverse the current ice-shelf thinning (as ice advection overcompensates the weakened basal melt), potentially permitting a readvance of the grounding line. However, conditions in the months leading up to the 2012 observations were unusual (see also supplementary materials). Most of 2011 was marked by strong easterly wind anomalies over the Amundsen Sea (Fig. 4, A and B), weakening the typically cyclonic wind stress curl over the continental shelf (Fig. 4B) and curtailing the westerlies north of the shelf edge that are thought to enhance onshore CDW transport (*21*). Integrated over the preceding year, the zonal wind north of the continental shelf even reversed to easterly in 2011 (red line in Fig. 4B), an occurrence that is unique in the reanalysis wind record dating back to 1979. Such conditions potentially decreased the flux of CDW onto the continental shelf and enhanced coastal downwelling, creating the 2012 thermohaline configuration with a relatively thin CDW layer in PIB.

The wind variability over the Amundsen Sea has both local and remote origins. In particular, convective anomalies in the equatorial Pacific troposphere are known to radiate an atmospheric wave train toward the area (*29*), affecting winds at the continental shelf edge. The strong easterly anomaly in January 2012 can be attributed to exceptionally weak convection in the western tropical Pacific associated with a major La Niña event developing in late 2011 (Fig. 4C). The relevance of remote forcing from the tropical Pacific is illustrated by the statistically significant correlation (0.48) between the Niño 3.4 sea-surface temperature (SST) anomaly and the zonal wind over the continental shelf edge (Fig. 4A, see also supplementary materials). Although other factors affect the thermohaline structure in PIB, such as eddy variability at the shelf edge (*30*), coastal downwelling (*1*), and buoyancy forcing (*25*, *26*, *31*), the conjunction of the January 2012 ocean conditions and the atmospheric anomalies in the preceding months confirms the important

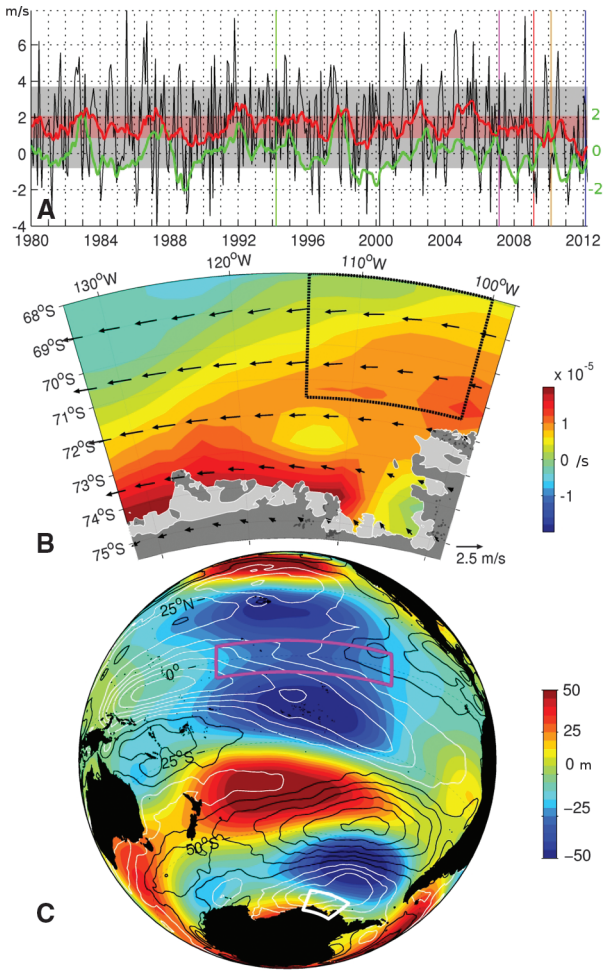


Fig. 4. Exceptional forcing before the 2012 anomaly. (**A**) Monthly-mean 10-m-height zonal wind velocity (*34*) (black) and its running integral over the preceding 12 months (red), averaging over the area indicated by the black-dotted box in (B). Shaded areas indicate 1 SD around the mean for each. The green line shows the sea-surface temperature monthly anomaly in the Niño 3.4 area. Dates of ocean observations are indicated by colored vertical lines. (**B**) 2011 annual mean of anomalies in surface wind (vector) and wind-stress curl (color) with respect to the 1979–2011 monthly climatology of each. (**C**) 2011 annual mean of anomalies in atmospheric geopotential height at 200 hPa (color) and sea surface zonal wind (contour) with respect to the 1979–2011 monthly climatology. White (black) contour are negative (positive), with 1 m s^{-1} interval. The white and magenta boxes indicate the area depicted in (B) and the Niño 3.4 area, respectively.

role of tropical forcing in determining the variability of melt rates under the PIG ice shelf (*18*).

Neighboring ice shelves closer to the continental shelf edge and exposed to greater ocean variability are naturally prone to a larger variability in melting (*32*). However, the presence of the ridge in front of the grounding line of PIG enhances its sensitivity to changes in oceanic and climatic forcing. Specifically, the blocking effect of the ridge makes the vertical distribution of heat a key element of the melting response. This study therefore stresses the importance of both local geometry and climate variability in determining ice-shelf melting. With the added realization that this melting varies appreciably over kilometer scales (*19*, *20*) and that oceanic variability is expected on intraseasonal to interannual time scales, it is clear that progress in the understanding and prediction of ice-sheet contributions to sea-level rise requires observations and models that capture a wide range of spatial and temporal scales.

References and Notes

1. S. S. Jacobs *et al.*, *Oceanography* **25**, 154–163 (2012).
2. S. S. Jacobs, A. Jenkins, C. F. Giulivi, P. Dutrieux, *Nat. Geosci.* **4**, 519–523 (2011).
3. S. S. Jacobs, H. H. Hellmer, A. Jenkins, *Geophys. Res. Lett.* **23**, 957–960 (1996).
4. A. Jenkins *et al.*, *Nat. Geosci.* **3**, 468–472 (2010).
5. D. J. Wingham, D. W. Wallis, A. Shepherd, *Geophys. Res. Lett.* **36**, L17501 (2009).
6. A. Shepherd *et al.*, *Science* **338**, 1183–1189 (2012).
7. E. Rignot, *Geophys. Res. Lett.* **35**, L12505 (2008).
8. I. Joughin, E. Rignot, C. E. Rosanova, B. K. Lucchitta, J. Bolhander, *Geophys. Res. Lett.* **30**, 1706 (2003).
9. I. Joughin, B. E. Smith, D. M. Holland, *Geophys. Res. Lett.* **37**, L20502 (2010).
10. H. D. Pritchard *et al.*, *Nature* **484**, 502–505 (2012).
11. A. Shepherd *et al.*, *Geophys. Res. Lett.* **37**, L13503 (2010).
12. A. Shepherd, D. Wingham, E. Rignot, *Geophys. Res. Lett.* **31**, L23402 (2004).
13. J. W. Park *et al.*, *Geophys. Res. Lett.* **40**, 2137–2142 (2013).
14. C. Schoof, *J. Geophys. Res.* **112**, F03S28 (2007).
15. S. S. R. Jamieson *et al.*, *Nat. Geosci.* **5**, 799–802 (2012).
16. G. H. Gudmundsson, J. Krug, G. Durand, L. Favier, O. Gagliardini, *Cryosphere* **6**, 1497–1505 (2012).
17. R. M. Gladstone *et al.*, *Earth Planet. Sci. Lett.* **333-334**, 191–199 (2012).
18. E. J. Steig, Q. Ding, D. S. Battisti, A. Jenkins, *Ann. Glaciol.* **53**, 19–28 (2012).
19. P. Dutrieux *et al.*, *Cryosphere* **7**, 1543–1555 (2013).
20. T. P. Stanton *et al.*, *Science* **341**, 1236–1239 (2013).
21. M. Thoma, A. Jenkins, D. Holland, S. Jacobs, *Geophys. Res. Lett.* **35**, L18602 (2008).
22. M. P. Schodlok, D. Menemenlis, E. Rignot, M. Studinger, *Ann. Glaciol.* **53**, 156–162 (2012).
23. P. Heimbach, M. Losch, *Ann. Glaciol.* **53**, 59–69 (2012).
24. Y. Nakayama, M. Schröder, H. H. Hellmer, *Deep Sea Res. Part I Oceanogr. Res. Pap.* **77**, 50–62 (2013).
25. A. A. Petty, D. L. Feltham, P. R. Holland, *J. Phys. Oceanogr.* **43**, 920–940 (2013).
26. P. R. Holland, A. Jenkins, D. M. Holland, *J. Geophys. Res.* **115**, C05020 (2010).
27. E. Rignot, S. Jacobs, J. Mouginot, B. Scheuchl, *Science* **341**, 266–270 (2013).
28. M. A. Depoorter *et al.*, *Nature* **502**, 89–92 (2013).
29. Q. Ding, E. J. Steig, D. S. Battisti, M. Küttel, *Nat. Geosci.* **4**, 398–403 (2011).
30. P. St-Laurent, J. M. Klinck, M. S. Dinniman, *J. Phys. Oceanogr.* **43**, 51–64 (2013).
31. L. Padman *et al.*, *J. Geophys. Res.* **117**, C01010 (2012).
32. S. S. Jacobs *et al.*, *J. Geophys. Res. Ocean.* **118**, 4152–4168 (2013).
33. R. Timmermann *et al.*, *Earth Syst. Sci. Data* **2**, 261–273 (2010).
34. D. P. Dee *et al.*, *Q. J. R. Meteorol. Soc.* **137**, 553–597 (2011).

Acknowledgments: P.D. and J.D.R. were supported by Natural Environment Research Council grants NE/G001367/1, NE/H02333X/1, and NE/J005770/1. H.K.H. and S.H.L. were supported by Korea Polar Research Institute grants PP12010 and PP13020. The European Centre for Medium-Range Weather Forecasts is acknowledged for serving the ERA-Interim reanalysis data set, and Center for Remote Sensing of Ice Sheets (with support from NSF grant ANT-0424589 and NASA grant NNX10AT68G) is acknowledged for generating and serving radar observations.

Supplementary Materials

www.sciencemag.org/content/343/6167/174/suppl/DC1
Materials and Methods
Figs. S1 to S10
Tables S1
References (*35*–*60*)

6 August 2013; accepted 6 December 2013
Published online 2 January 2014;
10.1126/science.1244341

A Spatial Accommodation by Neighboring Cells Is Required for Organ Initiation in *Arabidopsis*

Joop E. M. Vermeer,[1*] Daniel von Wangenheim,[2,3] Marie Barberon,[1] Yuree Lee,[1] Ernst H. K. Stelzer,[2] Alexis Maizel,[3] Niko Geldner[1*]

Lateral root formation in plants can be studied as the process of interaction between chemical signals and physical forces during development. Lateral root primordia grow through overlying cell layers that must accommodate this incursion. Here, we analyze responses of the endodermis, the immediate neighbor to an initiating lateral root. Endodermal cells overlying lateral root primordia lose volume, change shape, and relinquish their tight junction–like diffusion barrier to make way for the emerging lateral root primordium. Endodermal feedback is absolutely required for initiation and growth of lateral roots, and we provide evidence that this is mediated by controlled volume loss in the endodermis. We propose that turgidity and rigid cell walls, typical of plants, impose constraints that are specifically modified for a given developmental process.

Epithelia are central to multicellular life. Their ringlike paracellular barriers separate different environments, and their polar surfaces mediate selective and vectorial uptake of substances (*1*). The crucial barrier function of epithelia must be maintained during growth and development. In animals, epithelial remodeling involves a complex, supracellular interplay of force generating cytoskeleton and dynamically remodeled adherens junctions (*2*). In plants, the root endodermis has a function very similar to that of animal epithelia, yet its independent evolution in the context of a multicellular organism with turgid, wall-bearing, nonmotile cells has led to profoundly different cellular structures (*3*). Instead of being mediated by direct protein-protein interactions, the paracellular diffusion barrier of the endodermis is set up by the Casparian strips, ringlike, hydrophobic impregnations of the primary cell wall that fuse into a supracellular network between endodermal cells. These impregnations consist of lignin, an inelastic phenolic polymer that is resistant to chemical degradation (*4*). The Casparian strip establishment is locally guided by the Casparian strip domain proteins (CASPs). These transmembrane proteins, which form a ring-like plasma membrane subdomain, establish a lateral diffusion barrier and recruit biosynthetic enzymes for Casparian strip formation (*5*, *6*). Yet, despite the presence of a Casparian strip, the endodermis has to be remodeled during lateral root formation.

Lateral roots are formed from the pericycle, a cell layer located deep within the primary root, confined between the vascular bundle and the endodermis. As the lateral root primordium grows, it has to traverse the endodermis, cortex, and epidermis in order to emerge from the primary root. The hormone auxin triggers lateral root development and also signals to the overlying cell layers (*7*). Outer cortex and epidermal cell layers assist lateral root emergence after auxin from the lateral root primoridum triggers degradation of the SOLITARY-ROOT repressor protein, which permits expression of pectinases that disrupt intercellular adhesions (*8*, *9*). The endodermis, however, must be breached first, and its Casparian strip network cannot be degraded by pectinases. An-

[1]Department of Plant Molecular Biology, Biophore, UNIL-Sorge, University of Lausanne, 1015 Lausanne, Switzerland. [2]Buchmann Institute for Molecular Life Sciences, Goethe University Frankfurt, D-60438 Frankfurt Am Main, Germany. [3]Center for Organismal Studies, University of Heidelberg, D-69120 Heidelberg, Germany.

*Corresponding author. E-mail: joop.vermeer@unil.ch (J.E.M.V.); niko.geldner@unil.ch (N.G.)

other repressor protein, SHORT HYPOCOTYL 2 (SHY2), mediates endodermis responses (*9*).

Older electron microscopy studies suggest a profound remodeling of endodermal cell walls during lateral root formation (*10*, *11*). In order to allow for imaging of the deep-lying endodermal cell layer, we specifically developed a set of fluorescent marker lines (*12*). A transcriptional fluorescent reporter for *SHY2* shows expression in two to three endodermal cells overlying newly formed primordia during stage I to stage IV (fig. S1, A to D, and movies S1 to S4). Subsequently, we used markers for the Casparian strip domain (CSD), as well as plasma and vacuole membranes, that we expressed specifically in differentiating endodermal cells. We observed that the CSD marker CASP1-mCherry was locally degraded in two to three endodermal cells overlying stage II and III primordia (Fig. 1A); at the same time, endodermal cells overlying the primordium became thinner (Fig. 1J and fig. S2). We used the plasma membrane–localized soluble *N*-ethylmaleimide–sensitive factor attachment protein receptor (SNARE) SYP122, CITRINE-SYP122, to visualize the endodermal protoplast during lateral root primordium growth.

We observed that the protoplast progressively flattened in parts of the cells, which sometimes led to a donut-shaped structure (Fig. 1, B and C; fig. S3; and movies S5 and S6) that could arise from a flattening of the endodermal cell to the point where plasma membranes from both sides are fusing. Using the tonoplast marker γ-TIP-CITRINE, we observed similar accommodating responses (Fig. 1, D and E; fig. S4; and movies S7 and S8). The vacuole appeared to be remodeled and to fragment into smaller vacuoles but otherwise remained intact. The integrity of the plasma membrane of endodermal

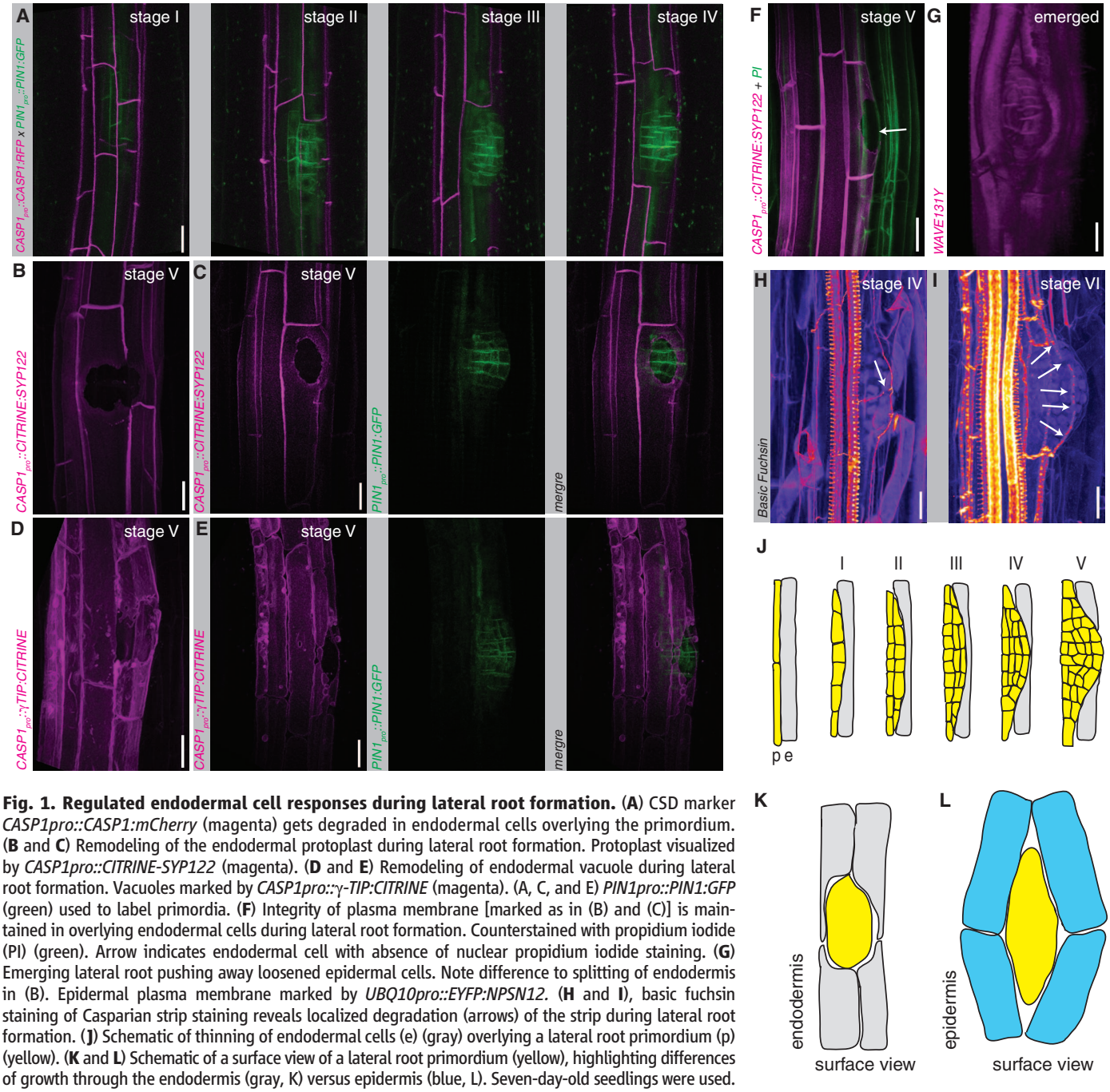


Fig. 1. Regulated endodermal cell responses during lateral root formation. (**A**) CSD marker *CASP1pro::CASP1:mCherry* (magenta) gets degraded in endodermal cells overlying the primordium. (**B** and **C**) Remodeling of the endodermal protoplast during lateral root formation. Protoplast visualized by *CASP1pro::CITRINE-SYP122* (magenta). (**D** and **E**) Remodeling of endodermal vacuole during lateral root formation. Vacuoles marked by *CASP1pro::γ-TIP:CITRINE* (magenta). (A, C, and E) *PIN1pro::PIN1:GFP* (green) used to label primordia. (**F**) Integrity of plasma membrane [marked as in (B) and (C)] is maintained in overlying endodermal cells during lateral root formation. Counterstained with propidium iodide (PI) (green). Arrow indicates endodermal cell with absence of nuclear propidium iodide staining. (**G**) Emerging lateral root pushing away loosened epidermal cells. Note difference to splitting of endodermis in (B). Epidermal plasma membrane marked by *UBQ10pro::EYFP:NPSN12.* (**H** and **I**), basic fuchsin staining of Casparian strip staining reveals localized degradation (arrows) of the strip during lateral root formation. (**J**) Schematic of thinning of endodermal cells (e) (gray) overlying a lateral root primordium (p) (yellow). (**K** and **L**) Schematic of a surface view of a lateral root primordium (yellow), highlighting differences of growth through the endodermis (gray, K) versus epidermis (blue, L). Seven-day-old seedlings were used. Images (A) to (I): Maximal projections of confocal image stacks. Scale bar, 20 μm.

cells was at no point compromised during these rearrangements, as indicated by the absence of nuclear propidium iodide stain (used as an indicator of cell death in plants) (Fig. 1F and movie S9).

The protoplast of the endodermis and epidermal cells behaved differently. Epidermal cells do not seem to lose volume, but rather are pushed away after loss of cell-to-cell adherence (compare Fig. 1G with 1B and Fig. 1K with 1L). By contrast, the Casparian strip network keeps the endodermal cells tightly connected, which forces the endodermis to accommodate growth through dramatic volume losses and the required minimal separation of cell walls for lateral root emergence. When we visualized the Casparian strip during lateral root formation, we did not observe a complete disappearance of the strip that would parallel the disappearance of the CASP1 membrane protein (Fig. 1A). Instead, we observed small holes and/or breaking points that allowed for a localized opening of the network in parts of the cell where the primordium penetrates (Fig. 1, H and I).

The SHY2 repressor is thought to regulate endodermal responses during lateral root emergence. Yet SHY2 is widely expressed, and mutants with the dominant *shy2-2* allele show many different developmental phenotypes (*13*–*16*), which makes it difficult to discern primary from secondary defects. To overcome this problem and to specifically block auxin responses in differentiated endodermal cells, we expressed the stabilized form of SHY2, *shy2-2*, under the control of the CASP1 promoter. In these *CASP1pro::shy2-2* plants, the altered leaf shape, severe dwarfism of shoots and roots, and stunted inflorescence phenotypes of the *shy2-2* mutant were all absent, although the plants remained smaller than wild type (Fig. 2A). This smaller stature can easily be explained as a secondary consequence of the only other phenotype observed in these plants, which was a complete absence of emerged lateral roots (Fig. 2, B to D). This very strong phenotype became even more apparent under hydroponic growth conditions. Whereas 3-week-old Col-0 plants had a well-developed root system, *CASP1pro::shy2-2* plants only showed one long primary root (Fig. 2C). This complete suppression of lateral root emergence was specific for *shy2-2* expression in the endodermis, as lines expressing *shy2-2* in the cortex (PEPpro) or epidermis (PGP4pro) (*13*, *17*) still had emerged lateral roots. The lower rate of emerged lateral roots of the *PGP4pro::shy2-2* plants may be due to weak PGP4 promoter expression in endodermis and pericycle (fig. S5).

Our experiments suggest that endodermal auxin signaling is crucial for lateral root emergence. We then analyzed at which stage of lateral root formation *CASP1pro::shy2-2* plants were blocked. Unexpectedly, even the earliest lateral root primordia stages were absent (fig. S6). We concluded that endodermal auxin signaling already affects initiation of lateral roots in the pericycle. We therefore characterized the expression of the lateral root founder cell marker *GATA23pro::NLSGFPGUS* (*18*). Onset of *GATA23* expression in *CASP1pro::shy2-2* roots was similar to that in wild type, but the staining intensity did not increase to mark initiating and early lateral root primordia as in wild type (Fig. 3, A and B). This supports a very early block in lateral root initiation in *CASP1pro::shy2-2* plants, placing it before the first asymmetric divisions of the founder cells.

We tested whether auxin treatments could rescue the lateral root phenotype of *CASP1pro::shy2-2* plants. Primary root growth in both backgrounds was equally sensitive to auxin treatments (Fig. 3, C and D). *CASP1pro::shy2-2* plants, however, formed very few lateral roots in response to auxin. High concentrations resulted in some degree of lateral root formation in *CASP1pro::shy2-2* plants (fig. S7). Lateral roots formed when 1 μM auxin was present hardly managed to emerge (fig. S7); this was the initially expected emergence phenotype. Auxin treatment of wild-type plants resulted in correctly shaped primordia with normal emergence through the endodermis (Fig. 3, I and J). By contrast, *CASP1pro::shy2-2* primordia were often flattened and appeared to have difficulties in growing through the endodermis (Fig. 3, K and L). In addition, the endodermis appeared to stay turgid much longer than wild-type endodermis, where it becomes flattened to the point of being imperceptible (see asterisks, Fig. 3, I and K). These experiments suggest that blocking auxin responses specifically in the endodermis affects lateral root formation at two stages: first, at initiation and, second, at the stage when the

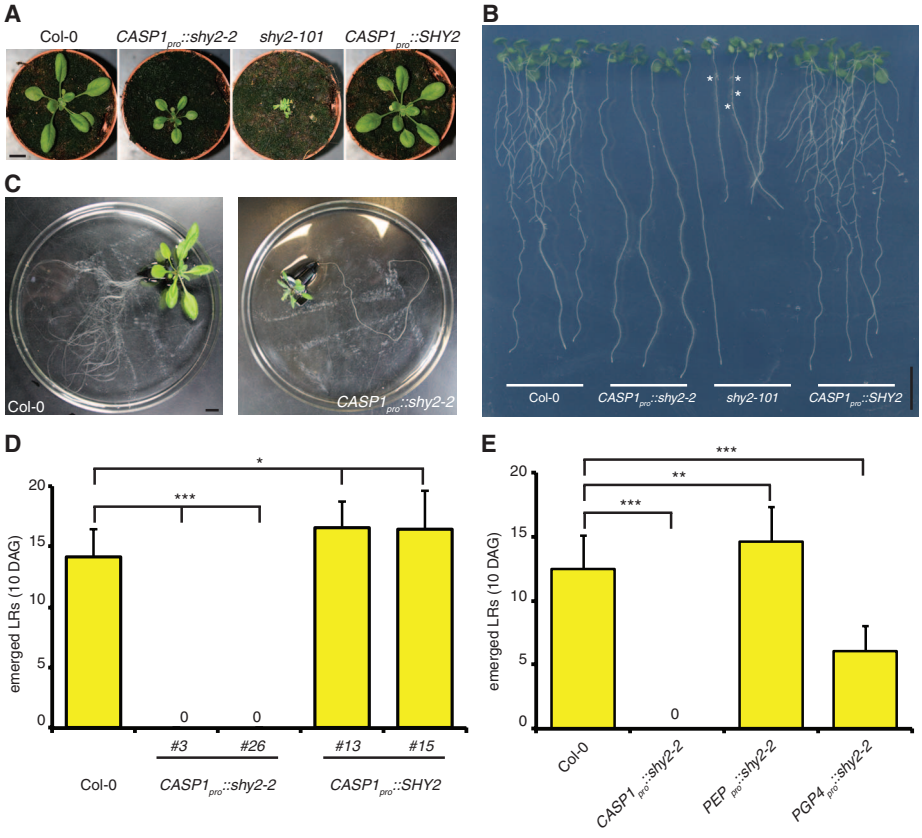


Fig. 2. Endodermal auxin responses are essential for lateral root formation. (**A**) Three-week-old *CASP1pro::shy2-2* plants do not display *shy2-101* phenotypes but are smaller than Col-0 and *CASP1pro::SHY2* controls. (**B**) *CASP1pro::shy2-2* seedling roots grow as controls do but show no emerged lateral roots. *CASP1pro::shy2-2* seedlings also do not display clusters of emerged lateral roots (asterisks) sometimes observed in *shy2-101*. (**C**) Three-week-old hydroponically grown plants show highly branched root system in wild-type (Col-0). *CASP1pro::shy2-2* plants still show no emerged lateral roots. (**D**) *CASP1pro::shy2-2* seedlings [10 days after germination (DAG)] have no emerged lateral roots (LRs). Asterisks indicate significant differences among means. (**E**) Blocking auxin responses in endodermis inhibits lateral root emergence, whereas blocks in cortical (PEP_{pro}*::shy2-2*) and epidermal ($PGP4_{pro}$*::shy2-2*) responses do not. Asterisks indicate significant differences among means (*$P < 0.5 \times E^{-5}$, **$P < 0.5 \times E^{-10}$, ***$P << 0.5 \times E^{-15}$) by Tukey's test ($n = 20$). All experiments were performed at least three times.

primordium needs to emerge. Thus, blocking responses in the endodermis has a non–cell autonomous effect on the ability of auxin to induce cell divisions in the pericycle. This effect was confirmed by using the auxin signaling reporter *DR5pro::NLS3xVENUS* (*19*). Under control conditions, there was no obvious difference between the two backgrounds (Fig. 3, E and F), whereas, after short-term auxin treatments, not only the endodermis but also the pericycle responded less in *CASP1pro::shy2-2* (Fig. 3, G and H).

Several lines of evidence exclude the possibility that this effect on auxin response competence in the pericycle is due to the direct presence of shy2-2 protein in those cells, either because of leaky promoter activity or protein movement. First, unlike CASP1pro, PGP4pro also displays weak expression in the pericycle (fig. S5), yet it causes a much weaker lateral root phenotype (Fig. 2E). Second, we ruled out movement of shy2-2 protein from endodermis into the pericycle by interfering with plasmodesmatal transport between these two cell layers through endodermal expression of *cals3m*, which has been shown to obstruct plasmodesmatal connections (*20*). The phenotype of *CASP1pro::shy2-2*/*CASP1pro::cals3m* plants was very similar to *CASP1pro::shy2-2* plants (fig. S8), which indicated that protein movement from endodermis to pericycle is not the cause for the non–cell autonomous effect that we observe.

Having excluded direct effects of shy2-2 in the pericycle, we postulated that communication between the endodermis and the primed pericycle cells is required much earlier than previously assumed. We therefore investigated whether remodeling of endodermis and pericycle already occurs at stage I or earlier. We used light sheet fluorescence microscopy to noninvasively image and quantify the dynamics of pericycle and endodermis before and during the first asymmetric cell division. We could show that the transverse area of the pericycle cells increased by ~50% (Fig. 4, B and C, and movie S10). Average increase in cell surface was 22 ± 15 μm^2/hour (mean ± SD, $n = 9$ cells, two biological replicates). This indicates that, before the first division, the pericycle cells swell and the endodermis slightly shrinks or deforms.

Under short-term auxin treatments, we observed a significant increase of pericycle cell width in Col-0. However, this increase was absent in *CASP1pro::shy2-2* plants (Fig. 4D and fig. S9). This suggests that the ability of pericycle cells to swell is dependent on an early auxin perception in the endodermis. In *CASP1pro::shy2-2* plants, pericycle-derived auxin would be unable to induce an early accommodation response of the endodermis, which would make it impossible for

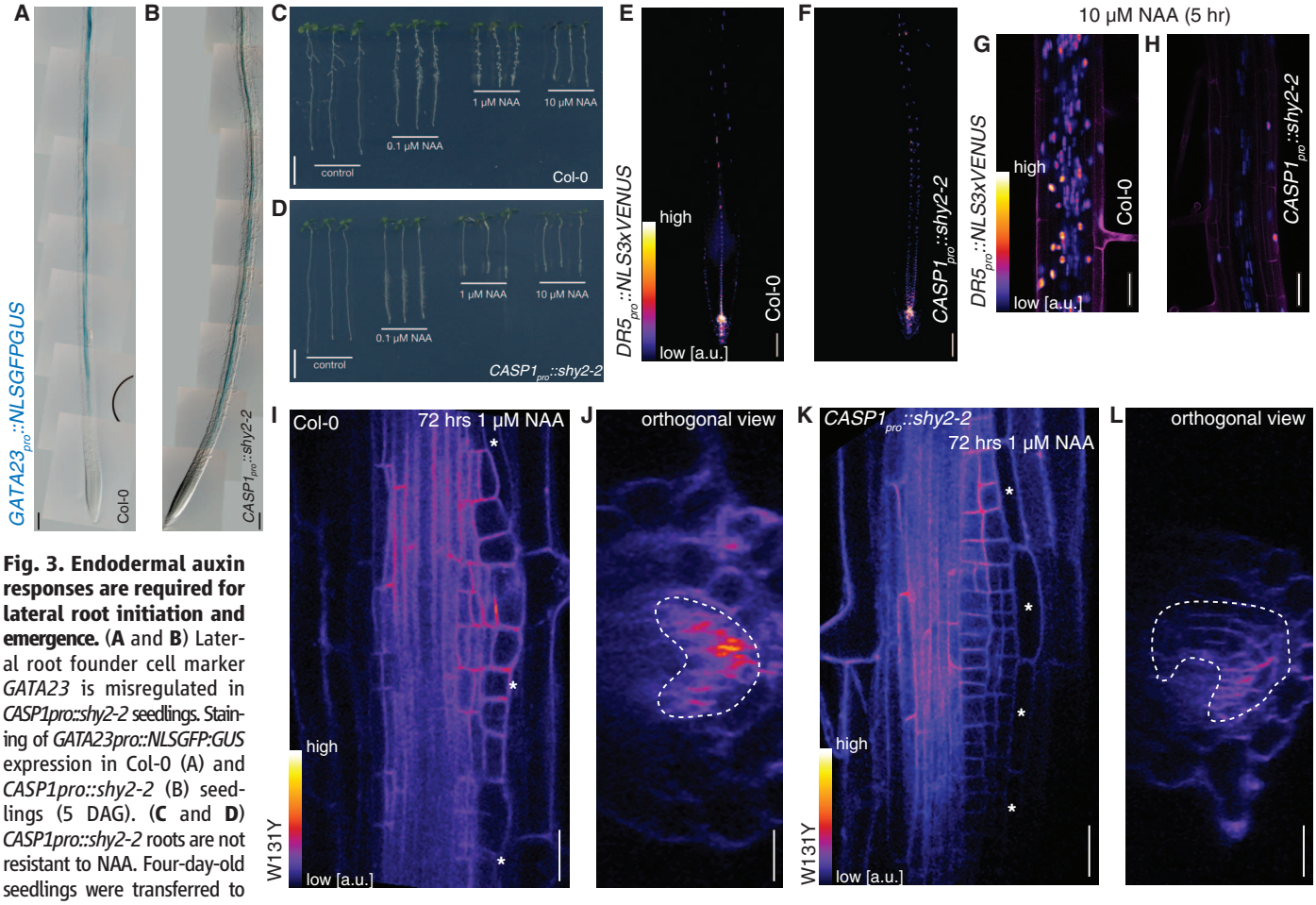


Fig. 3. Endodermal auxin responses are required for lateral root initiation and emergence. (**A** and **B**) Lateral root founder cell marker *GATA23* is misregulated in *CASP1pro::shy2-2* seedlings. Staining of *GATA23pro::NLSGFP:GUS* expression in Col-0 (A) and *CASP1pro::shy2-2* (B) seedlings (5 DAG). (**C** and **D**) *CASP1pro::shy2-2* roots are not resistant to NAA. Four-day-old seedlings were transferred to indicated amounts of NAA for 3 days. Compared to Col-0 (C), *CASP1pro::shy2-2* seedlings (D) show no emerged lateral roots after prolonged NAA treatment. (**E** to **H**) The auxin signaling reporter *DR5pro::N7-3xVENUS* shows comparable fluorescence intensity in control situation in both Col-0 (E) and *CASP1pro::shy2-2* seedlings (F). Both endodermis and pericycle of *CASP1pro::shy2-2* seedlings (H) are less responsive to auxin, compared to Col-0 (G). a.u., arbitrary units. Five-day-old plants were incubated in liquid medium for the indicated time and concentration. (**I** to **L**) Blocking endodermal auxin responses severely affects lateral root primordium shape. Four-day-old seedlings expressing the plasma membrane marker *UBQ10pro::EYFP:NPSN12* in Col-0 (I and J) and *CASP1pro::shy2-2* (K and L) were transferred to auxin-containing plates. (J and L) Orthogonal views of (I) and (K), respectively. Note that induced primordium of *CASP1pro::shy2-2* is much broader than Col-0 [compare outlines in (J and L)]. In addition, the endodermis does not become flattened in *CASP1pro::shy2-2* roots (highlighted by asterisks). Scale bars: 0.1 mm in (A), (B), (E), and (F); 1 cm in (C) and (D); 50 µm in (G) and (H); and 20 µm in (I) to (L).

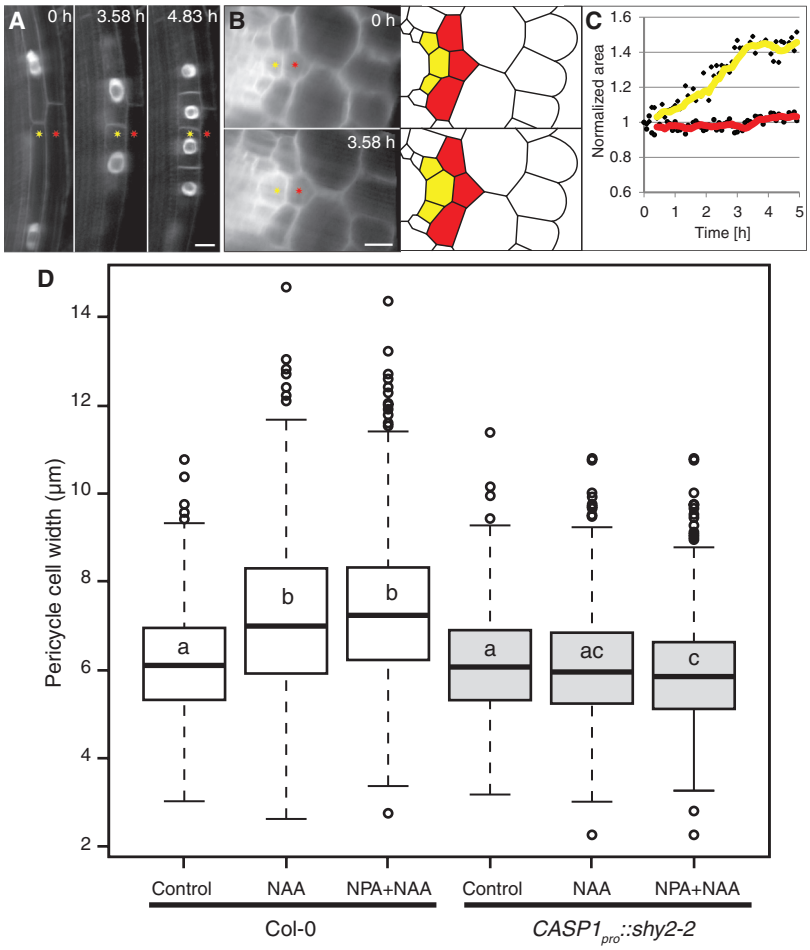


Fig. 4. Pericycle cells swell before formative divisions. (**A** to **C**) Four-dimensional light sheet fluorescence microscopy reveals that pericycle cells swell before formative divisions. Seedlings (7 DAG) expressing *UBQ10pro::EYFP:PIP1;2* as the plasma membrane marker (gray) and nuclear *GATA23pro::NLSGFPGUS* (gray) as the lateral root founder cell marker imaged for 30 hours. (A) Single slice of two dividing pericycle cells. Yellow star indicates pericycle; red star indicates endodermis. (B) Orthogonal views of (A) at $t = 0$ hours and $t = 3.58$ hours and segmented versions of the images (right). Pericycle is indicated with yellow asterisk and/or filled, endodermis with red asterisk and/or filled. (C) The sum area of the three cells, normalized to its initial value, is plotted as black dots; the yellow and red lines are sliding window averages over six time points. (**D**) Boxplot showing the quantification of the distribution of pericycle cell widths under control, either 10 μM NAA or 10 μM NPA with 10 μM NAA conditions in Col-0 (white boxes) and *CASP1pro::shy2-2* background (gray boxes). Measurements were performed on orthogonal projections of confocal Z-stacks of *UBQ10pro::EYFP:NPSN12* roots as depicted in fig. S9. Different letters indicate significant differences among means ($P < 0.5 \times E^{-4}$ by Tukey's test). (n = 25 roots, three independent experiments.) Scale bar, 20 μm.

the primed pericycle cell to increase in volume and execute the first cell division. Auxin transporter–mediated "reflux" of auxin from the endodermis to the pericycle was reported to assist the progression of founder cells into stage I primordium (*14*). Yet the weak effects of endodermal auxin transporters on lateral root formation indicate that it cannot account for the strong block of lateral root formation reported here. Nevertheless, we included measurements of pericycle cell widths after simultaneous treatment of 1-naphthylacetic acid (NAA) and an auxin transport inhibitor (*15*). Inhibition of auxin transport affected neither the auxin-induced changes in pericycle cell width nor the ability of *CASP1-pro::shy2-2* expression to block this increase (Fig. 4D and fig. S9). Hence, the non–cell autonomous effects observed are not mediated by alterations of auxin transport through the endodermis.

We propose that pericycle cells perceive a nonresponsive endodermis through an increased resistance to its expansion growth. This mechanical stress would then result in an early block of lateral root initiation. Auxin-mediated regulation of the mechanical properties of overlying cell layers was proposed to contribute to the shape of already-formed lateral root primordial (*16*). Here, we reveal that the requirement for accommodating responses is much more fundamental, being even required for initiation of cell division. Moreover, we show that it is specifically the endodermis that plays a key role in lateral root formation and emergence, because of the strong phenotypes of *CASP1pro::shy2-2* plants. Our findings fit with a recent report that auxin-mediated regulation of aquaporins contributes to emergence (*21*). Clearly, auxin regulation of aquaporins or ion channels might execute the very early accommodating responses of the endodermis that we observe. It will be interesting to specifically manipulate such proteins in the endodermis and study their effects on endodermal shrinkage and lateral root formation. The pericycle-endodermis interaction that we have uncovered now provides a promising system to study how plant cells sense and accommodate to growth of their neighbors—besides lateral root formation, such "mechanical" communication might be of importance to maintain tissue integrity in growing apical meristems or during secondary growth, as well as during the penetration of fungi or pollen tubes into plant tissue or infection thread formation. Generally, the need for coordinated accommodation responses by turgor and/or volume loss might be widespread, wherever there is growth and division of inner cell layers. This might impact on tissue and organ patterning, just as perception of mechanical stresses at surface cell layers shapes growth of the shoot apical meristem (*22*).

References and Notes

1. M. Cereijido, R. G. Contreras, L. Shoshani, *Physiol. Rev.* **84**, 1229–1262 (2004).
2. C. Guillot, T. Lecuit, *Science* **340**, 1185–1189 (2013).
3. N. Geldner, *Annu. Rev. Plant Biol.* **64**, 531–558 (2013).
4. S. Naseer *et al.*, *Proc. Natl. Acad. Sci. U.S.A.* **109**, 10101–10106 (2012).
5. D. Roppolo *et al.*, *Nature* **473**, 380–383 (2011).
6. Y. Lee, M. C. Rubio, J. Alassimone, N. Geldner, *Cell* **153**, 402–412 (2013).
7. J. Lavenus *et al.*, *Trends Plant Sci.* **18**, 450–458 (2013).
8. H. Fukaki, S. Tameda, H. Masuda, M. Tasaka, *Plant J.* **29**, 153–168 (2002).
9. K. Swarup *et al.*, *Nat. Cell Biol.* **10**, 946–954 (2008).
10. J. K. Bell, M. E. Mccully, *Protoplasma* **70**, 179–205 (1970).
11. H. T. Bonnett Jr., *J. Cell Biol.* **40**, 144–159 (1969).
12. Materials and methods are available as supplementary materials on *Science* on the Web.
13. A. Mustroph *et al.*, *Proc. Natl. Acad. Sci. U.S.A.* **106**, 18843–18848 (2009).
14. P. Marhavý *et al.*, *EMBO J.* **32**, 149–158 (2013).
15. I. Casimiro *et al.*, *Plant Cell* **13**, 843–852 (2001).
16. M. Lucas *et al.*, *Proc. Natl. Acad. Sci. U.S.A.* **110**, 5229–5234 (2013).
17. M. Cho, S. H. Lee, H. T. Cho, *Plant Cell* **19**, 3930–3943 (2007).
18. B. De Rybel *et al.*, *Curr. Biol.* **20**, 1697–1706 (2010).
19. M. G. Heisler *et al.*, *Curr. Biol.* **15**, 1899–1911 (2005).
20. A. Vatén *et al.*, *Dev. Cell* **21**, 1144–1155 (2011).

21. B. Péret *et al.*, *Nat. Cell Biol.* **14**, 991–998 (2012).
22. O. Hamant *et al.*, *Science* **322**, 1650–1655 (2008).

Acknowledgments: We thank the Central Imaging Facility (CIF) of the University of Lausanne for technical support, T. Beeckman, M. Bennett, B. De Rybel, Y. Heluriatta and H. Fukaki for sharing published material. We thank T. Beeckman, M. Bennett and T. Goh for helpful comments. We thank B. de Rybel for sharing unpublished results.

This work was supported by a Marie-Curie Intra-European Fellowship grant to J.E.M.V., an EMBO long-term fellowship for M.B., and grants of the Swiss National Science Foundation (SNSF) and the European Research Council (ERC) (to N.G.); the land Baden-Württemberg, the Chica und Heinz Schaller Stiftung, and the CellNetworks cluster of excellence (to A.M.); and the Cluster of Excellence at Frankfurt for Macromolecular Complexes (CEF-MC) and the Deutsche Forschungsgemeinschaft (to D.v.W., E.H.K.S.).

Supplementary Materials
www.sciencemag.org/content/343/6167/178/suppl/DC1
Materials and Methods
Figs. S1 to S9
References (*23*–*30*)
Movies S1 to S10

11 September 2013; accepted 26 November 2013
10.1126/science.1245871

Bacterial Vesicles in Marine Ecosystems

Steven J. Biller,[1]* Florence Schubotz,[2] Sara E. Roggensack,[1] Anne W. Thompson,[1] Roger E. Summons,[2] Sallie W. Chisholm[1,3]*

Many heterotrophic bacteria are known to release extracellular vesicles, facilitating interactions between cells and their environment from a distance. Vesicle production has not been described in photoautotrophs, however, and the prevalence and characteristics of vesicles in natural ecosystems is unknown. Here, we report that cultures of *Prochlorococcus*, a numerically dominant marine cyanobacterium, continuously release lipid vesicles containing proteins, DNA, and RNA. We also show that vesicles carrying DNA from diverse bacteria are abundant in coastal and open-ocean seawater samples. *Prochlorococcus* vesicles can support the growth of heterotrophic bacterial cultures, which implicates these structures in marine carbon flux. The ability of vesicles to deliver diverse compounds in discrete packages adds another layer of complexity to the flow of information, energy, and biomolecules in marine microbial communities.

Cells from all domains of life produce membrane vesicles (*1*). In Gram-negative bacteria, spherical extracellular vesicles (between ~50 and 250 nm in diameter) are thought to be formed when regions of the outer membrane "pinch off" from the cell and carry with them an assortment of proteins and other molecules (*2*, *3*). Vesicle release occurs during the normal growth of many species, and although growth conditions, stressors, and membrane structure can influence the number of vesicles produced (*4*), the regulation of vesicle production is still unclear (*2*). These structures have been shown to contribute to diverse processes in model bacteria, including virulence (*5*, *6*), quorum signaling (*7*), biofilm formation (*8*), redox reactions (*9*), cellular defense (*10*, *11*), and horizontal gene transfer (*12*, *13*). Despite the numerous ways in which vesicles may affect microbial communities, their abundance and functions in marine and other ecosystems remain unknown.

While examining scanning electron micrographs of an axenic culture of the marine cyanobacterium *Prochlorococcus*, we noticed the presence of numerous small spherical structures near the cell surface (Fig. 1A). This strain has no prophage or gene transfer agents in its genome; thus, we suspected the spheres to be membrane vesicles. Because *Prochlorococcus* is the numerically dominant marine phytoplankter—with a global population of ~10^{27} cells (*14*) accounting for 30 to 60% of the chlorophyll a in oligotrophic regions (*15*)—*Prochlorococcus*-derived vesicles could have a notable influence on the function of marine microbial systems. To study the phenomenon of vesicle release, we first isolated the <0.2-μm fraction from a *Prochlorococcus* culture and visualized these structures by transmission electron microscopy (TEM) (*16*). Negative stain and thin-section micrographs (Fig. 1, B and C) of samples from exponentially growing cultures of healthy, intact cells (fig. S1) confirmed the presence of membrane-bound vesicles ~70 to 100 nm in diameter (Fig. 1D). Their presence was independently observed using nanoparticle tracking analysis of unperturbed cultures, which showed that the particle size distributions were as would be predicted for *Prochlorococcus* cells and vesicles (Fig. 1E). Vesicles were produced under both constant light and diel light-dark cycling conditions and were found in cultures of all six axenic *Prochlorococcus* strains available (representing both high-light– and low-light–adapted ecotype groups) (table S1). A *Synechococcus* strain (WH8102) also produced vesicles (fig. S2), which demonstrated that vesicle release is a feature of the two most numerically abundant primary producers in the oligotrophic oceans.

Because membrane vesicles were the dominant small particle between 50 and 250 nm in our cultures as seen by TEM, we used the concentration of all particles in this size range, determined using nanoparticle tracking analysis, as a measure of vesicle concentration. Vesicles were at least as abundant as *Prochlorococcus* cells in growing cultures, and in some strains they could be 10 times as numerous as cells in exponential and/or stationary phase (Fig. 1F and fig. S3). Vesicles appear to be produced continually during exponential growth, consistent with observations in other bacteria (*17*), and by our estimates, the rate of vesicle production varied from about two to five vesicles per cell per generation among three different *Prochlorococcus* strains (table S1; supplementary text). Vesicles are stable under laboratory conditions, as their size and concentration remained essentially unchanged over the course of 2 weeks in sterile seawater at 21°C (fig. S4). Although many factors could influence vesicle production by *Prochlorococcus* in the wild, production estimates based on these initial data yield global release rates on the order of 10^{27} to 10^{28} per day (supplementary text).

To explore the potential roles of vesicles from marine cyanobacteria, we analyzed the content of *Prochlorococcus* vesicles. As one might expect for membrane-bound vesicles, they contained both lipopolysaccharides, a common component of the Gram-negative outer membrane, and a number of typical cyanobacterial lipids (*18*). The most abundant lipid species in the vesicles were monoglycosyldiacylglycerol, sulfoquinovosyldiacylglycerol, and some unidentified glycolipids (fig. S5A). The lipid fatty acids from vesicles of *Prochlorococcus* MED4 were dominated by saturated $C_{14:0}$, $C_{16:0}$, and $C_{18:0}$ species, which suggested that these vesicles' membranes are relatively rigid (fig. S5B).

We examined the proteome associated with vesicles produced by two ecologically distinct *Prochlorococcus* strains (the high-light–adapted MED4 and low-light–adapted MIT9313) and found these vesicles to contain a diverse set of proteins, including nutrient transporters, proteases, porins, hydrolases, and many proteins of unknown function (tables S2 and S3). Although it is presently unclear whether these enzymes are bioactive, vesicles released by other bacteria can contain active enzymes (*2*), and proteins enclosed within related liposomal structures are known to be protected from degradation by marine bacteria (*19*). Bacterial membrane vesicle release may account, in part, for the relative abundance of membrane proteins among all dissolved proteins in seawater (*20*).

Prochlorococcus MED4 vesicles also contained DNA (fig S6A). To be certain that the detected DNA was associated with vesicles, purified vesicles were treated with deoxyribonuclease (DNase) before lysis and DNA purification. DNA fragments associated with vesicles were heterogeneous in size, with some measuring at least 3 kilobase pairs (kbp) (fig. S7)—enough to encode multiple genes. We amplified and sequenced DNA from ~10^{11} MED4 vesicles and found that it

[1]Department of Civil and Environmental Engineering, Massachusetts Institute of Technology, Cambridge, MA 02139, USA. [2]Department of Earth, Atmospheric and Planetary Sciences, Massachusetts Institute of Technology, Cambridge, MA 02139, USA. [3]Department of Biology, Massachusetts Institute of Technology, Cambridge, MA 02139, USA.

*Corresponding author. E-mail: chisholm@mit.edu (S.W.C.); sbiller@mit.edu (S.J.B.)

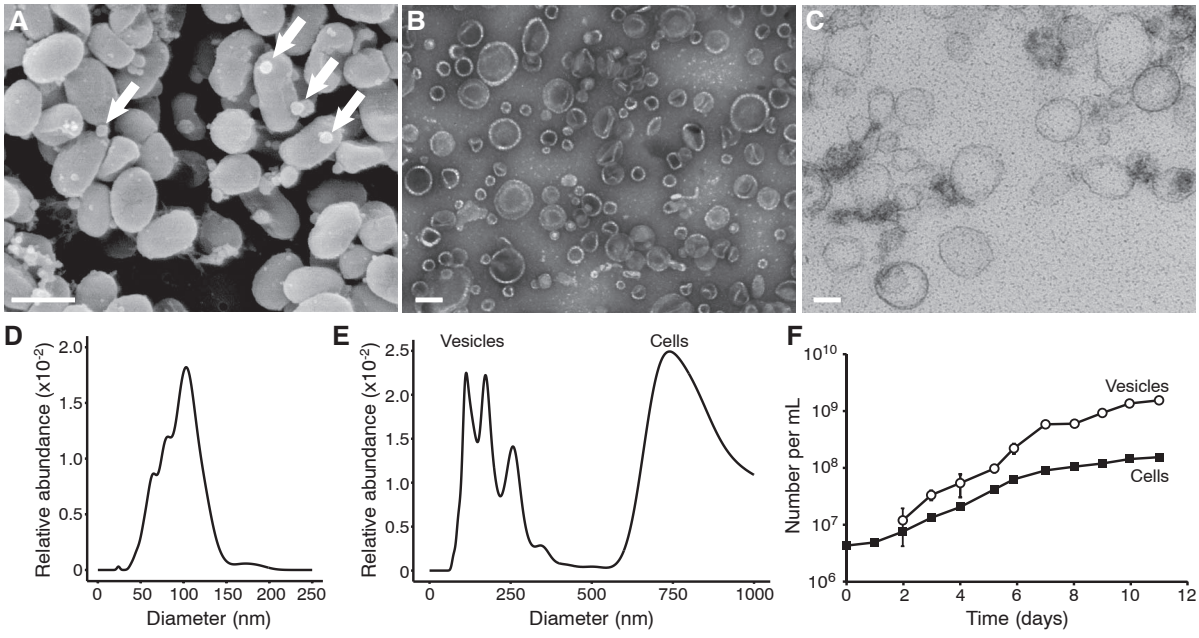


Fig. 1. *Prochlorococcus* releases membrane vesicles. (**A**) Scanning electron micrograph of *Prochlorococcus* strain MIT9313 shows the presence of numerous small spherical features (vesicles, indicated by arrows) near the cells. Scale bar, 1 μm. (**B**) Purified *Prochlorococcus* vesicles as seen by negative-stain TEM. Scale bar, 100 nm. (**C**) Thin-section electron micrographs confirm that *Prochlorococcus* vesicles are circular, membrane-enclosed features lacking notable internal structure. Scale bar, 100 nm. (**D**) Particle size distribution of purified *Prochlorococcus* vesicles as determined by nanoparticle tracking analysis. (**E**) Particle size analysis of an unperturbed culture confirms the presence of particles of two broad size classes consistent with whole cells and vesicles. (**F**) Vesicle production during growth of MIT9313, comparing the number of vesicles (open circles) with cells (squares) in the culture. Values represent means ± SD of three biological replicates. Vesicle limit of detection was ~10^7 ml^{-1}.

encoded broadly distributed regions of the MED4 genome, representing over 50% of the entire chromosomal sequence (Fig. 2 and table S4). We noted a reproducible overabundance of reads from a region of the chromosome roughly centered on the terminus region, which suggested a possible link to the cell cycle; however, the mechanisms through which these DNA fragments are generated and packaged into vesicles are unclear. The vesicles also contained RNA (fig. S6B), and sequences from 95% of open reading frames in the genome were recovered (fig. S8). Membrane vesicles have been shown to facilitate horizontal gene transfer among a number of bacteria including *Escherichia coli* (*12*) and *Acinetobacter* (*13*). Given the abundance of *Prochlorococcus* in the oceans, our finding that it releases DNA within vesicles could have important implications for mechanisms of horizontal gene transfer in marine ecosystems.

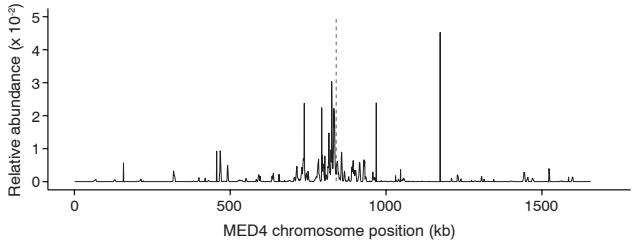


Fig. 2. *Prochlorococcus* membrane vesicles contain genomic DNA sequences. Distribution of DNA associated with vesicles from *Prochlorococcus* MED4 cultures. Sequence reads were mapped against the MED4 chromosome; mean relative abundance from two replicate samples is plotted over a 1-kb window. In total, 948,424 bp of the 1,657,990 bp chromosome (56%) was sequenced at least once from the vesicle populations. Dashed vertical line indicates the predicted chromosome terminus location.

To explore the prevalence of vesicles in the oceans, we examined surface samples from both nutrient-rich coastal seawater (Vineyard Sound, MA) and from the oligotrophic Sargasso Sea [at the Bermuda Atlantic Time-series Study (BATS) station]. Using density-gradient purification to separate vesicles from other small particles in seawater, we isolated numerous structures from both sites with a morphology and size distribution similar to those of the vesicles found in *Prochlorococcus* cultures (Fig. 3, A and B, and fig. S9A). Although some particles resembling filamentous phage copurified with the vesicles (thin white lines in Fig. 3B), we observed negligible numbers of apparent tailed or tailless phage, gene transfer agents, viruslike particles (*21*), and inorganic colloids in our enriched fractions. Examination of the putative vesicles by thin-section electron microscopy showed numerous examples of circular, membrane-bound features lacking internal structure or electron density (Fig. 3C), consistent with vesicle morphology and not that of bacteria. These samples contained protein as well as diverse lipid species, also consistent with membrane vesicles (fig. S10 and supplementary text). Although it is possible that some of these structures could have been formed by other mechanisms, the combination of culture and field data support the interpretation that these are membrane vesicles.

Vesicle abundances in the coastal surface water and Sargasso Sea samples were ~6×10^6 ml^{-1} and 3×10^5 ml^{-1}, respectively (Fig. 3D)—similar to the concentrations of bacteria at these sites. We analyzed a depth profile in the Sargasso Sea, and vesicles were observed both within and below the euphotic zone, declining with depth down to 500 m (Fig. 3D and fig. S9, B to D). The steady-state concentration of vesicles in the ocean is a function of rates of production, consumption, decay, and perhaps association with other ocean features such as marine microgels. Although we do not yet know enough about these processes to interpret the mechanisms that result in this distribution within the water column, the concordance between vesicle and bacterial abundance is consistent with the argument that the vesicles are of microbial origin.

It has been suggested that total *Prochlorococcus*-derived dissolved organic carbon (DOC) could support a substantial fraction of total bacterial production in oligotrophic regions (*22*). The release of vesicles by *Prochlorococcus*, with their diverse contents, implicates their secretion as a

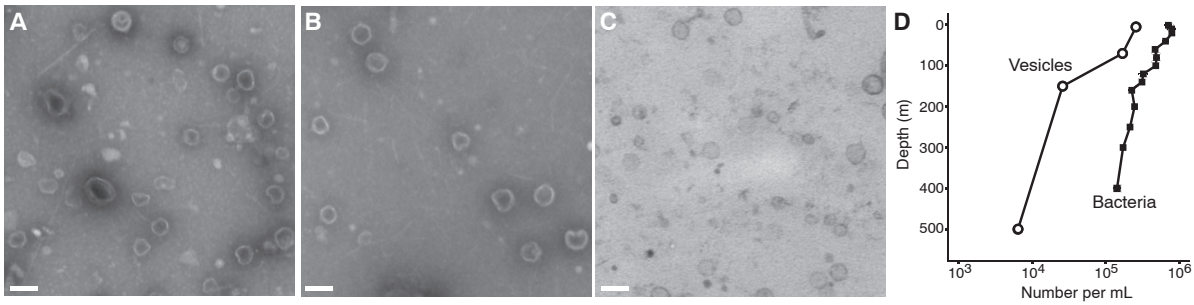


Fig. 3. Membrane vesicles are abundant in natural seawater samples. Negative-stain electron micrographs of membrane vesicles isolated from surface (**A**) coastal (Vineyard Sound, MA) and (**B**) oligotrophic waters (Sargasso Sea). (**C**) Thin-section electron micrograph of the sample from (B) shows that these structures are circular, enclosed by a membrane, and lack internal structure. Scale bars, 100 nm in (A) to (C). (**D**) Concentrations of vesicles (open circles) and total bacteria [squares; bacterial 4′,6′-diamidino-2-phenylindole (DAPI) count data from BATS] in the upper Sargasso Sea, December 2012. Vesicle concentrations are based on measurements of purified vesicle samples and represent lower-bound estimates of in situ abundance.

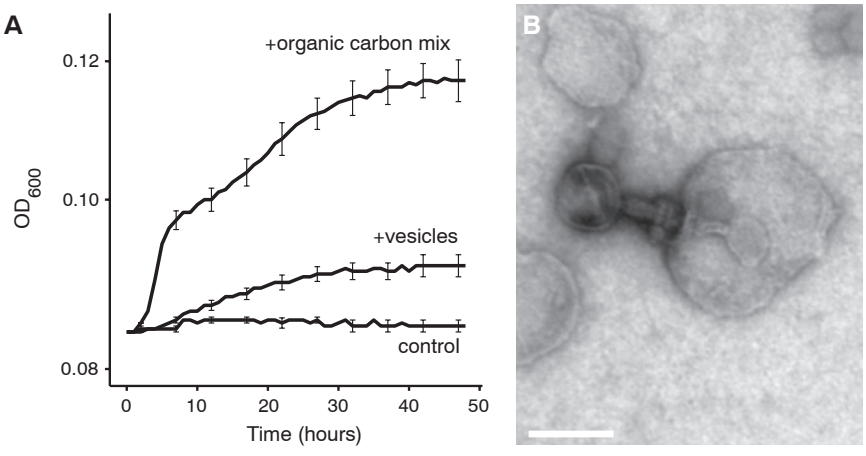


Fig. 4. Potential roles of bacterial vesicles in marine ecosystems. (**A**) Purified *Prochlorococcus* vesicles can support the growth of a heterotrophic marine *Alteromonas*. *Alteromonas* growth patterns are shown in a seawater-based minimal medium supplemented with media only (control), vesicles (+vesicles), or a defined mixture of organic carbon compounds (+organic carbon mix) as the only added carbon source. Growth curves represent the mean ± SEM of three replicates. The optical density at 600 nm (OD_{600}) increase of the "+vesicles" and "+organic carbon" trials both corresponded with a significant increase in *Alteromonas* cell concentration (measured by plate counts) as compared with the control after 48 hours (*t* test; $P < 0.05$). (**B**) Marine phage-vesicle interactions. TEM micrograph of cyanophage PHM-2 bound to a vesicle from *Prochlorococcus* MED4 (see also fig. S12). The shortened tail indicates that this phage has "infected" the vesicle and is therefore unable to infect a bacterial cell. Scale bar, 100 nm.

mechanism for production of some of this DOC. Given the data in hand, the lower bound of global *Prochlorococcus* vesicle production would represent roughly 10^4 to 10^5 tonnes of fixed C exported into the oceans per day (supplementary text). Lipids make up a notable component of total DOC in seawater (*23*), which is consistent with the presence of vesicle material among the high molecular mass fraction (>1000 daltons) of DOC. Although bacterial membrane vesicles have structural similarities to liposomes previously described as a component of DOC, they differ in two important respects: Vesicles are smaller [~50 to 150 nm diameter versus 400 to 1500 nm for liposomes (*24*)] and are not formed from the products of lysed or incompletely digested bacteria.

These observations implicate vesicle release by *Prochlorococcus* and other organisms in the flow of organic carbon in the oceans. To explore whether vesicles could serve as an organic carbon source for heterotrophs in marine food webs, we examined whether *Prochlorococcus* vesicles could support the growth of marine heterotrophic bacteria in culture. We found that marine isolates of both *Alteromonas* and *Halomonas* each grew in seawater media supplemented with purified *Prochlorococcus* vesicles as the only added carbon source (Fig. 4A and fig. S11), which illustrated that at least some of the vesicles' carbon is labile. Although vesicles may not constitute a large fraction of the total organic carbon consumed by heterotrophs in the oceans (each *Prochlorococcus* vesicle contains roughly 1/100th the carbon of an average bacterial cell in the open ocean) (supplementary text), they are clearly capable of moving fixed carbon from primary producers into the microbial food web. The presence of proteins and nucleic acids within vesicles implies that they could function as sources of N and P as well.

It is perhaps surprising that *Prochlorococcus*, or other microbes growing in the nutrient-poor oligotrophic oceans, would continually export nutrients in the form of membrane vesicles. *Prochlorococcus*, for example, has adaptations that reduce its phosphorus and nitrogen requirements, including the use of sulfolipids instead of phospholipids (*18*) and a proteome with relatively low nitrogen demand (*25*). Vesicle release seems inconsistent with the need to make efficient use of limited resources that presumably underlies these adaptations. What potential ecological roles, then, might vesicles play within marine microbial communities that could provide a fitness benefit sufficient to justify their costs? We can only speculate at this point, but what follows are some possibilities.

The growth of *Prochlorococcus* is often positively influenced by the presence of heterotrophs (*26*, *27*), so the release of DOC into the local environment could provide some fitness advantage by facilitating heterotroph growth. Vesicles might also play a role in defending cells against infection by phage—viruses that infect bacteria (*10*). Phage are abundant in the oceans, and cyanophage that infect *Prochlorococcus* can represent a substantial fraction of the total viral population (*28*). As vesicles contain bacterial outer membrane material, such as the external protein receptors phage use to identify their host, they represent a class of small particles that could influence marine phage infection dynamics. To explore this possibility, we mixed purified *Prochlorococcus* vesicles with a phage (PHM-2) known to infect the strain from which they originated and examined the population by electron microscopy. We observed numerous examples of phage bound to vesicles; in addition, many vesicle-attached phage had a shortened stalk and altered capsid staining density, which suggested that they had injected their DNA into the vesicle (Fig. 4B and fig. S12). Thus, the export of vesicles by marine bacteria could reduce the probability of a cell's becoming infected and killed by phage.

The finding that *Prochlorococcus* releases DNA within membrane vesicles suggests that they may also serve as a reservoir of genetic information and possible vector for horizontal gene transfer in marine systems. To characterize the nature of the vesicle-associated DNA pool in natural seawater, we sequenced the "metagenome" from purified and DNase-treated vesicles isolated from our two field sites. Based on the unique sequences recovered, these "wild" vesicles contained a diverse pool of DNA with significant homology to members of 33 phyla from all three domains, although bacterial sequences were dominant (table S5). The majority of unique bacterial sequences were most similar to members of the *Proteobacteria*, *Cyanobacteria*, and *Bacteroidetes*. Since *Prochlorococcus* and other bacteria (*29*) export fragments of their genome within vesicles, the taxonomic diversity of DNA we observed in the field samples implies that diverse marine microbes release vesicles. We also identified sequences with homology to tailed and other marine phage, despite the fact that these were not apparent in the fractions by TEM (table S5 and supplementary text). Although we cannot completely rule out the presence of phage in the samples, these sequences could reflect either the export of prophage sequences within vesicles or DNA arising from phage infection of vesicles in the field.

Although membrane vesicles constitute only a fraction of the $>10^9$ small (<200-nm) colloidal particles per ml observed in seawater (*30*), that they are known to move diverse compounds between organisms in other systems (*5*, *7*) suggests that they could serve specific functions in marine ecosystems. By transporting relatively high local concentrations of compounds, providing binding sites, or acting as reactive surfaces, vesicles may mediate interactions between microorganisms and their biotic and abiotic environment that would otherwise be impossible in the extremely dilute milieu of the oligotrophic oceans.

References and Notes

1. B. L. Deatherage, B. T. Cookson, *Infect. Immun.* **80**, 1948–1957 (2012).
2. A. Kulp, M. J. Kuehn, *Annu. Rev. Microbiol.* **64**, 163–184 (2010).
3. J. W. Schertzer, M. Whiteley, *MBio* **3**, e00297-11 (2012).
4. I. A. MacDonald, M. J. Kuehn, *J. Bacteriol.* **195**, 2971–2981 (2013).
5. J. L. Kadurugamuwa, T. J. Beveridge, *J. Bacteriol.* **177**, 3998–4008 (1995).
6. J. Rivera *et al.*, *Proc. Natl. Acad. Sci. U.S.A.* **107**, 19002–19007 (2010).
7. L. M. Mashburn, M. Whiteley, *Nature* **437**, 422–425 (2005).
8. H. Yonezawa *et al.*, *BMC Microbiol.* **9**, 197 (2009).
9. Y. Gorby *et al.*, *Geobiology* **6**, 232–241 (2008).
10. A. J. Manning, M. J. Kuehn, *BMC Microbiol.* **11**, 258 (2011).
11. J. A. Roden, D. H. Wells, B. B. Chomel, R. W. Kasten, J. E. Koehler, *Infect. Immun.* **80**, 929–942 (2012).
12. G. L. Kolling, K. R. Matthews, *Appl. Environ. Microbiol.* **65**, 1843–1848 (1999).
13. C. Rumbo *et al.*, *Antimicrob. Agents Chemother.* **55**, 3084–3090 (2011).
14. P. Flombaum *et al.*, *Proc. Natl. Acad. Sci. U.S.A.* **110**, 9824–9829 (2013).
15. F. Partensky, L. Garczarek, *Annu. Rev. Mar. Sci.* **2**, 305–331 (2010).
16. Materials and methods are available as supplementary material on *Science* on the Web.
17. D. Mug-Opstelten, B. Witholt, *Biochim. Biophys. Acta* **508**, 287–295 (1978).
18. B. A. S. Van Mooy, G. Rocap, H. F. Fredricks, C. T. Evans, A. H. Devol, *Proc. Natl. Acad. Sci. U.S.A.* **103**, 8607–8612 (2006).
19. N. Borch, D. Kirchman, *Aquat. Microb. Ecol.* **16**, 265–272 (1999).
20. E. Tanoue, S. Nishiyama, M. Kamo, A. Tsugita, *Geochim. Cosmochim. Acta* **59**, 2643–2648 (1995).
21. H. X. Chiura, K. Kogure, S. Hagemann, A. Ellinger, B. Velimirov, *FEMS Microbiol. Ecol.* **76**, 576–591 (2011).
22. S. Bertilsson, O. Berglund, M. Pullin, S. Chisholm, *Vie Milieu* **55**, 225–232 (2005).
23. L. Aluwihare, D. Repeta, R. Chen, *Nature* **387**, 166–169 (1997).
24. A. Shibata, K. Kogure, I. Koike, K. Ohwada, *Mar. Ecol. Prog. Ser.* **155**, 303–307 (1997).
25. J. J. Grzymski, A. M. Dussaq, *ISME J.* **6**, 71–80 (2012).
26. D. Sher, J. W. Thompson, N. Kashtan, L. Croal, S. W. Chisholm, *ISME J.* **5**, 1125–1132 (2011).
27. J. J. Morris, Z. I. Johnson, M. J. Szul, M. Keller, E. R. Zinser, *PLOS ONE* **6**, e16805 (2011).
28. R. J. Parsons, M. Breitbart, M. W. Lomas, C. A. Carlson, *ISME J.* **6**, 273–284 (2012).
29. A. V. Klieve *et al.*, *Appl. Environ. Microbiol.* **71**, 4248–4253 (2005).
30. M. L. Wells, E. D. Goldberg, *Nature* **353**, 342–344 (1991).

Acknowledgments: We thank the members of the Chisholm laboratory, D. McLaughlin, and W. Burkholder for helpful discussions and advice; J. Jones for advice on particle analysis and providing access to equipment; N. Watson for microscopy assistance; and the J. King laboratory, Massachusetts Institute of Technology (MIT) for equipment use. J. Roden, L. Kelly, and P. Berube provided helpful suggestions on the manuscript. We also thank the captain and crew of the R/V Atlantic Explorer, R. Johnson, S. Bell, R. Parsons, and the rest of the BATS team for assistance with field sampling and providing access to data. Sequence data are available from the National Center for Biotechnology Information Sequence Read Archive (*Prochlorococcus* MED4 vesicles: SRP031649; field vesicles: SRP031871). This work was supported by grants from the Gordon and Betty Moore Foundation, the NSF Center for Microbial Oceanography: Research and Education (C-MORE), NSF-Biological Oceanography, and the MIT Energy Initiative Seed Grant program to S.W.C. F.S. and R.E.S. were supported by an award (NNA13AA90A) from the NASA Astrobiology Institute.

Supplementary Materials

www.sciencemag.org/content/343/6167/183/suppl/DC1
Materials and Methods
Supplementary Text
Figs. S1 to S13
Tables S1 to S6
References (*31*–*63*)

18 July 2013; accepted 25 November 2013
10.1126/science.1243457

Progenitor Outgrowth from the Niche in *Drosophila* Trachea Is Guided by FGF from Decaying Branches

Feng Chen[1,2,3] and Mark A. Krasnow[1,3]*

Although there has been progress identifying adult stem and progenitor cells and the signals that control their proliferation and differentiation, little is known about the substrates and signals that guide them out of their niche. By examining *Drosophila* tracheal outgrowth during metamorphosis, we show that progenitors follow a stereotyped path out of the niche, tracking along a subset of tracheal branches destined for destruction. The embryonic tracheal inducer *branchless* FGF (fibroblast growth factor) is expressed dynamically just ahead of progenitor outgrowth in decaying branches. Knockdown of *branchless* abrogates progenitor outgrowth, whereas misexpression redirects it. Thus, reactivation of an embryonic tracheal inducer in decaying branches directs outgrowth of progenitors that replace them. This explains how the structure of a newly generated tissue is coordinated with that of the old.

Many adult stem cells reside in specific anatomical locations, or niches, and are activated during tissue homeostasis and after injury (*1*–*4*). Although considerable effort has been made to identify factors that control stem cell proliferation and differentiation, how stem or progenitor cells move out of the niche and how they form new tissue are not well understood (*4*–*6*). Tissue formation in mature animals faces challenges not present in the embryo (*7*, *8*). The new cells migrate longer distances and navigate around and integrate into a complex milieu of differentiated tissues. In this work, we investigated the substratum and signals that guide *Drosophila* tracheal imaginal progenitor cells into the posterior during metamorphosis to form the pupal abdominal tracheae (PAT) that replace the posterior half of the larval tracheal system (tracheal metameres Tr6 to Tr10), which decays at this time (*9*, *10*) (Fig. 1A).

The PAT extend from the transverse connective (TC) branches in Tr4 and Tr5 (Fig. 1A). Each PAT consists of a multicellular stalk with many secondary branches, each of which has dozens of terminal cells that form numerous fine terminal branches (tracheoles) (*10*). There are two known tracheal progenitor populations at metamorphosis: dedifferentiated larval tracheal cells and spiracular branch (SB) imaginal tracheal cells set aside during embryonic tracheal

[1]Department of Biochemistry, Stanford University School of Medicine, Stanford, CA 94305–5307, USA. [2]Department of Genetics, Stanford University School of Medicine, Stanford, CA 94305–5307, USA. [3]Howard Hughes Medical Institute, Stanford University School of Medicine, Stanford, CA 94305–5307, USA.
*Corresponding author E-mail: krasnow@stanford.edu

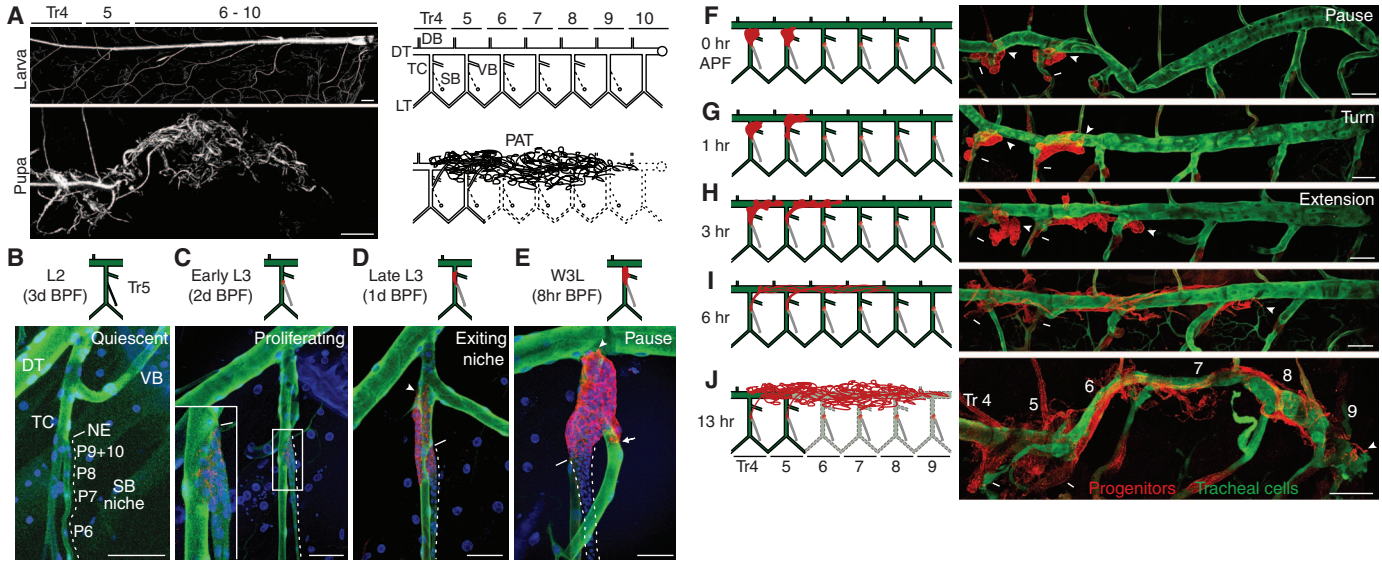


Fig. 1. Progenitor outgrowth during *Drosophila* tracheal metamorphosis. (**A**) Air-filled trachea (reflected light) (left) and schematics (right) in L3 larva and pupa ~13 hours after puparium formation. Tr, tracheal metamere; DB, dorsal branch; LT, lateral trunk; VB, visceral branch. Circles denote spiracles. Tracheal branches in the posterior (Tr6 to Tr10) are lost (dashed lines) during metamorphosis and are replaced by PAT from Tr4 and Tr5. (**B** to **E**) Fluorescence micrographs and schematics of Tr5 of *ppk4-Gal4>UAS-GFP; btl-RFP-moe* larva of the indicated ages stained to show activated tracheal progenitors (anti-RFP, red), larval tracheal cells (anti-GFP, green), and nuclei (4′,6-diamidino-2-phenylindole, blue). BPF, approximate time before puparium formation; W3L, wandering third-instar larva. (B) Quiescent progenitors in a Tr5 SB niche. Progenitors are also present in the SB niche of Tr2 to Tr4 and Tr6 to Tr9, but only those in Tr4 and Tr5 are activated to form PAT. P6 to P10, progenitors 6 to 10; the other five progenitors (P1 to P5) are shown in fig. S1A. NE, niche exit site (SB-TC junction). (C) Activated progenitors proliferating in the niche. (Inset) Progenitors near the niche exit site (dash), which have begun expressing *btl-RFP-moe* (red). (D) Progenitors exiting the niche. *btl-RFP-moe* expression increases and *ppk4>GFP* decreases as progenitors leave the niche and migrate dorsally along TC branches. Arrowhead, progenitor migration front. (E) Progenitors paused at the DT (arrowhead). Several progenitors have extended onto the VB (arrow). (**F** to **J**) Schematics and micrographs [as in (B) to (E)] of trachea (Tr4 to Tr9) of pupa of indicated ages APF. Paused progenitors (F) move onto the DT and turn posteriorly (G), extending along the DT (H and I) before ramifying into the PAT (J). Posterior tracheal branches start to collapse 9 hours APF and are fully collapsed and no longer conduct air by 13 hours APF. The larval cells die during metamorphosis (*10*), although we did not detect the apoptosis marker anticleaved caspase-3 during collapse (fig. S9). Scale bars: 100 μm, (A) and (F) to (J); 50 μm, (B) to (E).

development (*11*–*14*). Lineage tracing showed that PAT derive from imaginal progenitors (fig. S1, B and C).

To determine how progenitors in Tr4 and Tr5 reach the posterior, we used a *btl-RFP-moe* transgene (*15*) (RFP, red fluorescent protein) to label activated progenitor cells, and *ppk4>GFP* (*16*) (GFP, green fluorescent protein) to label larval tracheal branches (fig. S2A). Before metamorphosis, there are 7 to 10 quiescent progenitor cells in each SB niche (Fig. 1B and fig. S1A) (*11*, *13*). In early third larval instar (L3), progenitors proliferate but remain in the niche (Fig. 1C). Later in L3, progenitors leave the niche, moving onto the larval TC branches toward the dorsal trunk (DT) (Fig. 1D), while progenitors within the niche continue to proliferate (*13*). Progenitors in other metameres also proliferate but do not move out of the niche (fig. S2B). Migrating progenitors in Tr4 and Tr5 crawl along the basal surface of larval tracheal cells, with cytoplasmic projections emanating from cells at the leading edges of the progenitor cluster (fig. S3C). Progenitors maintain epithelial polarity and a lumen continuous with the SB and TC branches, forming a saclike structure (fig. S3, A and B) (*9*). By wandering L3, progenitors reach the DT (Fig. 1E), where they pause (~12 hours) until the onset of puparium formation (Fig. 1F).

Around 1 hour after puparium formation (APF), progenitors move onto the DT and turn posteriorly (Fig. 1G). Posterior migration continues for 9 hours, extending half the animal's length (~0.8 mm) past Tr9 (Fig. 1, H to J). Live imaging showed that progenitors move at ~1.7 μm/min, crawling along and wrapping around the DT as they migrate (movie S1).

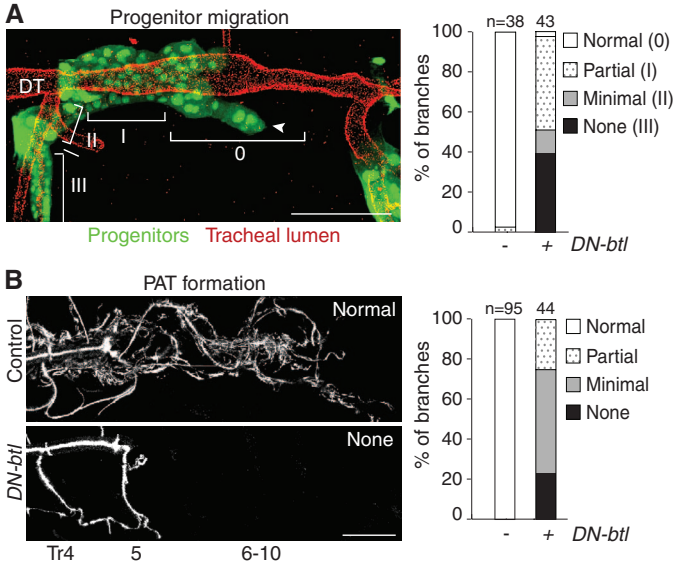


Fig. 2. Progenitor outgrowth requires *breathless* FGFR. (**A**) PAT progenitor migration in a control *esg^{P127}-Gal4, UAS-GFP/ act5c>Y>Gal4, UAS-GFP; UAS-FLP* pupa 6 hours APF at 18°C with progenitors marked with GFP (green) and tracheal lumens stained (red). Brackets show position of progenitor migration front in the four phenotypic classes (0, I, II, III) scored in control and in *esg^{P127}-Gal4, UAS-GFP/act5c>Y>Gal4, UAS-GFP; UAS-FLP/ UAS-DN-btl* pupae, in which dominant-negative *breathless* (*DN-btl*) is selectively expressed in progenitors. Examples of each phenotypic class can be found in fig. S5, A to D. Arrowhead, progenitor migration front. The graph at right shows quantification. n, number of branches. (**B**) PAT formation in control (top) and *DN-btl* pupae (bottom) as above, except reared for 1 to 2 additional days to allow formation of mature, air-filled pupal tracheae (reflected light). No PAT have formed in the *DN-btl* pupa. The graph shows quantification, with phenotypes classified as in fig. S5, E to H. Scale bars, 100 μm.

Differentiation begins as progenitors migrate. At the beginning of puparium formation (0 hours APF, Fig. 1F), a subset of progenitors that have exited the niche begins to express the terminal cell master regulator Pruned SRF (serum response factor) (*17*), initiating cell specialization (fig. S4A). As progenitors migrate along the DT, budlike structures composed of Pruned-expressing cells are detected at the tips of progenitor clusters, whereas Pruned-negative cells form the stalks of new trachea (fig. S4B). By 6 hours APF, Pruned-expressing progenitors in the tips adopt an elongated and differentiated morphology (fig. S4, C and D), flattening along the DT as they extend further posteriorly (movie S1). Around 13 hours APF, the PAT mature and fill with gas as posterior tracheal branches collapse (Fig. 1, A and J).

What guides tracheal progenitors on their stereotyped path along specific branches of the larval tracheal system? Expression of *breathless* (*btl*) FGFR (fibroblast growth factor receptor) is induced in PAT progenitors (*11*, *13*), as shown by the *btl-RFP-moe* reporter (Fig. 1, B to J). We tested whether the Btl pathway, which directs tracheal branch outgrowth in embryos (*18*–*20*) and larvae (*21*) and induces adult air-sac primordium formation (*22*), is involved. Expression of dominant-negative Btl FGFR (*19*) in the progenitors and their descendants (*23*) blocked migration and diminished or eliminated PAT formation (Fig. 2 and fig. S5). To determine the source of the only known Btl ligand, Branchless (Bnl) FGF (*20*), we used a *bnl* reporter, *bnl-Gal4* enhancer trap line NP2211 (*24*) driving *UAS-GFP*. Unlike previously described examples of tracheal outgrowth (*20*–*22*), *bnl* was not expressed in surrounding tissue. Instead, it was expressed within the tracheal system, specifically by larval tracheal cells along which progenitors migrate. The expression pattern is dynamic and precise, almost perfectly matching the positions and timing of progenitor migration (Fig. 3A and fig. S6A). In L3 animals, when progenitors are observed along the TC branches, *bnl>GFP* was expressed in TC larval cells in Tr4 and Tr5, but not in other metameres. Shortly after puparium formation, when PAT progenitors turn to migrate toward the posterior, DT larval cells in the segment just posterior to PAT

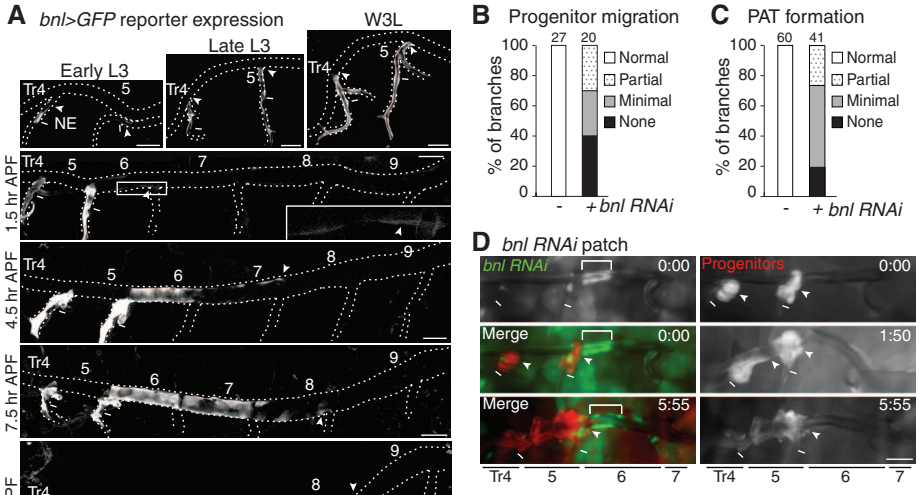
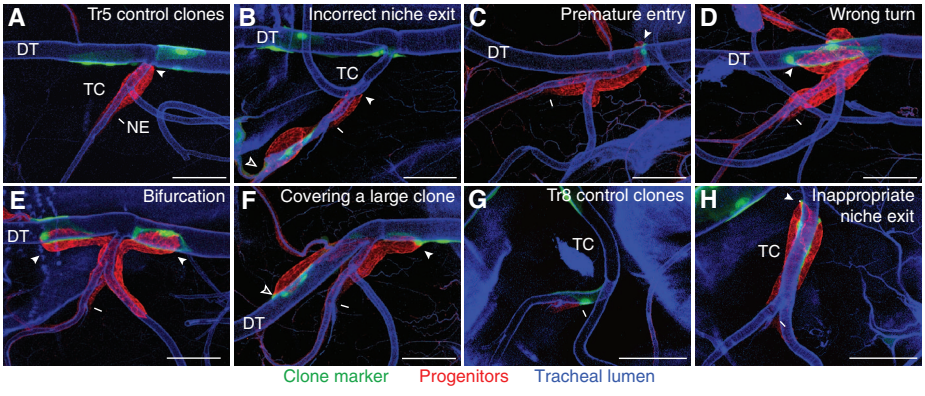


Fig. 3. Expression and requirement of *branchless* FGF during progenitor outgrowth. (**A**) *branchless* reporter expression during progenitor outgrowth visualized by GFP immunostaining (white) of *UAS-GFP; bnl-Gal4 NP2211/ btl-RFP-moe* larvae and pupae of indicated ages. Reporter expression dynamically expands along the progenitor outgrowth path, initially turning on in isolated larval cells in each area. Arrowheads denote furthest detected reporter expression. (**B** and **C**) Quantification (as in Fig. 2) of progenitor migration 3 hours APF (B) and PAT formation (C) phenotypes in control (*ppk4-Gal4, UAS-GFP; btl-RFP-moe*) and *ppk4-Gal4, UAS-GFP; btl-RFP-moe/ UAS-bnl RNAi* pupae, in which *bnl* was inactivated in larval tracheal cells. For examples of the phenotypic classes, see fig. S7, A and B. (**D**) Frames at indicated times (hours:minutes) APF from live imaging of an *act5c>Y>Gal4, UAS-GFP/ UAS-FLP; prd-Gal4, btl-RFP-moe/ UAS-bnl RNAi* pupa in which *bnl* expression was inactivated in a DT patch (brackets). Tr5 progenitors (*btl-RFP-moe*) exit the niche (dashes) and move onto the DT but never pass the patch. Scale bars, 100 μm.



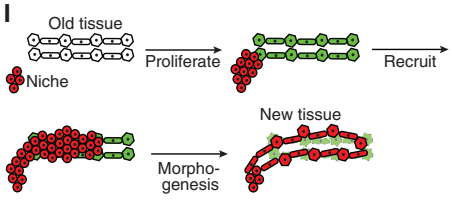


Fig. 4. Effect of ectopic *bnl* on progenitor migration. Tracheal progenitors (red, anti-RFP) in Tr4 or Tr5 [(**A**) to (**F**)] and Tr8 [(**G**) and (**H**)] of control (*dfr-FLP/ act5c>Y>Gal4, UAS-GFP; btl-RFP-moe*) and experimental (*dfr-FLP/ act5c>Y>Gal4, UAS-GFP; btl-RFP-moe/ UAS-bnl*) wandering third-instar larvae showing control clones of larval tracheal cells expressing GFP alone (green) [(A) and (G)] or experimental clones expressing GFP and ectopic *bnl* FGF [(B to F) and (H)]. Blue, tracheal lumen (Alexa Fluor 350-conjugated wheat germ agglutinin). Arrowheads denote progenitor migration fronts. (A) Progenitors have exited the niche and reached the TC-DT junction (arrowhead). Control clones (green) have no effect. (B) Some progenitors have exited the niche in the wrong direction along TC branches (open arrowhead), extending toward the *bnl*-expressing clone ventral to the niche exit. Other progenitors (solid arrowhead) have exited the niche normally toward DT. (C) Progenitors have prematurely moved onto DT, extending toward a single larval DT cell expressing *bnl*. (D) Inappropriate anterior migration of progenitors along DT (arrowhead) toward the *bnl*-expressing clone. (E) Bifurcation of progenitor cluster (arrowheads) toward a pair of *bnl*-expressing clones located anterior and posterior to the TC-DT junction. (F) Bifurcation (arrowheads) where progenitors extend to fill the shape of a large *bnl*-expressing clone (open arrowhead). (G) Progenitors in Tr8 (as well as Tr3 and Tr6 to Tr9) normally remain within the niche and are unaffected by control clones. (H) Tr8 progenitors exit the niche toward a clone of *bnl*-expressing cells on TC branches. Scale bars [(A) to (H)], 100 μm. (**I**) Model of progenitor outgrowth guided by a signal produced by decaying tissue (green). Progenitors (red) are attracted to and form new tissue at the site of decay.

progenitors express *bnl>GFP*. As progenitors continue along the DT, DT larval cells activate *bnl>GFP* expression one segment at a time from anterior to posterior, matching progenitor movement.

This dynamic *bnl* expression along the migration path is required for progenitor outgrowth. Knockdown of *bnl* expression by RNA interference (RNAi) in larval tracheal cells blocked migration and resulted in diminished or absent PAT (Fig. 3, B and C; fig. S7, A to C; and movie S2). Mosaic expression of *bnl RNAi* in small patches along the path (*23*) also arrested migration, so long as the patch encompassed the full DT circumference (Fig. 3D; fig. S7, D and E; and movies S3 and S4). Thus, Bnl is required all along the migration path, and the signal does not cross even short gaps.

Ectopic *bnl* expression in GFP-labeled clones of larval tracheal cells induced by *dfr-FLP* (*23*) redirected progenitor migration. Depending on the location of the clones, ectopic *bnl* caused incorrect exit from the niche, premature entry onto the DT, or wrong turns on the DT (Fig. 4, B to D). Dual clones induced bifurcation with groups of progenitors moving toward each ectopic *bnl* source (Fig. 4E). Clones in Tr3 and posterior metameres caused progenitors in these regions to leave the niche, even though they do not normally do so (Fig. 4, G and H, and fig. S8, D and E). When there was a large clone, progenitors migrated throughout the clone (Fig. 4F), implying that progenitors do not require a gradient and will spread to cover an entire region of cells expressing *bnl* at equivalent levels. When *bnl*-expressing clones failed to induce migration, the clones appeared to be too far from the progenitors or there was competition from another clone close by (fig. S8, A and B). Ectopic *bnl* expression within the progenitor cluster arrested migration (fig. S8C).

The results show that the embryonic tracheal inducer Bnl FGF guides tracheal progenitors out of the niche and into the posterior during tracheal metamorphosis. The source of Bnl is the larval tracheal branches destined for destruction, which serve both as the source of the chemoattractant and as the substratum for progenitor migration. Several days earlier in embryos, these larval tracheal branches were themselves induced by Bnl provided by neighboring tissues. But after embryonic development, most tracheal cells, including those in the decaying larval branches, downregulate *btl* FGFR expression (fig. S2A) and thus do not respond to (or sequester) the Bnl signal they later express. One of the most notable aspects of this larval Bnl is its exquisitely specific pattern in decaying larval branches, which presages progenitor outgrowth. It is unclear how Bnl expression is controlled, though it does not appear to require signals from migrating progenitors because the *bnl* reporter expression front progressed normally when progenitor outgrowth was stalled by a tracheal break (fig. S6C). Perhaps expression of Bnl involves gradients in the tracheal system or spatial patterning cues established during embryonic development in conjunction with temporal signals mediated by molting hormones.

Because the signal guiding progenitor migration is provided by tracheae destined for destruction, progenitors become positioned along the larval branches they replace (Fig. 4I). Perhaps during tissue repair and homeostasis, recruitment of adult stem or progenitor cells from the niche is similarly guided by signals from decaying tissue, thereby ensuring that new tissue is directed to the appropriate sites.

References and Notes

1. N. Barker, S. Bartfeld, H. Clevers, *Cell Stem Cell* **7**, 656–670 (2010).
2. G. B. Adams, D. T. Scadden, *Nat. Immunol.* **7**, 333–337 (2006).
3. A. Alvarez-Buylla, D. A. Lim, *Neuron* **41**, 683–686 (2004).
4. C. Blanpain, E. Fuchs, *Nat. Rev. Mol. Cell Biol.* **10**, 207–217 (2009).
5. E. Sancho, E. Batlle, H. Clevers, *Curr. Opin. Cell Biol.* **15**, 763–770 (2003).
6. G. L. Ming, H. Song, *Neuron* **70**, 687–702 (2011).
7. E. Nacu, E. M. Tanaka, *Annu. Rev. Cell Dev. Biol.* **27**, 409–440 (2011).
8. K. D. Poss, *Nat. Rev. Genet.* **11**, 710–722 (2010).
9. T. Matsuno, *Jap. J. Appl. Entomol. Zool.* **34**, 165–167 (1990).
10. G. Manning, M. A. Krasnow, in *The Development of* Drosophila melanogaster, M. Bate, A. Martinez-Arias, Eds. (Cold Spring Harbor Laboratory Press, Woodbury, NY, 1993), vol. 1, pp. 609–685.
11. M. Weaver, M. A. Krasnow, *Science* **321**, 1496–1499 (2008).
12. A. Guha, L. Lin, T. B. Kornberg, *Proc. Natl. Acad. Sci. U.S.A.* **105**, 10832–10836 (2008).
13. C. Pitsouli, N. Perrimon, *Development* **137**, 3615–3624 (2010).
14. M. Sato, Y. Kitada, T. Tabata, *Dev. Biol.* **318**, 247–257 (2008).
15. C. Ribeiro, M. Neumann, M. Affolter, *Curr. Biol.* **14**, 2197–2207 (2004).
16. L. Liu, W. A. Johnson, M. J. Welsh, *Proc. Natl. Acad. Sci. U.S.A.* **100**, 2128–2133 (2003).
17. K. Guillemin *et al.*, *Development* **122**, 1353–1362 (1996).
18. C. Klämbt, L. Glazer, B. Z. Shilo, *Genes Dev.* **6**, 1668–1678 (1992).
19. M. Reichman-Fried, B. Z. Shilo, *Mech. Dev.* **52**, 265–273 (1995).
20. D. Sutherland, C. Samakovlis, M. A. Krasnow, *Cell* **87**, 1091–1101 (1996).
21. J. Jarecki, E. Johnson, M. A. Krasnow, *Cell* **99**, 211–220 (1999).
22. M. Sato, T. B. Kornberg, *Dev. Cell* **3**, 195–207 (2002).
23. Materials and methods are available as supporting material on *Science* Online.
24. S. Hayashi *et al.*, *Genesis* **34**, 58–61 (2002).

Acknowledgments: We thank M. Weaver, M. Metzstein, and other lab members for advice and reagents. This work was supported by a Genentech Graduate Fellowship and a Ruth L. Kirschstein NIH training grant (F.C.) and the Howard Hughes Medical Institute.

Supplementary Materials

www.sciencemag.org/content/343/6167/186/suppl/DC1
Materials and Methods
Figs. S1 to S10
References (*25*–*39*)
Movies S1 to S4

4 June 2013; accepted 12 November 2013
10.1126/science.1241442

Mutational Analysis Reveals the Origin and Therapy-Driven Evolution of Recurrent Glioma

Brett E. Johnson,[1]* Tali Mazor,[1]* Chibo Hong,[1] Michael Barnes,[2] Koki Aihara,[3,4] Cory Y. McLean,[1]† Shaun D. Fouse,[1] Shogo Yamamoto,[3] Hiroki Ueda,[3] Kenji Tatsuno,[3] Saurabh Asthana,[5,6] Llewellyn E. Jalbert,[7] Sarah J. Nelson,[7,8] Andrew W. Bollen,[2] W. Clay Gustafson,[9] Elise Charron,[10] William A. Weiss,[1,9,10] Ivan V. Smirnov,[1] Jun S. Song,[11,12] Adam B. Olshen,[6,11] Soonmee Cha,[1] Yongjun Zhao,[13] Richard A. Moore,[13] Andrew J. Mungall,[13] Steven J. M. Jones,[13] Martin Hirst,[13] Marco A. Marra,[13] Nobuhito Saito,[4] Hiroyuki Aburatani,[3] Akitake Mukasa,[4] Mitchel S. Berger,[1] Susan M. Chang,[1] Barry S. Taylor,[5,6,11]‡ Joseph F. Costello[1]‡

Tumor recurrence is a leading cause of cancer mortality. Therapies for recurrent disease may fail, at least in part, because the genomic alterations driving the growth of recurrences are distinct from those in the initial tumor. To explore this hypothesis, we sequenced the exomes of 23 initial low-grade gliomas and recurrent tumors resected from the same patients. In 43% of cases, at least half of the mutations in the initial tumor were undetected at recurrence, including driver mutations in *TP53*, *ATRX*, *SMARCA4*, and *BRAF*; this suggests that recurrent tumors are often seeded by cells derived from the initial tumor at a very early stage of their evolution. Notably, tumors from 6 of 10 patients treated with the chemotherapeutic drug temozolomide (TMZ) followed an alternative evolutionary path to high-grade glioma. At recurrence, these tumors were hypermutated and harbored driver mutations in the RB (retinoblastoma) and Akt-mTOR (mammalian target of rapamycin) pathways that bore the signature of TMZ-induced mutagenesis.

The genetic landscape of tumors is continually evolving, which can be an impediment to the clinical management of cancer patients with recurrent disease (*1*, *2*). In contrast to the clonal evolution of hematological malignancies (*3*, *4*) and solid tumor metastases (*5*–*7*), the local regrowth of solid tumors after surgery occurs under a unique set of evolutionary pressures, which are further affected by adjuvant therapies. Through the acquisition of new mutations, residual tumor cells can progress to a more aggressive state. Grade II astrocytic gliomas are

particularly troublesome from this perspective. Although surgery is the standard of care, these invasive brain tumors typically recur (*8*). Many remain grade II at recurrence, while others progress to a higher histological grade with a poor prognosis (*9*). The incidence and timing of malignant progression are variable and unpredictable (*8*).

We undertook genome sequence analysis of initial and recurrent human gliomas to address two questions: (i) What is the extent to which mutations in initial tumors differ from their subsequent recurrent tumors? (ii) How does chemotherapy with temozolomide (TMZ), a drug commonly used in the treatment of glioma, affect the mutational profile of recurrent tumors? We sequenced the exomes of 23 grade II gliomas at initial diagnosis and their recurrences resected from the same patients up to 11 years later (table S1). We selected initial tumors of predominantly astrocytic histology that capture the full spectrum of glioma progression (histological grade II to IV at recurrence) and adjuvant treatment history. Tumor and matched normal DNA were sequenced to an average 125-fold coverage, enabling the sensitive detection of mutations down to a 10% variant frequency, small insertions and deletions, and DNA copy number alterations (CNAs) (Fig. 1A and tables S2 and S3) (*10*).

We identified an average of 33 somatic coding mutations in each initial tumor, of which an average of 54% were also detected at recurrence (shared mutations) (Fig. 1A). The shared mutations included those in *IDH1*, *TP53*, and *ATRX* in most but not all cases (fig. S1) (*11*–*13*). All other somatic mutations were identified only in the initial tumor or only in the recurrent tumor from a given patient (private mutations) and thus presumably arose later in tumor evolution. For example, mutations in *SMARCA4* were private to the initial or recurrent tumor in six of seven patients and therefore may confer a selective advantage in the context of preexisting early driver events (*14*, *15*). Overall, the initial and recurrent gliomas displayed a broad spectrum of genetic relatedness (fig. S2 and table S4). At one end of this spectrum were four patients whose tumors showed a pattern of linear clonal evolution; we infer that the recurrent tumors in these patients were seeded by cells bearing ≥75% of the mutations detected in the initial tumors (as in patient 27, Fig. 1B). At the other end of the spectrum, tumors from three patients showed branched clonal evolution; we infer that the recurrent tumors in these patients were seeded by cells derived from the initial tumor at an early stage of its evolution, as the recurrent tumors shared ≤25% of mutations detected in the initial tumors. Patient 17 was an extreme example of branched clonal evolution, as the initial and recurrent tumors shared only the *IDH1* R132H ($Arg^{132} \rightarrow His$) mutation (Fig. 1C). This further implicates *IDH1* mutations as an initiating event in low-grade gliomagenesis (*12*). Indeed, *IDH1* mutation was the only shared mutation in every patient—an observation that supports the current interest in IDH1 as a therapeutic target (*16*). Paired tumors from the remaining 16 patients formed a continuum between linear and branched clonal evolution. Together, these data illustrate the extent to which genetically similar low-grade gliomas diverge after surgical resection, and suggest that recurrences may emerge from early stages in the evolution of the initial tumor.

Many solid tumors, including glioblastoma (GBM), display intratumoral heterogeneity (*17*, *18*). For example, geographically distinct parts of the tumor may have different mutations. Intratumoral heterogeneity could be a confounding factor in estimates of genetic divergence when only one relatively small fraction of a tumor is sampled. To explore the extent of intratumoral heterogeneity in our cases, we first analyzed the *BRAF* V600E ($Val^{600} \rightarrow Glu$) mutation that was subclonal in the initial tumor of patient 18 and undetectable in the recurrent tumor by either exome sequencing or droplet digital polymerase chain reaction (PCR) (Fig. 1D and fig. S3) (*10*). *BRAF* V600E was present in three of six additional samples from geographically distinct regions of the initial tumor, whereas seven additional samples of the recurrence all lacked this mutation. These results suggest that the *BRAF*-mutant clone did not expand, despite the proliferative advantage typically conferred by this mutation. Such a finding contrasts sharply with the selection and outgrowth of subclonal drivers during the evolution of chronic lymphocytic leukemias (*3*).

Beyond the actionable *BRAF* mutation, we sequenced the exomes of additional, geographically distinct samples from three cases to further determine the extent to which apparently private mutations might be misclassified because of intratumoral heterogeneity. In patient 17, for whom all mutations except *IDH1* were private, intratumoral heterogeneity was observed in the initial and recurrent tumor. From the mutational profiles, however, we inferred that three samples of the initial tumor and four samples of the recurrence all derived from a common tumor cell of origin that possessed only an *IDH1* R132H mutation (Fig. 2A and table S5). Moreover, the recurrent tumor contained driver mutations in *TP53* and *ATRX* distinct from those observed in the initial tumor. We found no evidence of these new *TP53* or *ATRX* mutations in the initial tumor at allele frequencies of ~0.1% (figs. S3 and S4), implying convergent phenotypic evolution (*5*) via a strong ongoing selection for loss of these genes. The initial and recurrent tumors likely did not arise independently, as they also shared three somatic noncoding mutations (fig. S5). Thus, the initial and recurrent tumors were only distantly related and, despite the local and relatively rapid recurrence (fig. S6), exonic mutations other than *IDH1* R132H were only transiently present during the course of this patient's disease. Finally, we sequenced the exomes of additional distinct samples of the initial and recurrent tumors from patients 26 and 27, broadening our assessment of the impact of intratumoral heterogeneity on the reported genetic divergence. We found that only a small minority of private mutations were actually shared events (7%; table S3) (*10*). Intratumoral heterogeneity therefore could not explain the majority of the genetic divergence between the initial and recurrent tumors in our cohort, including the driver mutations in initial tumors that were undetected in their recurrence.

To investigate whether sequential recurrences from a single patient could each be traced to the same evolutionary stage of the initial tumor, we sequenced the exomes of the second and third recurrent tumors from patient 04 and constructed a disease phylogeny by clonal ordering (Fig. 2B, fig. S7, and table S5) (*5*, *19*). The initial tumor and three sequential local recurrences were clonally related, as indicated by the shared phylogenetic branch containing early driver mutations in *IDH1* and *TP53*. We infer that the tumor cells seeding the second recurrence branched off from the initial tumor at a slightly earlier evolutionary stage than the cells seeding the first recurrence. In contrast, the third recurrent tumor was a direct outgrowth of the second recurrence. These results show that branched and linear patterns of clonal evolution occurred at differing times in the same patient and are therefore not intrinsic properties of the tumor.

Beyond maximal, safe, surgical resection, there is currently no standard of care for patients with low-grade glioma; options include surveillance, adjuvant radiation alone, TMZ alone, or radiation and TMZ. TMZ is an alkylating agent that induces apoptosis in glioma cells and is sometimes used to defer or delay the use of radiation. However, there is currently no information on whether treatment of grade II astrocytomas with TMZ confers longer overall survival (*8*). Because TMZ is also mutagenic (*20*), we sought to determine how adjuvant chemotherapy with TMZ affects the mutational profile of recurrent tumors by comparing the initial low-grade gliomas to their recurrence after treatment. Although the initial tumors and most of the recurrent tumors in our cohort had 0.2 to 4.5 mutations per megabase (Mb) (*21*, *22*), 6 of the 10 patients treated with

[1]Department of Neurological Surgery, University of California, San Francisco, CA 94158, USA. [2]Department of Pathology, University of California, San Francisco, CA 94158, USA. [3]Genome Science Laboratory, Research Center for Advanced Science and Technology, University of Tokyo, Meguro-ku, Tokyo 153-8904, Japan. [4]Department of Neurosurgery, University of Tokyo, Bunkyo-ku, Tokyo 113-8655, Japan. [5]Department of Medicine, University of California, San Francisco, CA 94158, USA. [6]Helen Diller Family Comprehensive Cancer Center, University of California, San Francisco, CA 94158, USA. [7]Department of Bioengineering and Therapeutic Sciences, University of California, San Francisco, CA 94158, USA. [8]Department of Radiology and Biomedical Imaging, University of California, San Francisco, CA 94158, USA. [9]Department of Pediatrics, University of California, San Francisco, CA 94158, USA. [10]Department of Neurology, University of California, San Francisco, CA 94158, USA. [11]Department of Epidemiology and Biostatistics, University of California, San Francisco, CA 94158, USA. [12]Institute for Human Genetics, University of California, San Francisco, CA 94158, USA. [13]Michael Smith Genome Sciences Centre, British Columbia Cancer Agency, Vancouver, BC V5Z 4E6, Canada.

*These authors contributed equally to this work.
†Present address: 23andMe Inc., Mountain View, CA 94043, USA.
‡Corresponding author. E-mail: jcostello@cc.ucsf.edu (J.F.C.); barry.taylor@ucsf.edu (B.S.T.)

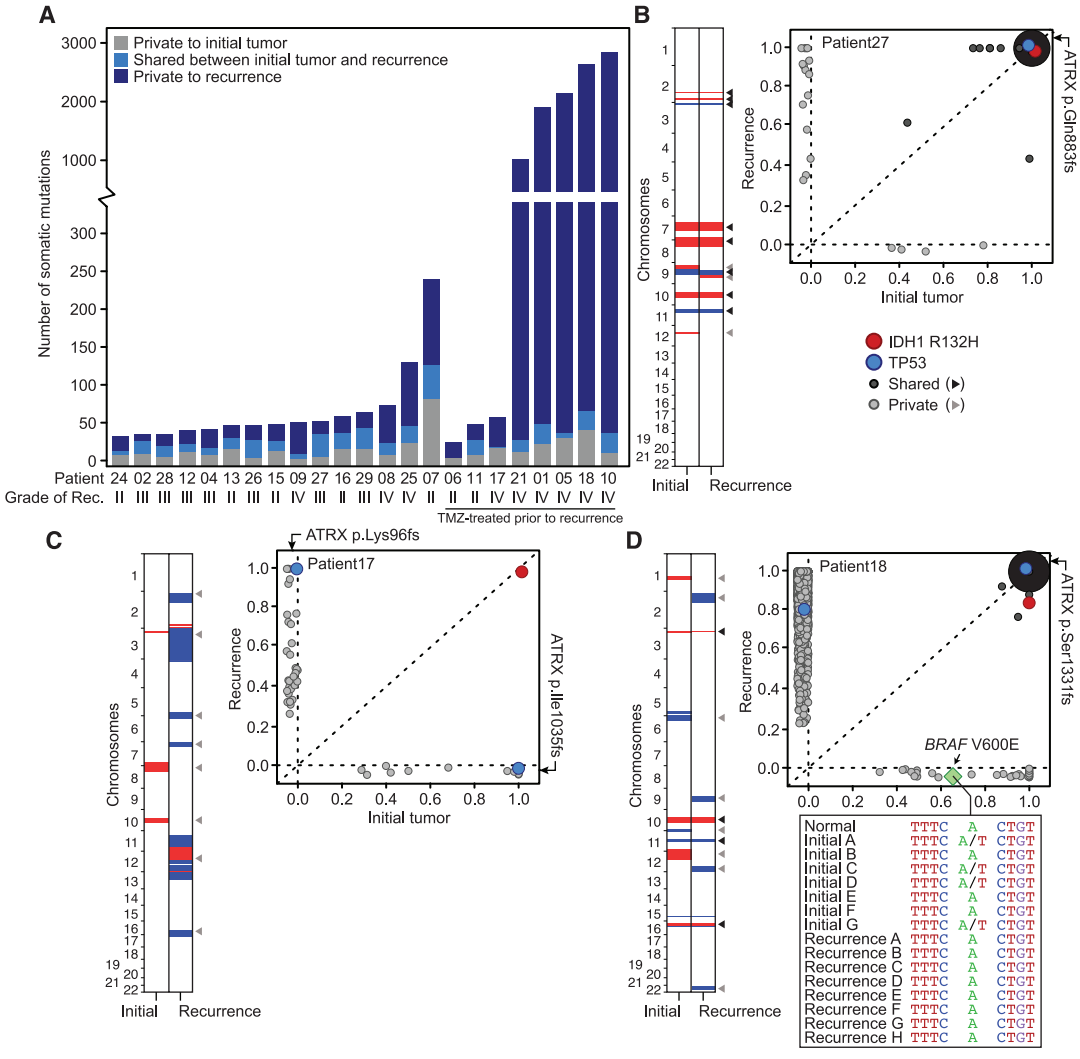


Fig. 1. Genetic landscapes of low-grade gliomas and their patient-matched recurrences. (**A**) Total number of mutations private to or shared between the initial and first recurrent glioma of 23 patients. (**B** to **D**) Shared and private somatic mutations in paired initial and recurrent tumors (*x* and *y* axes, respectively) as a function of the estimated fraction of tumor cells carrying the mutant allele. Mutations present in all the cells in both tumors are represented by a single point whose radius is scaled by the log count of such mutations. Shared and private CNAs are indicated (red and blue are gains and losses, respectively; white is copy-neutral). In (C), clonal *TP53* and *ATRX* mutations in the initial tumor were not identified in the recurrent tumor, but different clonal mutations in these two genes were acquired. (D) Inset shows the DNA sequence encompassing *BRAF* V600E in the normal tissue and in 15 geographically distinct samples of the initial and recurrent tumors.

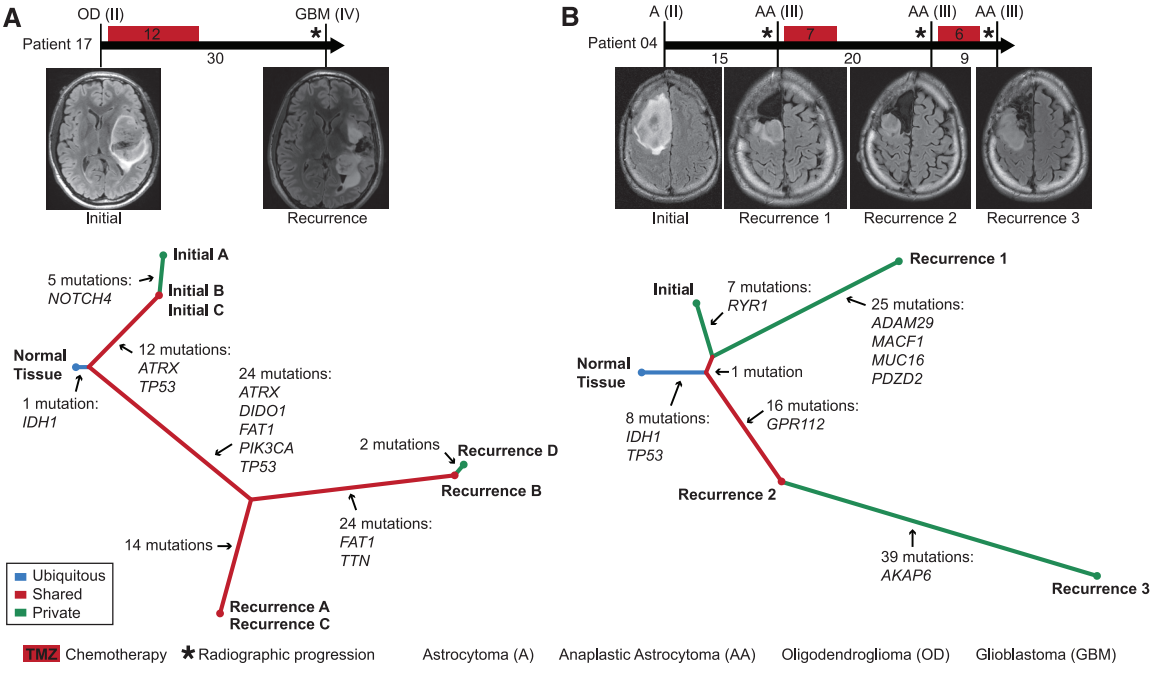


Fig. 2. Temporal and spatial patterns of clonal evolution in the tumors of two glioma patients. (**A** and **B**) A timeline of treatment histories for patient 17 (A) and patient 04 (B) (top, intervals labeled in months). Vertical bars correspond to the time of tumor resection and are labeled with the tumor diagnosis and grade. Representative MRIs are also shown. A phylogenetic tree (bottom) depicts the patterns of clonal evolution of these tumors inferred from the pattern and frequency of somatic mutations, highlighting genes frequently mutated in cancer.

TMZ had recurrent tumors that were hypermutated; that is, they harbored 31.9 to 90.9 mutations per Mb (table S6). Overall, 97% of these were C>T/G>A transitions predominantly occurring at CpC and CpT dinucleotides, which is a signature of TMZ-induced mutagenesis distinct from nonhypermutated tumors (fig. S8) (*20*, *22*, *23*). We classified C>T/G>A transitions in each hypermutated tumor as TMZ-associated if they were undetected in the matched initial tumor, which was resected before TMZ treatment (Fig. 3A). Although it is difficult to definitively attribute any single mutation to TMZ exposure, comparing the C>T/G>A mutation rates in each tumor pair suggested that >98.7% are due to TMZ-induced mutagenesis (*10*). To determine whether intratumoral heterogeneity in initial tumors resulted in the misclassification of some mutations as TMZ-associated, we sequenced the exomes of three additional geographically distinct samples of the untreated initial tumor from patient 18. For mutations classified as TMZ-associated, sequencing reads with the mutation were rare in the additional exomes and were found at rates no higher than expected by chance ($1.7 \pm 0.08\%$; $P = 0.5$, Wilcoxon rank-sum test) (*10*), further suggesting that they are induced by TMZ.

Resistance to TMZ develops in part through the acquisition of mutations that inactivate the DNA mismatch repair (MMR) pathway. MMR pathway dysfunction and continued TMZ exposure can in turn result in hypermutation (*22*–*25*). Indeed, we found that hypermutated tumors acquired somatic mutations in MMR genes that were not detected in their initial tumors, as well as aberrant DNA methylation of O^6-methylguanine-DNA methyltransferase (MGMT) (fig. S3, fig. S9, and table S1).

The introduction of thousands of de novo mutations may drive the evolution of TMZ-resistant glioma cells to higher states of malignant potential (*1*, *23*). Indeed, all six recurrent tumors that showed evidence of TMZ-induced hypermutation underwent malignant progression to GBM, a high-grade tumor with a worse prognosis (*8*, *9*). To investigate this hypothesis and to identify TMZ-associated mutations that may drive the outgrowth of GBM from low-grade glioma, we focused on the RB and Akt-mTOR signaling pathways, which are associated with high-grade gliomas (Fig. 3B) (*22*, *26*–*28*). In each hypermutated recurrence, TMZ-associated mutations affected genes coding for essential signaling molecules in these two pathways. For example, in the RB pathway we identified a TMZ-associated RB1 c.2520+1G>A splice-site mutation found previously in the germ line of patients with hereditary retinoblastoma (*29*, *30*). Transcriptome sequencing confirmed that this mutation triggered aberrant splicing, premature termination, and loss of the RB1 C-terminal domain necessary for growth suppression (Fig. 3C) (*31*). Recurrent tumors from patients 05 and 10 each had a TMZ-associated *CDKN2A* $Pro^{114} \rightarrow Leu$ mutation, which prevents $p16^{INK4A}$ protein encoded by this gene from inhibiting CDK4 or inducing cell cycle arrest (*32*). The same mutation has been reported in other tumor types (*33*) and in the germ line of patients with familial melanoma (*34*). Gene set enrichment analysis further confirmed the deregulation of RB1-mediated cell cycle control upon tumor recurrence (Fig. 3D), which suggests that TMZ-associated mutations compromise the function of the RB tumor suppressor pathway.

We also investigated TMZ-associated mutations that may activate the Akt-mTOR signaling pathway. We identified a TMZ-associated mutation (*PIK3CA* $Glu^{542} \rightarrow Lys$) in the recurrent tumor of patient 18 that drives Akt hyperactivation and induces mTOR-dependent oncogenic transformation (*35*). Similarly, the TMZ-treated second recurrence of patient 24 had TMZ-associated mutations in *PTEN* ($Ala^{121} \rightarrow Thr$ and $Gly^{165} \rightarrow Arg$) at residues critical to its phosphatase activity (*36*) that are recurrently mutated in GBM (*33*). Finally, we validated in vitro that a TMZ-associated *MTOR* S2215F ($Ser^{2215} \rightarrow Phe$) mutation in the recurrent tumor of patient 01 was constitutively

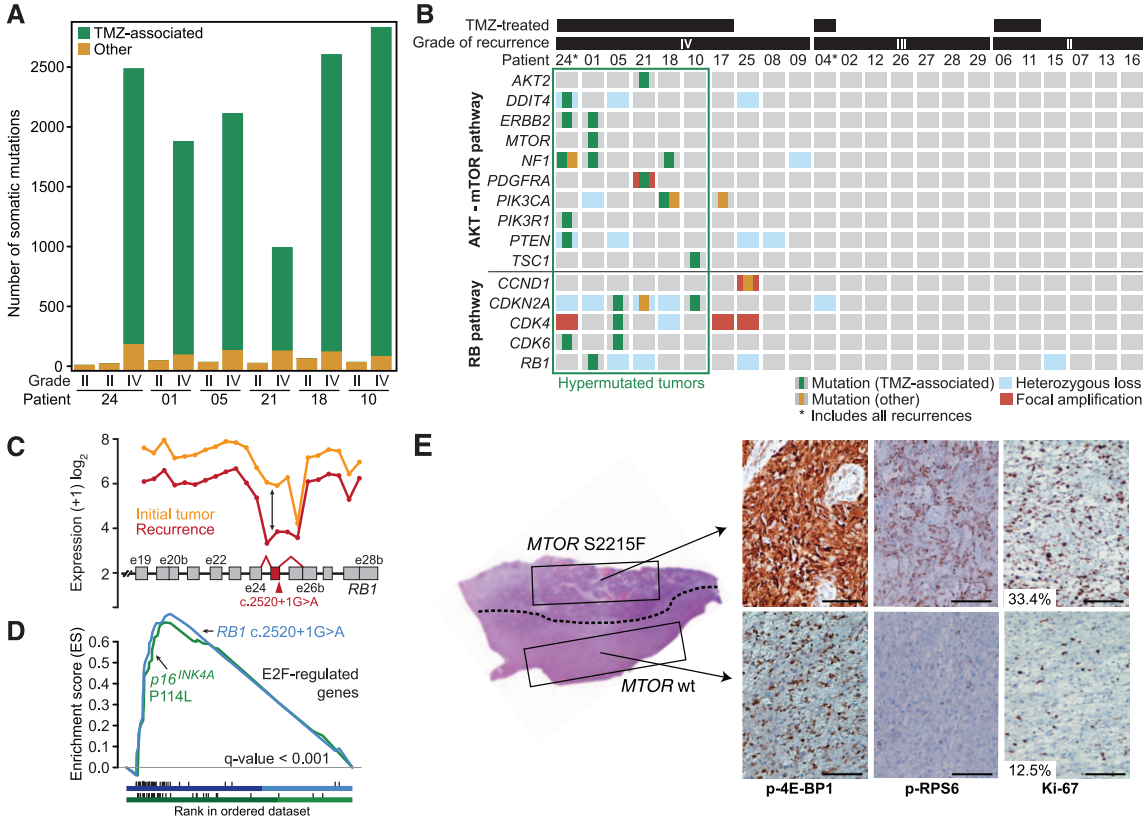


Fig. 3. Recurrent tumors from patients treated with TMZ harbor genetic alterations in the RB and Akt-mTOR signaling pathways. (**A**) Numbers of TMZ-associated mutations and other mutations identified in the six patients with hypermutated recurrent tumors. (**B**) Somatic mutations and CNAs acquired upon recurrence in key genes of pathways associated with GBM. (**C**) Expression level of *RB1* at each exon and exon-exon junction in the initial and recurrent tumor of patient 01 showing aberrant splicing of the *RB1* transcript in the recurrent tumor harboring the *RB1* c.2520+1G>A splice-site mutation. The *RB1* exon and exon junctions with significant differential usage (red) and the location of the splice-site mutation are shown. (**D**) Gene set enrichment analysis shows significant enrichment of genes down-regulated by *RB1* and up-regulated by *E2F* in the recurrent tumors of patients 01 (blue) and 10 (green), coincident with the acquisition of TMZ-associated mutations in the RB pathway. (**E**) Hematoxylin and eosin (H&E)–stained tumor sample from the first recurrent tumor of patient 01. A dotted line separates the two morphologically distinct regions. Immunohistochemistry (IHC) for phospho-RPS6, phospho-4E-BP1, and Ki-67 shows differential activation of mTORC1 targets and proliferation rates in the two adjacent regions. Scale bars, 100 μm.

activating (fig. S10), similar to the previously identified *MTOR* $Ser^{2215} \rightarrow Tyr$ (*37*). Moreover, adjacent regions of this recurrence showed heterogeneous mTOR complex 1 (mTORC1) activity (Fig. 3E and fig. S11). Microdissection revealed that although these adjacent regions shared a subset of the mutations found in the initial tumor, *MTOR* S2215F and other TMZ-associated mutations were present only in the region that stained strongly for mTORC1 activation, which also had higher staining of the proliferation marker Ki-67, implying that the TMZ-associated mutations conferred a proliferative advantage. A distal second recurrence harbored the same TMZ-associated mutations and stained strongly and homogeneously for mTORC1 targets (fig. S12). Although both regions of the first recurrence were GBM, the hypermutated subclone underwent in vivo selection, invaded distally, and seeded the second recurrence (figs. S13 and S14). Across our cohort, Akt-mTOR pathway mutations corresponded with elevated phospho-4E-BP1 and RPS6 in vivo, indicating hyperactivated mTORC1 in recurrent GBMs relative to their initial tumors (fig. S12).

There was no evidence that the mutations in the RB and Akt-mTOR signaling pathways preceded TMZ treatment, according to analysis of additional geographically distinct samples of initial tumors from four of the six patients with hypermutated recurrent tumors (table S7). Non-hypermutated recurrent tumors that progressed to GBM also acquired genetic changes in these signaling pathways, but through alternative mechanisms. In contrast, none of the grade II-III recurrences acquired mutations in these pathways. These data suggest a connection among TMZ treatment, driver mutations in oncogenic signaling pathways, and malignant progression.

Through direct comparison of the genomic landscape of gliomas at initial diagnosis and recurrence, we were able to infer the mutational character of the infiltrating tumor cells that give rise to recurrence and that adjuvant therapy with TMZ is intended to eliminate. Recurrences did not typically arise from cells bearing the full set of mutations found in the initial tumor, as would be expected from a local recurrence in the absence of selective pressure from adjuvant chemotherapy. This finding complicates the use of tumor genomics to design precision therapies targeting residual disease. We also demonstrated an alternative evolutionary path of low-grade glioma that is largely determined by adjuvant chemotherapy with TMZ. This extends earlier studies of primary GBMs (*23*, *25*), unpaired recurrent tumors (*22*), and a cell culture model (*20*). Future basic and clinical studies must weigh the initial antitumor effects of TMZ against the potential risk of inducing new driver mutations and malignant progression. Ultimately, a better understanding of the invading cells that give rise to recurrent tumors and the effect of adjuvant therapeutics on their evolution will facilitate the development of new strategies to delay or prevent recurrence and malignant progression.

References and Notes

1. M. Gerlinger, C. Swanton, *Br. J. Cancer* **103**, 1139–1143 (2010).
2. M. Greaves, C. C. Maley, *Nature* **481**, 306–313 (2012).
3. D. A. Landau *et al.*, *Cell* **152**, 714–726 (2013).
4. L. Ding *et al.*, *Nature* **481**, 506–510 (2012).
5. M. Gerlinger *et al.*, *N. Engl. J. Med.* **366**, 883–892 (2012).
6. S. Yachida *et al.*, *Nature* **467**, 1114–1117 (2010).
7. X. Wu *et al.*, *Nature* **482**, 529–533 (2012).
8. N. Sanai, S. Chang, M. S. Berger, *J. Neurosurg.* **115**, 948–965 (2011).
9. M. Westphal, K. Lamszus, *Nat. Rev. Neurosci.* **12**, 495–508 (2011).
10. See supplementary materials on *Science* Online.
11. Y. Jiao *et al.*, *Oncotarget* **3**, 709–722 (2012).
12. T. Watanabe, S. Nobusawa, P. Kleihues, H. Ohgaki, *Am. J. Pathol.* **174**, 1149–1153 (2009).
13. K. Watanabe *et al.*, *Clin. Cancer Res.* **3**, 523–530 (1997).
14. P. P. Medina *et al.*, *Hum. Mutat.* **29**, 617–622 (2008).
15. S. Glaros, G. M. Cirrincione, A. Palanca, D. Metzger, D. Reisman, *Cancer Res.* **68**, 3689–3696 (2008).
16. D. Rohle *et al.*, *Science* **340**, 626–630 (2013).
17. N. J. Szerlip *et al.*, *Proc. Natl. Acad. Sci. U.S.A.* **109**, 3041–3046 (2012).
18. A. Sottoriva *et al.*, *Proc. Natl. Acad. Sci. U.S.A.* **110**, 4009–4014 (2013).
19. L. M. F. Merlo, J. W. Pepper, B. J. Reid, C. C. Maley, *Nat. Rev. Cancer* **6**, 924–935 (2006).
20. W. J. Bodell, N. W. Gaikwad, D. Miller, M. S. Berger, *Cancer Epidemiol. Biomarkers Prev.* **12**, 545–551 (2003).
21. C. Greenman *et al.*, *Nature* **446**, 153–158 (2007).
22. Cancer Genome Atlas Research Network, *Nature* **455**, 1061–1068 (2008).
23. C. Hunter *et al.*, *Cancer Res.* **66**, 3987–3991 (2006).
24. D. P. Cahill *et al.*, *Clin. Cancer Res.* **13**, 2038–2045 (2007).
25. S. Yip *et al.*, *Clin. Cancer Res.* **15**, 4622–4629 (2009).
26. G. Reifenberger, J. Reifenberger, K. Ichimura, P. S. Meltzer, V. P. Collins, *Cancer Res.* **54**, 4299–4303 (1994).
27. H. Wang *et al.*, *Lab. Invest.* **84**, 941–951 (2004).
28. D. N. Louis, *Annu. Rev. Pathol.* **1**, 97–117 (2006).
29. T. Tsai *et al.*, *Arch. Ophthalmol.* **122**, 239–248 (2004).
30. C. Houdayer *et al.*, *Hum. Mutat.* **23**, 193–202 (2004).
31. X. Q. Qin, T. Chittenden, D. M. Livingston, W. G. Kaelin Jr., *Genes Dev.* **6**, 953–964 (1992).
32. J. Koh, G. H. Enders, B. D. Dynlacht, E. Harlow, *Nature* **375**, 506–510 (1995).
33. S. A. Forbes *et al.*, *Curr. Protoc. Hum. Genet.* Chapter 10, Unit 10.11 (2008).
34. M. C. Fargnoli *et al.*, *J. Invest. Dermatol.* **111**, 1202–1206 (1998).
35. S. Kang, A. G. Bader, P. K. Vogt, *Proc. Natl. Acad. Sci. U.S.A.* **102**, 802–807 (2005).
36. S. Y. Han *et al.*, *Cancer Res.* **60**, 3147–3151 (2000).
37. T. Sato, A. Nakashima, L. Guo, K. Coffman, F. Tamanoi, *Oncogene* **29**, 2746–2752 (2010).

Acknowledgments: We thank S. Gonzalez for assistance with the collection of clinical information; R. Kang for assistance with mutation validation; H. van Thuijl for assistance with MGMT methylation; and J. Wiencke and G. Hsuang for assistance with droplet digital PCR. Supported by Accelerate Brain Cancer Cure (J.F.C.), the Grove Foundation, the TDC Foundation, the Anne and Jason Farber Foundation, the Samuel Waxman Cancer Research Foundation, the Alex Lemonade Stand Foundation, the Entertainment Industry Foundation and Anne Feeley, and a generous gift from the Dabbiere family. Also supported by National Institute of General Medical Sciences grant T32GM008568 (T.M.); NIH grants 1T32CA15102201 and R25NS070680 (M.B.); NIH grant P50CA097257 (L.E.J., S.J.N., M.S.B., S.M.C., J.F.C., and B.S.T.); National Cancer Institute grants R01CA169316-01 (J.F.C.), P01CA81403 (W.C.G., E.C., and W.A.W.), P30CA82103 (A.B.O.), and R01CA163336 (J.S.S.); National Institute of Neurological Disorders and Stroke grant K08NS079485 (W.C.G., E.C., and W.A.W.); the UCSF Academic Senate and the Sontag Foundation (J.S.S., J.F.C., and B.S.T.); the BC Cancer Foundation, Genome BC, and Genome Canada (M.A.M.); the Goldhirsh Foundation (J.F.C.); and a research program of the Project for Development of Innovative Research on Cancer Therapeutics (P-Direct) (A.M., N.S., and H.A.), Grant-in-Aid for Scientific Research on Innovative Areas (no. 23134501) (A.M.), and Grant-in-Aid for Scientific Research (S) (no. 24221011) (H.A.) from the Ministry of Education, Culture, Sports, Science and Technology of Japan. C.Y.M. was a Damon Runyon Cancer Research Postdoctoral Fellow. M.A.M. is a Canada Research Chair in Genome Science. All exome and transcriptome sequencing data have been deposited in the European Genome-phenome Archive under accession number EGAS00001000579, and data from patients 24 to 29 have also been deposited to the Japanese Genotype-phenotype Archive under accession number JGAS00000000004.

Supplementary Materials

www.sciencemag.org/content/343/6167/189/suppl/DC1
Materials and Methods
Figs. S1 to S14
Tables S1 to S7
References (*38*–*61*)

2 May 2013; accepted 27 November 2013
Published online 12 December 2013;
10.1126/science.1239947

Single-Cell RNA-Seq Reveals Dynamic, Random Monoallelic Gene Expression in Mammalian Cells

Qiaolin Deng,[1]* Daniel Ramsköld,[1,2]* Björn Reinius,[1,2] Rickard Sandberg[1,2]†

Expression from both alleles is generally observed in analyses of diploid cell populations, but studies addressing allelic expression patterns genome-wide in single cells are lacking. Here, we present global analyses of allelic expression across individual cells of mouse preimplantation embryos of mixed background (CAST/Ei × C57BL/6J). We discovered abundant (12 to 24%) monoallelic expression of autosomal genes and that expression of the two alleles occurs independently. The monoallelic expression appeared random and dynamic because there was considerable variation among closely related embryonic cells. Similar patterns of monoallelic expression were observed in mature cells. Our allelic expression analysis also demonstrates the de novo inactivation of the paternal X chromosome. We conclude that independent and stochastic allelic transcription generates abundant random monoallelic expression in the mammalian cell.

In diploid organisms, the zygote inherits one set of autosomal chromosomes from each parent. Although it is widely believed that transcription of autosomal genes occurs from both parental alleles, specific classes of genes have been shown to express only one, randomly

selected, allele (allelic exclusion) (*1*–*3*). Analyses of clonally amplified lymphocytes by using single-nucleotide polymorphism (SNP)–sensitive microarrays revealed that 8% of human autosomal genes and 16% of mouse genes showed a type of random, monoallelic expression that was stably maintained during clonal expansion (*4*, *5*). Furthermore, parental-specific (imprinted) expression has been demonstrated for 1% of autosomal genes (*6*, *7*) and, perhaps most strikingly, in the inactivation of one X chromosome in female cells (*8*). Although RNA fluorescent in situ hybridization (RNA-FISH) has been used to study a few individual genes (*9*, *10*), little is known about general patterns of allelic expression in single cells.

To investigate allele-specific gene expression at single-cell resolution, we isolated 269 individual cells dissociated from in vivo F1 embryos (CAST/EiJ × C57BL/6J, hereafter abbreviated as CAST and C57, respectively) from oocyte to blastocyst stages of mouse preimplantation development (PD) (*11*). We generated transcriptome profiles with Smart-seq (*12*) or Smart-seq2 (*13*) from each individual cell (table S1 and fig. S1, A and B). Principal component analysis (PCA) clustered the cells by developmental stage and embryo, effectively reconstructing the dynamics of PD (Fig. 1A). Next, using strain-specific SNPs (*14*) to distinguish transcription from the maternal and paternal chromosomes (*15*) we observed that 82% of all genes expressed during PD contained ≥1 informative SNP (fig. S1C) and that different SNPs within the same gene gave coherent allelic calls (fig. S2). Because maternal RNA lingers from the oocyte (*16*), we expected the maternal genotype to dominate the zygotic transcriptome. Indeed, the zygote, and also the early two-cell, contained essentially only maternal RNA, but in the subsequent stages, the maternal fraction gradually declined to reach parity with paternal transcripts at the four-cell stage (Fig. 1B), which is consistent with rapid maternal transcript clearance and zygotic genome activation. As a control for the accuracy in alignments and SNP annotation, we analyzed individual cells of pure C57 or CAST background and found 99.4 and 99.7% correctly classified reads, respectively (Fig. 1B).

We next investigated the gene activation across paternal chromosomes. We found that genes on the paternal X chromosome (Xp) of female embryos were indeed transcriptionally activated similarly to those on paternal autosomes during a defined time window of the PD. Subsequent reinactivation occurred first beyond the four-cell stage (Fig. 2A), demonstrating de novo Xp inactivation (*17*, *18*) rather than inheritance and propagation of a pre-inactivated Xp (*19*). X chromosome inactivation initiates from the X-inactivation center (*Xic*), from which *Xist* is transcribed, and spreads in cis (*18*). Our data provided a high-resolution map of silencing over Xp at the four-cell, 16-cell, and early blastocyst stages (Fig. 2B) that substantiates the observation of a silencing gradient (*19*) and demonstrated that the spread of Xp silencing is not a simple function of the distance to *Xic* (Fig. 2B, and escapee genes in fig. S3 and table S2).

These findings gave us confidence in inferring biological signals from the allelic information in single-cell RNA sequencing (RNA-seq). To further explore allelic expression of autosomal genes, we classified their expression as biallelic, maternal monoallelic, or paternal monoallelic according to SNP-containing reads. Surprisingly, this revealed a great degree of monoallelic expression (on average, 54% of genes) across all stages of PD (figs. S4 to S24). The monoallelic calls were similar or more abundant than in available RNA-FISH data (fig. S25) (*9*, *10*). Because single-cell transcriptome methods suffer from stochastic losses of RNA species, it was necessary to determine to what extent random sampling effects inflate observed monoallelic calls. We therefore lysed individual cells (from 8- or 16-cell embryos) and split the lysate into two equal volume fractions that were independently processed into sequencing libraries. Using the allelic calls from the split-pairs, we modeled the stochastic losses and inferred the underlying levels of biallelic and monoallelic expression in sets of genes binned by expression level (figs. S26 and S27). We estimated that 60% of all polyadenylated [poly $(A)^+$] RNA molecules are lost in the Smart-seq2 protocol (Fig. 3A) (*13*) because inferred losses stabilized at levels equal to a single RNA molecule. This analysis uncovered coherent monoallelic expression estimates across independent split-cell experiments with a median of 17% of genes (Fig. 3B). Although technical losses of RNA contributed as much as 66% of observed monoallelic expression, this strategy allowed us to determine the underlying amount of biological monoallelic expression in single cells.

In subsequent analyses of monoallelic expression, we focused only on transcripts expressed at sufficient abundances to be little influenced by random sampling, as determined in our control experiments (fig. S28). Exploring the levels of monoallelic expression among cells from the four-cell stage to the late blastocyst stage, we observed similar levels throughout the PD, with an average of 12 to 24% monoallelic expression for mRNAs (Fig. 3D) and 19 to 26% for noncoding poly$(A)^+$ RNAs. In contrast, consistent biallelic expression was observed for only a few hundred genes (table S3), often with housekeeping functions (*4*, *9*). Allele classification of single-cell data of pure C57 and CAST background gave 97.3 and 99.5% correct monoallelic calls, respectively (Fig. 3D).

[1]Ludwig Institute for Cancer Research, Box 240, 171 77 Stockholm, Sweden. [2]Department of Cell and Molecular Biology, Karolinska Institutet, 171 77 Stockholm, Sweden.

*These authors contributed equally to this work.
†Corresponding author. E-mail: rickard.sandberg@ki.se

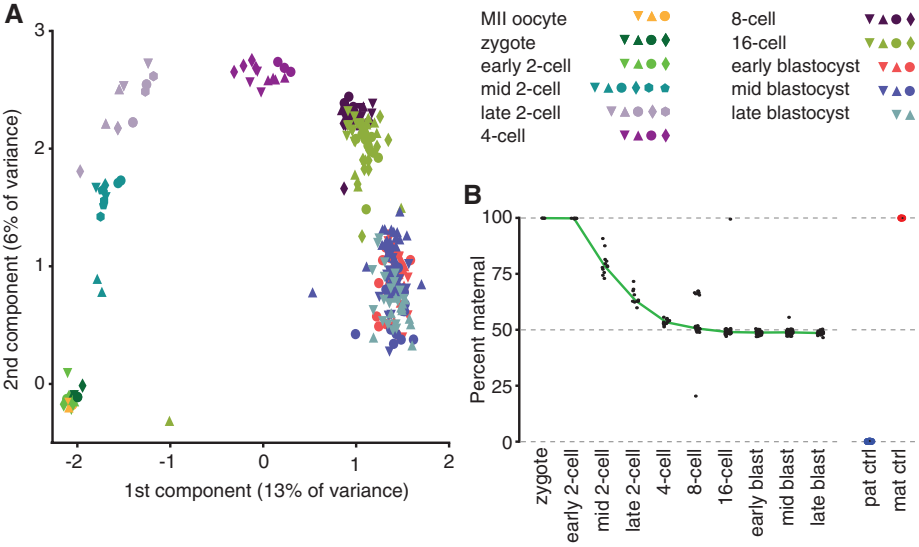


Fig. 1. Single-cell transcriptomes reconstruct preimplantation development. (**A**) Single-cell gene expression profiles projected onto the first two principal components. Cells from different stages and embryos are designated by colors and symbols. (**B**) The percentage (by mass) of maternal RNA observed in single-cell transcriptomes (black dots; median is in green) at different stages of development and in controls from pure maternal (CAST, red) and paternal (C57, blue) backgrounds. The eight-cell stage outlier cells with maternal bias are all from one embryo (supplementary text).

Pooling cells by embryo removed essentially all monoallelic expression (Fig. 3E), demonstrating a high degree of cell-specific randomness in monoallelic expressions. We therefore concluded that a dynamic type of random monoallelic expression is abundant in blastomeres.

Pioneer studies on interleukin-4 (*20*, *21*) found transcription of the two alleles to occur independently, but it remained unknown whether such

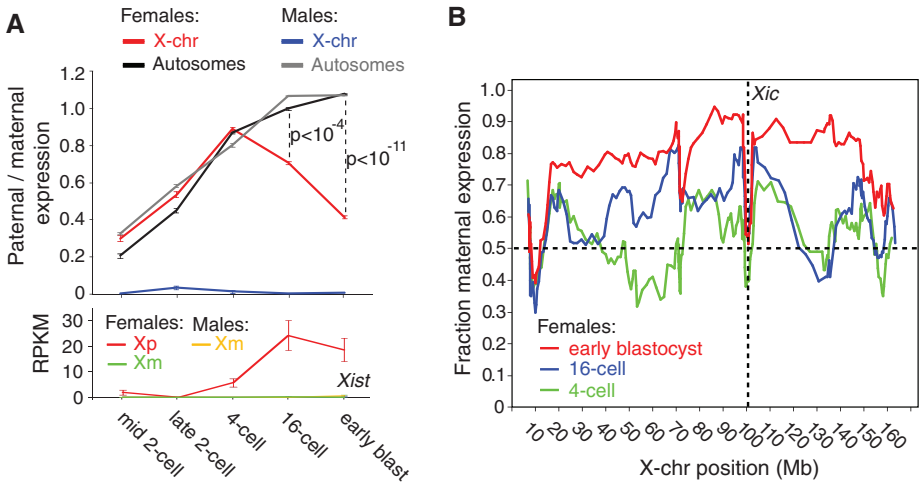


Fig. 2. De novo paternal X-chromosome inactivation. (**A**) (Top) Average ratio of SNP-containing reads (paternal, C57; maternal, CAST) per autosome or X chromosome in cells of embryos (male and female, separately) at stages of preimplantation development. Error bars denote SEM (n = 3 to 28 cells), and P values were calculated using Student's t-test. (Bottom) Allele-resolution gene expression (RPKM) of *Xist* in cells from different developmental stages. Colors indicate embryos according to sex and allele-specific expression. Only stages for which female embryos were available are shown. Error bars denote SEM (n = 3 to 28 cells). (**B**) Spread of Xp inactivation, shown as the fraction maternal reads for genes on the X chromosome by using a moving window average of 10 genes. *Xic* is marked by a dashed line.

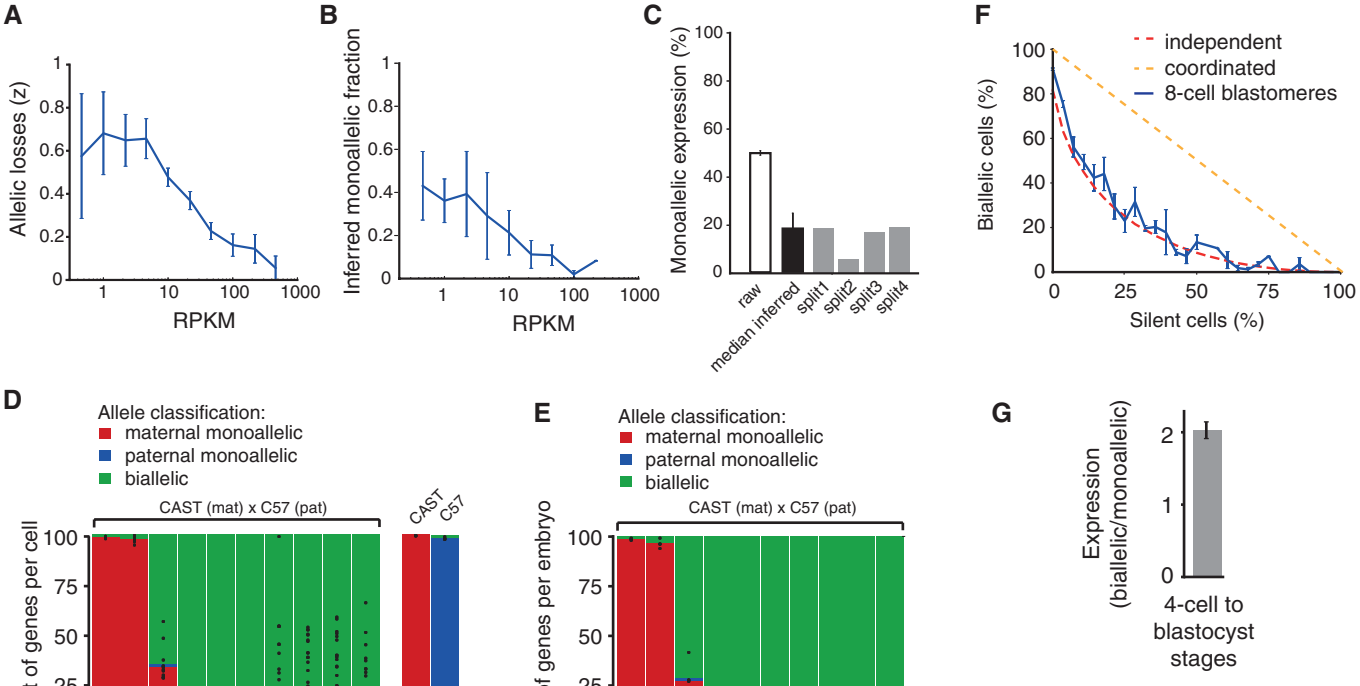


Fig. 3. Quantitative characterization of allelic transcription patterns. (**A**) Estimated levels of allelic losses (z) for genes binned by expression level from split-cell experiments (n = 4 cells) on cells from 8- or 16-cell stage embryos. In (A) and (B), error bars denote 95% CIs (bootstrap over genes). (**B**) Inferred fraction of genes with monoallelic expression for genes binned by expression level, using split-cell experiments as in (A). (**C**) Percent of genes with monoallelic expression in 8- or 16-cell stage embryo cells, from raw observations, individual split-cell experiments, and their median. Error bars denote 95% CIs. (**D**) Mean percent of genes with monoallelic expression across cells at each developmental stage for genes with mean expression ≥90 RPKM per stage (fig. S28). Individual cell percentages are shown as black dots. (**E**) Mean percent of genes with monoallelic expression per embryonic stage, when pooling cells from the same embryo stage. Individual embryo percentages are shown as black dots. Colors and RPKM threshold are as in (D). (**F**) Mean fraction of cells (eight-cell stage) with biallelic expression for genes binned by their fraction of nondetected (silent) cells; error bars give SEM ($n \geq 3$ genes). The expected biallelic fraction was computed on the basis of either a model of independent allele activation or coordinated activation (*11*). (**G**) Mean ratio of total expression between cells with biallelic or monoallelic expression of the same genes. Error bars give SEM (n = 120 genes).

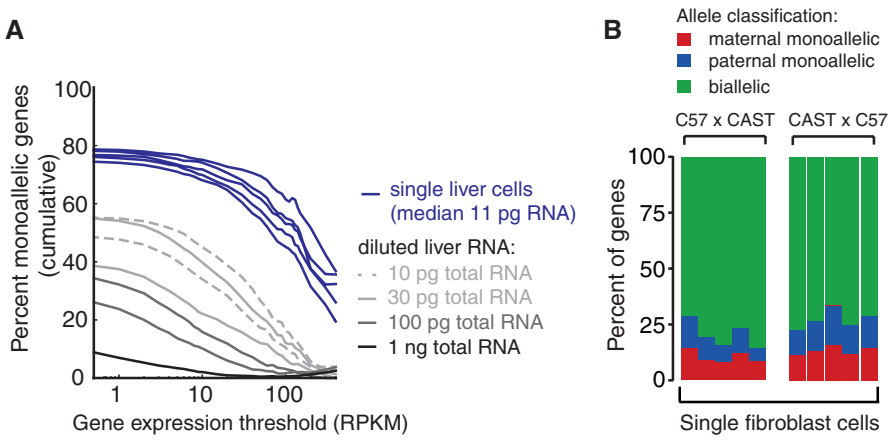


Fig. 4. Monoallelic expression in different mature cell types. (**A**) The cumulative fraction of monoallelic expression as a function of the expression levels for individual liver cells and at different dilutions. (**B**) Percentage of genes with monoallelic expression in individual cultured adult fibroblasts (C57 × CAST and CAST × C57) for genes with mean expression ≥20 RPKM per stage (fig. S28).

independence applies on the genomic scale. Using our comprehensive allelic expression data for thousands of genes, we therefore investigated whether expression from the two alleles occurred independently of one another. Independent allelic expression would yield a specific relationship between the fraction of cells with biallelic, monoallelic, or no expression (*10*), which is different from scenarios of coordinated allelic expression. Markedly, the observed fraction of cells with biallelic expression followed the fraction expected under the independence model (Fig. 3F, eight-cell stage data, and fig. S29, all stages), demonstrating independent allelic transcription for genes across all expression levels, substantially extending results on individual genes (*20*, *21*) to a global principle. Under independent allelic expression, biallelic expression of a particular gene would on average result in twofold higher RNA copy numbers than would the same gene in cells in which the gene is monoallelically expressed because cells with biallelic expression have transcriptional output from two alleles. To test this hypothesis, we analyzed mean gene expression levels in cells with biallelic expression and indeed observed them to be 2.0 ± 0.1 times higher [95% confidence interval (CI), bootstrap] than the levels in cells with monoallelic expression at all developmental stages (Fig. 3G). Thus, both the allelic expression patterns and the expression levels point to independent allelic transcription.

Because embryonic cells are uncommitted progenitors, it was important to determine whether abundant random monoallelic expression also occurs in mature cells. To this end, we investigated single-cell transcriptomes of in vivo liver cells (C57 × CAST), together with a control dilution series of RNA extracted from liver tissue (C57 × CAST) (Fig. 4A and fig. S30). The monoallelic expression levels in single liver cells were higher than sampling effects measured in control dilutions across all expression levels (Fig. 4B), and the fraction of true monoallelic calls increased with the expression threshold. We also profiled 10 individual adult mouse fibroblasts (five from each reciprocal cross) and detected similar random monoallelic expression, on average 24% of expressed genes per cell. We therefore conclude that random monoallelic expression is abundant in both embryonic and mature cells.

In this study, we uncovered a stochastic pattern of monoallelic expression that differs from the stable allelic regulation of genomic imprinting and allelic exclusion (*22*, *23*). It also differs from the stably maintained monoallelic expression observed in clonal lymphoid cell populations (*4*, *5*). Instead, the rapid expression dynamics that we uncovered in individual cells are consistent with models of transcriptional bursting (*24*). In each cell, independent bursts of transcription occur from both alleles over time, but RNA from only one allele is often present at any given time. Because stochastic losses of RNA substantially inflates naive estimates of allelic expressions, stringent controls such as split-cells and dilution series are of critical importance for accurate allelic expression analyses in single cells. It is likely that stochastic transcription of heterozygous alleles contributes to variable expressivity—phenotypic variation among cells and individuals of identical genotypes—which may have fundamental implications for variable disease penetrance and severity (*25*–*28*).

References and Notes

1. B. Pernis, G. Chiappino, A. S. Kelus, P. G. Gell, *J. Exp. Med.* **122**, 853–876 (1965).
2. M. Malissen *et al.*, *Immunol. Today* **13**, 315–322 (1992).
3. A. Chess, I. Simon, H. Cedar, R. Axel, *Cell* **78**, 823–834 (1994).
4. A. Gimelbrant, J. N. Hutchinson, B. R. Thompson, A. Chess, *Science* **318**, 1136–1140 (2007).
5. L. M. Zwemer *et al.*, *Genome Biol.* **13**, R10 (2012).
6. W. Reik, J. Walter, *Nat. Rev. Genet.* **2**, 21–32 (2001).
7. B. DeVeale, D. van der Kooy, T. Babak, *PLOS Genet.* **8**, e1002600 (2012).
8. J. T. Lee, *Nat. Rev. Mol. Cell Biol.* **12**, 815–826 (2011).
9. Y. Miyanari, M.-E. Torres-Padilla, *Nature* **483**, 470–473 (2012).
10. S. Kalantry, S. Purushothaman, R. B. Bowen, J. Starmer, T. Magnuson, *Nature* **460**, 647–651 (2009).
11. Materials and methods are available as supplementary materials on *Science* Online
12. D. Ramsköld *et al.*, *Nat. Biotechnol.* **30**, 777–782 (2012).
13. S. Picelli *et al.*, *Nat. Methods* **10**, 1096–1098 (2013).
14. T. M. Keane *et al.*, *Nature* **477**, 289–294 (2011).
15. T. Babak *et al.*, *Curr. Biol.* **18**, 1735–1741 (2008).
16. L. Pikó, K. B. Clegg, *Dev. Biol.* **89**, 362–378 (1982).
17. I. Okamoto, A. P. Otte, C. D. Allis, D. Reinberg, E. Heard, *Science* **303**, 644–649 (2004).
18. I. Okamoto *et al.*, *Nature* **438**, 369–373 (2005).
19. K. D. Huynh, J. T. Lee, *Nature* **426**, 857–862 (2003).
20. I. Rivière, M. J. Sunshine, D. R. Littman, *Immunity* **9**, 217–228 (1998).
21. M. Bix, R. M. Locksley, *Science* **281**, 1352–1354 (1998).
22. S. Feng, S. E. Jacobsen, W. Reik, *Science* **330**, 622–627 (2010).
23. P. K. Yang, M. I. Kuroda, *Cell* **128**, 777–786 (2007).
24. A. Raj, A. van Oudenaarden, *Cell* **135**, 216–226 (2008).
25. M. Muenke *et al.*, *Proc. Natl. Acad. Sci. U.S.A.* **91**, 8102–8106 (1994).
26. P. Janku *et al.*, *Am. J. Med. Genet.* **5**, 117–123 (1980).
27. J. C. Carey, D. H. Viskochil, *Am. J. Med. Genet.* **89**, 7–13 (1999).
28. A. Raj, S. A. Rifkin, E. Andersen, A. van Oudenaarden, *Nature* **463**, 913–918 (2010).

Acknowledgments: Q.D. designed and performed mouse work and generated RNA-seq libraries. D.R. designed and performed computational analyses and prepared figures and tables. B.R. analyzed X chromosome data, prepared figures, and generated RNA-seq libraries. R.S. coordinated and designed the study and wrote the manuscript with input from other authors. We are grateful to C. Burge, T. Perlmann, S. Linnarsson, G. Winberg, and other members of our laboratory for comments on the manuscript and A. Johnsson for managing sequencing. This work was supported by the Swedish Research Council grants 2011-965 (Q.D.) and 2008-4562 (R.S.), by the European Research Council Starting Grant 243066 (R.S.), by the Foundation for Strategic Research (R.S.), and Åke Wiberg Foundation grant 756194131 (R.S.). Sequence data have been deposited in National Center for Biotechnology Information Gene Expression Omnibus (GSE45719) and Sequence Read Archive (SRP020490).

Supplementary Materials

www.sciencemag.org/content/343/6167/193/suppl/DC1
Materials and Methods
Supplementary Text
Figs. S1 to S30
Tables S1 to S3
References (*29*–*32*)

29 August 2013; accepted 22 November 2013
10.1126/science.1245316

Modular Organization of Axial Microcircuits in Zebrafish

Martha W. Bagnall and David L. McLean*

Locomotion requires precise control of spinal networks. In tetrapods and bipeds, dynamic regulation of locomotion is simplified by the modular organization of spinal limb circuits, but it is not known whether their predecessors, fish axial circuits, are similarly organized. Here, we demonstrate that the larval zebrafish spinal cord contains distinct, parallel microcircuits for independent control of dorsal and ventral musculature on each side of the body. During normal swimming, dorsal and ventral microcircuits are equally active, but, during postural correction, fish differentially engage these microcircuits to generate torque for self-righting. These findings reveal greater complexity in the axial spinal networks responsible for swimming than previously recognized and suggest an early template of modular organization for more-complex locomotor circuits in later vertebrates.

Animals make effective progress through unpredictable environments by rapidly adjusting ongoing locomotor movements (*1*, *2*). In limbed vertebrates, spinal microcircuits are organized into modules for efficient coordination of joints, limbs, and trunk during locomotion (*3*, *4*). However, it is unknown how the modular organization of complex spinal circuitry in tetrapods and bipeds could have arisen from the simpler, ancestral axial network of fish (*5*). Current models of axially based locomotion in fish engage left-right alternation circuits but do not include equivalent ipsilaterally organized microcircuits akin to those seen in higher vertebrates (*6*). Instead, it is thought that differential activation of dorsal and ventral musculature for behaviors such as postural control is achieved by supraspinal descending commands (*7*). To address this gap, we explored whether axial circuitry in fish contains more complexity than previously recognized.

In larval zebrafish, as with adults, swimming is produced by the left-right alternation of axial muscles activated in waves by segmentally iterated pools of motor neurons (MNs). In each spinal hemisegment is a cohort of four early-developing "primary" MNs, whose axon arborizations collectively tile the dorsal and ventral musculature (Fig. 1H) (*8*, *9*). Because all primary MNs exhibit identical recruitment patterns during swimming (*9*, *10*), there should be no confounding effects of speed-dependent differences on the configuration of their premotor circuits (*11*). Thus, current models would predict that they are embedded in a shared premotor network.

To test this prediction, we performed voltage-clamp recordings from pairs of MNs during fictive swimming. As expected (*12*, *13*), all MNs received barrages of excitatory postsynaptic currents (EPSCs) in phase with ipsilateral motor activity (Fig. 1A). To evaluate whether these barrages, which are synchronous on a large temporal scale (tens of ms), were derived from a shared premotor network, we assessed whether they were also synchronous at a fine temporal scale (tens of μs) (*14*).

Department of Neurobiology, Northwestern University, Evanston, IL 60208, USA.

*Corresponding author. E-mail: david-mclean@northwestern.edu

In pairs of MNs innervating the same muscle quadrant, EPSCs during fictive swimming were indeed highly synchronous (Fig. 1B), as exemplified by an overlay of 100 consecutive EPSCs from one neuron and the associated EPSC-triggered average in the other (Fig. 1C). Unexpectedly, excitatory inputs to MN pairs innervating different muscle quadrants lacked synchrony at fine time scales (Fig. 1D), with accordingly small EPSC-triggered average responses (Fig. 1E). Analysis of all data revealed significantly larger EPSC-triggered averages for "in quadrant" (i.e., either dorsal/mid-dorsal or ventral/mid-ventral pairs), as opposed to "out-of-quadrant," pairs (Fig. 1F). Similarly, a measure of event cross-correlation scores for the pooled data revealed a significant peak at 0 ms for in-quadrant versus out-of-quadrant pairs (Fig. 1G) (see also materials and methods and figs. S1 and S2). The low synchrony for out-of-quadrant pairs is incompatible with the

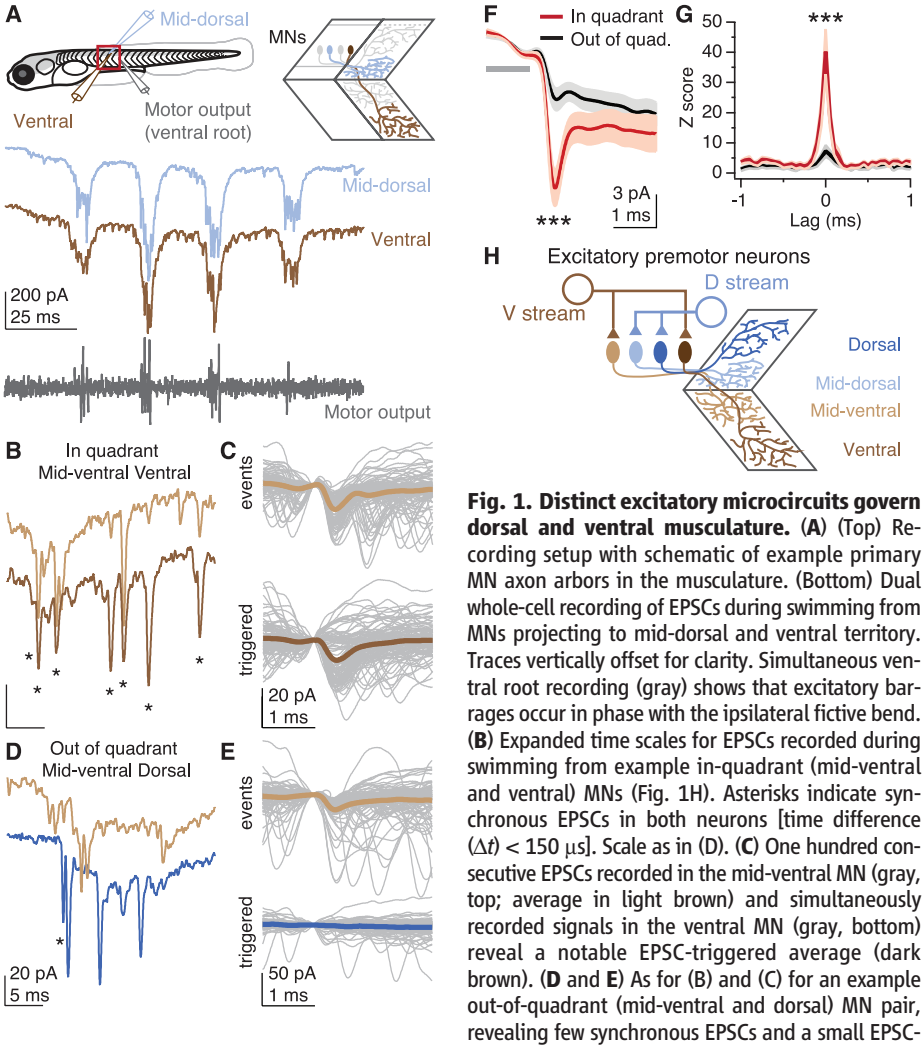


Fig. 1. Distinct excitatory microcircuits govern dorsal and ventral musculature. (**A**) (Top) Recording setup with schematic of example primary MN axon arbors in the musculature. (Bottom) Dual whole-cell recording of EPSCs during swimming from MNs projecting to mid-dorsal and ventral territory. Traces vertically offset for clarity. Simultaneous ventral root recording (gray) shows that excitatory barrages occur in phase with the ipsilateral fictive bend. (**B**) Expanded time scales for EPSCs recorded during swimming from example in-quadrant (mid-ventral and ventral) MNs (Fig. 1H). Asterisks indicate synchronous EPSCs in both neurons [time difference (Δt) < 150 μs]. Scale as in (D). (**C**) One hundred consecutive EPSCs recorded in the mid-ventral MN (gray, top; average in light brown) and simultaneously recorded signals in the ventral MN (gray, bottom) reveal a notable EPSC-triggered average (dark brown). (**D** and **E**) As for (B) and (C) for an example out-of-quadrant (mid-ventral and dorsal) MN pair, revealing few synchronous EPSCs and a small EPSC-triggered average (dark blue). (**F**) Summary EPSC-triggered averages, means ± SEMs, for in-quadrant (n = 15) and out-of-quadrant (n = 19) MN pairs. ***P < 0.001, unpaired t test of peak EPSC amplitude. Gray bar indicates period of baseline normalization. (**G**) Cross-correlogram of EPSC timing, averages from all MN pairs. Means ± SEMs; bin = 50 μs, n as in (F). ***P < 0.001, unpaired t test at 0 ms. (**H**) Schematic of proposed premotor excitatory circuitry. An individual excitatory premotor neuron (open circles) preferentially synapses on either dorsal (D)– or ventral (V)–projecting MNs (solid lines) but not both.

assumption that dorsal- and ventral-projecting MNs are embedded in a shared presynaptic network. Instead, premotor excitatory inputs are segregated into two largely distinct microcircuits governing dorsal and ventral musculature (Fig. 1H).

Are inhibitory premotor pathways similarly segregated? On a longer time scale, barrages of inhibitory postsynaptic currents (IPSCs) recorded in two MNs during fictive swimming occurred synchronously, predominantly out of phase with the motor output (Fig. 2A). Similar to EPSCs, at fine temporal scales in-quadrant pairs exhibited strong synchrony of IPSCs and a large IPSC-triggered average (Fig. 2, B and C), whereas out-of-quadrant MN pairs revealed weaker evidence for IPSC correlation and smaller IPSC-triggered averages (Fig. 2, D and E). These observations were borne out by analysis of group data, showing that in-quadrant pairs exhibited a ~2.3-fold larger IPSC-triggered average (Fig. 2F) and twice the magnitude of cross-correlation at 0 ms (Fig. 2G; see also fig. S2) as out-of-quadrant pairs. Thus, similar to premotor excitatory networks, premotor inhibitory networks are also segregated into two distinct microcircuits for the differential control of dorsal and ventral musculature, although the smaller magnitude difference between in-quadrant and out-of-quadrant cross-correlograms (compare Figs. 1G and 2G) suggests, as a conservative estimate, less-stringent specificity for inhibitory connectivity (Fig. 2H).

In mammalian cortex, pyramidal neurons that receive shared excitatory inputs are also more likely to be connected to each other (*14*). Similarly, there is preferential gap junctional coupling between mammalian limb MNs of shared modular function, for example, ankle flexors (*15*). We found that electrical coupling between MNs was twofold higher for in-quadrant as compared with out-of-quadrant pairs (fig. S3). Thus, the segregated microcircuits at the premotor level are supported by increased connectivity among MNs themselves.

To assess whether excitatory segregation derives from spinal sources and to identify specific premotor populations of relevance, we used an optogenetic approach to selectively drive firing in the V2a population expressing the transcription factor *Chx10* (Fig. 3A and fig. S4). V2a/*Chx10*+ neurons are the largest class of ipsilaterally projecting glutamatergic premotor neurons in the spinal cord and have a conserved function during locomotion in both zebrafish and mice (*16*, *17*). Subsequent recording from MN pairs revealed that the EPSCs elicited by pulses of illumination were highly synchronous between in-quadrant pairs (Fig. 3B) but asynchronous between out-of-quadrant pairs (Fig. 3C). Analysis of group data showed that EPSC-triggered averages were 15-fold larger for in-quadrant than out-of-quadrant MN pairs (Fig. 3D). Thus, V2a/*Chx10*+ neurons in the spinal cord are segregated into two subtypes, yielding distinct excitatory control over dorsal and ventral musculature.

Premotor inhibition can derive from both ipsilateral and contralateral spinal sources. Are

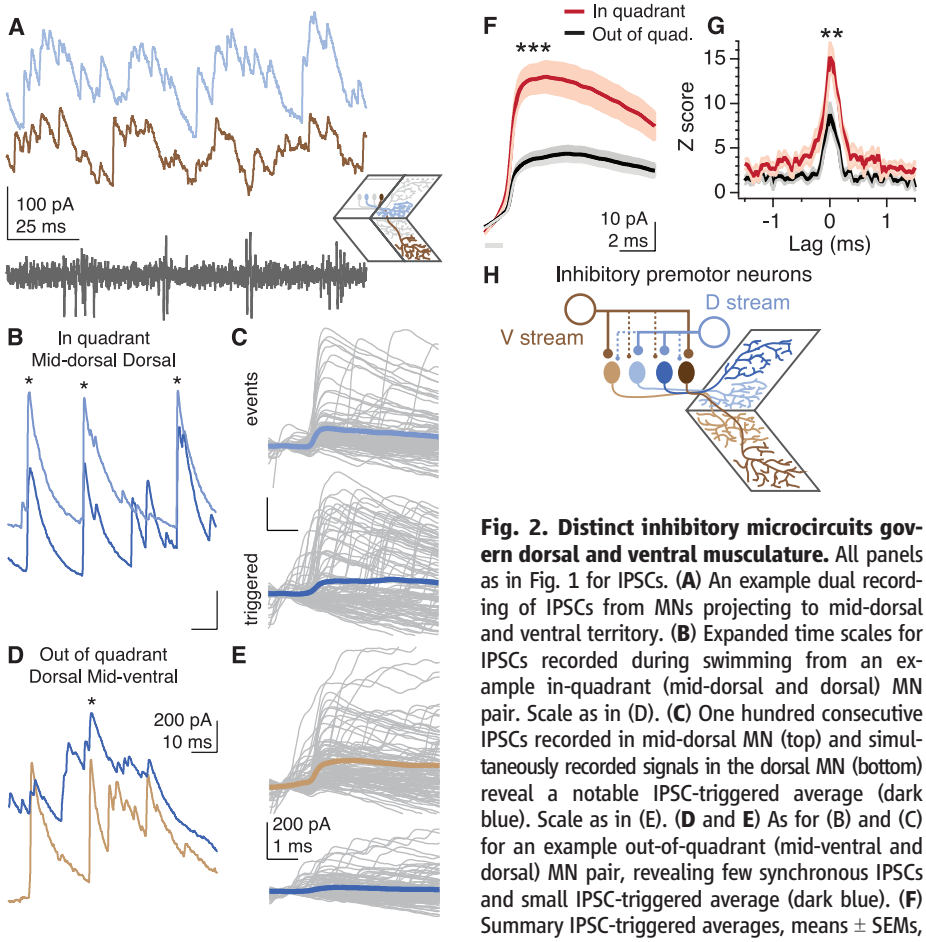


Fig. 2. Distinct inhibitory microcircuits govern dorsal and ventral musculature. All panels as in Fig. 1 for IPSCs. (**A**) An example dual recording of IPSCs from MNs projecting to mid-dorsal and ventral territory. (**B**) Expanded time scales for IPSCs recorded during swimming from an example in-quadrant (mid-dorsal and dorsal) MN pair. Scale as in (D). (**C**) One hundred consecutive IPSCs recorded in mid-dorsal MN (top) and simultaneously recorded signals in the dorsal MN (bottom) reveal a notable IPSC-triggered average (dark blue). Scale as in (E). (**D** and **E**) As for (B) and (C) for an example out-of-quadrant (mid-ventral and dorsal) MN pair, revealing few synchronous IPSCs and small IPSC-triggered average (dark blue). (**F**) Summary IPSC-triggered averages, means ± SEMs, for in-quadrant (n = 13) and out-of-quadrant (n = 17) MN pairs. ***P < 0.001, unpaired t test of peak IPSC amplitude. (**G**) Cross-correlogram of IPSC timing, averages from all MN pairs. Means ± SEMs; bin = 50 μs, n as in (F). **P < 0.01, unpaired t test at 0 ms. (**H**) Schematic of proposed premotor inhibitory circuitry. An individual inhibitory premotor MN preferentially synapses either on D or V MNs (solid lines) but rarely on both (dotted lines).

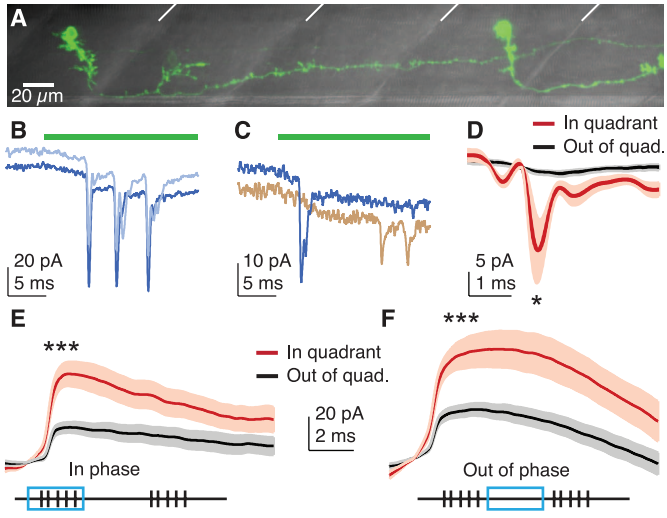


Fig. 3. Intraspinal premotor inputs are segregated into dorsal and ventral microcircuits. (**A**) Sagittal view of 4 days post fertilization (dpf) larva expressing alx:Gal4::UAS:CatCh (see materials and methods for more information) in two premotor neurons with typical V2a morphology (ipsilateral axon, primarily descending). Rostral is to the left; white bars mark muscle segments. (**B**) Example of synchronous EPSCs evoked optogenetically in a dorsal/mid-dorsal MN pair. Green bar indicates light exposure. (**C**) Asynchronous EPSCs evoked in a dorsal/mid-ventral MN pair in another fish. (**D**) Summary of EPSC-triggered averages for in-quadrant and out-of-quadrant MN pairs (n = 5 pairs each). *P < 0.05, unpaired t test of peak amplitudes. Varying baseline period is due to frequent barrages of light-elicited EPSCs [as in (B)]. (**E**) IPSC-triggered average responses in phase with ipsilateral motor activity, as measured by ventral root recordings (schematic, bottom), from in-quadrant (n = 7) and out-of-quadrant (n = 14) pairs. ***P < 0.001, unpaired t test of peak amplitudes. (**F**) As in (E), but for recordings during midcycle, out of phase with ipsilateral motor activity.

both sources of spinal inhibition similarly segregated? We took advantage of the fact that inhibition arriving in phase with the locomotor signal derives exclusively from ipsilateral spinal sources, whereas inhibition arriving out of phase derives from commissural spinal sources (*18*). Both IPSCs occurring in phase and those occurring out of phase with ipsilateral activity exhibited ~2.5-fold larger IPSC-triggered average responses for in-quadrant than for out-of-quadrant pairs (Fig. 3, E and F). We conclude that both ipsilaterally and contralaterally derived spinal inhibitory drive is also segregated into two microcircuits.

To assess the utility of these parallel axial microcircuits for ethologically relevant behaviors, we focused on their recruitment during postural correction, which is known to rely on differential dorsal and ventral muscle activity (*7*, *19*). Normally, a side-lying larval zebrafish will right itself at the beginning of a swim bout (Fig. 4A) (*20*). We quantified the motor activity underlying this behavior by using calcium imaging, which allowed visualization of the activity of the dorsal- and ventral-projecting primary MNs on both sides of the fish (fig. S5A). At the onset of evoked swim bouts, bursts of activity are visible as Ca^{2+} transients (Fig. 4B). In side-lying fish, the amplitude of the Ca^{2+} transient was larger in ventral-projecting than in dorsal-projecting MNs on the ear-up side, but this pattern was inverted on the ear-down side of the fish (Fig. 4C). This asymmetric motor drive thus produces self-righting torque to roll the fish dorsal side up (Fig. 4D) (*7*) and is likely to reflect the overall motor activation pattern in more modest postural correction as well. In contrast, when fish were embedded dorsal side up in a normal orientation, no significant differences were seen in the pattern of activation (fig. S5B).

Is this bias in activity driven by differential excitation or inhibition? Paired physiological recordings from MNs on the ear-up side of side-lying fish revealed that, during swimming, EPSCs were significantly more frequent in ventral-projecting than dorsal-projecting MNs. In addition, IPSCs occurred more frequently in MNs controlling dorsal than ventral musculature (Fig. 4F). Average EPSC and IPSC amplitudes did not differ between the MN types, however (fig. S6).

To test whether vestibular signals were responsible for these asymmetries in behavioral and physiological activity, we evaluated the *rock solo* mutant fish line, in which the anterior otolith [the sole gravity sensor at this stage (*21*)] is absent (*22*). *rock solo* mutant fish failed to develop self-righting during the first week post fertilization, in contrast with their heterozygous and wild-type siblings (13 wild-type or heterozygous fish had 82% successful righting over 49 trials; for 20 *rock solo*, 48% righting, 50 trials; $P < 0.0001$, Fisher exact test). MN imaging in side-lying *rock solo* mutant fish revealed no reliable asymmetry of activity (Fig. 4E), consistent with the absence of self-righting behavior. Similarly, physiological recordings from *rock solo*$^{-/-}$ fish, or from fish in which the otoliths were surgically removed immediately before the experiment to avoid developmental confounds (*23*), revealed no consistent bias for synaptic events in the MNs controlling dorsal and ventral musculature (Fig. 4G).

Critically, however, the differences in EPSC and IPSC synchrony for in-quadrant versus out-of-quadrant pairs persisted in otolith-deficient animals (Fig. 4H). This observation confirms that spinal axial microcircuitry exhibits segregated, modular connectivity to different motor pools even in the absence of structured descending vestibular signals. Collectively, our findings challenge the traditional view of axial network organization (*12*, *13*, *24*) and shift the locus of distinct dorsal or ventral control in fish from supraspinal regions to modular, intrinsic spinal circuits.

The evolution of vertebrates from fishes to mammals involved fundamental changes in body plan, muscle distribution, and posture (*25*). These changes involved not only reorganization of the trunk musculature but also an increasing reliance on the limbs to locomote (*26*). Commensurate with these changes, locomotor networks in the spinal cord must have adapted. Studies of the molecular mechanisms responsible for generating spinal locomotor circuitry have identified conserved programs regulating the differentiation of axial and limb spinal microcircuitry (*27*, *28*).

Although limb microcircuits must have originated from more primitive axial ones, it is unclear

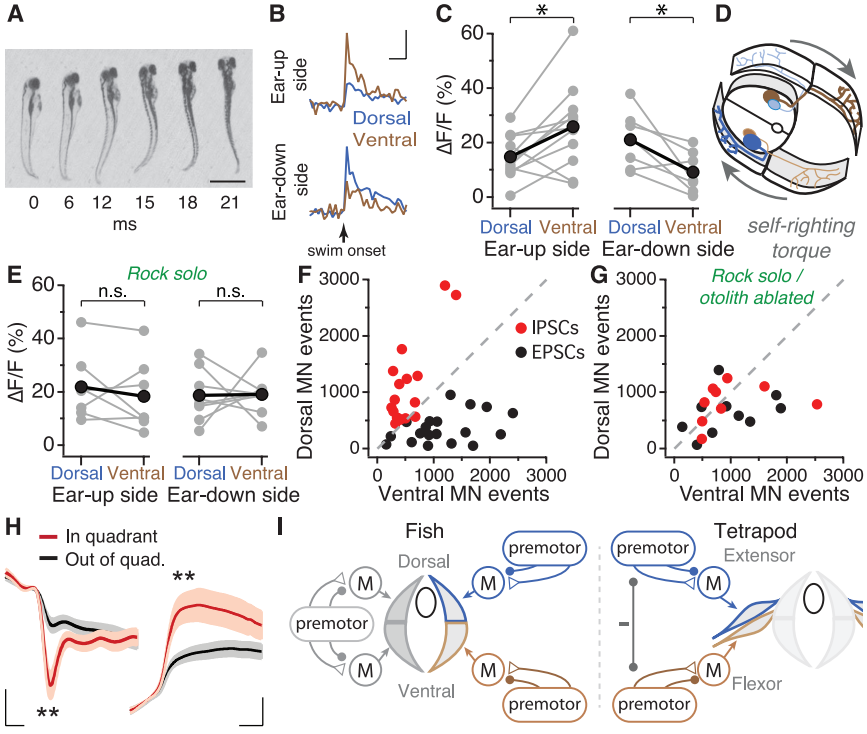


Fig. 4. Descending vestibular information differentially recruits dorsal and ventral microcircuits. (**A**) Time-lapse images of a 3-dpf larva engaging in self-righting from right ear up to dorsal-up orientation. Pictures were taken under normal illumination for display purposes only; behavioral data were gathered with infrared illumination. Scale bar, 1 mm. (**B**) Example Ca^{2+} imaging data from primary MNs in one segment of a side-lying fish. Arrow indicates time of brief electrical stimulus applied to tail to induce swimming. Scale bars, 20% $\Delta F/F$ (where F is fluorescence signal), 5 s. (**C**) Ventral-projecting MNs exhibit larger Ca^{2+} signals than dorsal-projecting MNs on ear-up side (left; $n = 13$ MN pairs from nine fish); pattern is reversed on ear-down flank (right; seven pairs from seven fish). *$P < 0.05$, paired t test. (**D**) Schematic of asymmetric drive to the four quadrants of musculature, producing torque for self-righting. (**E**) Ca^{2+} imaging summary as in (D), for *rock solo* mutant animals (ear-up, $n = 7$ pairs from seven fish; ear-down, $n = 8$ pairs from eight fish). n.s., not significant, paired t test. (**F**) Physiological recordings from MN out-of-quadrant pairs on the ear-up side of wild-type (WT) animals during fictive swimming reveal that EPSCs are more frequent in ventral-projecting MNs than dorsal ($P < 0.001$, paired t test, $n = 19$ pairs), whereas IPSCs are more frequent in dorsal-projecting MNs than ventral ($P < 0.001$, 17 pairs). Each dot represents either EPSC or IPSC data from a single out-of-quadrant pair. Unity line is shown in dashed gray. (**G**) As in (F), for vestibular-deficient animals. No differences are seen in the number of EPSCs ($P = 0.11$, $n = 10$ pairs) or IPSCs ($P = 0.50$, $n = 9$ pairs) between dorsal- and ventral-projecting MNs. (**H**) Higher in-quadrant than out-of-quadrant synchrony persists in *rock solo* mutants and otolith-ablated animals for both EPSCs and IPSCs. **$P < 0.01$, unpaired t test of peak amplitude (EPSCs, $n = 6$ in-quadrant, 10 out-of-quadrant pairs; IPSCs, $n = 6$ in-quadrant, 9 out-of-quadrant pairs). Scale bars: 4 pA, 0.5 ms; 10 pA, 1.5 ms. (**I**) Schematic summary of results: prior models of a single premotor circuit for dorsal and ventral control in fish (left); current model supporting parallel, modular microcircuits (middle); and proposed homology to limb control in tetrapods (right). M, motor.

how the modular organization of limb networks could have arisen from a single, homogeneous axial network (*5*). Our work demonstrates that axial networks, like limb networks, are organized in a modular fashion to facilitate differential control of muscles during locomotor-related behaviors such as postural correction (*29*). Thus, the modular organization of axial locomotor control systems may have served as a functional template for the evolution of limb control systems (Fig. 4I). We suggest that refinement and reweighting of inhibition between these modules is a plausible candidate mechanism for generating new locomotor patterns from ancient axial circuits.

References and Notes

1. T. G. Deliagina, P. V. Zelenin, G. N. Orlovsky, *Curr. Opin. Neurobiol.* **22**, 646–652 (2012).
2. A. Büschges, *Curr. Opin. Neurobiol.* **22**, 602–608 (2012).
3. M. Hägglund *et al.*, *Proc. Natl. Acad. Sci. U.S.A.* **110**, 11589–11594 (2013).
4. S. Grillner, *Physiol. Rev.* **55**, 247–304 (1975).
5. S. Grillner, T. M. Jessell, *Curr. Opin. Neurobiol.* **19**, 572–586 (2009).
6. A. Kozlov, M. Huss, A. Lansner, J. H. Kotaleski, S. Grillner, *Proc. Natl. Acad. Sci. U.S.A.* **106**, 20027–20032 (2009).
7. P. V. Zelenin, G. N. Orlovsky, T. G. Deliagina, *J. Neurosci.* **27**, 1024–1032 (2007).
8. M. Westerfield, J. V. McMurray, J. S. Eisen, *J. Neurosci.* **6**, 2267–2277 (1986).
9. E. Menelaou, D. L. McLean, *J. Neurosci.* **32**, 10925–10939 (2012).
10. D. L. McLean, J. Fan, S. Higashijima, M. E. Hale, J. R. Fetcho, *Nature* **446**, 71–75 (2007).
11. D. L. McLean, M. A. Masino, I. Y. Koh, W. B. Lindquist, J. R. Fetcho, *Nat. Neurosci.* **11**, 1419–1429 (2008).
12. S. Grillner, *Neuron* **52**, 751–766 (2006).
13. A. Roberts, W. C. Li, S. R. Soffe, *Front. Behav. Neurosci.* **4**, 16 (2010).
14. Y. Yoshimura, J. L. Dantzker, E. M. Callaway, *Nature* **433**, 868–873 (2005).
15. K. D. Walton, R. Navarrete, *J. Physiol.* **433**, 283–305 (1991).
16. Y. Kimura, Y. Okamura, S. Higashijima, *J. Neurosci.* **26**, 5684–5697 (2006).
17. S. A. Crone *et al.*, *Neuron* **60**, 70–83 (2008).
18. A. Roberts, W. C. Li, S. R. Soffe, *J. Comp. Physiol. A* **194**, 185–193 (2008).
19. C. M. Rovainen, *J. Neurophysiol.* **42**, 745–766 (1979).
20. F. Ullen, T. G. Deliagina, G. N. Orlovsky, S. Grillner, *J. Exp. Biol.* **198**, 665 (1995).
21. B. B. Riley, S. J. Moorman, *J. Neurobiol.* **43**, 329–337 (2000).
22. W. Mo, F. Chen, A. Nechiporuk, T. Nicolson, *BMC Neurosci.* **11**, 110 (2010).
23. T. Kohashi, N. Nakata, Y. Oda, *J. Neurosci.* **32**, 5810–5820 (2012).
24. A. J. Ijspeert, A. Crespi, D. Ryczko, J. M. Cabelguen, *Science* **315**, 1416–1420 (2007).
25. N. Schilling, *Front. Zool.* **8**, 4 (2011).
26. H. M. King, N. H. Shubin, M. I. Coates, M. E. Hale, *Proc. Natl. Acad. Sci. U.S.A.* **108**, 21146–21151 (2011).
27. S. Arber, *Neuron* **74**, 975–989 (2012).
28. M. Goulding, *Nat. Rev. Neurosci.* **10**, 507–518 (2009).
29. A. Miri, E. Azim, T. M. Jessell, *Neuron* **80**, 827–834 (2013).

Acknowledgments: We are grateful to E. Cadoff and S. Kishore for generating DNA constructs; E. Cadoff for behavioral experiments; and the McLean lab, E. B. Han, G. B. Edgerton, J. Fetcho, M. Scanziani, M. E. Hale, and M. A. MacIver for feedback on the manuscript. *rock solo* fish were a gift from T. Nicolson; the CatCh construct was a gift from E. Bamberg. Funding for these experiments came from NIH grants K99 DC012536 (M.W.B.) and R01 NS067299 (D.L.M.) Additional support was provided by the Esther A. and Joseph Klingenstein Fund, the Searle Scholars Program, and the Alfred P. Sloan Foundation (D.L.M.). The authors declare no competing financial interests.

Supplementary Materials

www.sciencemag.org/content/343/6167/197/suppl/DC1
Materials and Methods
Figs. S1 to S6
References (*30*, *31*)

6 September 2013; accepted 26 November 2013
10.1126/science.1245629

Apical Abscission Alters Cell Polarity and Dismantles the Primary Cilium During Neurogenesis

Raman M. Das and Kate G. Storey*

Withdrawal of differentiating cells from proliferative tissue is critical for embryonic development and adult tissue homeostasis; however, the mechanisms that control this cell behavior are poorly understood. Using high-resolution live-cell imaging in chick neural tube, we uncover a form of cell subdivision that abscises apical cell membrane and mediates neuron detachment from the ventricle. This mechanism operates in chick and mouse, is dependent on actin-myosin contraction, and results in loss of apical cell polarity. Apical abscission also dismantles the primary cilium, known to transduce sonic-hedgehog signals, and is required for expression of cell-cycle-exit gene p27/Kip1. We further show that N-cadherin levels, regulated by neuronal-differentiation factor Neurog2, determine cilium disassembly and final abscission. This cell-biological mechanism may mediate such cell transitions in other epithelia in normal and cancerous conditions.

Newborn neurons detach an apical cell-process from the ventricular surface and then migrate to the lateral neural tube or to form cortical layers within the brain (*1*, *2*). This step is required for the generation of neuronal and tissue architecture (*2*, *3*), and its failure leads to human periventricular heterotopia (*4*). Down-regulation of N-cadherin is associated with this event (*3*, *5*), as is loss of apical complex proteins (*6*, *7*). The latter may be mediated by down-regulation; protein modification/degradation or relocalization; or loss of apical membrane.

Neural Development Group, Division of Cell and Developmental Biology, College of Life Sciences, University of Dundee, Dundee DD1 5EH, UK

*Corresponding author. E-mail: k.g.storey@dundee.ac.uk

To investigate cell behavior underlying neuron birth, we labeled membranes of individual cells by mosaic transfection of green fluorescent protein– glycosylphosphatidylinositol (pCAGGS-GFP-GPI) into the chick embryonic spinal cord (*8*). We then monitored neurogenesis in ex vivo embryo slice cultures (*1*) using wide-field time-lapse microscopy (*8*). Newborn neurons have a basally located cell body and extend a long, thin cell-process to the apical/ventricular surface. Movies of such cells revealed that shedding of the apical-most cell membrane preceded withdrawal of this cell-process (Fig. 1A). This event, which we name apical abscission, takes ~1 hour (56 min, SD = 18 min, n = 21 cells). It begins with formation of a bulb-like "bouton," followed by subapical constriction, membrane thinning, and eventual abscission, after which the apical cell-process withdraws (42 abscising cells in 34 embryos; all stages observed in 21 cells) (Fig. 1A, fig. S1, and movies S1 to S3). Abscised particles tracked so far remain at the ventricle.

Using structured illumination microscopy (*8*) to generate super-resolution images of abscising cells transfected with membrane-localized Tag–red fluorescent protein–Farnesyl (TagRFP-Farn) revealed a thin membranous connection between apical cell-process and the abscising particle. This confirmed the existence of abscission events in fixed tissue not subject to culture and imaging regimes (n = 5 cells in 3 embryos) (fig. S2 and movie S4). We also observed apical abscission in completely unmanipulated embryos fixed and labeled to reveal the early neuronal marker Tuj1 (class III beta-tubulin). Some Tuj1$^+$ cells with a basally localized nucleus and a ventricle-contacting apical cell-process were found to have a distinct constriction, coincident with subapical actin (n = 31 of 78 cells in 5 embryos) (Fig. 1B and movie S5). To characterize the abscised membrane, we assessed localization of endogenous apical Par-complex protein, atypical protein kinase C (aPKC) (*9*) in such Tuj1$^+$ cells; aPKC was confined to the abscising particle (n = 31 of 31 cells in 5 embryos) (Fig. 1B and movie S5). This indicates that differentiating neurons experience rapid loss of apical polarity. It is also consistent with the absence of Par-complex proteins from withdrawing cell-processes (*6*, *7*), which, now liberated from apical-junctional complexes, extend transient membrane protrusions (18 cells in 9 embryos) (e.g., see movies S1 and S2). Similar apical constrictions were visible in Tuj1$^+$ ventricle-contacting cells in mouse spinal cord (22 of 40 cells in 4 embryos) (Fig. 1C and movie S6),

with aPKC confined to the abscising particle (22 of 22 cells). This demonstrates that apical abscission is conserved across species. In chick, we further characterized cells poised to abscise as indicated by a basally located nucleus and ventricle-contacting apical cell-process revealed by TagRFP-Farn labeling and found a similar localization of actin and aPKC (21 of 21 cells in 6 embryos) (Fig. 1D and movie S7). Many such TagRFP-Farn–labeled cells with this morphology also express low levels of the early neuronal marker, NeuroM (26 of 29 cells in 5 embryos) (Fig. 1, E to G). These NeuroM-positive cells were further found to express the interneuron marker Lim1/2 (23 of 23 cells) but not the later neuronal marker HuC/D (0 of 12 cells) nor the postmitotic cell marker Cdk-inhibitor p27/Kip1 (0 of 11 cells) [(*10*) and see (*7*)], identifying these cells as immature neurons that have yet to commit to cell cycle exit (Fig. 1, E to G).

Neuroepithelial cells contain a subapical actin cable that mediates normal cell constriction at the ventricular surface. To investigate whether apical abscission involves actin dynamics, we cotransfected GFP-GPI and Actin-TagRFP vectors into chick neural tube and monitored protein localization. Subapical actin was visible in cells poised to abscise and coincided with the region of constriction before abscission (Fig. 2A and movie S8). As abscission began, Actin-TagRFP signal intensity increased (*8*), reaching a maximum shortly before abscission completion (Fig. 2B); actin was then depleted from the withdrawing cell-process

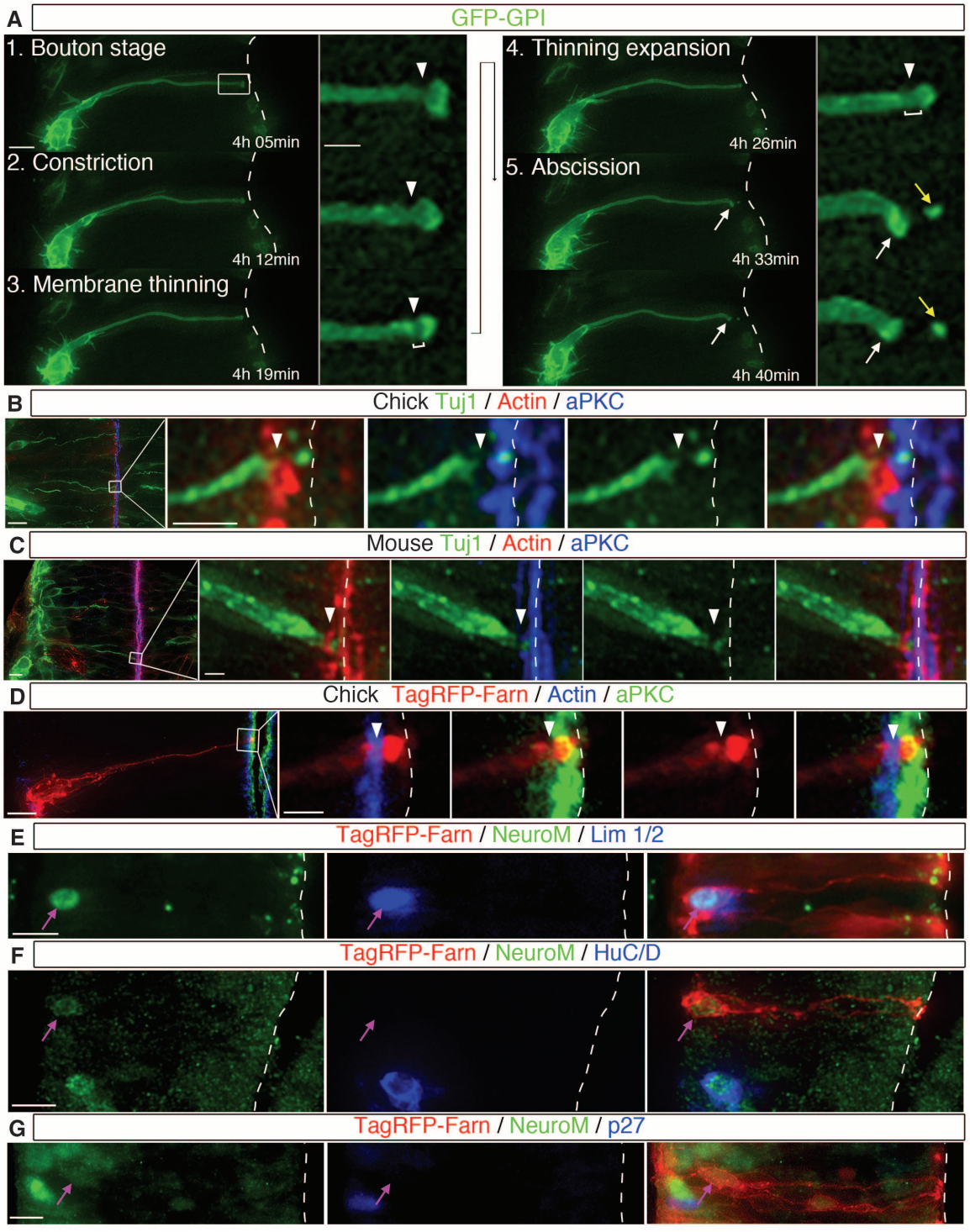


Fig. 1. Apical abscission during neuronal differentiation. (**A**) Time-lapse sequence of a cell undergoing distinct stages of apical abscission [movie S1; these are additional frames of a cell shown in supplementary movie 2 in (6).]. (**B** to **D**) Maximum intensity projections of constricting abscission site (white arrowheads) visible in Tuj1^{+} ventricle-contacting cells in chick (B) and mouse (C) embryos and TagRFP-Farn–labeled cell in chick (D); the abscising particle is distal to actin and contains the apical Par-complex, marked by aPKC [three-dimensional reconstructions of (B), (C), and (D) in movies S4, S5, and S6, respectively]. (**E** to **G**) Cells poised to abscise express NeuroM and Lim1/2 (E) but not HuC/D (F) nor p27 (G) (magenta arrows). Abscission site (white arrowheads), withdrawing apical cell-process (white arrows), abscised particle (yellow arrows), and apical surface (white dashed line) here and in all figures. Scale bars, 10 μm; enlarged regions, 2 μm.

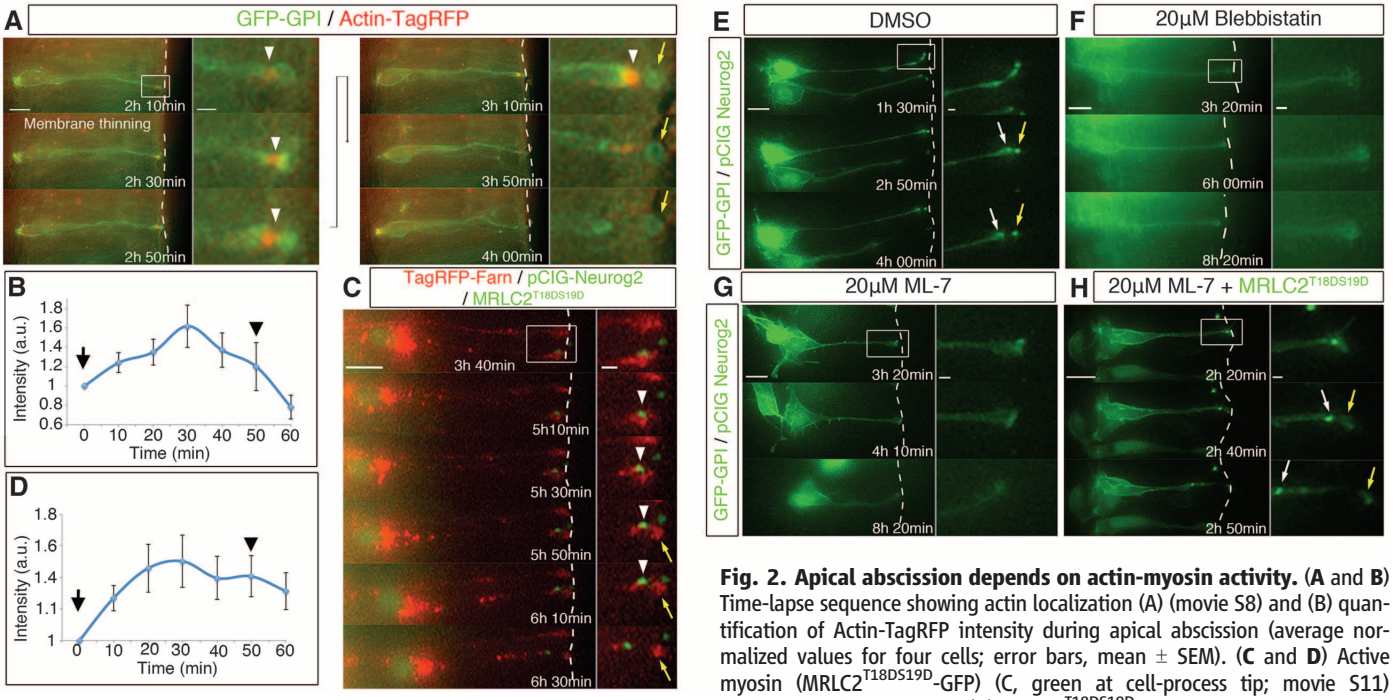


Fig. 2. Apical abscission depends on actin-myosin activity. (**A** and **B**) Time-lapse sequence showing actin localization (A) (movie S8) and (B) quantification of Actin-TagRFP intensity during apical abscission (average normalized values for four cells; error bars, mean ± SEM). (**C** and **D**) Active myosin ($MRLC2^{T18DS19D}$-GFP) (C, green at cell-process tip; movie S11) localizes to abscission site (D) $MRLC2^{T18DS19D}$-GFP intensity during apical abscission (average normalized values for five cells error bars, mean ± SEM). (**E** to **H**) Cells exposed to control DMSO undergo abscission (E) (movie S14), but not in the presence of blebbistatin (F) (movie S17) or ML-7 (G) (movie S20). ML-7 abscission inhibition is rescued by expression of $MRLC2^{T18DS19D}$-GFP (H) (movie S23). For definition of apical surfaces, N-cadherin, and aPKC localization, see fig. S6. [(B) and (D)] Membrane thinning, black arrow; abscission complete, black arrowhead. Scale bars, 10 μm; enlarged regions, 2 μm.

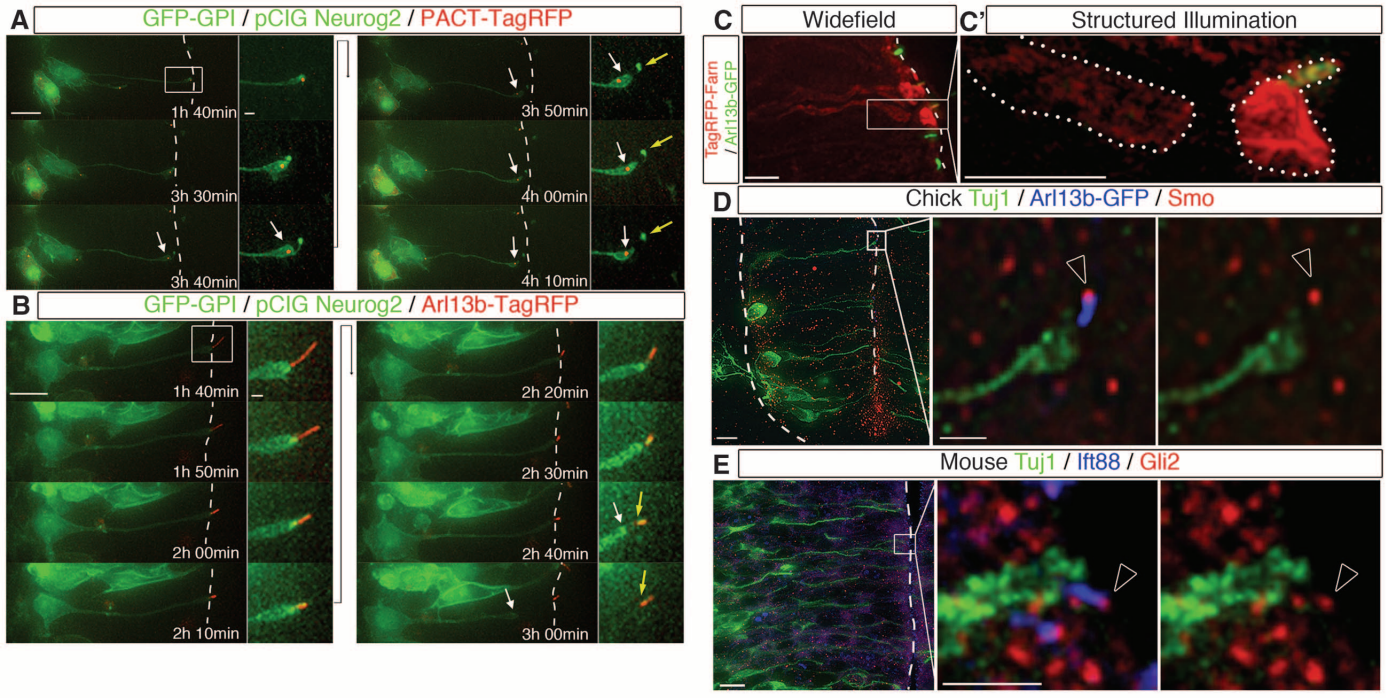


Fig. 3. Apical abscission dismantles the primary cilium. (**A** and **B**) Time-lapse sequences showing centrosome release into the apical cell-process (A) (movie S26), while Arl13b-labeled cilium is retained at the apical membrane (B) (movie S29). (**C**) Widefield and (**C'**) structured illumination imaging (white dotted outline) (movie S32) of TagRFP-Farn labeled apical cell-process and abscised particle containing Arl13b-GFP–labeled cilium. (**D** and **E**) $Tuj1^{+}$ cells with ventricle-contacting apical cell-processes exhibit Smo (D) (movie S33) and Gli2 accumulation (E) (movie S34) (empty arrowheads) in their primary cilium [identified with Arl13b-GFP or Ift88 (intraflagellar-transport-protein 88), respectively]. Scale bars, 10 μm; enlarged regions and C and C', 2 μm.

tip (n = 24 abscising cells in 18 embryos) (Fig. 2A, fig. S3, and movies S8 to S10). This local actin increase raised the possibility that actin-myosin contraction mediates apical abscission.

We therefore next surveyed myosin localization using a myosin regulatory light chain 2 GFP construct (MRLC2-GFP); this revealed strong subapical localization and diffuse cytosolic distribution in all cells (fig. S4). Because myosin phosphorylation is essential for actin-mediated apical constriction, we next discriminated sites of myosin activity by monitoring MRLC2^{T18DS19D}-GFP, a constitutively active form of MRLC2. To increase the incidence of neuronal differentiation, we cotransfected cells with a plasmid encoding the proneural gene *Neurog2* [pCAGGS-Neurog2-IRES-nucGFP (pCIG-Neurog2)], which promotes neuronal differentiation (*10*). In such cells, also coexpressing TagRFP-Farn to label cell membranes, active MRLC2 localized subapically until shortly after abscission (*8*) (n = 12 cells in 9 embryos) (Fig. 2, C and D, and movies S11 to S13). Thus, actin is localized and myosin is active in the subapical region of the abscising neuron.

To investigate the requirement for myosin activity, cells were transfected with GFP-GPI and pCIG-Neurog2, and slices were cultured in medium containing blebbistatin (inhibitor of myosin motor function), ML-7 (inhibitor of myosin light chain kinase MLCK, which phosphorylates Myosin II) (see fig. S5), or dimethyl sulfoxide (DMSO) control. Although few cells in control slices failed to abscise and retract their cell-processes within an 8-hour period (n = 4 of 33 cells in 5 embryos) (Fig. 2E and movies S14 to S16), the majority of cells exposed to blebbistatin (n = 33 of 36 cells in 6 embryos) (Fig. 2F and movies S17 to S19; apical surface definition, fig. S6) or ML7 (n = 68 of 83 cells in 15 embryos; Fig. 2G and movies S20 to S22; apical surface definition, fig. S6) remained attached at the ventricle. Furthermore, coexpression of active MRLC2 in the presence of ML-7 rescued its effects, with most cells now abscising within 8 hours (n = 14 of 18 cells in 7 embryos) (Fig. 2H and movies S23 to S25). Misexpression of active MRLC2 alone, however, did not increase neuron numbers, so the potential to increase actin-myosin contraction is by itself insufficient to promote apical abscission (fig. S7). These data indicate that myosin activity is required, but not sufficient, for apical abscission.

Neuroepithelial cells lining the ventricle possess a primary cilium. This projects from the basal body/centrosome located at the apical pole. While this cilium plays a key role in transducing sonic hedgehog (Shh) (and possibly other) signals that maintain neuroepithelial cells in a proliferative state (*11*), the centrosome is further implicated in positioning axon outgrowth (*12*). To observe the effect of apical abscission on the primary cilium, we transfected GFP-GPI and pCIG-Neurog2 into the neural tube together with a construct containing a pericentrin-AKAP450 centrosomal targeting (PACT) domain sequence that confers centrosomal localization fused to TagRFP (PACT-TagRFP). As abscission began, the centrosome localized to the withdrawing cell-process (n = 45 cells in 15 embryos) (Fig. 3A and movies S26 to S28). Conversely, the primary cilium, identified with ciliary membrane–associated Arl13b-TagRFP, remained attached to the abscised apical membrane (n = 21 cells in 7 embryos) (Fig. 3B and movies S29 to S31). During apical abscission, the Arl13b-labeled cilium also shortened [two-fold reduction in cilium length; n = 5 abscising cells (*8*)]. We further used structured illumination microscopy to confirm the presence of Arl13b-GFP in particles abscised from TagRFP-Farn–labeled cells in tissue not subject to culture and live imaging (n = 5 cells) (Fig. 3C and movie S32).

Active Shh signaling is indicated by accumulation of the Shh transducer Smoothened (Smo) and its key pathway effector Gli2 in the primary cilium (*13*, *14*). Shh signaling is highest in the ventral half of the neural tube, and we therefore assessed localization of endogenous Smo and Gli2 in Tuj1$^+$ cells with ventricle-contacting cell-processes in this region. This revealed many cells with ciliary accumulation of Smo (n = 38 of 43 cells in 4 chick embryos) (Fig. 3D and movie S33) or Gli2 (n = 33 of 35 cells in 3 mouse embryos) (Fig. 3E and movie S34). This localization of proteins suggests that cells poised to abscise are responding to Shh signals and predicts that disjunction of the centrosome and Arl13b-labeled cilium during apical abscission curtails Shh signaling.

Onset of neuronal differentiation is characterized by down-regulation of N-cadherin (*3*, *5*), which forms subapical adherens junctions between neuroepithelial cells (*15*), and abnormal persistence of N-cadherin inhibits apical cell-process withdrawal (*3*). Cadherins are connected intracellularly to the contractile actin cable, and this serves to maintain tension at apical junctions and cell-cell adhesion (*15*). Declining N-cadherin levels within the prospective neuron may therefore trigger apical abscission by loosening cell-cell junctions and connection with the intracellular actin-myosin cable. Because the centrosome is localized in the withdrawing cell-process, it must be released from the cilium before final abscission. To determine how persistent N-cadherin affects apical abscission, we misexpressed N-cadherin-YFP (yellow fluorescent protein) together with GFP-GPI and PACT-TagRFP. Increased N-cadherin blocked cell-process withdrawal, and the centrosome remained at the apical pole (16 cells in 10 embryos) (Fig. 4A and movies S35 to S37). This indicates that

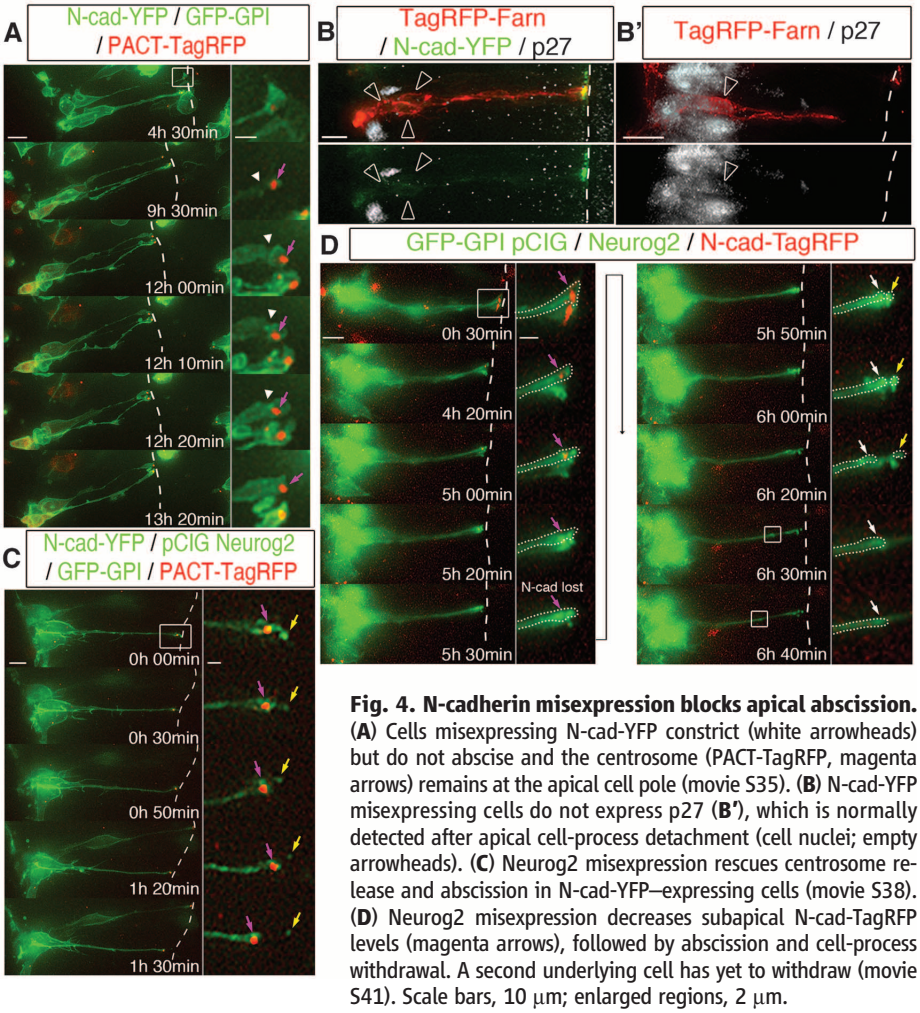


Fig. 4. N-cadherin misexpression blocks apical abscission. (**A**) Cells misexpressing N-cad-YFP constrict (white arrowheads) but do not abscise and the centrosome (PACT-TagRFP, magenta arrows) remains at the apical cell pole (movie S35). (**B**) N-cad-YFP misexpressing cells do not express p27 (**B'**), which is normally detected after apical cell-process detachment (cell nuclei; empty arrowheads). (**C**) Neurog2 misexpression rescues centrosome release and abscission in N-cad-YFP–expressing cells (movie S38). (**D**) Neurog2 misexpression decreases subapical N-cad-TagRFP levels (magenta arrows), followed by abscission and cell-process withdrawal. A second underlying cell has yet to withdraw (movie S41). Scale bars, 10 μm; enlarged regions, 2 μm.

N-cadherin down-regulation is required for centrosome release from the apical surface, as well as for final abscission of apical membrane.

One consequence of failure to undergo N-cadherin down-regulation and apical abscission might therefore be maintenance of Shh signaling and therefore inhibition of cell cycle exit. To assess the relationship between cell cycle regulation and apical abscission, we next determined the effect of persistent N-cadherin on expression of p27/Kip1, which normally begins after apical cell-process withdrawal [Figs. 1G and 4B′ and see (*7*)]. N-cadherin misexpressing cells lacked p27/Kip1 after 24 hours [N-cad-YFP+TagRFP-Farn misexpressing cells 3% p27/Kip1 positive (25 of 689 cells in 4 embryos) (Fig. 4B); control TagRFP-Farn only expressing cells 13% p27/Kip1 positive (76 of 649 cells in 4 embryos) (Fig. 4B′]. These findings therefore place N-cadherin loss and apical abscission, including cilium disassembly, upstream of cell cycle exit as defined by p27/Kip1 expression. Furthermore, driving premature cell cycle exit by p27/Kip1 misexpression did not promote apical abscission or neuronal differentiation (fig. S8), consistent with proneural genes promoting expression of Cdk inhibitors, which then act in concert with other proneural targets to orchestrate neuronal differentiation (*16*).

N-cadherin down-regulation in prospective neurons is mediated by the transcription factor FoxP2/4, expression of which is promoted by the proneural gene Neurog2 (*3*, *10*). To determine whether Neurog2 misexpression is sufficient to overcome excess N-cadherin, we cotransfected constructs encoding these two genes into the neural tube. Despite excess N-cadherin, cells with excess Neurog2 dismantled their cilium and underwent abscission and cell-process withdrawal (16 cells in 7 embryos) (Fig. 4C and movies S38 to S40). In this context, N-cadherin-TagRFP was localized to the abscission site and then lost before abscission (n = 19 cells in 8 embryos) (Fig. 4D and movies S41 to S43). This indicates that localization and regulation of N-cadherin protein [(as well as transcriptional down-regulation of endogenous N-cadherin (*3*)] is directed by factors downstream of Neurog2.

These findings uncover a cell biological mechanism, apical abscission, that takes place downstream of N-cadherin loss and involves actin-myosin–dependent cell constriction and dismantling of the primary cilium. This abscission event detaches newborn neurons from the ventricular surface and results in loss of apical-complex–containing cell membrane and therefore apical polarity. By separating centrosome from Arl13b-labeled cilium, apical abscission may curtail active Shh signaling, as indicated by ciliary accumulation of Smo and Gli2 in cells poised to abscise. Consistent with a loss of mitogenic Shh, abscission is also required for expression of cell-cycle exit gene p27/Kip1 (fig. S9). Apical abscission is thus a decisive event in the neuronal differentiation program, which triggers reorganization of the newborn neuron and its withdrawal from the ventricular environment. Abscising the apical membrane and leaving this, at least initially, at the apical surface may also help to maintain tissue integrity. During mitosis, cilia are resorbed or partially internalized (*17*) rather than shed, and regulated cilium shedding has only been reported in the alga *Chlamydomonas* (*18*). Loss of apical complex proteins also characterizes cells undergoing an epithelial to mesenchymal transition, including tumor cell metastasis (*19*), and some cancers exhibit cilia loss (*20*). Investigation of apical abscission in normal and also oncogenic epithelia may therefore provide insight into mechanisms that direct critical cell state transitions.

References and Notes

1. A. C. Wilcock, J. R. Swedlow, K. G. Storey, *Development* **134**, 1943–1954 (2007).
2. S. C. Noctor, V. Martínez-Cerdeño, L. Ivic, A. R. Kriegstein, *Nat. Neurosci.* **7**, 136–144 (2004).
3. D. L. Rousso *et al.*, *Neuron* **74**, 314–330 (2012).
4. V. L. Sheen, *Scientifica* **2012**, 480129 (2012).
5. G. K. W. Wong, M.-L. Baudet, C. Norden, L. Leung, W. A. Harris, *J. Neurosci.* **32**, 223–228 (2012).
6. R. M. Das, K. G. Storey, *EMBO Rep.* **13**, 448–454 (2012).
7. S. Ghosh *et al.*, *Proc. Natl. Acad. Sci. U.S.A.* **105**, 335–340 (2008).
8. Materials and methods are available as supplementary material on *Science* Online.
9. S. Ohno, *Curr. Opin. Cell Biol.* **13**, 641–648 (2001).
10. N. Bertrand, D. S. Castro, F. Guillemot, *Nat. Rev. Neurosci.* **3**, 517–530 (2002).
11. A. Louvi, E. A. Grove, *Neuron* **69**, 1046–1060 (2011).
12. M. Kuijpers, C. C. Hoogenraad, *Mol. Cell. Neurosci.* **48**, 349–358 (2011).
13. K. C. Corbit *et al.*, *Nature* **437**, 1018–1021 (2005).
14. J. Kim, M. Kato, P. A. Beachy, *Proc. Natl. Acad. Sci. U.S.A.* **106**, 21666–21671 (2009).
15. A. Ratheesh, A. S. Yap, *Nat. Rev. Mol. Cell Biol.* **13**, 673–679 (2012).
16. H. Gui, S. Li, M. P. Matise, *Dev. Biol.* **301**, 14–26 (2007).
17. J. T. M. L. Paridaen, M. Wilsch-Bräuninger, W. B. Huttner, *Cell* **155**, 333–344 (2013).
18. L. M. Quarmby, in *Int. Rev. Cytol.* (Academic Press, 2004), vol. 233, pp. 47–91.
19. B. Xue, K. Krishnamurthy, D. C. Allred, S. K. Muthuswamy, *Nat. Cell Biol.* **15**, 189–200 (2013).
20. N. B. Hassounah, T. A. Bunch, K. M. McDermott, *Clin. Cancer Res.* **18**, 2429–2435 (2012).

Acknowledgments: We thank C. Weijer, A. Muller, and J. Januschke for comments; J. Swedlow for imaging advice; and S. Swift and C. Thomson in the College of Life Sciences Light Microscopy Facility (LMF) for technical support. Structured-illumination microscopy was carried out with assistance of M. Posch (LMF) and L. Ferrand (GE Healthcare) and supported by the Medical Research Council Next Generation Optical Microscopy Award (MR/K015869/1). R.M.D. and K.G.S. are funded by Wellcome Trust program grant 083611/Z/07/Z.

Supplementary Materials

www.sciencemag.org/content/343/6167/200/suppl/DC1
Materials and Methods
Figs. S1 to S9
Movies S1 to S43
References (*21*–*30*)

22 October 2013; accepted 2 December 2013
10.1126/science.1247521

Internalization of *Salmonella* by Macrophages Induces Formation of Nonreplicating Persisters

Sophie Helaine,* Angela M. Cheverton,† Kathryn G. Watson,† Laura M. Faure, Sophie A. Matthews, David W. Holden*

Many bacterial pathogens cause persistent infections despite repeated antibiotic exposure. Bacterial persisters are antibiotic-tolerant cells, but little is known about their growth status and the signals and pathways leading to their formation in infected tissues. We used fluorescent single-cell analysis to identify *Salmonella* persisters during infection. These were part of a nonreplicating population formed immediately after uptake by macrophages and were induced by vacuolar acidification and nutritional deprivation, conditions that also induce *Salmonella* virulence gene expression. The majority of 14 toxin-antitoxin modules contributed to intracellular persister formation. Some persisters resumed intracellular growth after phagocytosis by naïve macrophages. Thus, the vacuolar environment induces phenotypic heterogeneity, leading to either bacterial replication or the formation of nonreplicating persisters that could provide a reservoir for relapsing infection.

Many studies, mostly focusing on bacteria grown in laboratory media, have shown that persisters are an unstable, nongrowing, multidrug-tolerant subpopulation that result from phenotype switching (*1*–*3*). In contrast to antibiotic-resistant bacteria arising from heritable mutations, the progeny of persisters are mainly antibiotic-sensitive cells. Most studies on persistent infections are based on the assumption that a proportion of the bacterial population is nonreplicating (*4*); however, this consensus was challenged recently in studies that showed replicating antibiotic-

Section of Microbiology, Medical Research Council Centre for Molecular Bacteriology and Infection, Imperial College London, Armstrong Road, London SW7 2AZ, UK.

*Corresponding author. E-mail: s.helaine@imperial.ac.uk (S.H.); d.holden@imperial.ac.uk (D.W.H.)
†These authors contributed equally to this work.

tolerant mycobacteria (*5*, *6*). Moreover, direct evidence for nongrowing persister bacteria in infected tissues is lacking.

Previously, we reported the use of a fluorescence dilution (FD) technique to study intracellular replication dynamics of *Salmonella* Typhimurium. FD can be used to monitor the extent of bacterial replication at the single-cell level by dilution of a preformed pool of fluorescent protein after its induction has been stopped. The technique reveals the presence of bacteria that maintained bright fluorescence during infection, indicating that they are nongrowing (*7*). We used FD to investigate whether nonreplicating *Salmonella* were persisters.

Infection of susceptible mice by *S.* Typhimurium results in an acute typhoid-like disease characterized by intracellular proliferation of bacteria in organs including the Peyer's Patches (PP), mesenteric lymph nodes (MLNs), spleen, and liver. C57 Bl6 or BALB/c mice were inoculated per os (p.o.) with wild-type (WT) *S.* Typhimurium carrying a plasmid from which mCherry is produced constitutively (to provide a marker for bacterial cells) and green fluorescent protein (GFP) dilutes proportionally with bacterial cell division (*8*). At different time points, tissues were extracted, homogenized, and lysed. The released *Salmonella* cells were subjected to flow cytometry analysis (fig. S1). As early as 2 hours after inoculation, the majority of bacteria that were detected in the PP and MLNs had not undergone any replication (50 and 95%, respectively) (Fig. 1A). Nonreplicating bacteria were also found in these organs and in the spleen at later time points. To determine the viability of these nonreplicating cells, bacteria released from MLNs were incubated in Luria Bertani (LB) medium and analyzed by flow cytometry. Dilution of fluorescence (indicated by a decrease in bacterial fluorescence intensity) (Fig. 1B) revealed resumption of growth of the previously identified nonreplicating population. Regrowth of bacteria that had not undergone any replication in vivo was also observed with time-lapse microscopy (Fig. 1C). To clear the infection and reveal persisters, mice were treated with enrofloxacin at 24 hours after inoculation. Five days later, all of the remaining bacteria (~10^2) extracted from MLNs [a known site of persistence (*9*)] had not undergone any replication (Fig. 1D), indicating an incomplete clearance of the nonreplicating population. We transferred these nongrowing cells to LB medium and observed resumption of growth in the absence of antibiotic treatment (Fig. 1E), indicating that they were persisters.

In the mouse typhoid model, *Salmonella* proliferates in macrophages (*10*, *11*). Internalization of *Salmonella* by resting or interferon-γ (IFN-γ)–activated bone marrow–derived macrophages (BMMs) from different mouse strains for 24 hours or 30-min periods produced a 100- to 1000-fold increase in the proportion of antibiotic-tolerant bacteria as compared with those already present in the inoculum (Fig. 2, A and B, and fig. S2). The progeny of BMM-derived bacteria that survived antibiotic exposure were as antibiotic-sensitive as the initial inoculum, indicating that they are bona fide persisters (Fig. 2A). Macrophage-induced persisters were tolerant to several antibiotics (Fig. 2C). FD was used to investigate the replication status of these bacteria. As was observed in mice, the BMM-derived persisters

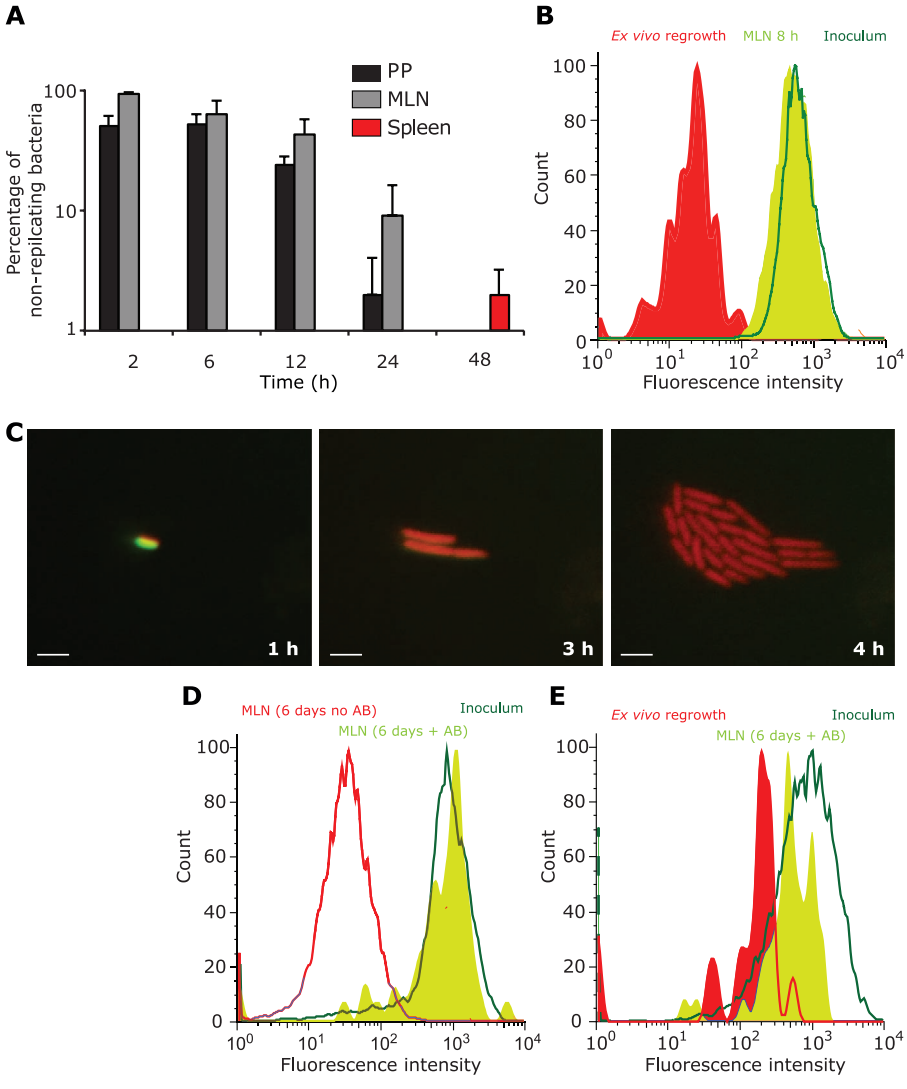


Fig. 1. Nonreplicating *Salmonella* persisters in immune organs. (**A**) The average percentage of nonreplicating bacteria in the PP, MLNs, and spleens of mice, detected with flow cytometry by use of FD at different times after inoculation. Data represent the mean ± SEM and were analyzed by using a Student's *t* test. $^{**}P < 0.01$. (**B**) Representative FD profiles of bacteria recovered from MLNs of five mice, 8 hours after infection (light green) and 16 hours after inoculation in LB (red) (number of bacteria ≥ 10^4), showing regrowth of nonreplicating bacteria isolated from MLNs. (**C**) Regrowth of a nonreplicating bacterium recovered from MLNs 24 hours after inoculation on LB agar. Scale bar, 2 μm. (**D** and **E**) FD profiles of bacteria recovered 6 days after inoculation from MLNs of 10 mice, treated (light green) or not (red) with enrofloxacin, and 12 hours after inoculation in LB medium (red) (number of bacteria ≥ 10^2) showing regrowth of nonreplicating bacteria that survived antibiotic treatment (AB) of animals.

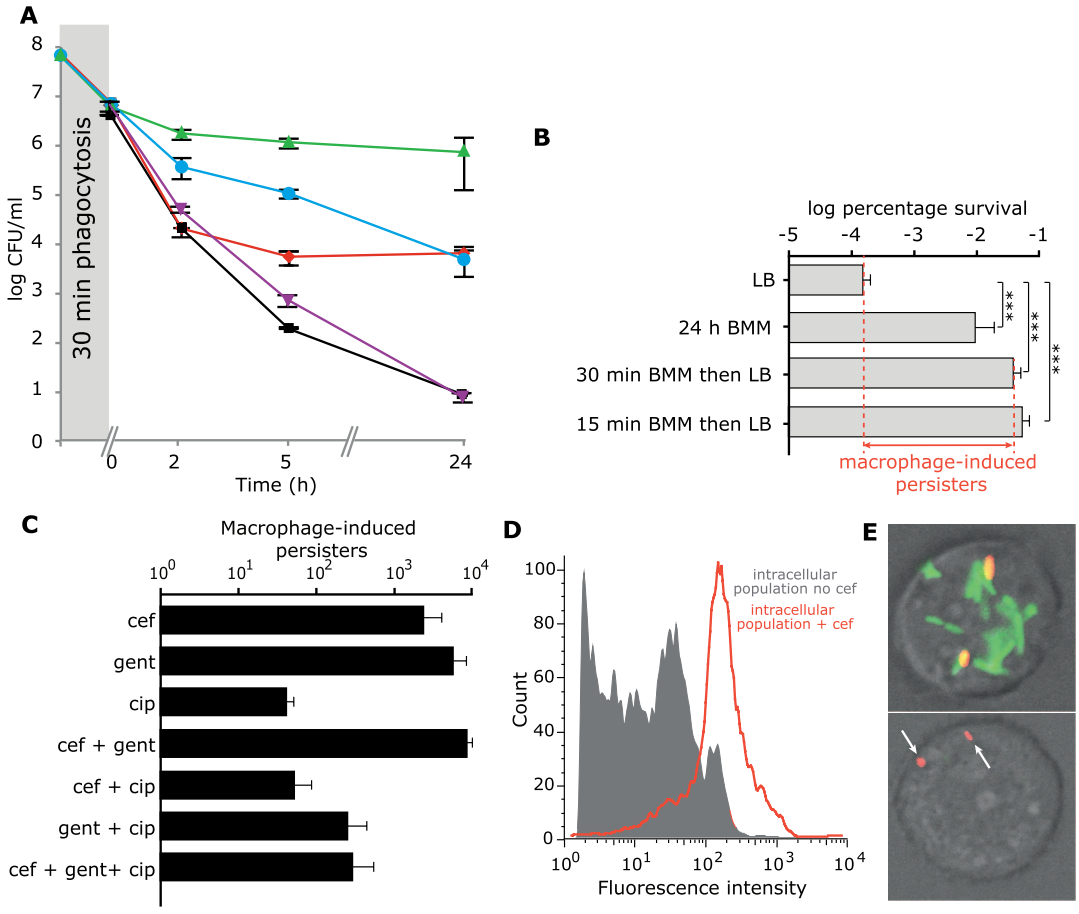


Fig. 2. Rapid formation of nonreplicating persisters in macrophages. (**A**) Cefotaxime (cef) survival kinetics of *Salmonella* grown in LB medium (black), BMMs (blue), LB medium after 30-min internalization (red), compared with survival of bacteria in BMM without cef treatment (green). Progeny of persisters (24 hours time-point, red kinetics) were subjected to a second exposure to cef in LB medium (purple). (**B**) Log percentage survival after 24 hours of cef treatment of LB medium–grown bacteria, or bacteria within BMM for 24 hours, 30 min, or 15 min followed by transfer to LB medium. Formation of macrophage-induced persisters was measured as the fold-increase in persister levels quantified in bacterial populations either grown exclusively in LB medium or in LB medium after 30-min internalization in BMM. Data were analyzed by using a Student's *t* test. ***$P < 0.001$. (**C**) Macrophage-induced persister formation measured after exposure to cef, gentamicin (gent), ciprofloxacin (cip), or different antibiotic combinations. Replication status of intracellular bacteria, by using FD and detected by (**D**) flow cytometry before (gray area) or after (red line) 16 hours exposure to cef, added 18 hours after uptake; or (**E**) live-imaging microscopy before (top) and after (bottom) 12 hours exposure to cef, added 18 hours after uptake. The bacteria that remained after cef exposure were non-replicating [(D), red line, and (E), white arrows]. Data represent the mean ± SEM.

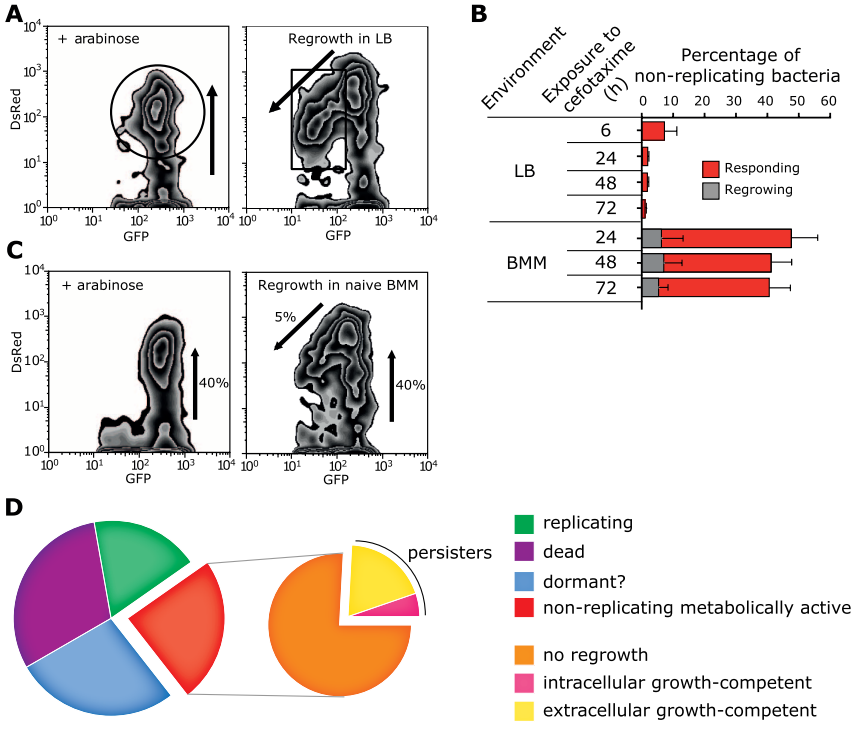


Fig. 3. Metabolic status of persisters. (**A**) Analysis of metabolic activity (left) and regrowth (right) of persisters, analyzed by means of flow cytometry. (Left) Intracellular antibiotic-tolerant bacteria retained high GFP intensity because of a lack of replication, and their metabolic activity was revealed by appearance of DsRed fluorescence upon addition of arabinose (circle). (Right) After release from macrophages and transfer to LB medium, regrowth of some bacteria was revealed through concomitant dilution of DsRed and GFP fluorescence (rectangle). (**B**) Quantification of proportion of nonreplicating bacteria showing metabolic activity upon addition of inducer (production of DsRed fluorescence; red bars) and resuming growth (indicated by fluorescence dilution; gray bars), from LB medium-grown or intracellular nonreplicating cells in activated BMM over time. Data represent the mean ± SEM. (**C**) Representative example of quantification of proportion of intracellular nonreplicating bacteria, after 24 hours within activated BMM, showing (left) metabolic activity revealed by appearance of DsRed upon addition of arabinose and (right) quantification of growth resumption of metabolically active bacteria within newly infected BMM. (**D**) Chart showing relative proportions and heterogeneity of different *Salmonella* subpopulations in BMM. Thick arrows in (A) and (C) indicate direction of fluorescence shift, either representing production of DsRed upon arabinose addition (vertical arrows) or dilution of DsRed and GFP fluorescence during regrowth (oblique arrow).

consisted of nonreplicating cells that formed before any bacterial division had occurred (as indicated by an absence of fluorescence dilution) (Fig. 2, D and E). These results contrast with those obtained with mycobacteria, in which persisters were shown to be replicating bacteria (*5*, *6*).

We showed previously that intracellular nonreplicating *Salmonella* are composed of subpopulations of unresponsive and metabolically active bacteria whose numbers decline with time (*7*). To determine which of these subpopulations were persisters, we used a double-inducible fluorescent reporter (Fig. 3, A and B, and fig. S3). Bacteria preloaded with GFP were used to infect macrophages for up to 72 hours. Replicating bacteria gradually lost the GFP signal and were killed by exposure to cefotaxime. Nonreplicating bacteria retained green fluorescence, and their metabolic status was determined through addition of DsRed inducer (*7*). Under improved growth culture conditions (*12*), as many as 40% showed evidence of metabolic activity for the 72-hour observation period (Fig. 3B). This contrasted with a rapid decrease in metabolic activity of antibiotic-tolerant *Salmonella* that formed in LB medium (Fig. 3B), a phenomenon that has been observed with *Escherichia coli* (*13*).

We released nonreplicating intracellular bacteria by lysis of infected macrophages and monitored subsequent growth in LB medium by FD. Regardless of how long they had been internalized, ~20% of the metabolically active subpopulation resumed growth within 2 hours after their release from macrophages, as indicated by concomitant dilution of green and red fluorescence (Fig. 3, A and B, and fig. S4). No regrowth of the metabolically inactive population was detected (Fig. 3A). Therefore, intracellular persisters are derived exclusively from the metabolically active subpopulation of nonreplicating *Salmonella*.

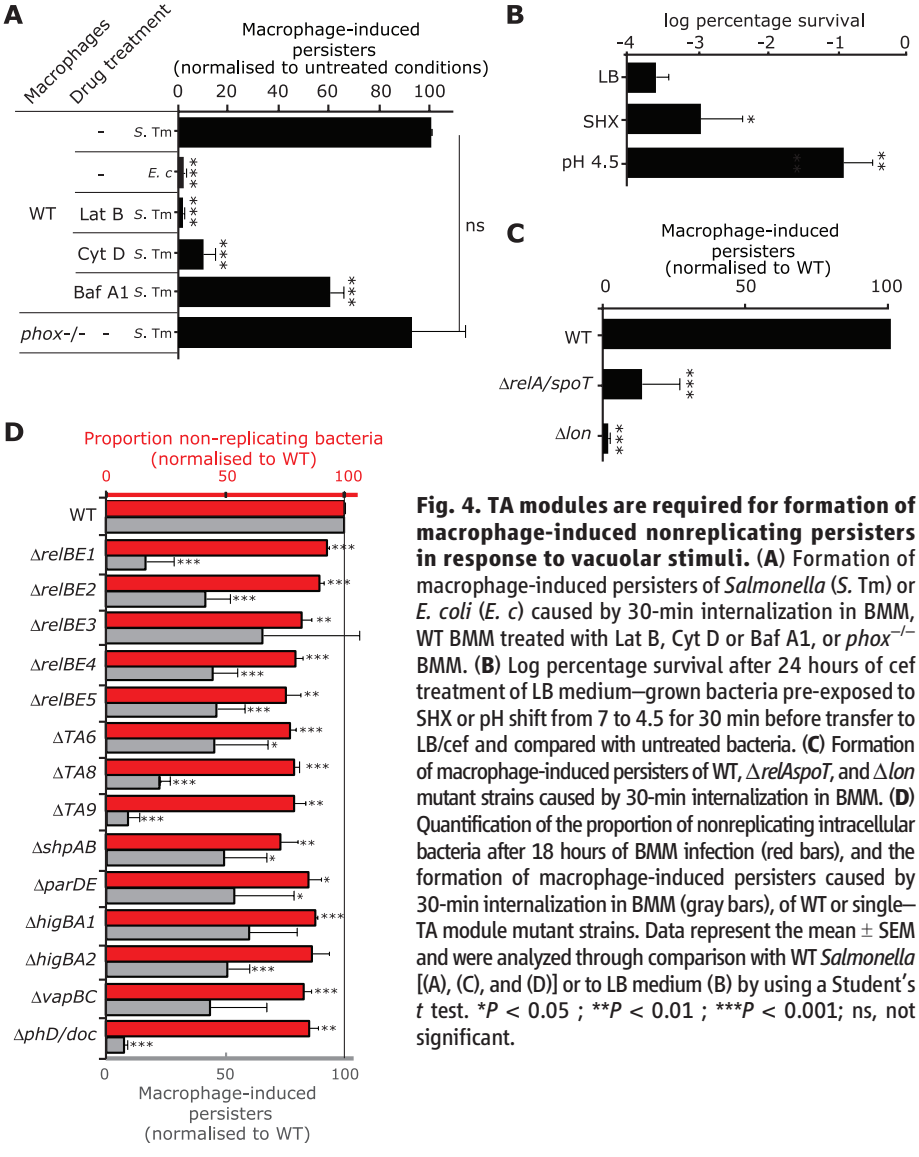


Fig. 4. TA modules are required for formation of macrophage-induced nonreplicating persisters in response to vacuolar stimuli. (**A**) Formation of macrophage-induced persisters of *Salmonella* (*S.* Tm) or *E. coli* (*E. c*) caused by 30-min internalization in BMM, WT BMM treated with Lat B, Cyt D or Baf A1, or *phox*$^{-/-}$ BMM. (**B**) Log percentage survival after 24 hours of cef treatment of LB medium–grown bacteria pre-exposed to SHX or pH shift from 7 to 4.5 for 30 min before transfer to LB/cef and compared with untreated bacteria. (**C**) Formation of macrophage-induced persisters of WT, Δ*relAspoT*, and Δ*lon* mutant strains caused by 30-min internalization in BMM. (**D**) Quantification of the proportion of nonreplicating intracellular bacteria after 18 hours of BMM infection (red bars), and the formation of macrophage-induced persisters caused by 30-min internalization in BMM (gray bars), of WT or single–TA module mutant strains. Data represent the mean ± SEM and were analyzed through comparison with WT *Salmonella* [(A), (C), and (D)] or to LB medium (B) by using a Student's *t* test. *$P < 0.05$; **$P < 0.01$; ***$P < 0.001$; ns, not significant.

Nonreplicating bacteria recovered from macrophages after 24 hours were incubated with naïve macrophages. After re-phagocytosis, ~5% of the population that was metabolically active in the initial host cells resumed growth (Fig. 3C) and may thus be a source of relapsing infection (*9*). These results show that macrophages contain heterogeneous subpopulations of nonreplicating *Salmonella*, including cells that are (i) metabolically inactive (possibly dormant), (ii) metabolically active but which fail to regrow following their release from BMMs, (iii) competent for regrowth in LB medium, and (iv) competent for regrowth in naïve macrophages (Fig. 3D).

Next, we investigated processes required for macrophage-induced persister formation. Activation of BMMs with IFN-γ had little effect on the proportion of persisters (fig. S2). Exposure of *Salmonella* to BMMs that had been pretreated with Latrunculin B (Lat B) or Cytochalasin D (Cyt D) to prevent phagocytosis did not generate more persisters than the basal levels detected in LB medium. This indicated that internalization is required to stimulate macrophage-induced persister formation (Fig. 4A and fig. S5). There was no detectable decrease in macrophage-induced persister frequency obtained from *phox*$^{-/-}$ BMMs that are unable to produce reactive oxygen species (Fig. 4A). However, preventing *Salmonella*-containing vacuole (SCV) acidification with Bafilomycin A1 (Baf A1) caused a significant decrease in persister frequency (Fig. 4A and fig. S5). Transient exposure of *Salmonella* to acidified laboratory medium or serine hydroxamate (SHX) (to induce starvation) (*14*) both enhanced persister formation (Fig. 4B). These results indicate that acidification and probably nutritional deprivation within SCVs (*15*) contribute to formation of persisters (Fig. 4B).

Nonpathogenic *E. coli* K12 persisters are induced at low frequency in laboratory medium by class II toxin-antitoxin (TA) modules (*16*), and their formation was not enhanced by passage through BMMs (Fig. 4A). Activation of the stringent response through the ppGpp synthases RelA and SpoT leads to activation of the Lon protease (*17*, *18*). Lon degrades antitoxins of Class II TA modules, releasing intrabacterial toxins that cause transient growth arrest. As a result, *E. coli lon* mutants produce low levels of persisters in vitro (*18*). In contrast, a *Salmonella lon* mutant had no defect in persister formation when grown in laboratory media (fig. S6, A and B). However, deletion of *Salmonella relA* and *spoT* or *lon* significantly reduced macrophage-induced persister numbers (Fig. 4C). Thus, the Lon-dependent persister induction pathway of *Salmonella* is specifically responsive to conditions encountered within macrophage vacuoles. Analysis of the *Salmonella* genome revealed 14 putative class II TA operons (*19*), all of which were up-regulated from 4- to 30-fold in a *relA*, *spoT*-dependent manner within 30 min of phagocytosis, which is in broad agreement with previous work (fig. S7A) (*20*). Transient acidification of

the culture medium or exposure to SHX also activated the TA modules (fig. S7B).

Single-deletion mutant strains were obtained for each of the TA loci. Although the majority of mutants did not show any impairment of intracellular replication rates, they showed a 10 to 30% reduction in the proportion of nonreplicating bacteria in infected BMM as compared with the WT strain (Fig. 4D and fig. S8). Mutation of TA genes had an even greater effect on persister frequency (Fig. 4D and fig. S9). Thus, after phagocytic uptake 14 class II TA modules were activated by acidification and/or nutrient starvation within the SCV, leading to the rapid formation of nonreplicating persisters.

Because the *Salmonella shpAB* locus has been shown to encode a functional TA module (*21*), we investigated its contribution to persister formation during infection of mice. To do this, groups of 10 animals were inoculated p.o. with an equal mixture of WT and *shpAB* mutant strains. Animals were given enrofloxacin 24 hours later and for a further 5 days, at which time MLNs were extracted to recover persisters. The relative proportions of WT and *shpAB* mutant strains were determined by colony-forming units, and a competitive index (CI) value (*12*) of 0.85 ($P = 0.01$) was obtained. The reduced rate of persister formation by the mutant strain correlated with its enhanced net growth over the wild type in the absence of antibiotic [CI value of 1.83 ($P = 0.05$)]. Together, these experiments show that the *shpAB* TA locus contributes to the generation of persisters in the mouse model of typhoid fever.

Overall, these results reveal several important characteristics of nonreplicating intracellular *Salmonella*. First, all persisters that were detected, both in mice and macrophages, formed within minutes upon infection and failed to replicate. Second, nonreplicating bacteria displayed unexpected phenotypic heterogeneity (Fig. 3D). Third, in contrast to nonpathogenic *E. coli*, the *Salmonella lon*–dependent persister induction pathway responded specifically to the host cell environment. The acidified and nutritionally poor vacuolar environment is also required for the expression of many *Salmonella* virulence genes (*22*), which are required for bacterial replication in macrophages (*7*). Thus, the vacuolar environment stimulates some bacterial cells to initiate replication and others to enter a nonreplicating state in which they are more likely to survive long-term host-induced damage and exposure to antibiotics (fig. S10). The generation of such cell-to-cell heterogeneity is likely to provide a strong selective advantage to *Salmonella* and other bacterial pathogens that encounter the antimicrobial activities of macrophages.

References and Notes

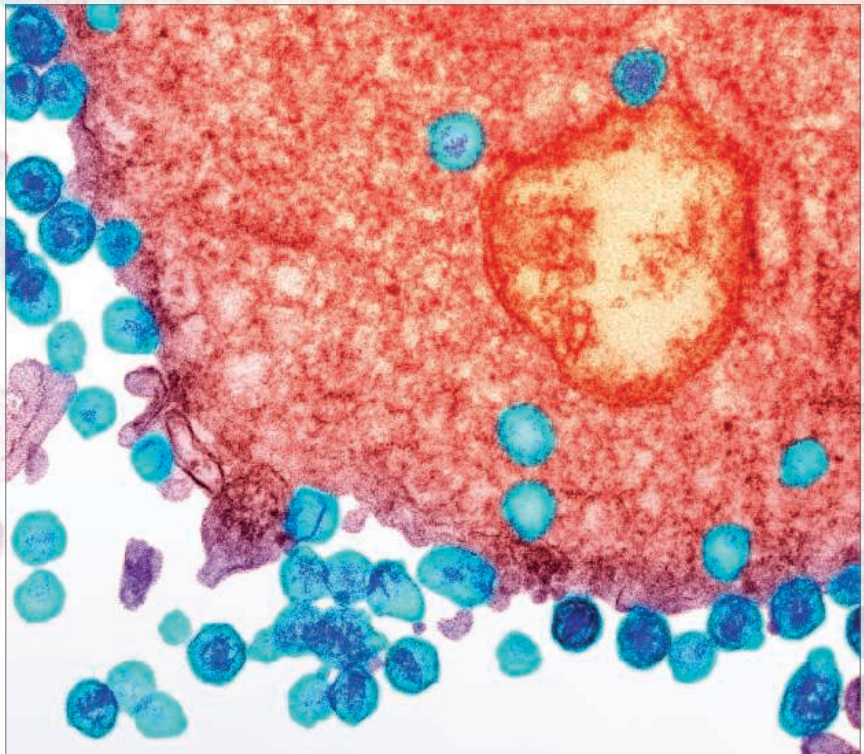
1. N. Q. Balaban, J. Merrin, R. Chait, L. Kowalik, S. Leibler, *Science* **305**, 1622–1625 (2004).
2. J. W. Bigger, *Lancet* **244**, 497–500 (1944).
3. I. Keren, D. Shah, A. Spoering, N. Kaldalu, K. Lewis, *J. Bacteriol.* **186**, 8172–8180 (2004).
4. N. Q. Balaban, K. Gerdes, K. Lewis, J. D. McKinney, *Nat. Rev. Microbiol.* **11**, 587–591 (2013).
5. K. N. Adams *et al*., *Cell* **145**, 39–53 (2011).
6. Y. Wakamoto *et al*., *Science* **339**, 91–95 (2013).
7. S. Helaine *et al*., *Proc. Natl. Acad. Sci. U.S.A.* **107**, 3746–3751 (2010).
8. R. Figueira, K. G. Watson, D. W. Holden, S. Helaine, *MBio* **4**, e00065 (2013).
9. A. J. Griffin, L. X. Li, S. Voedisch, O. Pabst, S. J. McSorley, *Infect. Immun.* **79**, 1479–1488 (2011).
10. A. Richter-Dahlfors, A. M. Buchan, B. B. Finlay, *J. Exp. Med.* **186**, 569–580 (1997).
11. S. P. Salcedo, M. Noursadeghi, J. Cohen, D. W. Holden, *Cell. Microbiol.* **3**, 587–597 (2001).
12. Materials and methods are available as supplementary materials on *Science* Online.
13. E. Rotem *et al*., *Proc. Natl. Acad. Sci. U.S.A.* **107**, 12541–12546 (2010).
14. D. Nguyen *et al*., *Science* **334**, 982–986 (2011).
15. B. Steeb *et al*., *PLOS Pathog.* **9**, e1003301 (2013).
16. E. Maisonneuve, M. Castro-Camargo, K. Gerdes, *Cell* **154**, 1140–1150 (2013).
17. A. Kuroda *et al*., *Science* **293**, 705–708 (2001).
18. E. Maisonneuve, L. J. Shakespeare, M. G. Jørgensen, K. Gerdes, *Proc. Natl. Acad. Sci. U.S.A.* **108**, 13206–13211 (2011).
19. Y. Shao *et al*., *Nucleic Acids Res.* **39** (Database), D606–D611 (2011).
20. S. Eriksson, S. Lucchini, A. Thompson, M. Rhen, J. C. Hinton, *Mol. Microbiol.* **47**, 103–118 (2003).
21. A. Slattery, A. H. Victorsen, A. Brown, K. Hillman, G. J. Phillips, *J. Bacteriol.* **195**, 647–657 (2013).
22. D. M. Cirillo, R. H. Valdivia, D. M. Monack, S. Falkow, *Mol. Microbiol.* **30**, 175–188 (1998).

Acknowledgments: We thank members of the Holden laboratory for comments on the manuscript. We are grateful to A. Ryan and I. Glegola-Madejska for technical support. This research was supported by an Imperial College London Junior Research Fellowship to S.H. and grants to D.W.H. from the Wellcome Trust and Medical Research Council (UK). The data are included in the main and the supplementary figures.

Supplementary Materials

www.sciencemag.org/content/343/6167/204/suppl/DC1
Materials and Methods
Figs. S1 to S10
Tables S1
References (*23*–*28*)

14 August 2013; accepted 21 November 2013
10.1126/science.1244705



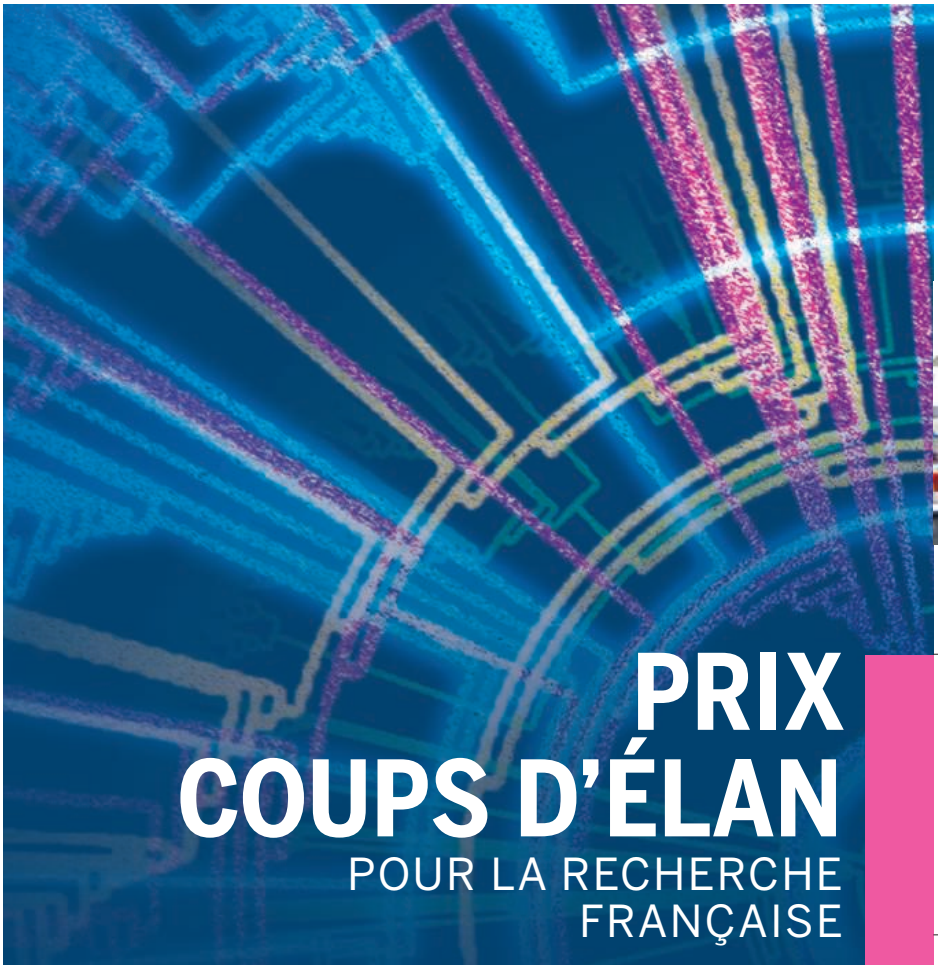
The Scientific World Journal

Hindawi Publishing Corporation
http://www.hindawi.com

Volume 2014

Hindawi

- Impact Factor **1.730**
- **28 Days** Fast Track Peer Review
- All Subject Areas of Science
- Submit at http://www.tswj.com



PRIX COUPS D'ÉLAN
POUR LA RECHERCHE FRANÇAISE



2013 **PRIZE WINNERS**

CÉLINE GALÉS
Reducing adverse effects of GPCR-acting medications and exploring cardiac cell surface architecture in cardiac diseases
INSTITUTE OF CARDIOVASCULAR AND METABOLIC DISEASES
INSERM / PAUL SABATIER UNIVERSITY
TOULOUSE FRANCE

PATRICK LEMAIRE
Understanding the relationship between genetic and morphological evolution
MACROMOLECULAR BIOCHEMISTRY RESEARCH CENTER
CNRS / UNIVERSITY OF MONTPELLIER
FRANCE

OLIVIER NEYROLLES
Developing new tools to combat tuberculosis
INSTITUTE OF PHARMACOLOGY AND STRUCTURAL BIOLOGY
CNRS / PAUL SABATIER UNIVERSITY TOULOUSE
FRANCE

BENOÎT SALOMON
New therapeutic approaches for autoimmune diseases and cancer
CENTER FOR IMMUNOLOGY AND MICROBIAL INFECTION
INSERM / CNRS / UNIVERSITY PIERRE ET MARIE CURIE PARIS
FRANCE

Now in its 13th year, the Bettencourt Schueller Foundation "Prix coups d'élan pour la recherche française" has been awarded to four top-performing French laboratories.

The prize rewards teams specifically chosen for the promising nature of their research programs. It enables them to optimize their infrastructure (construction / renovation of their premises, the purchasing of new equipment) and to receive practical assistance when required.

From the year 2000 onwards, 46 research laboratories, from both the Inserm (French National Institute of Health and Medical Research) and the CNRS (National Center for Scientific Research), have received € 250,000 each. As a direct result, over 500 researchers have been able to benefit from optimal physical working conditions.

Recognised in 1987 as a public interest foundation, the Bettencourt Schueller Foundation was set up by Liliane, André Bettencourt and their daughter Françoise Bettencourt Meyers, in memory of Eugène Schueller, a renowned researcher and chemist. Its goal is to constantly expand the boundaries of knowledge in the life sciences in order to improve public health; to reveal talent and pass on expertise within the field of artistic creativity; and to relieve suffering, combat exclusion and respond to social welfare emergencies.

FONDATION BETTENCOURT SCHUELLER

Fondation Bettencourt Schueller
27-29 rue des Poissonniers • 92200 Neuilly-sur-Seine • France
www.fondationbs.org • Contact: sciences@fondationbs.org

théra • Photo: ©Loubaton/CAPA



See how we're shaping the lab of the future at booth #405

At Tecan, we believe that the most valuable assets in any lab are the scientists. By starting with people rather than experiments, we're developing equipment that not only improves performance but also ignites imaginations.

By delivering:
- true 'walk away' levels of automation
- ready-to-go application and solution packages
- imminently flexible solutions

Come and see how we'll shape the laboratory of the future. Visit us at booth #405.

www.tecan.com

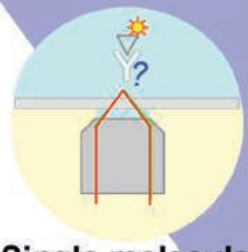
TECAN.

© 2014, Tecan Trading AG, Switzerland, all rights reserved. For disclaimer and trademarks please visit www.tecan.com

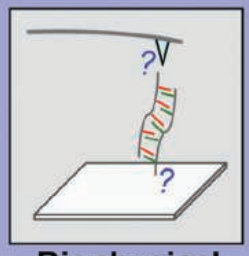
MicroSurfaces, Inc.
Website: http://proteinslides.com
E-mail: info@microsurfacesinc.com

How do I link bio- or organic molecules to a solid surface?

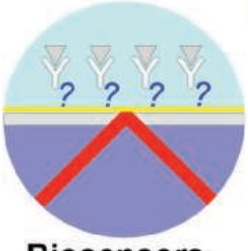
Save hundreds of hours and quickly turn your ideas into breakthrough results.



Single molecule microscopy



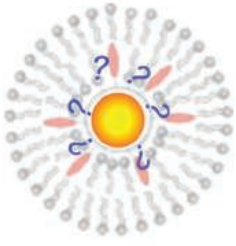
Biophysical measurements



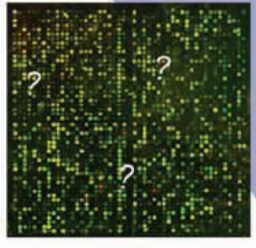
Biosensors



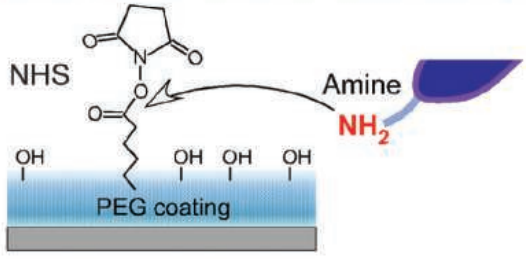
Microfluidics

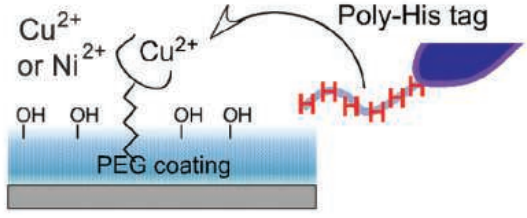


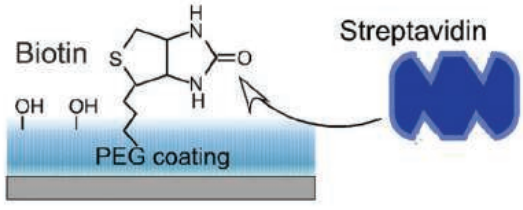
Nanoparticles

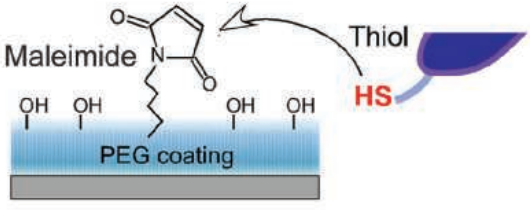


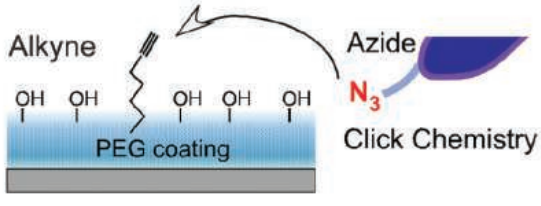
microarrays











Join thousands of researchers who have already discovered the perfect answer from MicroSurfaces' technologies.

***Products & Services*:**

- *ZeroBkg*® high density poly-ethylene glycol (PEG) brush coatings on a variety of surfaces, including standard glass coverslips & slides, quartz coverslips & slides, gold SPR sensors, ITO slides & chips, silicon wafers & chips, nanoparticles, or any customer surface.
- Surface functionalities include **PEG** for low background, **Biotin** for streptavidin/biotin linkage, **Chelated Cu^{2+}** or **Ni^{2+}** for His-tags, **NHS** for $–NH_2$ functional group, **Alkyne** for azide tags via Click chemistry, **Maleimide** for–SH group, & many more.
- Other customer functionalities, such as **silanes**, **thiols**, **acids**, **amines**, **poly-L-lysine**, **dextran**, supported **lipid bilayers**, etc.

1 West Forest Ave, Englewood, NJ 07631, USA. Phone: (201) 408-5596: Fax: (201) 408-5797

Deadline March 1

Science Translational Medicine AAAS

Science Translational Medicine is pleased to announce the

AAAS Martin and Rose Wachtel Cancer Research Award

This annual award honors early-career cancer researchers who have performed outstanding work in the field of cancer research. Nominees must have received their PhD or MD within the last 10 years. The award winner will be invited to deliver a public lecture on his or her research and will receive a cash award of $25,000. The award winner's Perspective will be published in *Science Translational Medicine*.

Call for Nominations for 2014 Award

Due by March 1st, 2014

Nomination packages must include the following materials, written in English:

- A letter describing the nominee's significant contributions to cancer research, including supporting publications. The letter should explain how the candidate's research promises to make a lasting impact on the cancer field. (Applicants may nominate themselves.)
- A letter of support from another scientist who knows the applicant's work.
- The nominee's curriculum vitae.
- A Perspective (1500 words maximum, 1 figure) written by the nominee describing their research project and explaining how it advances our understanding of cancer. The research described in the Perspective must be in the field of cancer and the nominee must have performed or directed the work within the last 10 years.

Submit nominations to **wachtelprize@aaas.org** and put "Wachtel Award Nomination" in the subject line. For more information see: **http://www.aaas.org/aboutaaas/awards/wachtel/.**

This award is funded by an endowment established through a bequest from Martin Wachtel and is presented by Science Translational Medicine.

AAAS *Travels*

Mystique of MOROCCO



Magical moments happen as you explore the Mystique of Morocco! From the capital of Rabat to fantastic Volubilis... the Atlas Mountains and Sahara Desert... Marrakech to the ancient Phoenician coastal city of Magador. Explore kasbahs, medinas and souks, ride camels in the Sahara desert, visit Roman ruins, and learn about a 1,200-year-old university heritage important to all of Western Civilization! $3,995 + air.

For a detailed brochure, please call (800) 252-4910

All prices are per person twin share + air

BETCHART EXPEDITIONS Inc.

17050 Montebello Rd, Cupertino, CA 95014
Email: AAASInfo@betchartexpeditions.com
www.betchartexpeditions.com

STAY INFORMED! STAY CONNECTED!

Get more from your AAAS membership



Are you currently registered to receive e-mails from AAAS and *Science*?

E-mail is the primary way that AAAS communicates with our members about AAAS programs, new member benefits, invitations to special events, and, of course, the latest news and research being published in *Science*.

Sign up today to receive e-mails from AAAS and ensure that you are getting the most out of your membership and *Science* subscription.*

To get started visit: **promo.aaas.org/stayconnected** You'll need your AAAS Member number. Find it above your name on your *Science* mailing label.

Don't miss a thing. Sign up for e-mail communications from AAAS today!

Science AAAS

*AAAS follows CAN-SPAM and European Safe Harbor guidelines for protecting your privacy. We will never sell your e-mail address and you can opt-out of receiving e-mails at any time.

BD High Quality Research Reagents

Everyday Low Prices with Institutional Discounts.



BD

Helping all people live healthy lives

Lower prices are already in your basket.



Before you go chasing after the latest "limited time offer," you may want to check your everyday low price on BD Biosciences research reagents available through your institutional buying agreement.

Your institutional discount applied to our recently reduced list prices makes your research reagent purchases easier than ever. Best of all you'll have the confidence of using BD high quality reagents in your research—all without spending your time researching promo codes or shopping for discounts.

You also can take full advantage of the wide BD portfolio of research reagents, including innovative new BD Horizon™ Brilliant Violet™ and Brilliant Ultraviolet™ dyes and leading tools to enable your multicolor panel design.

Not already receiving an institutional discount? Your sales representative is ready to help you get the best value for your research.

Visit **bdbiosciences.com/go/myprice.**

For Research Use Only. Not for use in diagnostic or therapeutic procedures.
BD, BD Logo and all other trademarks are property of Becton, Dickinson and Company. © 2013 BD
23-15938-00

BD Biosciences
2350 Qume Drive
San Jose, CA 95131
bdbiosciences.com

ULTRA X-RAY MICROSCOPE



The new X-ray microscopy (XRM) solution increases throughput for 3-D imaging at the nanoscale, by up to 10 times. Using a series of technical innovations to achieve better contrast, and in turn faster acquisition, the new Xradia 810 Ultra revolutionizes the X-ray imaging model in scientific and industrial research labs worldwide. Xradia 810 Ultra operates at 5.4 keV, a lower X-ray energy that delivers better contrast and image quality for many materials. Contrast improves significantly as these lower-energy X-rays are absorbed more strongly, enabling high-quality tomographies to be completed at vastly reduced imaging times. The Xradia 810 Ultra's architecture was engineered around this new source energy, using innovative optics to extend the capabilities of the Xradia Ultra family, the only lab-based nondestructive imaging solutions to achieve resolution down to 50 nm. Additionally, Xradia 810 Ultra leverages both absorption and Zernike phase contrast and advanced optics adapted from the synchrotron to deliver industry-leading resolution and contrast.

Carl Zeiss

For info: +49-3641-64-3949 | www.zeiss.com

2 mL DEEP-WELL PLATE

The first 96 round deep-well plate that genuinely delivers 2 mL liquid capacity/well in an automation compatible SLAS/ANSI footprint. The revolutionary "common wall" design provides a full 2 mL round well with a round bottom within a 45 mm height limit, thus ensuring full compatibility with most plate handling equipment. Unlike other 2 mL deep-well plates that typically offer just 1.80–1.90 mL/well, the new Porvair plate enables labs involved with fraction collecting, compound storage, plate replication, and mixing applications the chance to use the full 2 mL well capacity without compromise. Manufactured under Class 10,000 conditions from ultrapure grade polypropylene, Porvair's new 2 mL 96 deep-well plates are certified as RNase/DNase free and contain no measurable contaminants that could otherwise leach out and affect the sample. For sterile biological applications, Porvair 2 mL 96 deep-well plates are available irradiated.

Porvair Sciences

For info: +44-(0)-1978-666240 | www.porvair-sciences.com

DIGITAL SENSORS

The UniCond 4-E digital sensors are four-electrode sensors designed to provide highly accurate measurement across a very wide range: a single UniCond 4-E measures from pure potable water to acid or base concentrations. Applications for the UniCond 4-E series include Clean-in-Place and desalination processes, deionization regeneration, industrial processing, and wastewater treatment. Analog conductivity sensors are prone to signal degradation caused by sensor-to-transmitter cable resistance and capacitance. Technology incorporated into the UniCond sensors that convert the analog signal into a robust and reliable digital signal solves this issue. In addition, the sensors contain Mettler Toledo's Intelligent Sensor Management (ISM) concept. Features of ISM include Plug and Measure start up at the measurement point and sensor diagnostics for proactive maintenance. In addition, the UniCond 4-E can be calibrated without extraction from the process. This makes the sensors compliant with United States Pharmacopeia (USP) guidelines.

Mettler Toledo

For info: 800-352-8763 | www.mt.com/unicond-4e

FLUORESCENCE CELL COUNTER

The next generation automated cell counter, Luna-FL, is a breakthrough for life science researchers. By integrating dual fluorescence and bright field optics in one instrument, the Luna-FL provides researchers with maximum flexibility for cell counting without being limited by cell type. Researchers are rapidly moving from using glass hemocytometers to using automated cell counters. Various automated cell counters are available, but many of these instruments are not flexible or accurate enough to accommodate a wide range of cell types. Traditionally, primary cells such as peripheral blood mononucleated cells, splenocytes, and yeast cells have been difficult to count using conventional automated cell counters. The Luna-FL fluorescence cell counter is more compact and considerably less expensive compared with the other fluorescence cell counters currently available. The Luna-FL features dual fluorescence optics for sensitive cell analysis, trypan blue stained cell counting with bright field optics, GFP expression analysis, cell size gating, and an interactive user interface.

Logos Biosystems

For info: 703-622-4660 | www.logosbio.com

MICROPLATE HOTEL

The new microplate hotel is for use with the CompacT SelecT automated cell culture system and is compatible with LiCONiC plate incubators. It allows users to transfer entire stacks of plates between the CompacT SelecT and LiCONiC incubator-based screening systems, thus saving scientists' time and improving the efficiency of supplying consistent quality cells to increase throughput in cell-based screening operations. The new microplate hotel, developed in conjunction with LiCONiC AG, is compatible with their STR incubator range. This ensures researchers can significantly reduce plate transfer times and reduce the risks associated with manual plate relocations. The addition of the new LiCONiC-compatible plate hotel extends the functionality of CompacT SelecT to provide fully automated aseptic cell culture processing for a continuous supply of consistent quality cells, thereby increasing productivity in cell-based screening programs.

TAP Biosystems

For info: +44-(0)-1763-227200 | www.tapbiosystems.com

Electronically submit your new product description or product literature information! Go to **www.sciencemag.org/products/newproducts.dtl** for more information.

Newly offered instrumentation, apparatus, and laboratory materials of interest to researchers in all disciplines in academic, industrial, and governmental organizations are featured in this space. Emphasis is given to purpose, chief characteristics, and availability of products and materials. Endorsement by *Science* or AAAS of any products or materials mentioned is not implied. Additional information may be obtained from the manufacturer or supplier.

AAAS 2014 ANNUAL MEETING

13-17 FEBRUARY • CHICAGO

MEETING GLOBAL CHALLENGES:
DISCOVERY AND INNOVATION

Advance registration is open until 22 January. Register and book housing through AAAS for reduced rates.

The full scientific program is available online.

www.aaas.org/meetings



AAAS, publisher of *Science*, thanks the sponsors and supporters of the 2014 Annual Meeting

European Commission

SUBARU

ACS Chemistry for Life®
American Chemical Society

HELMHOLTZ ASSOCIATION

the Lemelson foundation
improving lives through invention

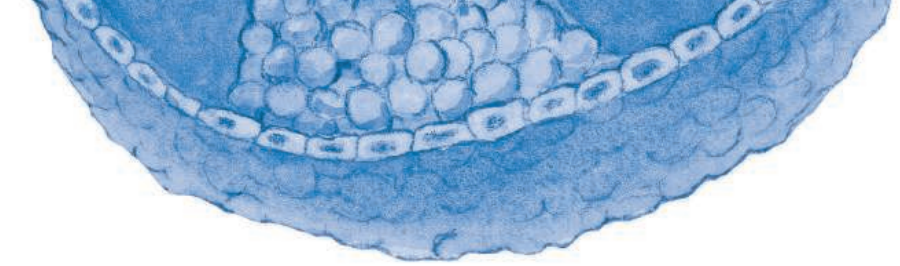
AMERICAN ACADEMY OF ARTS & SCIENCES

AAAS thanks

THE KAVLI FOUNDATION

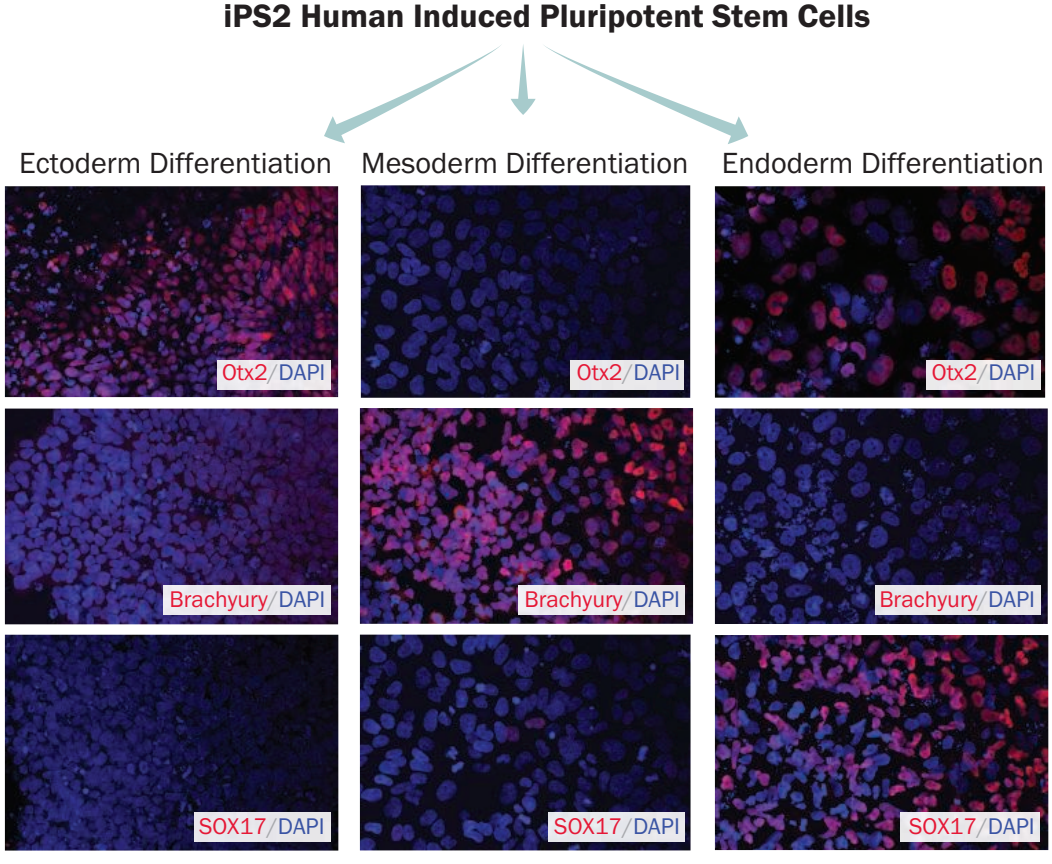
for its generous support of
the Science Journalism Awards

Sponsors as of 15 December 2013



Move Forward with Confidence

Verify stem cell potency with Functional Identification Kits from R&D Systems



Verification of iPS2 human induced pluripotent stem cells by directed differentiation using R&D Systems Human Pluripotent Stem Cell Functional Identification Kit.

Kits are available for verification of pluripotent, mesenchymal, and neural stem cells

- ✓ Save valuable time and reagents
- ✓ Reduce experimental variation
- ✓ Functionally verify stem cell potency

Find the right tools to verify potency by stem cell type

RnDSystems.com/stemcellverification

R&D SYSTEMS®

Science Careers online @sciencecareers.org



Science Careers Advertising

For full advertising details, go to ScienceCareers.org and click For Employers, or call one of our representatives.

Tracy Holmes
Worldwide Associate Director
Science Careers
Phone: +44 (0) 1223 326525

THE AMERICAS
E-mail: advertise@sciencecareers.org
Fax: 202-289-6742

Tina Burks
Phone: 202-326-6577

Marci Gallun
Phone: 202-326-6582

Online Job Posting Questions
Phone: 202-312-6375

EUROPE / INDIA / AUSTRALIA / NEW ZEALAND / REST OF WORLD
E-mail: ads@science-int.co.uk
Fax: +44 (0) 1223 326532

Axel Gesatzki
Phone: +44 (0)1223 326529

Sarah Lelarge
Phone: +44 (0) 1223 326527

Kelly Grace
Phone: +44 (0) 1223 326528

JAPAN
Yuri Kobayashi
Phone: +81-(0)90-9110-1719
E-mail: ykobayas@aaas.org

CHINA / KOREA / SINGAPORE / TAIWAN / THAILAND
Ruolei Wu
Phone: +86-1367-1015-294
E-mail: rwu@aaas.org

All ads submitted for publication must comply with applicable U.S. and non-U.S. laws. *Science* reserves the right to refuse any advertisement at its sole discretion for any reason, including without limitation for offensive language or inappropriate content, and all advertising is subject to publisher approval. *Science* encourages our readers to alert us to any ads that they feel may be discriminatory or offensive.

Science Careers
From the journal *Science* AAAS

ScienceCareers.org

Director, UW Carbone Cancer Center

University of Wisconsin School of Medicine and Public Health, Madison, Wisconsin

The UWSMPH invites applications and nominations for the position of Director of the UW Carbone Cancer Center (UWCCC). The Center has approximately 250 full and part-time faculty members, as well as a robust panel of senior scientists and staff. They provide outstanding clinical service, as well as nationally renowned research and educational programs.

UW-Madison has a long and rich history as an international leader in basic, translational and clinical cancer research reflected in its history of two NCI-designated and -funded cancer research centers. UWCCC has received continuous NCI funding since 1973 when it was one of the first six NCI comprehensive cancer centers and consolidated with McArdle Laboratory for Cancer Research (NCI funded since 1946) in 2001. The UWCCC has approximately 250 faculty members who generate >$80 million cancer-related peer-reviewed funding annually.

The UWCCC offers a complete and comprehensive array of clinical services at thirteen sites, including seven outside of Madison. The Center provides education and training programs at multiple levels, including medical student, graduate student, resident, and post-doctoral fellowship.

We seek a recognized leader with an outstanding academic background in cancer research, strong clinical and research credentials, demonstrated commitment to education, experience in mentoring junior faculty, and proven leadership and management skills. The Director will provide professional and administrative leadership of the highest quality to this distinguished center in its teaching, research, and clinical missions, and would be responsible for leadership in submitting the renewal of cancer center core grant in 2017.

The successful candidate will have a compelling vision for the future of cancer research in a leading academic medical center. Candidates must have an MD or PhD or MD/PhD degree or equivalent, evidence of sustained high-level leadership experience in an academic setting, a history of established peer-reviewed cancer research funding, and accomplishments as a clinical, basic, or translational, or population health scholar and teacher, that meet the standards for a tenured faculty appointment at the University of Wisconsin-Madison.

Send a letter of application or nomination, with CV, to:

Carol Diamond, MD and Richard Page, MD Co-Chairs of the UW Carbone Cancer Center Director Search Committee, Faculty HR, 4150 HSLC, 750 Highland Avenue, Madison, WI, 53705-2111, leadership_recruitments@med.wisc.edu

To receive full consideration, applications should arrive by **April 1, 2014**.

Unless confidentiality is requested in writing, information regarding applicants must be released upon request. Finalists cannot be guaranteed confidentiality. Wisconsin Caregiver Law applies. The University of Wisconsin is an equal opportunity, affirmative action employer. Applications from minorities and women are encouraged. For more information: www.med.wisc.edu, http://www.uwhealth.org/cancer-for-researchers/uwccc/28373

UNIVERSITY OF WISCONSIN-MADISON
SCHOOL OF MEDICINE AND PUBLIC HEALTH

Nanjing Agricultural University
Faculty Recruitment Notice

Nanjing Agricultural University(NAU) welcomes top talent in research and academics for full-time positions.

NAU is a national key university under the direct administration of the Ministry of Education of the People's Republic of China. NAU is a *Project 211* institution and one of the Innovation Platforms for Outstanding Disciplines under the *985 Excellence Initiative Project* launched by China's Ministry of Education.

● **Eligible applicants:**

Tenured professors at overseas universities or young scholars with PhDs from overseas universities.

Candidates should be involved in one or more of the following research areas: crop science, agriculture resource utilization and environment sciences, plant protection, veterinary medicine, horticulture, biology, agricultural and applied economics, land resource management, food science, history of science and civilization, ecology, animal husbandry, agrostology, public administration, industrial economics, business administration, finance, agricultural and bioinformatics, marine biology, and modern agriculture equipment engineering.

● **Employee benefits:**

1. Initial research funding ranging from RMB 500,000 to 10,000,000 will be provided, depending on discipline and applicants' status. Laboratory and office will be arranged.
2. NAU also provides housing and a relocation allowance.
3. Special support will be provided to each leading researchers, including a full-time administrative secretary, assistance in assembling a research team, and priority in recommendations for research funding and government talent schemes.

Tel: (86) 25-84399039 Ms. Chen Zhiying

E-mail: rcb@njau.edu.cn

Website: http://www.njau.edu.cn

Faculty Positions Available in Southwest University, Chongqing, China

Southwest University is a national key university of the "211" project directly under the Ministry of Education. It is located in Chongqing, the youngest municipality of China. The university hosts approximately 50,000 students, covering undergraduate, postgraduate and other programs. **For more detailed information, please visit the website: http://www.swu.edu.cn/#**

Applications for full-time professors, associate professors and distinguished scientists are welcome. Competitive salaries and start-up funds will be provided to successful candidates, in line with the national Recruitment Program of Young Experts.

The Recruitment Program of Young Experts (i.e. the Plan for Recruiting 1,000 Professorship for Young Talents): The candidates are required to be under the age of 40 and have obtained a PhD degree in a world-renowned university with at least 3 years of research experience abroad, or have obtained a PhD degree in Mainland China with at least 5 years of research and teaching experience abroad. Special offers will be granted to those who have excellent research achievements during their doctoral study.

Further information is available at http:// renshi.swu.edu.cn/rcgzbgs/ The Talents Recruitment Office, Southwest University,Beibei, Chongqing 400715, P. R. China. 0086-23-68254265.

Please kindly send applications or nominations in the form of an application letter enclosing a current CV to rencai@swu.edu.cn.

Faculty and Postdoctoral Positions at Peking-Tsinghua Center for Life Sciences

Applications are invited for Principal Investigator (PI) and postdoctoral positions at Peking-Tsinghua Center for Life Sciences (http://www.cls.edu.cn/english/).

We look for the best scientists in all areas of life sciences, with emphasis in the following areas: bioinformatics, biochemistry and biophysics, bioengineering, cancer biology, epigenetics, cell biology, chemical biology, computational biology, microbiology and virology, human genetics, genetics, genomics, molecular medicine, molecular neuroscience and cognitive neuroscience, modern imaging, physiology, plant biology, synthetic biology, and systems biology.

Each PI holds a joint (tenure track or tenured) appointment in one of the departments or schools at Peking University (such as Chemistry, Computer Science, Engineering, Life Sciences, Mathematics, Medicine, Physics and Psychology). Peking University provides excellent interdisciplinary research environment and outstanding core research facilities. We offer an internationally competitive package. The kindergarten and the primary school attached to Peking University will be available to the children of all Center PIs and postdocs.

PI application materials (with cover letter, summary of research interests, CV and less than 5 representative publications, all in a single PDF file) should be sent to Ms. Wei Xiao (gsmkyb@pku.edu.cn), to whom you should also ask your references to send in their recommendation letters. Postdoc applicants should indicate in the cover letter 1 or 2 laboratories as your intended host, and send application materials to Ms. Siyuan Gong (clspostdoc-peking@cls.edu.cn). Applications from both Chinese and non-Chinese nationals will be evaluated on an equal opportunity basis.

DIRECTOR
Arkansas Children's Nutrition Center

We are seeking to recruit a new Director of the Arkansas Children's Nutrition Center (ACNC) in Little Rock, AR. The Director will be a Professor (Tenure Track) in the Department of Pediatrics and Chief of the Division of Developmental Nutrition at the University of Arkansas for Medical Sciences (UAMS) College of Medicine.

Requirements include a PhD or MD degree and a national reputation in nutrition-related research. He/she should have demonstrated excellence in research as evidenced by accomplishments, such as a long-standing record of nationally competitive funding at the R01 level through NIH; an excellent record of publications in high quality peer-reviewed scientific journals; NIH Study Section Membership; and National Awards. The successful candidate must also have proven and effective management and interpersonal skills necessary to direct a large, interdisciplinary national human nutrition research program.

The ACNC is one of six Human Nutrition Research Centers funded by the USDA/ARS and is housed in a private research building on the campus of Arkansas Children's Hospital, which is one of the nation's largest state-of-the-art children's hospitals and the primary pediatric research and teaching site of UAMS. The position carries a competitive salary and benefits package and will remain open until February 15, 2014.

Interested parties should submit their curriculum vitae and full contact information via email to **RFJ@uams.edu** or mail to: **Richard Jacobs, MD, FAAP, Search Committee Chair, 13 Children's Way Slot 842, Little Rock, Arkansas 72202-3591.**

UAMS is an inclusive Equal Opportunity and Affirmative Action Employer and is committed to excellence.

AURA SOLICITS APPLICATIONS AND NOMINATIONS FOR THE PRESIDENT OF AURA

The Association of Universities for Research in Astronomy (AURA) seeks a new President, with the aim of filling this position by February 2015. AURA is a consortium of universities and educational institutions that operates world-class astronomical observatories on behalf of the National Science Foundation (NSF) and the National Aeronautics and Space Administration (NASA). AURA's mission is *"To promote excellence in astronomical research by providing access to state-of-the-art facilities."*

AURA acts as the Managing Organization for the National Optical Astronomy Observatory (NOAO), the National Solar Observatory (NSO), the International Gemini Observatory, the Large Synoptic Survey Telescope (LSST) Construction Project, and the Space Telescope Science Institute (STScI).

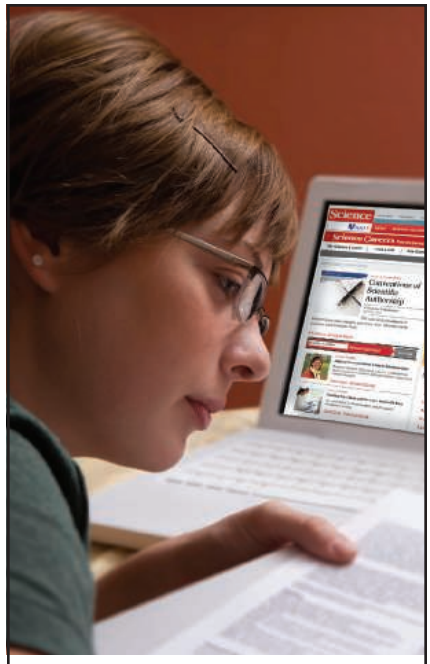
The President discharges all roles and responsibilities described in the AURA Policies and Procedures Manual (see ***www.aura-astronomy.org/about.asp?aboutType=policies***). S/he is also responsible for all AURA programmatic issues, including those at STScI, NOAO, NSO, Gemini, and concerning construction of LSST. These responsibilities relate to top-level AURA management commitments and policies, promotion of the mission of AURA and its centers, and identifying new business and scientific opportunities for AURA.

The AURA Corporate Office is located in Washington D.C. This is designated as the primary duty location for the President, though candidates should expect to travel frequently in the conduct of AURA business.

Candidates for the position of AURA President should have demonstrated strong leadership in science and administration and have an established record of achievement in those areas. Candidates should also have demonstrated talent for management, combined with skill in federal, institutional and international relations. AURA is inviting applications for this position and is also soliciting nominations from the community-at-large. Applications and nominations will be accepted until the position is filled. All complete applications received by **May 1, 2014** will be given full consideration. All applications will be held in confidence. Applications must include: a curriculum vitae, information on relevant experience and accomplishments, and the candidate's vision for leading AURA and/or the future evolution of AURA. Shortly after May 1, candidates should be prepared to submit the names of three professional references who have agreed to offer assessments.

Nominations, applications, and questions related to this search should be emailed to **presidentsearch@aura-astronomy.org**. Alternatively, written nominations and/or applications may be sent to: **Dr. Bruce W. Carney, Chair, Presidential Search Committee c/o AURA, 1212 New York Avenue NW, Suite 450, Washington, DC 20005.** Information and updates regarding the President position and all aspects of this search are available on AURA's website: **www.aura-astronomy.org**.

Women and minorities are encouraged to apply. AURA is an EOE/AA/F/D/V Employer.



AAAS is here –
helping scientists achieve career success.

Every month, over 400,000 students and scientists visit ScienceCareers.org in search of the information, advice, and opportunities they need to take the next step in their careers.

A complete career resource, free to the public, *Science* Careers offers a suite of tools and services developed specifically for scientists. With hundreds of career development articles, webinars and downloadable booklets filled with practical advice, a community forum providing answers to career questions, and thousands of job listings in academia, government, and industry, *Science* Careers has helped countless individuals prepare themselves for successful careers.

As a AAAS member, your dues help AAAS make this service freely available to the scientific community. If you're not a member, join us. Together we can make a difference.

To learn more, visit
aaas.org/plusyou/sciencecareers

AAAS + U = Δ

WOMEN IN SCIENCE

forging new pathways in green science



Read inspiring stories
of women working in
"Green Science"
who are blending
a unique combination of
enthusiasm for science
and concern for others
to make the world
a better place.

Download this free booklet ScienceCareers.org/LOrealWiS

Science
AAAS

FOR WOMEN IN SCIENCE
L'ORÉAL FOUNDATION

This booklet is brought to you by the
AAAS/*Science* Business Office
in partnership with the
L'Oreal Foundation

ÉCOLE POLYTECHNIQUE
FÉDÉRALE DE LAUSANNE

Dean of the School of Life Sciences

at the Ecole polytechnique fédérale de Lausanne (EPFL)

EPFL – the Swiss Federal Institute of Technology Lausanne – is a preeminent European institution of science and engineering. Engaged regionally, nationally and internationally, its campus provides an exciting intellectual community within the French-speaking region of Switzerland, on the shores of Lake Geneva, at the foot of the Alps. For more information about EPFL, please visit www.epfl.ch

The School of Life Sciences was created within EPFL to foster strong interactions, both in terms of teaching and research, with the Schools of Engineering, of Basic Sciences and of Computer and Communication Sciences leading to highly innovative transdisciplinary research. The School of Life Sciences aims at the highest standards, under the auspices of some fifty international faculty members, approximately 700 bachelor and master students, 200 PhD candidates and 160 postdoctoral fellows. Research is supported by high-end technological platforms, and funded through public and private sources including the Swiss Confederation, the European Union, private foundations, and industrial partners. Additional information about the School of Life Sciences is available at http://sv.epfl.ch

Reporting to the President as a member of EPFL's senior administration, the Dean provides vision and leadership across the School's teaching and research activities, manages its corporate business and administrative responsibilities, and represents the School at the campus, regional, national and international levels.

The successful candidate will be an inspirational leader with outstanding achievements in research, teaching and academic community service, demonstrated managerial capabilities in a university setting, and evident collegial skills. The successful candidate will be committed to promote interdisciplinary teaching and research, with the bandwidth to enthusiastically promote the broad scope of research endeavors in the School. Experience in organizing collaborative teams and programs, involving both internal and external partners, will be an important asset. The position offers competitive personal compensation, tenure at the full professor level, and a foundation of financial support for the candidate's research program.

Screening of applications will start on **February 15th, 2014** and will continue until the position has been filled. Please submit a curriculum vitae, a vision statement and the names of up to five professional references on the following website:
https://academicjobsonline.org/ajo/jobs/3741.

Inquiries, nominations, and expressions of interest can be addressed to:

Prof. Gisou van der Goot
Chair of the Search Committee
E-mail: gisou.vandergoot@epfl.ch

EPFL is committed to expanding the ranks of women on its faculty, and qualified women are enthusiastically encouraged to apply.

E.O. WILSON
BIODIVERSITY SYMPOSIUM
April 22-24, 2014
The University of Alabama
Tuscaloosa, AL, USA



Registration: www.biodiversity.ua.edu

Beginning on Earth Day at The University of Alabama

Join Dr. Edward O. Wilson and international biodiversity experts for three days of research briefings and forums on the state and future of biodiversity on our planet.

Featuring the international release of Dr. Wilson's new book, *A Window on Eternity: Gorongosa National Park, Mozambique*.

Distinguished Speakers

E. Virginia Armbrust
P. Dee Boersma
R. Scot Duncan
Ryan Earley
Scott V. Edwards
Harry W. Greene
Juan M. Lopez-Bautista
Jonathan B. Losos
Meg Lowman
D. Bruce Means
Michael B.A. Oldstone
Richard A. Richards
Leslie J. Rissler
Sahotra Sarkar
Diana H. Wall
Edward O. Wilson

Join Dr. Wilson and the College of Arts and Sciences as we explore biodiversity from a range of perspectives: biological, evolutionary, cultural, and philosophical.

Registration: www.biodiversity.ua.edu

THE UNIVERSITY OF ALABAMA
COLLEGE OF ARTS AND SCIENCES

Join the Conversation!

Twitter is a great way to connect with AAAS members and staff about the issues that matter to you most. Be a part of the discussion while staying up-to-date on the latest news and information about your personal member benefits.

Follow us @AAASmember and join the conversation with #AAAS

AAAS MemberCentral
MemberCentral.aaas.org

MONTANA STATE UNIVERSITY BOZEMAN

Assistant/Associate Professor Department of Microbiology and Immunology

An outstanding researcher and instructor is sought to establish a nationally competitive research program in the Department of Microbiology and Immunology at Montana State University (MSU) and teach in a new, cooperative veterinary medical education program with Washington State University School of Veterinary Medicine. Recruitment for this position (14-227) is concurrent with the recruitment for another recently listed position at MSU (14-226), and comes with a competitive institutional salary (9 months) and a generous start-up package. State-of-the-art facilities for flow cytometry, cell biology, molecular sciences, and pathogen containment (BSL-3) are available in support of the successful candidate's research program. Expertise in neuroimmunology is emphasized; however, expertise in other disciplines within the veterinary medical education program will also be considered, such as cell physiology, pathology/histology, neurobiology, immunology/infectious disease and anatomy. The successful candidate will be expected to mentor graduate and undergraduate students, and will also be responsible for providing service as applicable to the department, college, university, and scientific community. Requirements and preferred qualifications, as well as application procedures can be found at: **www.montana.edu/jobs/faculty/14-227**.

Interested applicants should send a letter of application addressing each of the required and preferred qualifications, as well as items listed for a successful candidate in the vacancy announcement (14-227), and a statement of specific research focus and objectives (2 page maximum), a statement of teaching experience and philosophy (2 page maximum), a current curriculum vitae, and the contact information of five professional references. Electronic submissions in PDF format are preferred, and must have the applicant's signature on the letter of application. Submit materials to: **Assistant/Associate Faculty Search Committee, c/o Cheryl Johnson, Montana State University, PO Box 173610, Bozeman MT 59717-3610, (406) 994-4706; cherylj@montana.edu**.

Montana State University values diverse perspectives and is committed to building a multicultural work force. We strongly encourage women, racial/ethnic/gender minorities, persons with disabilities, and veterans to apply. MSU is responsive to the needs of dual career couples and is dedicated to work-life integration. AA/ADA/EEO/VetPref Employer.

SAINT LOUIS UNIVERSITY

The Sylvia N. Souers Endowed Chair In basic, clinical or Translational Neuroscience

The Department of Neurology and Psychiatry at Saint Louis University, a Catholic, Jesuit institution dedicated to student learning, research, health care and service, is seeking a distinguished physician – scientist for the Sylvia N. Souers Endowed Chair in Neuroscience (basic, clinical or translational).

The candidate must be a well-funded senior investigator with an MD or MD/PhD and board certified in neurology or psychiatry. The candidate must have an excellent track record of research and publication in neuroscience consistent with appointment at the rank of professor with tenure. The appropriate recruitment package will be provided, including laboratory space and junior faculty positions if necessary. The successful candidate will spend the majority of their time in research activities including mentorship of residents and junior faculty, along with some clinical work in neurology or psychiatry or a subspecialty of either of those brain specialties.

Interested candidates must apply online at **http://jobs.slu.edu** as well as forward applications by both email and regular mail to:

Henry A. Nasrallah, MD
Sydney W. Souers Professor and Chair
Department of Neurology and Psychiatry
Saint Louis University School of Medicine
1438 S. Grand Blvd., Suite 105
St. Louis, MO 63104
hnasral@slu.edu

Saint Louis University is an Affirmative Action/Equal Opportunity Employer (AA/EOE) and encourages nominations of and applications from women and minorities.

UNIVERSITY OF CAMBRIDGE

www.jobs.cam.ac.uk

Li Ka Shing Professorship of Oncology

Department of Oncology

The Board of Electors to the Li Ka Shing Professorship of Oncology invite applications for this Professorship from persons whose work falls within the general field of cancer research.

Candidates will have an outstanding record of international stature in cancer research. They will also have the vision, leadership, experience and enthusiasm to build on current strengths across cancer research and related disciplines in Cambridge. It is envisaged that the appointee will also be Director of the Cambridge Cancer Centre (http://www.cambridgecancercentre.org.uk/). Candidates should hold a PhD or equivalent postgraduate qualification. Applications would be particularly welcome from clinician scientists.

Candidates will lead a significant personal programme of laboratory, translational and/or clinical research in a relevant area. Facilities and resources to enable this are available in the constituent elements of the Cambridge Cancer Centre. Standard professorial duties include teaching and research, potential contribution to clinical service delivery, examining, supervision and administration. The Professor will be based on the Cambridge Biomedical Campus. A competitive salary will be offered.

We particularly welcome female applicants and those from an ethnic minority as they are under-represented within the University at this level.

Further information is available at: www.admin.cam.ac.uk/offices/academic/secretary/professorships/ or contact the Academic Secretary, University Offices, The Old Schools, Cambridge, CB2 1TT, (email: ibise@admin.cam.ac.uk), to whom a letter of application should be sent, together with details of current and future research plans, a curriculum vitae, a publications list and form CHRIS/6 (parts 1 and 3 only) with details of two referees, so as to reach him no later than 23 January 2014.

Informal enquiries may be directed to Professor Patrick Maxwell, e-mail: regius@medschl.cam.ac.uk, telephone: 01223 336738.

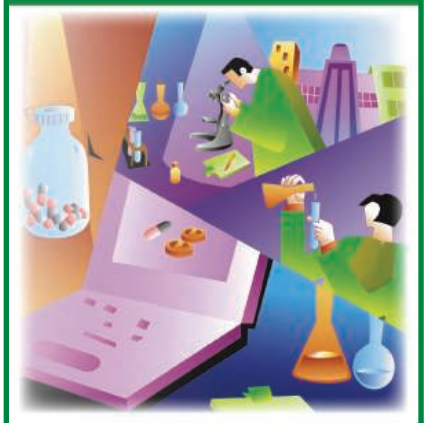
Please quote reference RD02394 on your application and in any correspondence about this vacancy.

Closing date: 23 January 2014

The University values diversity and is committed to equality of opportunity.

The University has a responsibility to ensure that all employees are eligible to live and work in the UK.

CAREER TRENDS Running Your Lab



Download your free copy today at ScienceCareers.org/booklets

Science Careers
From the journal *Science* AAAS

Brought to you by the AAAS/*Science* Business Office

Director and President
Monell Chemical Senses Center

The Monell Chemical Senses Center is the world's leading independent research organization dedicated to basic and translational science in the fields of taste, smell and chemesthesis. Over its 45 year history, Monell has become a globally-recognized leader in scientific discovery, expanding understanding of the chemical senses and their relation to human and animal health through research, training, and dissemination. The Center's highly collaborative scientific staff, with approximately 60 PhD-level investigators, includes organic chemists, molecular and cellular biologists, physiologists, psychologists, and nutrition and food scientists.

Competitive government research grants constitute the largest source of Monell's funding. The Center has been at the vanguard of successful academic-industry partnerships since its inception, and over 45 companies from around the world currently participate in its Corporate Sponsorship Program and help support its research programs. Foundation and philanthropic support also constitutes an important source of Center funding.

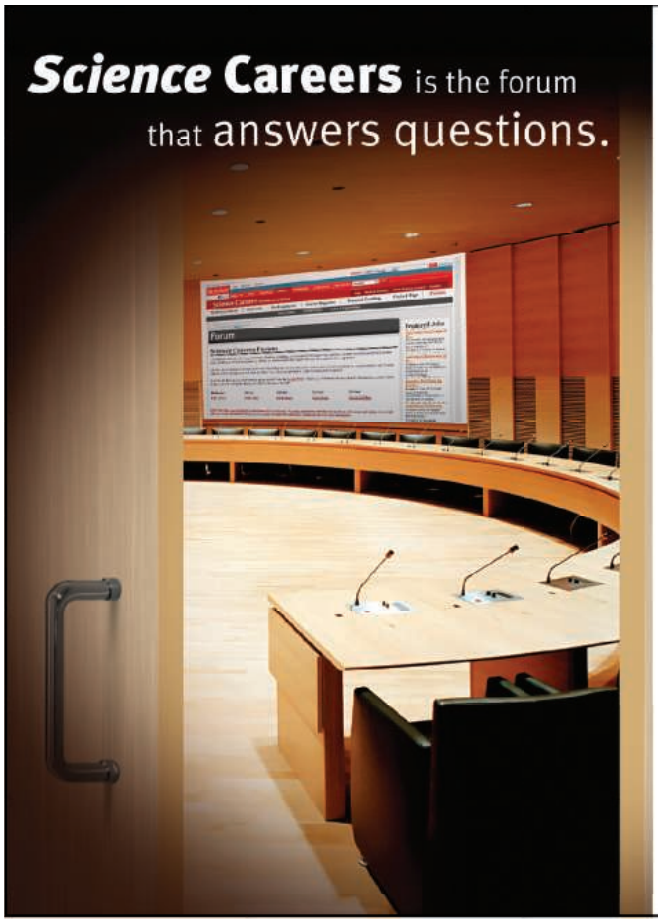
Monell is located in West Philadelphia adjacent to the campuses of the University of Pennsylvania and Drexel University. More details about Monell can be found at: www.monell.org.

The Director and President has overall responsibility for leadership of the Center. This includes strategic planning, scientific direction, program development and evaluation, fundraising, board development, public/community relations, marketing, financial management and operations. S/he provides oversight of Monell staff and its organizational budget. S/he serves on, and works closely with, the Board of Directors and designated committees to facilitate effective Board engagement and oversight.

The Director and President should have an international reputation as a scientist and a scholar. Although preference will be given to candidates who investigate the chemical senses, outstanding scientist/administrators from other areas will be given serious consideration. Senior administrative experience in non-profit scientific organizations is highly desired. An ability to foster collaboration within the Center and across collaborating academic, government and private institutions around the world is central to the success of the scientific, training and outreach missions of the Center.

Monell offers a competitive compensation and benefits package that includes medical and dental insurance for employees and their families, a 403(B) plan with a generous company contribution, disability and life insurance for employees, and holidays and paid time off. To apply, please email a complete biography including a letter of interest and contact information for at least three references, none of whom will be approached without first obtaining permission, to: **directorsearch@monell.org**. Evaluation of applicants will begin **February 24, 2014** and will continue until the search is successfully concluded.

Monell is an Equal Opportunity Employer.



Science Careers is dedicated to opening new doors and answering questions on career topics that matter to you. With timely feedback and a community atmosphere, our careers forum allows you to connect with colleagues and experts to get the advice and guidance you seek as you pursue your career goals.

Science Careers Forum:

- Relevant Career Topics
- Timely Advice and Answers
- Community, Connections, and More!

Visit the forum and join the conversation today!



Your Future Awaits.

Science Careers
From the journal *Science* AAAS
ScienceCareers.org

Assistant Professor: Molecular biology/genetics of aquatic infectious diseases

The Institute of Marine and Environmental Technology (IMET) of the University System of Maryland seeks applications for the position of Assistant Professor (tenure-track). The successful candidate will have a track-record of outstanding research using molecular biology/genetics approaches to study viral, bacterial or parasitic disease or the microbiome in shellfish or finfish. Candidates' research should address molecular or immunological aspects of major microbial and/or other infectious disease impacting aquaculture, fisheries, or ecologically important organisms in coastal or estuarine environments. Candidates with an interest in practical applications of their fundamental research, including interactions with industry, are encouraged to apply. A demonstrated ability to establish a well-funded research program is expected for the successful candidate. Primary appointment is in the Department of Marine Biotechnology at the University of Maryland Baltimore County, with a secondary appointment at the University of Maryland Baltimore. The primary focus of the appointee will be on research; teaching at the graduate level is encouraged. IMET's mission is to study the biology of coastal marine biosystems and ensure their sustainable use, as well as exploit marine-derived systems to improve human health (www.imet.usmd.edu). IMET brings together faculty members from three major USM research institutions - the University of Maryland Baltimore (UMB), the University of Maryland Baltimore County (UMBC), and the University of Maryland Center for Environmental Science (UMCES) - in a dedicated state-of-the-art research facility located in Baltimore's Inner Harbor.

A Ph.D. or equivalent terminal degree is required in molecular biology, microbiology, aquatic pathology or related fields and candidates should have postdoctoral experience and a strong publication record. Applicants should send the following in a single PDF file to Russell Hill, Director, IMET; email to **hill@umces.edu**: (1) detailed curriculum vitae, (2) statement of research interests and goals and (3) names and contact details of three to five references. To receive full consideration, application materials should be submitted by **February 15, 2014** (the position will be open until filled).

The USM is an Equal Opportunity, Affirmative Action Employer. UMBC values gender, ethnic and racial diversity; woman, members of ethnic minority groups, and individuals with disabilities are strongly encouraged to apply. UMBC is the recipient of an NSF ADVANCE Institutional Transformation Award to increase the participation of women in academic careers.



AAAS is here –
promoting universal science literacy.

In 1985, AAAS founded Project 2061 with the goal of helping all Americans become literate in science, matematics, and technology. With its landmark publications *Science for All Americans* and *Benchmarks for Science Literacy*, Project 2061 set out recommendations for what all students should know and be able to do in science, mathematics, and technology by the time they graduate from high school.

As a AAAS member, your dues help support Project 2061 as it works to improve science education. If you are not yet a member, join us. Together we can make a difference.

To learn more, visit aaas.org/plusyou/project2061

AAAS + U = Δ

UC DAVIS
UNIVERSITY OF CALIFORNIA

Assistant/Associate Professor in Plant Sciences – Postharvest Physiologist

Department of Plant Sciences

LOCATION: University of California, Davis, CA

RESPONSIBILITIES: The Department of Plant Sciences in the College of Agricultural and Environmental Sciences at the University of California Davis invites applications for a faculty appointment at the Assistant/Associate Professor level in Postharvest Biology. The successful candidate will establish a vigorous and dynamic research program as well as an innovative teaching program at both the undergraduate and graduate levels. The research will focus on postharvest biology of horticultural crops. It is expected that the research program will draw upon practical knowledge of postharvest processes and technology as well as upon related disciplines in genomics, plant pathogen interactions, biochemistry or plant developmental biology especially in areas such as senescence or fruit ripening. An intended outcome of these discoveries will be identification of processes or traits that can be manipulated to improve postharvest handling strategies and ultimately postharvest quality of fruits, vegetables or ornamentals. The position is a 9-month tenure track appointment. This position will include an appointment in the Agricultural Experiment Station, which includes the responsibility to conduct research and outreach relevant to the mission of the California Agricultural Experiment Station

QUALIFICATIONS: Ph.D. in plant biology, horticulture, biochemistry, genetics or related discipline with experience and documented interest in postharvest plant biology. International experience is desirable.

SALARY: Commensurate with qualifications and experience.

TO APPLY: Candidates should begin the application process by registering online at **http://apptrkr.com/411069** . Please include statements of research goals for this position and teaching philosophy, curriculum vitae, publication list, copies of 3 of your most important research publications, copies of undergraduate and graduate transcripts (if within 5 years of either degree), and the names, e-mail addresses, and telephone numbers of at least five professional references. For technical or administrative questions regarding the application process please email kgeer@ucdavis.edu . Review of the applications will begin April 1, 2014. The position will remain open until filled.

UC Davis is an affirmative action/equal employment opportunity employer and is dedicated to recruiting a diverse faculty community. We welcome all qualified applicants to apply, including women, minorities, veterans, and individuals with disabilities.

澳門大學
UNIVERSIDADE DE MACAU
UNIVERSITY OF MACAU



Recruitment of Vice Rector (Vice President) for Academic Affairs

The University of Macau is the leading higher educational institution in Macao: it enjoys generous support from the Macao SAR and the local community; and it is achieving international recognition for its excellence in teaching and research. The University is now embarked on an ambitious development plan, growing rapidly in terms of student numbers, and in terms of academic staff - who are recruited world-wide. A new purpose-designed campus, more than one square kilometre in size and comprising more than sixty buildings, was opened in November 2013, with the full relocation scheduled to take place in 2014. Further strategic initiatives will follow, including the establishment of the largest Residential College system in Asia. The University has a strong tradition of service to the local community; and, in keeping with its international perspective, English is the University's working language.

The University is conducting a global search for the position of Vice Rector (i.e. Vice President or Pro-Vice Chancellor) with special responsibility for Academic Affairs. In this role the successful candidate will deputise for the Rector in all academic and related matters, coordinating all academic activities at local, national and international levels that contribute to the University's strategic academic direction. He/she will also oversee the academic activities of the faculties, as well as other independent academic units, including both the appointment of academic staff and the oversight of those aspects of the University's assurance systems designed to underpin and guarantee the high quality of the University's teaching and research.

He/she should have strong academic credentials as a Full Professor or above in a reputable higher educational institution, and will preferably assume the position by the Fall of 2014.

The candidate is expected to have:

1. An earned doctorate degree;
2. Understanding of best international higher education practice, particularly in the areas of teaching and research;
3. At least 5 years experience in a senior academic management position;
4. Demonstrable competence in managing sizable groups of academics and professionals;
5. Keen interest in and strong commitment to upholding the academic quality and standard of the University.

Remuneration

The remuneration and rank offered will be competitive and commensurate with the successful applicants' academic qualifications, current position and professional experience. The current local maximum income tax rate is 12% but is effectively around 5% - 7% after various discretionary exemptions.

Application Procedure

More details about the job vacancy can be accessed at http://www.umac.mo/vacancy. Applicants and nominators are encouraged to send a cover letter, detailed curriculum vitae and other related materials with quotation of reference no. **VRAA/11/2013** preferably on or before **February 1, 2014** to the following address. The position will remain open until filled. The University has appointed Heidrick & Struggles International, Inc. to assist in the search process for this position. Review of applications and nominations will commence immediately. Applicants may consider their applications not successful if they were not invited for an interview within 3 months of application.

Human Resources Office, University of Macau
Av. Padre Tomás Pereira Taipa, Macau, China
Email: VRAA.recruit@umac.mo
Tel: +853 8397 8684 or +853 8397 8593

******Personal data provided by applicants will be kept confidential and used for recruitment purpose only******

University of Macau –
An ideal place to pursue your career

http://www.umac.mo

Science Careers online @sciencecareers.org

POSITIONS OPEN

EPPLEY INSTITUTE
FOR RESEARCH IN CANCER

FACULTY POSITIONS

The University of Nebraska Medical Center (UNMC) Eppley Institute, and the NCI-designated Fred & Pamela Buffett Cancer Center seek candidates for full-time tenure-track faculty positions. Candidates are expected to develop an independent, extramurally funded research program in basic/translational cancer research complementary to existing strengths and allied with the overall directions of the Cancer Center. They should expect to participate in graduate-level teaching in the Cancer Research Graduate Program and/or other UNMC graduate programs and engage in institutional service commensurate with their expertise.

Individuals with projects focused on (a) identifying novel therapeutic agents using high throughput/systems biology, (b) targeted cancer therapies, and/or (c) experimental cancer models are encouraged to apply.

The anticipated start date is July 1, 2014. *Equal Employment Opportunity/Affirmative Action individuals from diverse backgrounds are encouraged to apply.* To apply, go to **website: https://jobs.unmc.edu** and reference **requisition 2013-239.** Additional information at **website: http://www.unmc.edu/cancercenter.**

Your career is our cause.

Get help from the experts.

www.sciencecareers.org

- Job Postings
- Job Alerts
- Resume/CV Database
- Career Advice
- Career Forum

Science Careers
From the journal *Science* AAAS

☑ More scientists agree —we are the most useful website.
www.ScienceCareers.org

Download your free copy today.

ScienceCareers.org/booklets



From technology specialists to patent attorneys to policy advisers, learn more about the types of careers that scientists can pursue and the skills needed in order to succeed in nonresearch careers.

Science Careers
From the journal *Science* AAAS